Brown Dwarf Companions to Young Solar Analogs: An Adaptive Optics Survey Using Palomar and Keck

Thesis by
Stanimir A. Metchev

In Partial Fulfillment of the Requirements
for the Degree of
Doctor of Philosophy

California Institute of Technology
Pasadena, California

2006

(Defended August 18, 2005)

Acknowledgements

Stan, congratulations. I just can't believe you made it.
Cheers, Jeff Hickey

Having left this for last, I now finally have the peace of mind and hindsight to recollect and thank all the people that supported me, guided me, and kept me sane throughout my graduate work.

First and foremost are my parents, Anguel and Kalitchka, whom I have rarely seen for more than 2 weeks a year over the past 10 years, but whose faith in me has always pushed me forward, even from the distance of my home country, Bulgaria. I thank my father for showing me the stars and making me aware of a Universe open to endless exploration. I thank my mother for her unconditional support, even when she thought that I should have taken up Economics, rather than Astronomy. My parents and my brother, Anton, are the three people in this world that have defined how I think, feel, and love.

My advisor, Lynne Hillenbrand, is the person to whom I owe by far the most for my development as a scientist. I feel very fortunate to have been taken on as her student. Lynne's balance of encouragement and criticism, her ability to manage while allowing independence, and her camaraderie with her students form a rare ensemble of qualities in an advisor, with the benefits of which I hope to endebt my own students one day.

I would like to extend my sincere gratitude to the past and present members of my thesis committee: Lynne Hillenbrand, Andrew Blain, Shri Kulkarni, Richard Dekany, Re'em Sari, and David Stevenson. I have benefited from multiple discussions and guidance from every one of them, even before they were confronted with the present tome.

I have also been fortunate to be fully immersed in the Formation and Evolution of Planetary Systems (FEPS) *Spitzer* Legacy team, which combines a unique array of theoretical and observational expertise on topics ranging from young stars and circumstellar matter to space-based imaging and high-resolution spectroscopy.

Among the members and associates of the team that have been most influential on me, I single out Lynne Hillenbrand (again), Michael Meyer, Russel White, Sebastian Wolf, and John Carpenter, with whom I have had the pleasure to work in close collaboration. John also developed and maintains the FEPS team database, that has been of central importance in managing the large volume of data compiled in this thesis.

The quality of the data gathered for this work would have paled in comparison to its present state, had it not been for the dedication and professionalism of the Palomar and Keck adaptive optics (AO) teams, lead by Mitchell Troy, Richard Dekany, and Peter Wizinowich. Multiple discussions with Mitch and Rich, as well as with Tom Hayward, Matthew Britton, Hal Petrie, Keith Matthews, David Thompson, Randy Campbell, David Le Mignant, and Marcos van Dam have helped me overcome my initial frustrations with the complexity of AO and become a proficient AO user, excited about the tremendous possibilities offered by the technology. Rich and Hal also helped me design the Palomar AO astrometric experiment that proved crucial for the successful completion of the present work in a timely fashion. Keith provided the astrometric mask for the experiment, as well as key insights for interpreting the experiment data. Keith and David were also exceptionally kind in obtaining science observations for the present work on several occasions.

The Palomar 200-inch telescope was the backbone for my thesis research. With more than 70 nights spent at the observatory during my 5 years at Caltech, I am very grateful to the people who made me want to go back there every time: Dipali and Rose for the warm hospitality and the delicious meals at the Palomar Monastery; Jean Mueller and Karl Dunscombe for their professionalism at the telescope controls and for putting up with my erratic choices of music late at night; Rick Burress and Jeff Hickey for their selfless dedication to ensuring the flawless performance of the Palomar AO system, and Jeff—for the excellent email greeting on the day of my defense, quoted at the beginning; Steve, Greg, Dave, John, and the rest of the Palomar day-crew for routinely doing the huge amount of work that it takes every day to keep the observatory running and the astronomers

happy.

With this I come to my close friends. I thank all of you who kept me sane over the years and months before my defense, who came to support me during the defense itself, and who celebrated with me afterwards. In particular, I need to acknowledge my office mates and "brothers in arms" Dave Sand, Kevin Bundy, and Josh Eisner. Between them and Russel White, there would always be a good occasion for mid-week drinks at Amigos or Burger Continental. Also, having gone through the job-hunting and thesis ordeals at the same time as Josh and Dave has certainly helped me maintain focus and keep the pace.

My close friendship with Alex "Dude" Williamson and the warm hospitality of the Williamsons and the Redferns has been a staple of my American experience. Alex, Jon, Sue, and Drew Williamson, and Greg, Laurie, Rachel, and Dan Redfern: thank you all for being my family away from home.

Finally, there is one person who saw and heroically put up with the worst of it, and whose down-to-earth view on life carried me through. My lovely future wife, Anne Simon. I owe you an enormous debt of love and patience. Having you beside me over the past 4 years has given me a balance that I had never attained before.

Brown Dwarf Companions to Young Solar Analogs:
An Adaptive Optics Survey Using Palomar and Keck

by

Stanimir A. Metchev

In Partial Fulfillment of the
Requirements for the Degree of
Doctor of Philosophy

Abstract

We present results from an adaptive optics survey conducted with the Palomar and Keck telescopes over 3 years, which measured the frequency of stellar and sub-stellar companions to Sun-like stars. The survey sample contains 266 stars in the 3–10000 million year age range at heliocentric distances between 8 and 200 parsecs and with spectral types between F5–K5. A sub-sample of 101 stars, between 3–500 million years old, were observed in deep exposures with a coronagraph to search for faint sub-stellar companions. A total of 288 candidate companions were discovered around the sample stars, which were re-imaged at subsequent epochs to determine physical association with the candidate host stars by checking for common proper motion. Benefiting from a highly accurate astrometric calibration of the observations, we were able to successfully apply the common proper motion test in the majority of the cases, including stars with proper motions as small as 20 milli-arcseconds year^{-1}.

The results from the survey include the discovery of three new brown dwarf companions (HD 49197B, HD 203030B, and ScoPMS 214B), 43 new stellar binaries, and a triple system. The physical association of an additional, a priori-suspected, candidate sub-stellar companion to the star HII 1348 is astrometrically confirmed. The newly-discovered and confirmed young brown dwarf companions span a range of spectral types between M5 and T0.5, and will be of prime signifi-

cance for constraining evolutionary models of young brown dwarfs and extra-solar planets.

Based on the 3 new detections of sub-stellar companions in the 101 star sub-sample and following a careful estimate of the survey incompleteness, a Bayesian statistical analysis shows that the frequency of 0.012–0.072 solar-mass brown dwarfs in 30–1600 AU orbits around young solar analogs is $6.8^{+8.3}_{-4.9}\%$ (2σ limits). While this is a factor of 3 lower than the frequency of stellar companions to G-dwarfs in the same orbital range, it is significantly higher than the frequency of brown dwarfs in 0–3 AU orbits discovered through precision radial velocity surveys. It is also fully consistent with the observed frequency of 0–3 AU extra-solar planets. Thus, the result demonstrates that the radial-velocity "brown dwarf desert" does not extend to wide separations, contrary to previous belief.

Contents

1 Introduction **1**

1.1 Brown Dwarfs: A Brief Summary of Properties 2

1.1.1 Similarities to Stars 6

1.1.2 Similarities to Planets 6

1.1.3 A Matter of Terminology: Low-mass Brown Dwarfs vs. Planets 7

1.1.4 Theoretical Models of Sub-stellar Evolution 8

1.2 How Frequent are Brown Dwarf Companions and Why Study Them? 10

1.3 Observational Challenges and Constraints 15

1.4 The Observational Approach at a Glance 18

1.5 Thesis Outline 19

2 Survey Sample **20**

2.1 Overview 20

2.2 Selection Criteria 22

2.2.1 Spectral Types and Stellar Masses 22

2.2.1.1 Spectral Types: Dependence on Color, Reddening, and Surface Gravity 22

2.2.1.2 Masses: Dependence on Age 24

2.2.2 Stellar Ages 27

2.2.3 Distances and Proper Motions 32

2.3 Sample Selection 35

2.3.1 FEPS Sample Selection 35

2.3.2 AO Sample Selection: Further Constraints and Additions . 38
2.4 Sample Biases and Discussion 50
2.4.1 Examining the Biases 50
2.4.2 Discussion 52
2.5 Unique Advantages of the Present Survey in Comparison to Others 52
2.5.1 The Palomar/Keck AO Sample is Young 53
2.5.2 The Palomar/Keck AO Sample Has a High Median Mass . 54
2.5.3 The Palomar/Keck Survey Uses a High-Order AO System 58
2.5.4 Comparison to Recent, Higher-Contrast Surveys and Summary 58

3 Observations and Methodology 60
3.1 Overview 60
3.2 Adaptive Optics Observations of Vega: Eight Detected Sources and Upper Limits to Planetary-mass Companions 63
3.2.1 Introduction 64
3.2.2 Observations 65
3.2.3 Data Processing 67
3.2.4 Photometry of Detected Sources 70
3.2.5 Analysis 71
3.2.5.1 Sensitivity Limits 71
3.2.5.2 Comparisons to Models 73
3.2.6 Discussion 78
3.2.7 Conclusions 79
3.3 Initial Results from the Palomar Adaptive Optics Survey of Young Solar-type Stars: A Brown Dwarf and Three Stellar Companions . 80
3.3.1 Introduction 81
3.3.2 Observing Strategy 83
3.3.2.1 Imaging 83
3.3.2.2 Astrometric Calibration 90

3.3.2.3 Spectroscopy 91
3.3.3 Analysis 94
3.3.3.1 Photometry 94
3.3.3.2 Astrometry 99
3.3.3.3 Spectroscopy 105
3.3.4 Discussion 113
3.3.4.1 Likelihood of Physical Association 113
3.3.4.2 Stellar Ages and Companion Masses 116
3.3.4.3 HD 129333: Binary or Triple? 118
3.3.4.4 HD 49197B: A Rare Young L Dwarf 125
3.3.4.5 Sub-Stellar Companions to Main-Sequence Stars . 126
3.3.5 Conclusion 129

4 Pixel Scale and Orientation of PHARO 131

4.1 Pre-amble 131
4.2 Introduction 132
4.3 Experiment Description 134
4.3.1 Astrometric Mask Experiment 135
4.3.1.1 Assembly 135
4.3.1.2 Tests 139
4.3.1.3 Astrometric Measurements 141
4.3.2 Binary Star 142
4.3.2.1 Observations 144
4.3.2.2 Tests 147
4.3.2.3 Astrometric Measurements 147
4.4 Analysis and Results 150
4.4.1 Pixel Scale Distortion as a Function of Detector Position . 150
4.4.2 Pixel Scale Variation with Hour Angle and Declination . . 152
4.4.3 Absolute Calibration of the Pixel Scale Distortion 155
4.4.3.1 Additional Parameterization: Beam Tilt 155

4.4.3.2 Solving for the Beam Tilt 160
4.4.3.3 Complete Characterization of the Detector Distortion 161
4.4.4 Absolute Pixel Scale of the 25 mas pix^{-1} PHARO Camera 163
4.4.5 Other Sources of Pixel Scale Variations 168
4.4.5.1 Cassegrain Ring Orientation 168
4.4.5.2 Choice of Intermediate Optics 169
4.4.5.3 Detector Readout 169
4.5 Conclusion of the PHARO Pixel Scale Experiment 170
4.6 Astrometry with PHARO and NIRC2: Errors and Accuracy . . . 170

5 Complete Survey: Observations, Detection, and Association of Candidate Companions 174

5.1 Observations 174
5.1.1 Choice of PHARO Lyot Stop and the Use of a Neutral Density Filter 191
5.1.2 Choice of NIRC2 Coronagraphs and Pupil Mask 194
5.1.3 Rotating the Cassegrain Ring at Palomar: The Cons Outweigh the Pros 195
5.2 Object Detection—Limits 198
5.2.1 Automatic Source Detection Is Not Well-suited to High-Contrast AO Imaging 198
5.2.2 Visual Source Detection and Limits 200
5.2.3 R.M.S. Noise Detection Limits 202
5.2.4 Ensemble Detection Limits for the Deep Sample 204
5.3 Detected Candidate Companions 207
5.4 Deciding Physical Association 224
5.4.1 Proper Motion 227
5.4.1.1 Astrometric Example: The Candidate Companions to HD 49197 Re-visited 228

5.4.2 Absolute Magnitude, Near-IR Colors, and Background Object Density . . . 233
5.4.3 Source Extent . . . 236
5.4.4 Astrometry from the Literature . . . 238
5.4.5 Undecided Objects . . . 238

6 Survey Results and Analysis 240
6.1 Brown Dwarf Secondaries . . . 240
6.1.1 HD 49197B . . . 241
6.1.2 HD 203030B . . . 241
6.1.2.1 Astrometric Confirmation . . . 241
6.1.2.2 Spectral Type and Mass of HD 203030B . . . 246
6.1.3 ScoPMS 214B . . . 249
6.1.3.1 Astrometric Confirmation . . . 249
6.1.3.2 Spectral Type and Mass of ScoPMS 214B . . . 250
6.1.4 HII 1348B: A Secondary at the Stellar/Sub-stellar Boundary 252
6.1.4.1 Astrometric Confirmation . . . 252
6.1.4.2 Spectral Type and Mass of HII 1348B . . . 253
6.1.5 A Critical Discussion of Sub-stellar Model Masses: Are the Detected Companions Truly Brown Dwarfs? . . . 254
6.2 Incompleteness Analysis of the Deep Survey . . . 257
6.2.1 Factors Affecting Incompleteness . . . 257
6.2.2 Assumptions . . . 258
6.2.3 Incompleteness Analysis . . . 260
6.2.3.1 Geometrical Incompleteness . . . 261
6.2.3.2 Observational Incompleteness . . . 263
6.2.3.3 Orbital Incompleteness . . . 264
6.2.3.4 Further Incompleteness: Undecided Companion Candidates . . . 269
6.3 Frequency of Wide Sub-stellar Companions to Young Solar Analogs 270

6.4 Stellar Secondaries 274
6.4.1 Frequency of Multiple Systems 278
6.4.2 Distribution of Mass Ratios 280
6.4.3 Orbital Motion in Previously Known Binary and Multiple Systems 282

7 Discussion and Summary **283**
7.1 Comparison to the Results of McCarthy & Zuckerman (2004) . . . 284
7.1.1 Completeness Estimate of the McCarthy & Zuckerman (2004) Survey 285
7.1.2 Age Estimate of the McCarthy & Zuckerman (2004) Sample 287
7.1.2.1 A Space-motion Selected Sample Needs Independent Age Verification 287
7.1.2.2 The McCarthy & Zuckerman (2004) Sample Is Statistically 1 Gyr Old 288
7.1.3 Comparison of Sensitivities to Sub-stellar Companions . . . 290
7.2 Comparison to Previous Multiplicity Results 291
7.2.1 Other Direct Imaging Surveys for Sub-stellar Companions . 291
7.2.2 Comparison to Planetary and Stellar Multiplicity: No Brown Dwarf Desert at >30 AU from Solar Analogs 294
7.3 Future Directions 294
7.4 Summary 296

A Adaptive Optics Imaging of the AU Microscopii Circumstellar Disk: Evidence for Dynamical Evolution **298**
A.1 Introduction 299
A.2 Observations and Data Reduction 302
A.3 Results and Analysis 305
A.3.1 Circumstellar Dust Morphology 305
A.3.2 Disk Luminosity, Optical Depth, and Geometry 310
A.3.3 Detection Limits on Sub-Stellar Companions 311

A.4 Dust Disk Modeling 313
A.4.1 Model and Method 313
A.4.2 Breaking Degeneracies in the Model Parameters 315
A.5 Discussion 320
A.5.1 Minimum Grain Size as a Function of Disk Radius 320
A.5.2 The Change in the SBP Power-law Index: A Comparison with β Pic 322
A.5.2.1 Ice or Comet Evaporation 324
A.5.2.2 A Belt of Parent Bodies 324
A.5.2.3 Collisional Evolution 325
A.5.2.4 Poynting-Robertson Drag 326
A.5.2.5 Summary of Proposed Scenarios 327
A.6 Conclusion 328

List of Figures

1.1 Models of Sub-stellar Luminosity Evolution 4
1.2 Models of Sub-stellar Cooling 5
1.3 Color-magnitude Diagram of Brown Dwarfs vs. DUSTY and COND Models 11

2.1 Distribution of the Sample Stars as a Function of $T_{\rm eff}$ and M . . . 25
2.2 M_{K_S} vs. $J - K_S$ Diagram of the Survey Sample 30
2.3 Age Distribution of the Survey Sample 33
2.4 Distance and Proper Motion Distributions of the Survey Sample . 35
2.5 Age vs. Distance Diagram of the Survey Sample 55

3.1 Candidate Companions to Vega 69
3.2 H-band Sensitivity Limits of the Vega Observations 74
3.3 Near-IR Color-magnitude Diagrams of the Candidate Companions 76
3.4 Near-IR Color-color Diagram of the Candidate Companions 77
3.5 Images of the Brown Dwarf Companion to HD 49197 89
3.6 Images of the Three Stellar Companions 90
3.7 K-band Spectra of All Four Companions 95
3.8 J-band Spectra of HD 129333B and V522 PerB 96
3.9 Near-IR Color-color Diagram of the Detected Companions 100
3.10 Proper Motion Diagram for HD 49197B and "C" 102
3.11 Proper Motion Diagram for HD 129333B 103
3.12 Proper Motion Diagrams for V522 PerB and RX J0329.1+0118 . . 104

3.13 Comparison of Photometric and Spectroscopically Inferred Absolute Magnitudes 114
3.14 Radial Velocity Data for HD 129333 120

4.1 A Top View of the PALAO Bench 136
4.2 Set-up Diagram for the Astrometric Mask Experiment 137
4.3 A Sketch of the Reticle 138
4.4 A Background-subtracted Image of the Reticle Pattern 140
4.5 Pixel Distances between Neighboring Grid Spots in the Reticle Image 143
4.6 Images of the Calibration Binary WDS 16147+3352 148
4.7 Positional and Cassegrain Ring Angle Dependence of the PHARO Pixel Scale 149
4.8 Intrinsic Geometric Distortion of the PHARO Camera in 25mas pix^{-1} Mode 153
4.9 Two-dimensional Polynomial Fits to the Linear Coefficients in Eqns. 4.1 and 4.2 156
4.10 Diagram of the Intersection between the Image Plane and the Tilted-beam Plane 159
4.11 Positional and Cassegrain Ring Angle Dependence of the PHARO Pixel Scale after Correcting for Distortion 162
4.12 Total Distortion on the PHARO Camera in 25mas pix^{-1} Mode . . 164

5.1 Example Coronagraphic Images with the Big and Medium Lyot Stops 193
5.2 Survey Detection Limits at Palomar and Keck 203
5.3 Contrast and Flux Completeness of the Deep Survey 206
5.4 ΔK_S vs. Angular Separation for All Candidate Companions 225
5.5 Proper Motion Diagrams of Candidate Companion 1 to HD 49197 229
5.6 Proper Motion Diagrams of Candidate Companion 2 (HD 49197B) to HD 49197 232
5.7 M_{K_S} vs. $J - K_S$ Color-magnitude Diagram for Candidate Companions with J-band Photometry 235

6.1 H–R Diagrams of the New Brown Dwarfs and Model Predictions . 244
6.2 K_S-band Images of HD 203030A/B 245
6.3 Proper Motion Diagrams of HD 203030B 246
6.4 K_S-band Images of ScoPMS 214A/B 250
6.5 Proper Motion Diagrams of ScoPMS 214B 251
6.6 K_S-band Images of HII 1348A/B 253
6.7 Proper Motion Diagrams of HII 1348B 254
6.8 Projected Physical Separations Probed in the Deep Survey 262
6.9 Observational and Orbital Completeness of the Deep Sample Survey 265
6.10 Orbital Incompleteness (SVOC) 268
6.11 Probability Density Distribution for the Sub-stellar Companion Frequency in a Survey of 101 Stars 273
6.12 Distribution of Companion Mass Ratios 281

A.1 H-band Images of AU Mic 304
A.2 Median Ratios of the Radial Profiles of AU Mic and HD 195720 . . 306
A.3 Reduced Images of the AU Mic Disk 308
A.4 H-band Surface Brightness Profiles of the NW and SE Arms of the AU Mic Disk 309
A.5 H-band 5σ Detection Limits for Companions to AU Mic 312
A.6 Degeneracies in the Models of the AU Mic SED 317
A.7 SED of AU Mic and Disk 319

List of Tables

2.1 Median Sample Statistics 21
2.2 Survey Sample 40

3.1 Near-infrared Point Sources in the Vicinity of Vega 72
3.2 Observations 84
3.3 Properties of the Observed Stars 85
3.4 IR Magnitudes and Colors of the Companions 98
3.5 Astrometry of the Companions 101
3.6 Spectroscopic Measurements for the Companions 107
3.7 Estimated Properties of the Companions 108

4.1 Observed Calibration Binaries and Parameters of Their Relative Orbits 145
4.2 Observations of Calibration Binaries 146
4.3 Preliminary Distortion Coefficients for the 25 mas PHARO Camera with the Telescope Pointed at Zenith 154
4.4 Coefficients in the Expansions of a_1 (Eqn. 4.3) and b_2 (Eqn. 4.4) . 157
4.5 Final Distortion Coefficients and Expressions at Arbitrary Telescope Hour Angle and Declination 158
4.6 Pixel Scale and Orientation of the 25 mas pix^{-1} PHARO Camera . 165

5.1 Palomar Observations 176
5.2 Keck Observations 178
5.3 Deep Sample Observations 179

5.4 Shallow Sample Observations 186
5.5 Magnitude Extinction due to PHARO and NIRC2 Optics 194
5.6 Candidate Companions in the Deep Sample 209
5.7 Candidate Companions in the Shallow Sample 218
5.8 Deep Sample Stars without Candidate Companions 223
5.9 Shallow Sample Stars without Candidate Companions 223
5.10 Observed Change in Relative Position for Candidate Companions to HD 49197 230
5.11 Expected Change in Relative Position for Candidate Companions to HD 49197 231
5.12 Color Companions and Their Chance Alignment Probabilities . . . 237

6.1 Near-IR Photometry of the Confirmed and Candidate Brown Dwarfs 242
6.2 Estimated Physical Properties of the Sub-stellar Companions . . . 243
6.3 Properties of the Detected Stellar Companions 275

A.1 Preferred Model Parameters for the AU Mic System 318

Chapter 1

Introduction

Brown dwarfs make rare companions to stars. This is the current belief in the field of sub-stellar astronomy, based both on precision radial velocity (RV) surveys, probing orbital separations of <5 astronomical units (AU; Marcy & Butler, 2000), and on direct imaging efforts, probing orbital separations >100 AU (Oppenheimer et al., 2001; McCarthy & Zuckerman, 2004). However, while the radial velocity "brown-dwarf desert" remains nearly void, even after the discovery of numerous extra-solar planets over the last decade, the direct imaging brown-dwarf desert appears to be, slowly but surely, becoming populated. How confident are we of the lack of brown dwarfs in wide orbits around stars? Does the direct imaging brown-dwarf desert indeed exist? The few wide brown-dwarf companions that *have* been imaged around main sequence stars have provided a disproportionately large wealth of information on the physics of sub-stellar objects, in comparison with their isolated counterparts. A prime example for this is Gl 229B–the first decidedly sub-stellar object to be discovered through imaging (Nakajima et al., 1995) and still the prototype for the coolest objects at the bottom of the main sequence. The reason for this success is the scientifically optimal environment inhabited by brown-dwarf secondaries in wide orbits. Unlike close-in sub-stellar companions found from RV surveys, wide ($> 10 - 100$ AU) brown-dwarf companions are directly accessible for imaging and spectroscopy, thus allowing a characterization of their photospheric and thermodynamic properties. Unlike isolated free-floating brown dwarfs, brown

dwarfs in multiple systems have a well-constrained age (when physically associated with a star) and may allow a dynamical measurement of their mass (when in close binaries). That is, wide brown-dwarf companions to stars offer the best opportunity to fully determine the properties and trace the evolution of sub-stellar objects. From a scientific point of view, it would be rather unfortunate, if wide brown-dwarf companions to stars did indeed turn out to be rare.

With the present work, we aim to obtain a decisive determination of the frequency of wide brown-dwarf companions to stars. By targeting a large number of young Sun-like stars, we aim to establish a sample of young brown dwarfs with a well-determined age, whose physical properties can be used to improve our current knowledge of sub-stellar objects, and that can serve as reference in future studies.

The introductory chapter continues with a brief overview of definitions and brown-dwarf properties (§1.1). The main scientific goals of the thesis in their justification in the context of sub-stellar astronomy, are set forth in §1.2. Section §1.3 presents the observational challenges and constraints, and §1.4 summarizes the adopted observational approach for achieving the goals. Section §1.5 outlines the contents of the thesis by chapters.

1.1 Brown Dwarfs: A Brief Summary of Properties

We start with a brief overview of the physical and observable properties of brown dwarfs, and of their perceived place in our understanding of the Universe in between stars and extra-solar planets.

Brown dwarfs are the most recently discovered objects at the bottom of the main sequence. The new spectral types coined for these objects–L and T (Kirkpatrick et al., 1999)–represent the first major extension of the standard Morgan-Keenan OBAFGKM classification scheme (Cannon & Pickering, 1901; Morgan et al., 1943). Implied in this taxonomic expansion is the recognition of the discovery of a fundamentally new type of object. Their masses are too low, less than 0.07–0.08 of a solar mass ($M_{\odot}$; our Sun is $1M_{\odot}$), to ever raise the core tempera-

ture to sufficiently high values ($\sim 3 \times 10^6$ K) to induce hydrogen fusion (Kumar, 1963; Hayashi & Nakano, 1963; Burrows & Liebert, 1993; Baraffe et al., 1995). Thus, brown dwarfs are "sub-stellar" objects, and, unlike stars, cool eternally. The distinction between stellar and sub-stellar objects is illustrated in Figures 1.1 and 1.2, which show theoretical luminosity evolution tracks for low-mass stars and brown dwarfs from Burrows et al. (1997, 2001). The bifurcation in the luminosity and effective temperature ($T_{\rm eff}$) evolution at an age of 0.5–1.0 giga-years (Gyr) straddles the hydrogen-burning mass limit. The exact value of this limit is known to be metallicity-dependent, ranging from 0.083–0.085$M_\odot$ at zero metallicity, to 0.072–0.075$M_\odot$ at solar metallicity (Burrows & Liebert, 1993; Burrows et al., 1997; Chabrier & Baraffe, 1997; Chabrier et al., 2000). Figure 1.1 also demonstrates that, even though massive brown dwarfs may start out with star-like luminosity ($\gtrsim 10^{-3}$ solar luminosities [$L_\odot$]), they progressively dim with age to the point where all sub-stellar objects are less luminous than the dimmest, lowest-mass, stars after 0.5 Gyr. In terms of effective temperature ($T_{\rm eff}$) and spectral type, brown dwarfs may start as star-like objects hotter than 2200 K, with spectral type M (Kirkpatrick et al., 1999). As they get older, brown dwarfs pass through the later L ($1400 \lesssim T_{\rm eff} \lesssim 2200$ K; Kirkpatrick et al., 1999; Leggett et al., 2001) and T ($T_{\rm eff} \lesssim 1300$ K; e.g., Burgasser et al., 2002) spectral types (Fig. 1.2).

Because of the small amount of luminosity flux originating from their cores, gas pressure is insufficient to counteract gravity in the equation of state of sub-stellar objects. Brown dwarfs are thus compact objects, partially supported against gravitational collapse by electron degeneracy pressure (at early spectral types) and Coulomb pressure (at late spectral types; Stevenson, 1991; Burrows & Liebert, 1993). Hence, their radii R vary only slowly with mass M. The exact functional dependence $R(M)$ is dependent on the relative partition of gas, electron degeneracy, and Coulomb pressure, though for most of the sub-stellar regime varies between $R \propto M^{-1/3}$ and $R \propto M^0$ (Burrows & Liebert, 1993), i.e., the radii of brown dwarfs are nearly mass-independent.

More detailed, in-depth reviews of the physics of sub-stellar objects can be

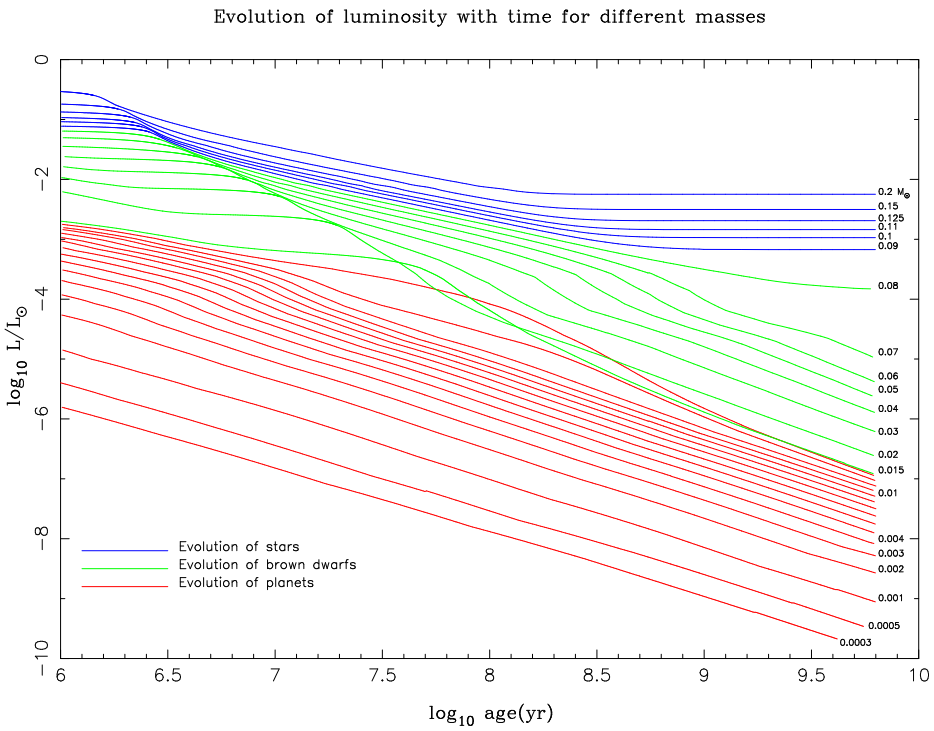

Figure 1.1: Sub-stellar and low mass stellar luminosity evolution tracks from Burrows et al. (1997). Object masses (in $M_{\odot}$) are marked to the right-hand side of the corresponding luminosity tracks. The top set of lines (0.08–0.2$M_{\odot}$) shows stellar evolutionary tracks, the middle set (0.015–0.08$M_{\odot}$) traces brown-dwarf tracks, and the lowest set (0.0003–0.015$M_{\odot}$) traces "planet" tracks. (Courtesy of A. Burrows)

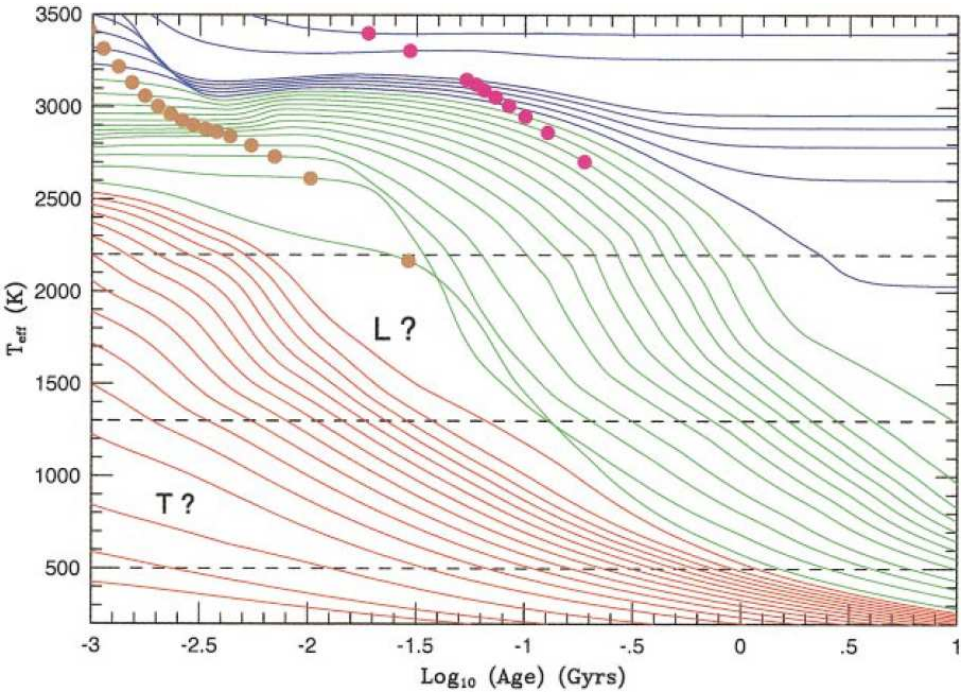

Figure 1.2: Evolution of the effective temperature of low-mass stars and brown dwarfs, as predicted by Burrows et al. (2001). The sets of continuous lines are the same as in Figure 1.1. Horizontal dashed lines mark the approximate effective temperature limits of the M, L, and T spectral types. Note that the lowest-mass ($\approx 0.08 M_{\odot}$) hydrogen-burning stars at >3 Gyr ages are L dwarfs, while all $>0.010 M_{\odot}$ brown dwarfs start as M dwarfs. The two sets of filled circles (not discussed in the present text) mark the 50% depletion loci for deuterium (left) and lithium (right). (Burrows et al., 2001)

found in Stevenson (1991); Burrows & Liebert (1993); Chabrier & Baraffe (2000), and Burrows et al. (2001).

1.1.1 Similarities to Stars

Despite their fundamentally different nuclear physics from that of main sequence (MS) stars, brown dwarfs are expected to follow the same mode of formation as (at least low-mass) stars (Bate et al., 2003; Padoan & Nordlund, 2004). That is, there does not exist an a priori set switch in nature that would distinguish between stellar and sub-stellar objects at the epoch of formation, other than the availability of sufficient accretable mass in the parent environment of the objects. Indeed, spectroscopic studies of the initial mass function in 1–5 million-year (Myr) old star-forming regions (Briceño et al., 2002; Luhman et al., 2003b; Slesnick et al., 2004) show no abrupt change in the abundance and spectroscopic signatures between objects above and below the hydrogen-burning mass limit. This smooth transition confirms that brown dwarfs are created as a result of a low-mass extension of the star-formation process. Discoveries of brown dwarfs have thus shed new light on the range of possible outcomes in environments of star formation.

1.1.2 Similarities to Planets

Given the similarity between brown dwarfs and main sequence stars, it may come as a surprise that brown dwarfs also share common features with planets. Nevertheless, starting with spectral type T0 and progressing toward later spectral types, the near-IR spectra of brown dwarfs exhibit increasingly stronger molecular absorption by CH_4 and H_2 (Burgasser et al., 2002), in addition to the H_2O absorption already present in L dwarfs (Kirkpatrick et al., 1999). Conversely, absorption by refractory elements (VO, TiO, and FeH), as characteristic of low-mass M stars in the optical and near-IR (e.g., Leggett et al., 2001), decreases in strength in the L dwarfs, and disappears in the Ts. Thus, at a spectral type of T6.5 ($T_{\rm eff} \sim 900$ K; Burgasser et al., 2002), the methane- and water-absorption dominated spectrum of the first discovered brown dwarf, Gl 229B (Nakajima et al., 1995; Oppenheimer

et al., 1995), resembles the spectra of solar-system objects, Jupiter and Titan, more than those of stars. This follows the theoretical expectation, that the ultimate state of a cooling brown dwarf, beyond the end of even the expanded spectral sequence, is a cold, fully degenerate object–much like a planet. Equations of state for degenerate interiors also dictate that the radii of L and T dwarfs are similar to those of giant gaseous planets, such as Jupiter.

1.1.3 A Matter of Terminology: Low-mass Brown Dwarfs vs. Planets

It is evident from the preceding description (§1.1.1 and §1.1.2) that brown dwarfs occupy an intermediate regime between that of stars and giant planets. High-mass brown dwarfs are likely to be as indistinguishable from stars at young ages, as low-mass and/or old brown dwarfs are from giant planets. Nevertheless, because of the existence of a minimum hydrogen-burning mass, there is a clear separation between brown dwarfs and stars in evolutionary context. Hence, the hydrogen-burning mass limit, albeit not emphasized by an observable transition between the photospheric properties of stars and brown dwarfs at young ages, is defined as the boundary separating the stellar from the sub-stellar regime.

At the low-mass end, the distinction between brown dwarfs and planets is less well-defined. Besides the similarities between their interiors and sizes, the mass regimes of known radial-velocity (RV) extra-solar planets and directly imaged brown dwarfs seem to overlap, in the range between 5 and 15 times the mass of Jupiter ($M_{\rm Jup}$[1]). This comes in contrast to the fact that the physical processes traditionally perceived as leading to the formation of planets–accretion of planetesimals and gas in a circum-stellar disk (e.g., Lissauer, 1993)–and of more massive, isolated objects (stars and brown dwarfs)–gravo-turbulent fragmentation of a molecular cloud (Bodenheimer et al., 1980; Padoan & Nordlund, 2004)–are very distinct. Recent theories have also proposed a hybrid process–gravitational instability in a massive circum-stellar disk–for the creation of both giant planets

[1] $1 M_{\rm Jup} = 0.954 \times 10^{-3} M_{\odot} \approx 0.001 M_{\odot}$

(Boss, 2002) and brown dwarfs and low-mass stars (Bate et al., 2002). Regardless of the outcome of the theoretical effort to model planet and brown-dwarf formation, the evidence for overlap between the two mass regimes is probably real.

The lack of distinction at the planet/brown-dwarf boundary has spurred some scientific debate as to what exactly should be considered a planet and what a brown dwarf. Oppenheimer et al. (2000b) have proposed a distinction analogous to the one established at the stellar/sub-stellar boundary: deciding the classification of an object based on its thermonuclear fusion capability. Although brown dwarfs do not possess sufficient mass to maintain hydrogen fusion, objects more massive than 0.013–0.015$M_{\odot}$ (depending on metallicity) are expected to undergo a brief deuterium-burning phase (Burrows et al., 1997). The deuterium-burning phase is expressed as a region of slower luminosity and effective temperature decline in $> 0.013\ M_{\odot}$ objects at 3–30 Myr ages in Figures 1.1 and 1.2. Oppenheimer et al. (2000b) choose to define such deuterium-burning objects as "brown dwarfs" and reason that lower-mass objects, which never fuse deuterium, should be referred to as "planets." Alternative to this is the traditional view of a planet, upheld by McCaughrean et al. (2001), as an object forming in a circum-stellar disk. The latter definition reserves the term "brown dwarf" for sub-stellar objects formed through a star-like process.

We will generally adhere to the latter terminology, recognizing the fundamental difference between the likely modes of formation of planets in our solar system and of brown dwarfs found in isolation. However, recognizing also the overlap in mass between the latter and known extrasolar-planets, we will occasionally refer to $< 13M_{\rm Jup}$ brown dwarfs as "planetary-mass objects" in the context of their gravitational association with main sequence stars.

1.1.4 Theoretical Models of Sub-stellar Evolution

Because sub-stellar objects never go through a star-like main-sequence phase, their luminosities and effective temperatures are functions of both mass and age. Observational brown-dwarf science is thus heavily reliant on theoretical models to

accurately predict masses and/or ages for sub-stellar objects. The present study will not be an exception, though model predictions will be tested against the limited existing body of empirical data, whenever possible and needed.

Two suites of sub-stellar evolutionary models are used predominantly in the brown-dwarf community, originally due to theoretical teams at the University of Arizona (Burrows et al., 1997)[2] and at École Normale Supérieure de Lyon (Chabrier et al., 2000; Baraffe et al., 2003).[3] The predictions from the two groups are consistent to within 20% in mass at <1Gyr ages. The present investigation will draw on comparisons to both sets of models whenever mass estimates of specific sub-stellar objects are required. Whenever calculations of solely upper limits are needed, the Lyon group models will be adopted. Unlike the model from the Arizona group, these tabulate predicted photometry for sub-stellar objects and low-mass stars over a vast range of masses (0.0005-0.1 $M_{\odot}$) and ages (1 Myr–10 Gyr).

The Lyon models come in two flavors: DUSTY (Chabrier et al., 2000) and COND (Baraffe et al., 2003), depending on the treatment of dust opacity in the brown-dwarf photosphere. The DUSTY models take into account the formation of dust in the equation of state, and its scattering and absorption in the radiative transfer equation. In this set of models, it is assumed that dust species remain where they form, according to chemical equilibrium conditions. These models are most appropriate for $T_{\rm eff} \gtrsim 1500$ K objects (L dwarfs). For cooler, $T_{\rm eff} \lesssim 1300$ K, objects (T dwarfs), the COND evolutionary tracks model the spectroscopic and photometric properties better (Baraffe et al., 2003). The COND models are based on the coupling between interior and non-grey atmosphere structures. The models neglect dust opacity in the radiative transfer equation, and applies when all grains have gravitationally settled below the photosphere.

Neither of the two sets of models from the Lyon group account well for the photometric properties of L-T transitions objects with effective temperatures in the 1300–1500 K range. The proper discussion of this issue requires cloud condensate

[2]Publicly available at http://jupiter.as.arizona.edu/~burrows/

[3]Publicly available at http://perso.ens–lyon.fr/isabelle.baraffe/

models (e.g., Ackerman & Marley, 2001; Tsuji, 2002; Cooper et al., 2003), none of which have however been tested in evolutionary context.

For this temperature range, we will adopt the COND models, which predict absolute near-IR magnitudes that are more consistent with those of late L and early T dwarfs with known trigonometric parallaxes (Fig. 1.3)

1.2 How Frequent are Brown Dwarf Companions and Why Study Them?

Returning to the principle motivation for this work, we re-iterate the presently established view on the frequency of brown dwarfs around stars. Brown dwarfs make rare companions to stars. The result has been borne out of the prolonged radial velocity (RV) effort to detect sub-stellar (i.e., brown dwarfs and planets) companions to stars, even before RV precision was sufficiently high to allow the detection of extra-solar planets. With more than 150 RV extra-solar planets now discovered and less than 10 possible brown dwarfs among them, the dearth of brown-dwarf secondaries in precision RV surveys remains so dramatic, compared to the relative abundance of planetary and stellar companions, that the phrase "brown-dwarf desert" is still as pertinent nowadays as when it was originally introduced (Marcy & Butler, 2000). The term provides not only a vivid representation of the lack of sub-stellar companions of intermediate mass between those of stars and planets, but presumably also of the tremendous scientific and psychological toil of the pioneering RV teams, before perseverance and technological progress laureated their efforts with success.

Precision RV surveys paint only a partial picture of other stellar systems. They are sensitive only to objects with orbital periods of duration comparable to the survey time-span: presently $\leq$ 17 years for the longest-running precision RV surveys, corresponding to orbital semi-major axes of $\leq$5–7 AU from solar-mass stars. At wider orbital separations, corresponding to the gas and ice giant planet zones (5–40 AU) in the solar system, and beyond, little is known. Sub-stellar objects

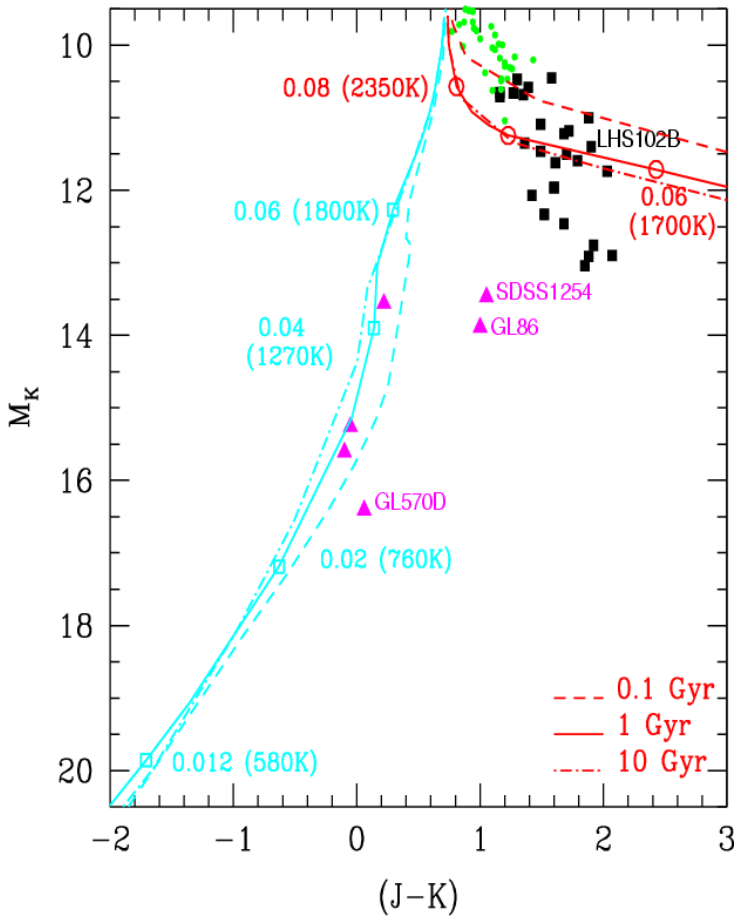

Figure 1.3: Color-magnitude diagram $(J-K)-M_{\rm K}$. Observations are taken from Leggett (1992) (mostly for M-dwarfs) and Dahn et al. (2002). Also shown: LHS 102B (EROS Collaboration et al., 1999), GL 86B[5] (Els et al., 2001). M dwarfs are shown by dots, L dwarfs by filled squares, and T dwarfs by triangles. DUSTY isochrones (Chabrier et al., 2000) are displayed in the upper right part of the figure, for different ages, as indicated. The COND isochrones (Baraffe et al., 2003) are displayed in the left part of the figure. Some masses (in $M_\odot$) and their corresponding $T_{\rm eff}$ are indicated on the 1 Gyr isochrones by open squares (COND) and open circles (DUSTY). The names of two L/T transition objects and of the faintest T-dwarf known with parallax are indicated. (Baraffe et al., 2003)

orbiting at >10 AU take too long to complete their orbits to incur a conclusive velocity trend in present RV surveys.

Our knowledge of sub-stellar multiplicity at such wide separations derives exclusively from imaging efforts. At small heliocentric distances, wide orbital companions may be sufficiently well-separated from their host stars to be resolved in direct images of the pair. Contrarily to RV surveys, the greater the orbital separation between the primary star and the secondary companion, the easier it is to detect the companion (at a fixed heliocentric distance). For example, given ability to do high-contrast imaging science at $\geq 0.5''$, the entire giant planet region outwards of 5 AU can be imaged around a nearby star at 10 pc can be imaged. In this manner, precision RV and direct imaging surveys explore two complementary orbital realms for sub-stellar companions to nearby stars, However, unlike RV monitoring, which can reveal sub-stellar companions a fraction of a Jupiter in mass, direct imaging searches for sub-stellar secondaries to stars are still constrained to companions of multiple Jupiter masses or larger: mainly brown dwarfs. Any sub-stellar companions imaged around other stars will therefore be more massive than any of the known solar system planets. [6]

While the pace of RV discoveries has increased steadily since the detection of the first extra-solar planet (Mayor & Queloz, 1995), despite concentrated efforts from a number of teams, the rate of brown-dwarf companions discovered via direct imaging has been steadily slow for most of the same period, despite concentrated efforts from several groups. Two large direct imaging surveys for sub-stellar companions (Oppenheimer et al., 2001; McCarthy, 2001) have produced only one brown dwarf (Gl 229B: the first one to be discovered; Nakajima et al., 1995) in a com-

[6] Another technique for detecting sub-stellar companions to stars is by astrometric, rather than spectroscopic (as in the RV approach), measurement of the stellar reflex motion. Similarly to the direct imaging approach, the astrometric technique is more sensitive to companions in wider orbits. Because, like the RV method, the astrometric technique also relies on the detection of orbital motion, it requires longer monitoring periods to probe the wider orbital separations. As a result, no extra-solar planets have been discovered from astrometric monitoring yet, though the first brown-dwarf companion was announced recently in Pravdo et al. (2005).

bined sample of over 340 stars and a combined separation range of 10–1200 AU. This result is in stark contrast both with the frequency of RV extra-solar planets within 3 AU (5–15%; Marcy & Butler, 2000; Fischer et al., 2002) and with the frequency of stellar companions to stars over 10–1200 AU (9–13% for M–G-dwarf primaries; Fischer & Marcy, 1992; Duquennoy & Mayor, 1991). Analogous reasoning has prompted McCarthy & Zuckerman (2004) to conclude that the brown-dwarf desert extends much beyond the 0–5 AU probed by RV surveys. More recent results from other, smaller efforts, have been mixed, with surveys performed with more sensitive instrumentation generally reporting higher, though statistically not inconsistent, rates of success (e.g., 1 out of 50).

This situation is reminiscent of the initial search for sub-stellar companions through the RV method, both in the amount of effort invested world-wide and in the, perhaps frustratingly, low yield. However, the sensitivity of precision RV surveys has much surpassed the brown-dwarf mass regime, whereas imaging efforts are still mostly limited to intermediate- to high-mass brown dwarfs. The RV brown-dwarf desert has remained nearly void even after the discovery of lower-mass extra-solar planets. Will this be the case with the direct imaging brown-dwarf desert?

The problem is most comprehensively addressed in the context of Sun-like stars, because of the large body of empirical data that exist on the stellar and sub-stellar multiplicity of solar analogs. The exhaustive study of stellar companions in $0 - 10^{10}$-day periods ($0 - 10^5$ AU) around G-dwarfs by Duquennoy & Mayor (1991) finds that the peak of the stellar companion period distribution occurs near 10^5 days ($\sim$35 AU). Duquennoy & Mayor also find that the distribution of the mass ratios $q \equiv M_1/M2$ in binary systems is nearly flat over $0.0 < q \leq 0.4$–a result that has been confirmed in more recent studies (e.g., Mazeh et al., 2003). Although the results for the $q \leq 0.1$ bin in these studies are largely (Mazeh et al., 2003) or entirely (Duquennoy & Mayor, 1991) extrapolated, beacuse of the severe incompleteness to low-mass companions, it appears plausible that more sensitive studies will detect significant numbers of such secondaries. From the standpoint

of precision RV surveys, the frequency of extra-solar planets is rising with orbital separation out to the present completeness limit of the surveys (Marcy et al., 2003; Udry et al., 2003). In addition, the last three years have seen the announcement of several RV "super-planets," objects with minimum masses in the 10–25 $M_{\rm Jup}$ range, i.e., likely brown dwarfs (Udry et al., 2002; Jones et al., 2002; Fischer et al., 2002; Endl et al., 2004). Most of these are at semi-major axes wider than 1.5 AU, suggestive of a positive correlation between mass and period for RV planets (Zucker & Mazeh, 2002; Udry et al., 2003). That is, even more massive sub-stellar objects may exist at wider orbital separations from Sun-like stars.

Connecting the above two lines of evidence, there is an indication that brown dwarfs, given their intermediate mass between those of stars and extra-solar planets, should exist with some appreciable frequency in wide orbits around Sun-like stars. *What fraction of Sun-like stars have such widely-separated brown-dwarf secondaries?*

This is the principle question guiding the present investigation. By undertaking a large direct imaging study of a carefully-selected sample of solar analogs, and by employing the modern high-contrast imaging capabilities at the Palomar 5 m and Keck 10 m telescopes, we are able to resolve the issue at a sufficient level of confidence.

Direct imaging investigations of sub-stellar multiplicity are also relevant to the study of the photospheric evolution of sub-stellar objects: both brown dwarfs and giant planets. As mentioned in §1.1, sub-stellar objects never go through a star-like main-sequence phase, during which their luminosity and effective temperature are largely independent of age and are determined mostly by mass. Instead, their luminosity and effective temperature are strongly age-dependent. With the ages of field brown dwarfs still practically indeterminable, theoretical brown-dwarf cooling models have had few empirical constraints beyond the late-M to early-L brown dwarfs found in young open clusters. Of strong interest, for example, is more accurate understanding of the transition between late L and early T dwarfs: a phenomenon occurring at approximately constant temperature ($\sim$1300–1500 K;

Ackerman & Marley, 2001; Tsuji, 2002) but during which the near-IR $J - K_S$ color of a brown dwarf changes by more than a magnitude (Kirkpatrick et al., 1999; Burgasser et al., 2002). No brown dwarfs later than L7 have been age-dated yet, as none have been confirmed in open clusters or as companions to stars of known age. The discovery of such late-type brown dwarfs as companions to stars with known ages can provide much-needed empirical calibration and theoretical constraints. This is a second issue that will be addressed as a result of the present survey in the near future. At an age of 400 Myr and a photometrically-estimated spectral type of T0.5, one of the newly-discovered brown-dwarf companions is likely the first known young L/T transition object.

Going beyond the concrete goal to test the existence of the brown-dwarf desert at wide separations, imaging studies of the multiplicity fraction and separation distribution of low mass ratio ($q < 0.1$) binaries provide important clues for the mechanism of their formation and dynamical stability (e.g., Close et al., 2003). By virtue of being optimized for the detection of sub-stellar companions, the present survey provides ample material for future investigations of low mass ratio systems.

1.3 Observational Challenges and Constraints

The main challenge in direct imaging of sub-stellar companions to stars is achieving sufficient contrast to detect a faint companion in the vicinity of its orders of magnitude brighter host star. Three main factors, addressed in turn below, contribute to this problem: imaging contrast capability, heliocentric distance to the star, and stellar youth.

Seeing-limited observations through the Earth's turbulent atmosphere suffer from the large extent ($1''$) of the imaging point-spread function (PSF). The contrast achieved in seeing-limited imaging is too poor to detect almost any sub-stellar companions within $\sim 10''$ from solar analogs, i.e., within 100 AU from a star at 10 pc. This problem has been aleviated over the past decade by the availability of space-based imaging with the *Hubble Space Telescope (HST)* and of ground-

based adaptive optics (AO)–a technique that compensates for atmospheric turbulence through the use of high operational frequency corrective optics. Large AO-equipped telescopes nowadays routinely produce diffraction-limited PSFs, of order 0.05–0.10″ on 5–10 m class telescopes in the near-IR. Such angular resolution rivals that obtained by the *HST* and allows unprecedented scrutiny of small angular scales. The contrast achieved by various AO systems and the *HST* is generally $10^3 - 10^5$ at 1″ from bright stars in the near-IR (1–2.5 μm)–far superior than the contrast of seeing-limited observations at the same angular separation (order unity). However, AO is strongly limited by the need of the corrective system for a sufficiently bright nearby ($\lesssim 60''$) beacon, a "guide star," above the turbulent layers in the atmosphere to probe the distortion of the incident radiation. Without the use of an artificial guide star (a laser beam), the celestial distribution of natural guide stars (NGSs) of sufficient apparent brightness allows the use of AO for only $\lesssim$1% of the total area of the sky. Fortunately, solar analogs within $\sim$200 pc are generally sufficiently bright to be used as guide stars themselves, thus allowing full use of the power of NGS AO for the present study.

The apparent angular scale of a stellar system is inversely proportional to its heliocentric distance: systems that are farther away are more challenging to resolve. Given an interest in imaging orbital separations of solar-system scales around other stars, we are limited in choice to relatively nearby stars, within 400 pc (40 AU at 0.1″ resolution). Furthermore, because of the inverse-squared dependence of flux on heliocentric distance, sub-stellar objects in faraway systems may be too faint to detect. In contrast-limited imaging, however, this factor is of lesser importance.

The contrast attained with AO or the *HST* may still be inadequate to detect any but the most massive sub-stellar companions in intrinsic light, and is $\sim$3–5 orders of magnitudes too poor to detect companions in reflected light. As the detection of intrinsic light offers a clear advantage at this contrast level, we will discuss only this approach. While stars maintain a constant brightness throughout their hydrogen-burning lifetime on the main sequence, sub-stellar objects cool and get intrinsically fainter with age (§1.1). Hence, the brightness ratio between the

primary star and the secondary sub-stellar companion progressively increases with time. Results from theoretical models of sub-stellar cooling (Burrows et al., 1997; Chabrier et al., 2000) indicate that, at an imaging contrast of 10^4, a stellar/sub-stellar binary with a solar analog as the primary needs to be younger than ≈3 Gyr (the Sun is 4.56 Gyr old) to have a 70 $M_{\rm Jup}$ companion detectable, and younger than ≈20 Myr to have a 10 $M_{\rm Jup}$ companion detectable (cf. Fig. 1.1). Therefore, searches for sub-stellar companions to young ($\lesssim$1 Gyr) stars will be expected to be more sensitive to sub-stellar masses than searches around older (1–10 Gyr) stars. Unfortunately, stellar age is not a direct observable, and is an elusive quantity to determine for isolated stars. Only in the past several years have extensive data sets of calibrated age characteristics become available for large volume-limited samples of nearby stars (§2.2.2). Recent high-contrast imaging surveys have, therefore, had an advantage over previous ones, in being able to selectively target known nearby young stars.

Ultimately, the design of an optimization scheme for detecting sub-stellar companions through direct imaging needs to take into account all three of the above factors. Because the maximum possible imaging contrast is not an adjustable parameter, but is fixed based on the available instrumentation, the factors that need to be weighted against each other are heliocentric distance and stellar age of the targets. Direct imaging of nearby ($\lesssim$10 pc) young ($\lesssim$30 Myr) stars with *HST* or with AO allows the best possible scenario for detecting sub-stellar companions. However, the star-formation history of the solar neighborhood is such that less than a dozen such known nearby young stars exist. Thus, minimizing heliocentric distance leads to the inclusion of stars that are older than optimal and conversely, minimizing stellar age requires expanding a survey to include targets at larger heliocentric distances. In §2.5 we argue that, given the known distance vs. age distribution of Sun-like stars in the solar neighborhood, a young, more distant sample optimizes sensitivity to sub-stellar mass (though at the cost of poorer resolution of orbital scale).

1.4 The Observational Approach at a Glance

The present survey uses the AO systems at the Palomar 5 m and Keck 10 m telescope to directly image 3–3000 Myr-old nearby solar analogs. Out of a total sample of 266 stars, a sub-sample of 101 young (<500 Myr) stars was selected to explore in deep exposures for sub-stellar companions. While youth was the main selection factor for stars in this "deep" sample, some priority was also given to nearby (<50 pc) stars, for closer scrutiny of solar-system (<40 AU) scales. The remaining 165 stars were imaged only in shallow observations, to improve the census of stellar multiplicity of Sun-like stars.

All of the sample stars were sufficiently bright to allow use of the AO systems in NGS mode, i.e., to have the wave-front sensing performed on the primaries themselves. For higher overall sensitivity and to improve contrast in the halos of the stars belonging to the deep sample, the primary in each case was obscured by an opaque circular spot–a coronagraph–selectable from the slit wheels of the two instruments. The combination of a highly-corrective ("high-order") AO system and a coronagraph is considered optimal for imaging faint objects around bright stars (e.g., Sivaramakrishnan et al., 2001). After an examination of the initial images, target stars which contained other objects in the same image–candidate companions–were followed up with additional imaging at later epochs to confirm the physical association of the candidate companions. This was done through the use of a common proper motion test, requiring that the primary and the companion share the same apparent motion with respect to field stars between the imaging epochs. Upon the establishment of common proper motion, the candidate companions were assumed to be physical, or "bona fide," companions.

The sample of stars itself was adopted largely from the already compiled list of Sun-like stars in the same age range, studied by the Formation and Evolution of Planetary Systems (FEPS) *Spitzer* Legacy team (Meyer et al., 2005). The focus on solar analogs arises from the primary scientific driver of the FEPS program, which is to study the formation and the evolution of the Solar System in time through

dust signatures. The lower age limit of the sample corresponds approximately to the epoch of giant planet formation, whereas the upper limit is chosen to include stars with evolved planetary systems, though still somewhat younger than the Sun. The combination of high-angular resolution, high-contrast observations obtained in this survey with the sensitive mid-IR *Spitzer* data collected by the FEPS team will create an unprecedentedly comprehensive picture of the link between (sub-)stellar multiplicity and planet formation around Sun-like stars.

1.5 Thesis Outline

A full description of the survey sample follows in §2. Chapter §3 contains an overview of the observing strategy, as described in two published papers: Metchev et al. (2003) and Metchev & Hillenbrand (2004). Chapter §4 presents an accurate astrometric calibration of the Palomar AO observations to allow the determination of physical association of candidate companions. Chapter §5 contains an analysis of the survey detection limits and presents the results from the common proper motion astrometric analysis. Chapter §6 presents results on new and confirmed sub-stellar and stellar companions to the solar analogs in the sample, a detailed analysis of the survey incompleteness to sub-stellar objects, and a robust estimate of the sub-stellar companion frequency. Chapter §7 puts the results of the current investigation in the context of the existing literature, and summarizes the impact of the work. The Appendix contains a published AO study (Metchev et al., 2005) of the scattered light dust disk around the nearby young star AU Mic. The study provides and example of how the combination of high-contrast resolved imaging and sensitive mid-IR photometry of circum-stellar disks can offer insights into their evolutionary state.

Chapter 2

Survey Sample

Careful construction of the parent sample in a survey for sub-stellar companions to stars is important both for optimizing the detectability of the companions, and for conducting an accurate estimate of the companion frequency afterwards. In this chapter we give an in-depth description of the sample generation.

An introductory overview of the selection criteria is given in §2.1. We follow this by a detailed presentation of the individual criteria (§2.2), their application (§2.3), and the resulting biases (§2.4). We summarize the unique characteristics of the survey sample in §2.5. The entire survey sample is listed in Table 2.2.

2.1 Overview

The main criteria used for selecting stars for the survey were: youth, Sun-like mass, heliocentric proximity, and visibility from the Northern hemisphere. The complete sample contains 266 F5–K5 IV–V stars in the 0.003–10 Gyr age within 200 pc from the Sun, at latitudes $\delta \geq -30°$. The vast majority (247) of the stars were chosen from the already compiled list of solar analogs studied by the Formation and Evolution of Planetary Systems (FEPS) *Spitzer* Legacy Team (Meyer et al., 2004, 2005). Twenty additional targets were added in the course of the survey.

In view of the focus on detection of low-mass and sub-stellar companions, the complete sample emphasizes young stars: 169 stars are in the 3–500 Myr age range and 97 are older (0.5–10 Gyr). We will henceforth refer to the stars in these two age

Table 2.1: Median Sample Statistics

Sample	Age (Myr)		Distance (pc)		Spectral Type	
	range	median	range	median	range	median
Deep	6.6–8.6	7.9	7.7–190	50	K5–F5	G5
Shallow	6.6–10.0	8.8	11–199	33	K5–F5	G7
Complete	6.6–10	8.3	7.7–199	45	K5–F5	G5

bins as members of the "young" and "old" samples, respectively. A sub-sample of 101 stars from the young sample were targeted with deep coronagraphic exposures to search for very faint nearby companions–possible brown dwarfs. To optimize sensitivity to companion luminosity (and hence, mass), the stars in this sample were chosen to be the youngest and nearest among the single stars in the young sample. We will refer to the sub-sample of young stars observed coronagraphically as the "deep" sample. The remaining 68 young and 97 old stars were observed primarily in short sequences of non-coronagraphic images to establish stellar multiplicity. These will be referred to as the "shallow" sample. Eleven stars older than 500 Myr were also observed with long coronagraphic exposures: 2 Hyades ($\sim$600 Myr) members and 9 other stars whose subsequent age-dating showed that they were older than originally assigned. These 11 stars are not considered part of the deep young sample. Median age, distance, and spectral-type statistics for the deep, shallow, and complete (deep+shallow) samples are given in Table 2.1.

A factor that is crucial for natural guide star (NGS) AO observations–the imaging approach used in the present survey–but has not been mentioned above, is sufficient optical brightness of the object used for wave-front sensing. The Palomar and Keck AO systems required stars brighter than R-band (0.7μm) apparent magnitude of 12 during the 2002–2003 observing seasons, and brighter than $R \approx$13.5 mag after 2003. As seen in the following section, all of the sample stars satisfy this requirement. This allowed adequate AO correction by guiding on the targets themselves.

A detailed discussion of the selection based on spectral type, age, and heliocentric distance of the sample stars ensues.

2.2 Selection Criteria

The sample for the companion survey is nearly identical to the FEPS source list. The following discussion is thus largely based on the choice of FEPS sample selection criteria, the implementation of which is outlined in Hines et al. (2005) and Hillenbrand et al. (2005).

2.2.1 Spectral Types and Stellar Masses

The goal of the high-angular resolution survey is to study the multiplicity of near-solar-mass stars. The quantity of primary importance in classifying each star as such is its mass (M_*). However, because stellar mass is not an observable, stars are more easily characterized based on luminosity and color, in effect using surface gravity ($g = GM_*/R_*^2$) and effective temperature ($T_{\rm eff}$) to estimate M_*. In spectral classification terms, the stars were selected to have a similar spectral type and class as the Sun (G2 V), ranging between F5 and K5 in spectral type (6300 K $> T_{\rm eff} >$ 4400 K) and, depending on stellar age, between IV and V in spectral class ($3.4 < \log g \leq 4.5$ in cgs units). The corresponding mass range, based on dynamical mass estimates in binary systems and on stellar thermodynamic models is approximately 0.7–1.3 $M_\odot$. In this section, we describe the concrete criteria that lead to the final spectral classification and mass estimates of the stars in the sample, taking into account the effects of interstellar reddening, surface gravity, and evolution.

2.2.1.1 Spectral Types: Dependence on Color, Reddening, and Surface Gravity

Spectral types for the stars in the sample were estimated from broadband Johnson and Tycho B and V photometry, requiring $0.46 \leq (B-V)_{\rm Johnson} \leq 1.20$, or

equivalently, $0.48 \leq (B-V)_{\rm Tycho} \leq 1.42$ (Mamajek et al., 2002). Empirical relations between $B-V$ colors, effective temperature, and spectral type for stars of solar metallicity (Houdashelt et al., 2000; Wright et al., 2003) were used to place all stars on a uniform classification system (Carpenter & Stauffer, 2003). The spectral types for the stars were checked against existing spectroscopic classifications in the literature and against new high-resolution optical spectra obtained with the Palomar $60''$ telescope (R. White, G. Gabor, & L. Hillenbrand, in preparation).

Because of interstellar reddening, visual extinction is an important factor to take into account when deriving spectral types from optical broad-band photometry. Extinction is insignificant for stars within 50 pc from the Sun, which reside within the Local Bubble, and less than $A_V \approx 0.01$ mag (i.e., comparable to photometric uncertainties) within 75 pc based on measurements of interstellar Na I column densities (Welsh et al., 1998; Carpenter & Stauffer, 2003). For isolated stars residing at >75 pc from the Sun, the following expression, relating transverse distance R, galactic latitude b, and scale height h (derived to be 70 pc), was adopted from Vergely et al. (1997):

$$A_V = A_{V,0} \frac{h}{|\sin b|} \left(1 - \exp\left(\frac{-R|\sin b|}{h}\right)\right). \tag{2.1}$$

The value of $A_{V,0}$ corresponds to 1.5 mag kpc^{-1} in the Galactic Plane. For stars that are known members of young open clusters, the nominal visual extinctions for the corresponding clusters were adopted: $A_V = 0.0$ for the Hyades (within the Local Bubble), $A_V = 0.12$ for the Pleiades (Crawford & Perry, 1976; Breger, 1986), and $A_V = 0.31$ for α Per (Pinsonneault et al., 1998). The A_V values are derived from the observed $E(B-V)$ color excess using the extinction law (Mathis, 1990):

$$A_V = 3.1E(B-V). \tag{2.2}$$

The overall effect of extinction is thus to redden stellar $B-V$ colors by up to 0.09 mag for the most distant stars in the sample, corresponding to a difference in 4 sub-types for the hottest (F5–F9) stars. This effect has been taken into account

in the adopted spectral types, as distances are available from *Hipparcos* for the vast majority of FEPS stars.

Surface gravities for the sample of solar analogs in their pre-main-sequence (PMS) evolutionary stage (younger than 50–100 Myr) were estimated by comparing their locations on the Hertzsprung-Russel (H-R) diagram to predictions from stellar evolutionary models from D'Antona & Mazzitelli (1997) and from a $T_{\rm eff}$—spectral type—$\log g$ relation tabulated in Gray (1992). Stars on the zero-age main sequence (ZAMS) and older were assumed to have $\log g = 4.5$–close to the solar value of $\log g = 4.44$. Surface gravities were also checked against the new Palomar $60''$ echelle spectra (R. White et al., in preparation).

Stellar surface gravity affects the estimated effective temperature at a given spectral type, but has a small effect on the $B - V$ colors. As a solar-mass star evolves in between the age limits of the sample, its surface gravity $g = GM_*/R_*^2$ is expected to change by approximately 0.7 dex: from $\log g = 3.8$ to 4.5 in cgs units. The corresponding change in $B-V$ at a fixed effective temperature is $\lesssim 0.01$ mag (Houdashelt et al., 2000; Carpenter & Stauffer, 2003), i.e., negligible.

A histogram of the number distribution of sample stars as a function of the inferred effective temperature is given in Figure 2.1a. The corresponding spectral types are given in column 9 of Table 2.2.

2.2.1.2 Masses: Dependence on Age

While surface gravity does not strongly influence inferred spectral types, it affects stellar mass through the mass—radius, or the equivalent, mass—luminosity—effective-temperature relation: $M_* \propto gR_*^2 \propto gL_*/T_{\rm eff}^4$. This dependence is particularly strong in PMS stars, which undergo factors of $\sim$10 changes in surface gravity as they contract toward the main sequence (MS). We rely on theoretical stellar evolution tracks to correctly account for the age-dependence of these parameters.

At MS ages ($\gtrsim$ 100 Myr), the theoretical models are well-calibrated with respect to empirical data from dynamical mass measurements in binary systems (e.g., Andersen, 1991; Delfosse et al., 2000). In the latest compilation of such

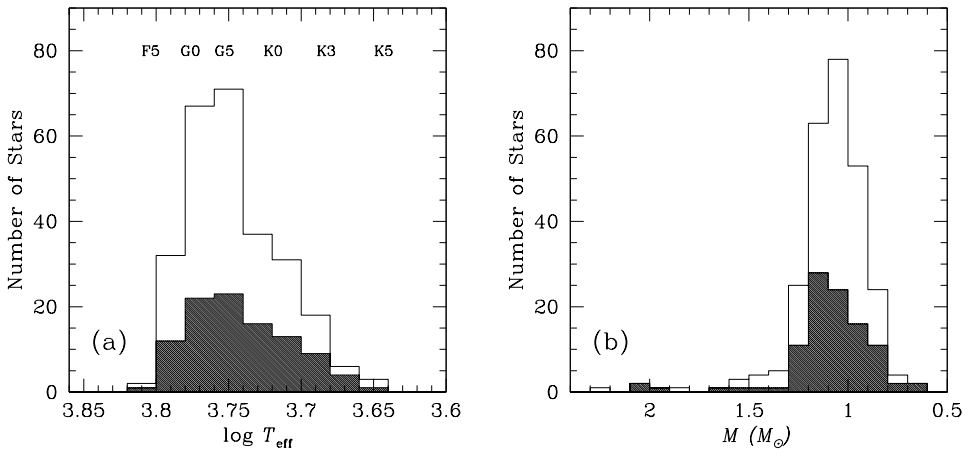

Figure 2.1: Distribution of the sample stars as a function of effective temperature (a) and mass (b). The non-shaded histograms refer to the entire sample of 266 stars, whereas the shaded histograms refer to the deep and young sub-sample of 101 stars. All stars fall in the F5–K5 range of spectral types and the majority are between 0.7 and 1.3 $M_\odot$. The tail toward higher masses is due mostly to close equal-magnitude binaries and less so the earliest-type and youngest fraction of stars in the sample.

data (Hillenbrand & White, 2004), a comparison between the empirical MS and predictions from various widely used theoretical models suggests that the models of Swenson et al. (1994) provide the most accurate overall representation of the MS (Fig. 2 in Hillenbrand & White, 2004). We therefore adopt the Swenson et al. tracks in estimating the masses of MS stars in the survey sample. The agreement of the Swenson et al. model mass estimates with dynamical masses over the range of interest in the present survey is better than 10%.

The Hillenbrand & White comparison is based on a compilation of dynamical masses of 88 MS stars with A–K spectral types: one of the largest data sets to date that cover the F5–K5 range of spectral types in the present survey. However, a similarly large sample of dynamical masses of PMS stars in the same spectral type range is currently lacking. As a result, PMS evolutionary tracks of solar analogs are much more poorly constrained. Hillenbrand & White's assessment of the limited amount of dynamical mass data for PMS binaries demonstrates that, in the 0.5–1.2 $M_{\odot}$ mass range, the Baraffe et al. (1998) stellar evolution code (with the value of the mixing parameter α set to 1) marginally outperforms other suites of models in reproducing the empirical data. The agreement with the dynamical masses is on average better than 10%, although with a scatter of up to 50%. Since the range of the Baraffe et al. (1998) models (0.05–1.4 $M_{\odot}$) encompasses most of the range of stellar masses (0.7–1.3 $M_{\odot}$ by design) in the present sample, we adopt the Baraffe et al. models. For the few $> 1.4 M_{\odot}$ PMS sample stars, masses have been extrapolated above the 1.4 $M_{\odot}$ limit of the Baraffe et al. models.

Because of the large scatter in the predictions from the PMS models, compared to the slow evolution in stellar luminosity and temperature in the final stages before reaching the ZAMS, we adopt the Baraffe et al. (1998) tracks only for stars younger than 30 Myr. For stars $\geq$ 30 Myr we adopt the MS models of Swenson et al. (1994). The use of MS models to obtain masses for 30–100 Myr-old stars results in a $\approx$10% over-estimate of the masses of the most slowly evolving stars in the sample, the K dwarfs.

The adopted primary mass for each star is listed in the last column of Table 2.2.

The distribution of primary masses in the full sample, and in the deep sub-sample, is plotted in Figure 2.1b. The majority of the masses are between 0.7 and 1.3 $M_{\odot}$, following the design of the FEPS sample. The tail toward high masses is almost entirely due to close equal-flux binaries, which were unknown as such prior to this survey. A smaller fraction of the stars more massive than 1.3 $M_{\odot}$ were among the earliest-type (F5–G0) and youngest (3 Myr) sample stars, which satisfied the spectral type selection criteria because of their youth (and hence, cooler-than-MS $T_{\rm eff}$).

The need for estimating masses for the sample stars goes beyond the original FEPS goal to focus on the evolution of solar-mass stars. We will use these masses in the context of the present survey in §6, when discussing the distribution of mass ratios in resolved binary systems.

2.2.2 Stellar Ages

Determination of stellar ages is done via a range of techniques all tied to the fundamental calibration of open and globular cluster ages that are known with respect to theoretical models. The classic method of main-sequence turn-off fitting uses the location of the giant branch turn-off on the color-magnitude diagram. The more novel method of lithium depletion boundary determination (Basri et al., 1996; Stauffer, 2000) estimates ages by finding the warmest fully convective ($< 0.25 M_{\odot}$) star that still has lithium present in its photosphere. The method relies on the fact that as soon as the temperature in the contracting core of a low-mass star reaches lithium fusion values ($2 - 4 \times 10^7$ K), the surface lithium abundance rapidly drops to zero since there is no mechanism for stable lithium production.

These two methods demonstrate that stellar ages are most reliably determined in *ensembles* of presumably co-eval stars with similar metallicities. They have been successfully used to age-date a large number of young open clusters (e.g., Mermilliod, 1981; Stauffer, 2000, and references therein). For the sample stars that are known members of these clusters, we have adopted the corresponding ages: 5 ± 1 Myr for the Upper Scorpius OB association (Preibisch et al., 2002),

90 ± 10 Myr for α Per (Stauffer et al., 1999), 125 ± 8 Myr for the Pleiades (Stauffer et al., 1998), and 625 ± 50 Myr for the Hyades (Perryman et al., 1998).

The two primary methods for estimating stellar ages of clusters have allowed the calibration of a number of secondary empirical relations, suitable for age-dating individual field stars. Most notable among the secondary methods are ones based on the evolution of the stellar dynamo, on the surface lithium abundance in stars with convective envelopes (but radiative cores), and on the "memory" of a star's space motion after leaving its molecular cloud progenitor. Since the majority of the stars in the sample are not members of young open clusters, age-dating of the sample relies heavily on these secondary techniques.

The full set of age indicators used were the following:

1. location on the H-R diagram in relation to stellar populations of known age and to theoretical evolutionary tracks, a.k.a. "isochrone fitting";
2. chromospheric Ca II H and K (3968 and 3933Å) line emission;
3. chromospheric Hα emission;
4. chromospheric UV continuum excess and line emission;
5. coronal x-ray emission;
6. rotation velocity $v \sin i$, as measured from rotational line broadening;
7. Li I 6707Å absorption;
8. UVW galactic space motion.

Comprehensive discussions of the above age indicators and their advantages and limitations can be found in Gaidos (1998) and Lachaume et al. (1999). Their application to age-dating the FEPS sample is detailed in Hillenbrand et al. (2005, and references therein). Here, we present only a brief description of each method. It is important to note that because of the larger uncertainties of the secondary age-dating methods compared to the primary ones, several secondary methods need to be used in conjunction for reliable age estimation.

The first technique is similar in spirit to the main-sequence turn-off fitting, in the sense that it uses theoretical and empirical isochrones. However, unlike the evolved stars on the main-sequence turn-off, for the young solar analogs in the FEPS sample (whose distances are known; §2.2.3), location above the ZAMS in the H-R diagram is an indication of youth, rather than old age. Whether this is truly the case is confirmed by some of the other methods. If the star is confirmed to be young, its age can be determined fairly precisely from PMS contraction tracks. The method is not suitable for age-dating stars on the MS (i.e., $>$ 100 Myr-old G stars) because of the very slow evolution of temperature and luminosity. Only a lower limit on the age can be established for such stars.

The M_{K_S} vs. $J - K_S$ plot in Figure 2.2 shows an example of the H-R diagram dating technique, as applied to the AO survey sample, based on models from Baraffe et al. (1998). Isochrones are plotted in continuous lines, while lines of constant mass are shown in dashed lines. The majority of the sample stars cluster near the 100 Myr (≈ZAMS) isochrone, indicating that their ages are $\gtrsim$100 Myr. The stars scattered above the 100 Myr isochrone are accordingly younger. This particular set of evolutionary tracks (with $\alpha = 1.0$) from Baraffe et al. over-predicts the luminosity of the ZAMS by $\Delta M_{K_S} \approx 0.3$ mag. Such a discrepancy is not unusual for theoretical PMS models. In this case, the discrepancy can be largely eliminated by adopting a different set of evolutionary tracks from the same authors, with the value of the mixing-scale parameter α set to 1.9. This is the setting required to reproduce the present Sun in the (Baraffe et al., 1998) suite of models. However, as already discussed in §2.2.1.2, the $\alpha = 1.0$ models were found to best approximate the masses of $<$30 Myr PMS stars on average, and are hence the choice of models for young PMS stars in this study.

Age-dating methods (2–6) are related to the evolution of the stellar dynamo. A relationship between rotation and dynamo-driven activity is expected theoretically, based on the conversion of mechanical to magnetic energy, though the calibration to stellar age is derived from empirical correlations of observed quantities. Such observational correlations were first presented in a brief paper by Skumanich (1972),

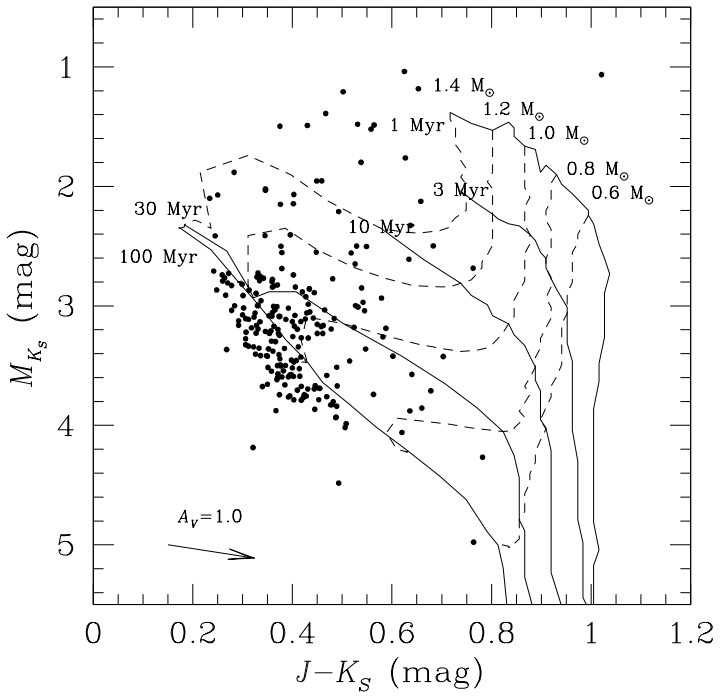

Figure 2.2: M_{K_S} vs. $J - K_S$ color-magnitude diagram of the AO survey sample with evolutionary tracks from Baraffe et al. (1998) over-plotted. Continuous curves delineate isochrones and dashed curves delineate tracks of constant mass. The vector at the bottom left represents the equivalent of 1 magnitude of V-band extinction. The apparent $\Delta M_{K_S} \approx 0.3$ mag displacement of the 100 Myr (approximately ZAMS) isochrone from the locus of the majority of the stars is an example of the uncertainties in theoretical models.

who observed that the decay of chromospheric emission and rotational velocity among stars in different young open clusters varies as the inverse square root of cluster age. Subsequent more-detailed analyses of the evolution of rotation velocity, $v \sin i$ (Soderblom, 1983), x-ray coronal luminosity (Vilhu, 1984; Randich, 2000), and chromospheric UV, Ca II H&K, and Hα emission (e.g., Simon et al., 1985; Donahue, 1993; Lyra & Porto de Mello, 2005), have established a variety of empirical laws suitable for determining approximate stellar ages in the 30–5000 Myr range. Best calibrated and most widely used among these age indicators is the R'_{HK} index, measuring the relative strength of Ca II H&K emission with respect to the stellar continuum (Noyes et al., 1984). This we adopt as the primary criterion for determining ages for post-PMS stars. Quantitatively, we employ the following empirical relation from (Donahue, 1993):

$$\log\left(\frac{t}{\text{year}}\right) = 10.725 - 1.334R_5 + 0.4085R_5^2 - 0.0522R_5^3, \tag{2.3}$$

where t is the stellar age in years and $R_5 = 10^5 R'_{HK}$. The observational scatter in the above relation has been estimated at $\leq$50% based on variations in the derived ages of the components of binaries, which can be assumed to be co-eval (Donahue, 1998). Where available, R'_{HK} measurements for the sample stars are listed in column 10 of Table 2.2.

The seventh method relies on the fact that as low-mass stars with radiative cores age, lithium is gradually mixed downward in the convective envelope until reaching the temperature at which it burns. Therefore, assuming that all stars start with primordial lithium abundances, presence of photospheric lithium is an indication of youth (e.g., Herbig, 1965; Bodenheimer, 1965; Duncan, 1981). While the equivalent width of the Li I 6707Å absorption resonance doublet (the strongest lithium feature in the optical) is not a direct measure of the absolute lithium abundance, its relative strength in populations of stars of similar temperature can be used to qualitatively compare their ages. However, the large observational scatter in lithium for stars of similar temperature and age, especially for G stars

(e.g., Duncan & Jones, 1983), precludes its use as an absolute chronometer, only a statistical one.

Finally, method (8) presents a statistical approach for selecting groups of co-eval co-moving stars. The underlying idea, originally due to Eggen (1965), is that stars are born in groups and are imprinted with the space motion of the parent molecular cloud even after escaping its gravitational influence. The method of calculating space motions in the Galactic (U, V, W) coordinate system from the celestial coordinates, parallax, radial velocity, and proper motion was standardized by Johnson & Soderblom (1987). Leggett (1992) defined criteria for assigning membership to the young disk, the old disk, or the halo of the Galaxy, representing young, intermediate-aged, and old stars. Thus, while the space motion of a star has no formulaic relation to its age, it can be compared to the space motions of ensembles of stars of known age, thus revealing tentative associations of young stars spread over the entire sky. However, confirmation of youth through one or more of the aforementioned methods is essential. A compilation of known and tentative young moving groups and their space motions is presented in Zuckerman & Song (2004b).

To summarize, ages for the sample solar analogs were determined based on two primary methods: isochrone fitting of the location on the H-R diagram for <30 Myr PMS stars (method 1) and strength of the R'_{HK} chromospheric activity index for older stars (method 2). The other techniques were applied where possible and necessary to confirm and further constrain the stellar ages. Histograms of the age distribution of the complete survey sample and of the deep sub-sample are presented in Figure 2.3. The determined stellar ages will be used in §6 and 6 to determine age-dependent masses for candidate and bona fide sub-stellar companions. The adopted ages for the sample stars are listed in column 12 of Table 2.2.

2.2.3 Distances and Proper Motions

Distances to sample stars with *Hipparcos* data were taken from the *Hipparcos* catalog (Perryman et al., 1997). These account for 166 of the 266 observed stars.

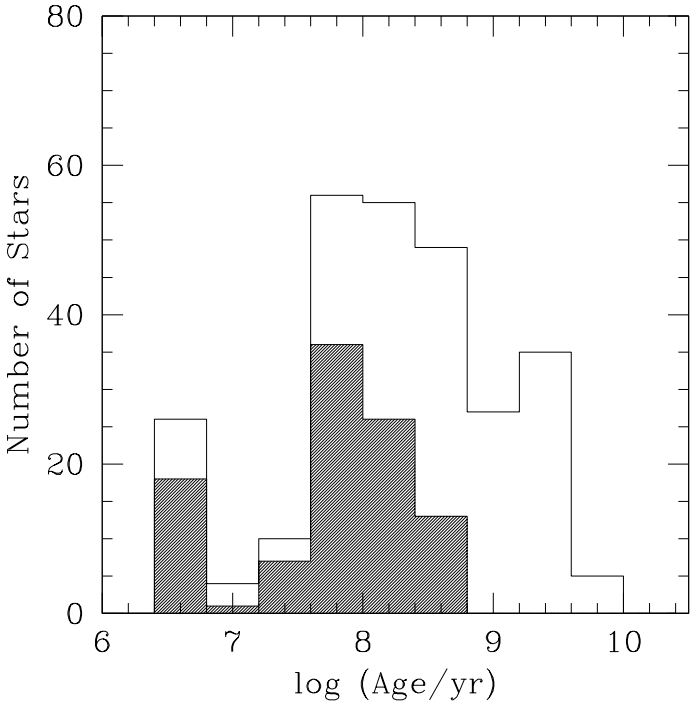

Figure 2.3: Age distributions of the complete survey sample (non-shaded histograms) and of the deep sub-sample (shaded histograms).

For a further 54 stars without *Hipparcos* data that are known members of young open clusters and OB associations, we adopted the mean cluster distance, calculated from a combination of trigonometric, orbital, secular, and cluster parallax methods, using *Hipparcos* and Tycho-2 (Høg et al., 2000) astrometry, long-baseline interferometry, and high-resolution spectroscopy. The adopted distances for cluster members were: 133 ± 6 pc for stars in the Pleiades (a weighted mean of the distances to 7 members presented in Pan et al., 2004, Munari et al., 2004, Zwahlen et al., 2004, Southworth et al., 2005, and assuming $\sim 1^\circ$ angular extent from Adams et al., 2001), and 191 ± 11 pc for stars in α Per (Robichon et al., 1999, assuming 1° cluster radius). For stars belonging to the Upper Scorpius association, we adopted 145 ± 40 pc (de Zeeuw et al., 1999; Mamajek et al., 2002). All of these distances agree with estimates from main-sequence fitting for the corresponding clusters. For 18 more stars, we have adopted secular parallaxes from Mamajek et al. (2002) and Mamajek (2004). Finally for the remaining 28 stars, we have adopted approximate distances based on spectroscopic parallaxes. For these, we have assumed distance uncertainties of 50%.

Heliocentric distances to the sample stars are listed in column 6 of Table 2.2. These will subsequently be used to determine absolute magnitudes and orbital separations in each of the systems with resolved companions (§6). Figure 2.4a presents histograms of the distances to the stars in the complete sample and in the deep sub-sample. The bi-modal distribution of the distances is a combined effect of the large heliocentric distances (130–200 pc) of the youngest (5–100 Myr) stars in the sample, and of given preference to closer systems at older ages.

Proper motions for the 166 stars with *Hipparcos* parallaxes were adopted from *Hipparcos*. For the remaining 100 stars, proper motions were adopted from The Second U.S. Naval Observatory CCD Astrograph Catalog (UCAC2; Zacharias et al., 2004) and from the Tycho–2 Catalog (Høg et al., 2000). The three catalogs provided similar astrometric accuracy (± 1.0 mas yr^{-1}) for the sample stars, though the UCAC2 and Tycho–2 catalogs went deeper. The proper motion along right ascension (corrected for declination: $\mu_\alpha \cos\delta$) and declination (μ_δ) for each

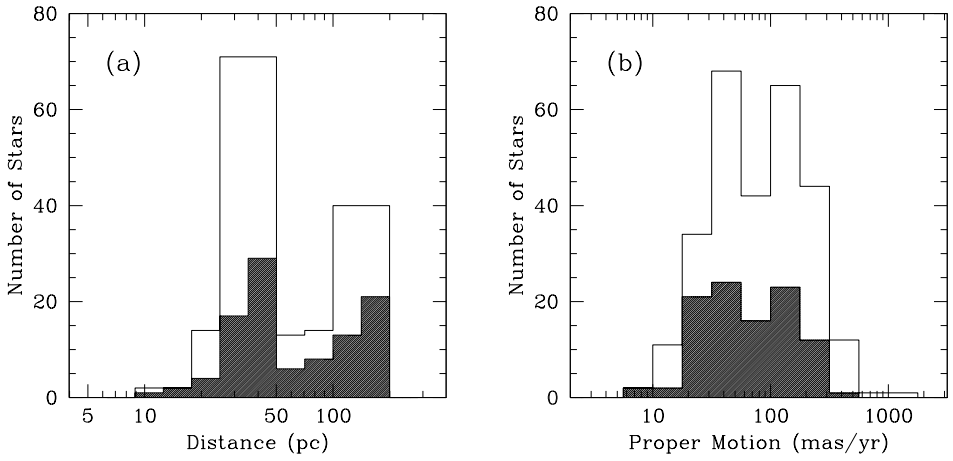

Figure 2.4: Heliocentric distance (a) and proper motion (b) distributions for stars in the complete sample (non-shaded histograms) and in the deep sub-sample (shaded histograms).

star is given in columns 4 and 5 of Table 2.2.

The distribution of the total ($\sqrt{(\mu_\alpha \cos\delta)^2 + \mu_\delta^2}$) proper motions for the sample stars is presented in Figure 2.4b. The proper motions of the sample stars will be essential in identifying bona fide companions to the sample stars through astrometry (§5).

2.3 Sample Selection

The description of the sample selection process presented in §2.3.1 is a summary of the algorithm employed for the FEPS sample selection, discussed in greater detail by Meyer et al. (2005). The limited number of target additions and further constraints are discussed in §2.3.2.

2.3.1 FEPS Sample Selection

The stars in the FEPS target list are drawn from three recently assembled compilations of solar analogs. The first compilation is that of Soderblom et al. (2000, private communication), who have produced a volume-limited (based on *Hippar-*

cos) set of approximately 5000 solar-type stars over the entire sky. The Soderblom et al. sample exhibits some overlap with the recently published Wright et al. (2004) sample, which will henceforth be used as the reference of choice. The stars in this sample have parallaxes that place them within 60 pc, $B-V$ colors between 0.52 mag and 0.81 mag (F8–K0 spectral types), and location on the H-R diagram within 1.0 mag of the solar-metallicity ZAMS. The sample is fully complete to 50 pc. From this sample, the FEPS team has extracted stars with ages between 0.1 and 3 Gyr, based on the R'_{HK} chromospheric activity index (§2.2.2). However, being located more than 100 pc from the nearest star-forming region, the Soderblom et al. list is deficient in stars younger than a few hundred Myr.

To fill in the gap at young ages, the volume limit was extended to include large enough samples of young stars. These were identified from new spectroscopic observations of x-ray and proper-motion-selected samples of late-type stars (e.g., Mamajek et al., 2002), and from an examination of the literature. The surface density distribution of x-ray sources in the ROSAT all-sky survey reveals a concentration of objects coincident with Gould's Belt: an expanding ring of atomic and molecular gas in the distant solar neighborhood (50–200 pc), which comprises nearly all star-forming regions within 1 kpc. Tycho-2 proper motion data allow the selection of the nearest of these x-ray emitting stars with space motions consistent with those of higher-mass, young stars with measured parallaxes. As in the case of the <50 pc sample, the youth of the stars is confirmed from follow-up high-resolution spectroscopic observations. There are approximately 600 stars in this sample, ranging from 3 to 100 Myr in age, with $B-V$ colors between 0.58 and 1.20 (spectral types G0–K5), strong x-ray emission, kinematics appropriate for the young galactic disk, and high lithium abundance compared to the 125 Myr old Pleiades.

Finally, all known members of nearby well-studied young open clusters (IC 2602, α Per, the Pleiades, and the Hyades) meeting the targeted spectral type range were also considered.

From this large sample, targets were selected for the FEPS *Spitzer* campaign

if they met all of the following criteria (Meyer et al., 2005):

1. $K < 10$ mag (<100 Myr x-ray selected and cluster samples) or $K < 6.75$ mag (0.1–3 Gyr *Hipparcos* and R'_{HK} selected samples);

2. low 24μm and 70μm *IRAS* background;

3. galactic latitude $|b| > 5^\circ$ (except for stars in IC 2602);

4. good quality JHK_S photometry from the Two-Micron All Sky Survey (2MASS; Cutri et al., 2003) with no flags;

5. no projected 2MASS companions closer than $5''$;

6. for >100 Myr-old stars: no projected 2MASS companions closer than $15''$ unless they are both bluer in $J-K_S$ and fainter at K_S by > 3 mag compared to the *Spitzer* target.

The above criteria were applied uniformly for the vast majority of the stars in the parent FEPS sample. In addition, approximately half of the stars older than ∼600 Myr were arbitrarily removed from the program to even out the age bins and to bring the program within the allocated time limits. However, some exceptions pertinent to our study of stellar multiplicity need to be noted. The following three cases provide an exhaustive list of potentially relevant exceptions:

7. stars appearing on *Spitzer* GTO programs were removed from the source list;

8. to a limited degree, stars identified in spectroscopy or high-resolution imaging literature published through March 2001 as being binary, with companions closer than $2''$, were removed. These were all either spectroscopic binaries or visual binaries with small magnitude differences between the components;

9. a set of 10 F3–K4 stars with known IR excesses from *IRAS* and *ISO*, likely due to circumstellar dust, was added[1];

[1]For an experiment aimed at detecting gas in known young dusty debris disks (Hollenbach et al., 2005).

10. three >3 Gyr-old stars with known extra-solar planets were added to the sample.

The final FEPS sample comprises 326 stars distributed uniformly in logarithmic age intervals between 3 Myr and 3 Gyr. Approximately 60 of these are members of open clusters, with the remainder being field stars between 11 and 180 pc.

2.3.2 AO Sample Selection: Further Constraints and Additions

In addition to the FEPS sample selection criteria outlined above, we applied the following additional criterion to the entire sample:

11. a minimum declination of $-30°$.

This constraint is imposed by the northern latitude of the Palomar $200''$ telescope– the main instrument for our companion survey.

Finally, to optimize the sensitivity to sub-stellar companions, we applied the following three criteria for stars in the deep sample only:

12. no stars older than 500 Myr in the deep sample;

13. no $\Delta K_S < 4$ objects between $0.8''$ and $13''$ from stars in the deep sample, as determined from real-time flux ratio measurements during survey observations;

14. nearby stars were given priority over more distanct stars;

15. isolated stars, not belonging to one of the open clusters, were given priority for deep observations.

The first criterion is motivated by the fact that sub-stellar companions should be intrinsically brightest at the youngest ages. The application of this criterion excludes the Hyades from the deep sample, which have already been imaged under high angular resolution through speckle interferometry by Patience et al. (1998). The second constraint was aimed at avoiding the loss of sensitivity to faint objects over a large portion of the $25'' \times 25''$ PHARO FOV because of the presence of a

bright neighboring star. Binaries with separations $\leq 0.8''$ had both their components sufficiently well-covered by the $0.97''$ coronagraph and were allowed in the deep sample. The motivation for the third constraint was optimization of sensitivity to sub-stellar companions at the smallest physical separations. Finally, the last criterion was applied to avoid duplication with previous sensitive high-angular resolution studies of open clusters: Bouvier et al. (1997, the Pleiades, AO) and Patience et al. (2002, α Persei, speckle).

No additional constraints on the objects' apparent brightness needed to be imposed to ensure nominal operation of the AO system in NGS mode. The FEPS requirement that $K < 10$ mag, combined with the range of spectral types studied ($R - K \approx 2.0$ at K5), meant that all targets are brighter than $R = 12$ mag, i.e., sufficiently bright for NGS AO.

Based on the additional criteria (11–15), 246 stars were selected from the FEPS program for the companion survey, 85 of which were observed in deep exposures. A further 20 solar analogs were added to the overall sample toward the end of the first epoch of observations in December 2003, mirroring the FEPS source-selection policy outlined in §2.3.1 (except for slightly down-sizing the no-companion radius in criterion 6 to match the half-width of the PHARO field: $12.8''$). Sixteen of these, selected from the compilations of nearby young stars by Montes et al. (2001b) and Wichmann et al. (2003), as well as from our Palomar $60''$ echelle survey, were in the deep sample.

The final target list for the AO companion survey comprises 266 solar-type stars with a similar age distribution as that of the stars in the FEPS list. The deep sub-sample consists of 101 stars younger than 500 Myr. All sample stars and their characteristics are listed in Table 2.2. Stars with names given in **bold** type belong to the deep sub-sample. The table columns list, in order: star name, R.A., DEC., proper motion along R.A., proper motion along DEC., heliocentric distance, Johnson or Tycho V-band magnitude, 2MASS K_S-band magnitude (not corrected for subsequently-discovered binarity), adopted spectral type, R'_{HK} index, cluster association, estimated age, and estimated mass.

Table 2.2: Survey Sample

Star	α (J2000.0)	δ (J2000.0)	$\mu_\alpha \cos\delta$ (mas yr^{-1})	$\mu_d elta$ (mas yr^{-1})	d (pc)	V or $V_{\rm T}$ (mag)	K_S (mag)	Sp.T.	R'_{HK}	Assoc.	Age (log Myr^{-1})	M ($M_\odot$)
HD 224873	00:01:23.66	+39:36:38.12	-28.7 ± 0.6	-43.3 ± 0.7	49.0 ± 5.0	8.6	6.7	K0	–4.38	···	$8.48^{+0.30}_{-0.30}$	1.01
HD 377	00:08:25.74	+06:37:00.50	85.2 ± 1.5	-2.6 ± 1.4	40.0 ± 2.0	7.6	6.1	G2V	–4.29	···	$7.59^{+0.30}_{-0.30}$	1.11
HD 691	00:11:22.44	+30:26:58.52	209.7 ± 1.0	35.5 ± 1.0	34.0 ± 1.0	8.0	6.2	K0V	–4.38	···	$8.46^{+0.30}_{-0.30}$	0.98
HD 984	00:14:10.25	–07:11:56.92	104.9 ± 1.3	-67.6 ± 1.2	46.0 ± 2.0	7.4	6.1	F7V	–4.29	···	$7.63^{+0.30}_{-0.30}$	1.22
HD 1405	00:18:20.78	+30:57:23.76	141.5 ± 2.2	-177.0 ± 2.1	29.0 ± 10.0	8.6	6.4	K2V	–5.18	···	$8.00^{+0.30}_{-0.30}$	0.84
QT And	00:41:17.32	+34:25:16.77	44.8 ± 0.7	-36.2 ± 0.8	50.0 ± 25.0	10.1	7.3	K4	···	···	7.79 ± 0.29	0.84
HD 6963	01:10:41.91	+42:55:54.50	-154.6 ± 0.9	-198.5 ± 0.9	27.0 ± 1.0	7.7	5.9	G7V	–4.54	···	$9.02^{+0.30}_{-0.30}$	0.93
HD 7661	01:16:24.19	–12:05:49.33	134.8 ± 1.1	-5.7 ± 1.1	27.0 ± 1.0	7.6	5.7	K0V	–4.41	···	$8.64^{+0.30}_{-0.30}$	0.96
HIP 6276	01:20:32.27	–11:28:03.74	116.0 ± 1.1	-140.2 ± 1.1	35.0 ± 1.0	8.5	6.5	G0	–4.38	···	$8.47^{+0.30}_{-0.30}$	0.91
HD 8467	01:24:28.00	+39:03:43.55	210.6 ± 1.8	-26.6 ± 1.0	31.0 ± 1.0	8.5	6.6	G5	–4.74	···	9.33 ± 0.30	0.82
HD 8941	01:28:24.36	+17:04:45.20	118.3 ± 0.7	-34.8 ± 0.7	50.0 ± 2.0	6.6	5.4	F8IV–V	–4.66	···	$9.22^{+0.30}_{-0.30}$	1.46
HD 8907	01:28:34.35	+42:16:03.70	51.7 ± 1.0	-99.2 ± 1.1	34.0 ± 1.0	6.6	5.4	F8	–4.39	···	8.25 ± 0.25	1.23
HD 9472	01:33:19.03	+23:58:32.19	0.0 ± 1.0	28.4 ± 0.9	33.0 ± 1.0	7.7	6.0	G0	–4.49	···	$8.93^{+0.30}_{-0.30}$	1.02
HD 224873	00:01:23.66	+39:36:38.12	-28.7 ± 0.6	-43.3 ± 0.7	49.0 ± 5.0	8.6	6.7	K0	–4.38	···	$8.48^{+0.30}_{-0.30}$	1.01
HD 377	00:08:25.74	+06:37:00.50	85.2 ± 1.5	-2.6 ± 1.4	40.0 ± 2.0	7.6	6.1	G2V	–4.29	···	$7.59^{+0.30}_{-0.30}$	1.11
HD 691	00:11:22.44	+30:26:58.52	209.7 ± 1.0	35.5 ± 1.0	34.0 ± 1.0	8.0	6.2	K0V	–4.38	···	$8.46^{+0.30}_{-0.30}$	0.98
HD 984	00:14:10.25	–07:11:56.92	104.9 ± 1.3	-67.6 ± 1.2	46.0 ± 2.0	7.4	6.1	F7V	–4.29	···	$7.63^{+0.30}_{-0.30}$	1.22
HD 1405	00:18:20.78	+30:57:23.76	141.5 ± 2.2	-177.0 ± 2.1	29.0 ± 10.0	8.6	6.4	K2V	–5.18	···	$8.00^{+0.30}_{-0.30}$	0.84
QT And	00:41:17.32	+34:25:16.77	44.8 ± 0.7	-36.2 ± 0.8	50.0 ± 25.0	10.1	7.3	K4	···	···	7.79 ± 0.29	0.84
HD 6963	01:10:41.91	+42:55:54.50	-154.6 ± 0.9	-198.5 ± 0.9	27.0 ± 1.0	7.7	5.9	G7V	–4.54	···	$9.02^{+0.30}_{-0.30}$	0.93
HD 7661	01:16:24.19	–12:05:49.33	134.8 ± 1.1	-5.7 ± 1.1	27.0 ± 1.0	7.6	5.7	K0V	–4.41	···	$8.64^{+0.30}_{-0.30}$	0.96
HIP 6276	01:20:32.27	–11:28:03.74	116.0 ± 1.1	-140.2 ± 1.1	35.0 ± 1.0	8.5	6.5	G0	–4.38	···	$8.47^{+0.30}_{-0.30}$	0.91
HD 8467	01:24:28.00	+39:03:43.55	210.6 ± 1.8	-26.6 ± 1.0	31.0 ± 1.0	8.5	6.6	G5	–4.74	···	9.33 ± 0.30	0.82
HD 8941	01:28:24.36	+17:04:45.20	118.3 ± 0.7	-34.8 ± 0.7	50.0 ± 2.0	6.6	5.4	F8IV–V	–4.66	···	$9.22^{+0.30}_{-0.30}$	1.46
HD 8907	01:28:34.35	+42:16:03.70	51.7 ± 1.0	-99.2 ± 1.1	34.0 ± 1.0	6.6	5.4	F8	–4.39	···	8.25 ± 0.25	1.23
HD 9472	01:33:19.03	+23:58:32.19	0.0 ± 1.0	28.4 ± 0.9	33.0 ± 1.0	7.7	6.0	G0	–4.49	···	$8.93^{+0.30}_{-0.30}$	1.02

continued on next page

Table 2.2 – continued from previous page

Star	α (J2000.0)	δ (J2000.0)	$\mu_\alpha \cos\delta$ (mas yr^{-1})	$\mu_d elta$ (mas yr^{-1})	d (pc)	V or $V_{\rm T}$ (mag)	K_S (mag)	Sp.T.	R'_{HK}	Assoc.	Age ($\log$ Myr^{-1})	M ($M_\odot$)
RE J0137+18A	01:37:39.41	+18:35:33.16	65.8 ± 1.9	-46.0 ± 2.5	64.0 ± 8.0	10.7	6.7	K3Ve	···	···	6.75 ± 0.25	1.02
HD 11850	01:56:47.27	+23:03:04.09	-83.8 ± 1.0	-18.1 ± 1.0	33.0 ± 1.0	7.9	6.2	G5	–4.44	···	$8.76^{+0.30}_{-0.30}$	0.98
HD 12039	01:57:48.98	–21:54:05.32	102.4 ± 1.2	-48.0 ± 1.1	42.0 ± 2.0	8.1	6.5	G3/5V	–4.21	···	7.50 ± 0.30	0.98
HD 13382	02:11:23.15	+21:22:38.39	273.1 ± 0.8	-12.6 ± 0.7	33.0 ± 1.0	7.4	5.8	G5V	–4.42	···	$8.71^{+0.30}_{-0.30}$	1.08
HD 13507	02:12:55.00	+40:40:06.00	56.9 ± 1.3	-99.2 ± 1.3	26.0 ± 1.0	7.2	5.6	G5V	–4.48	···	$8.89^{+0.30}_{-0.30}$	1.00
HD 13531	02:13:13.35	+40:30:27.34	57.6 ± 1.0	-96.4 ± 1.0	26.0 ± 1.0	7.4	5.7	G7V	–4.42	···	$8.67^{+0.30}_{-0.30}$	0.98
HD 13974	02:17:03.23	+34:13:27.32	1153.8 ± 0.8	-245.1 ± 0.8	11.0 ± 0.1	4.8	3.2	G0V	–4.64	···	$9.19^{+0.30}_{-0.30}$	1.10
HD 15526	02:29:35.03	–12:24:08.56	42.1 ± 1.3	-12.2 ± 1.1	106.0 ± 26.0	9.9	8.0	G5/6V	···	···	7.62 ± 0.12	1.13
1RXS J025216.9+361658	02:52:17.59	+36:16:48.14	53.4 ± 1.3	-40.1 ± 0.7	140.0 ± 70.0	10.7	7.6	K2IV	···	···	7.75 ± 0.25	1.11
1RXS J025223.5+372914	02:52:24.73	+37:28:51.83	22.5 ± 0.7	-24.5 ± 1.0	170.0 ± 85.0	10.8	9.1	G5IV	···	···	8.25 ± 0.25	1.16
HD 17925	02:52:32.14	–12:46:11.18	397.3 ± 1.2	-189.9 ± 1.3	10.0 ± 0.1	6.0	4.1	K1V	–4.311	···	7.87 ± 0.13	0.86
2RE J0255+474	02:55:43.60	+47:46:47.58	79.8 ± 0.6	-76.1 ± 0.7	50.0 ± 25.0	10.8	7.2	K5Ve	···	αPer	7.90 ± 0.15	0.82
1RXS J025751.8+115759	02:57:51.68	+11:58:05.83	31.4 ± 1.2	-28.4 ± 1.2	118.0 ± 16.0	10.8	8.5	G7V	···	···	7.75 ± 0.25	1.05
RX J0258.4+2947	02:58:28.77	+29:47:53.80	17.4 ± 1.2	-40.0 ± 0.6	100.0 ± 50.0	11.4	9.1	K0IV	···	···	8.00 ± 0.10	0.86
HD 18940	03:03:28.65	+23:03:41.19	111.4 ± 0.8	-0.7 ± 0.7	34.0 ± 1.0	7.1	5.5	G0	–4.47	···	$8.87^{+0.30}_{-0.30}$	1.15
HD 19019	03:03:50.82	+06:07:59.82	231.8 ± 1.8	50.7 ± 1.7	31.0 ± 1.0	7.0	5.6	F8	–4.62	···	9.16 ± 0.30	1.13
1RXS J030759.1+302032	03:07:59.20	+30:20:26.05	31.2 ± 0.6	-66.6 ± 0.7	75.0 ± 37.5	9.3	7.4	G5IV	···	···	8.25 ± 0.25	1.08
HD 19632	03:08:52.45	–24:53:15.55	226.7 ± 1.3	136.3 ± 1.3	30.0 ± 1.0	7.4	5.7	G3/5V	–4.40	···	$8.60^{+0.30}_{-0.30}$	1.07
HD 19668	03:09:42.28	–09:34:46.46	88.0 ± 1.2	-113.3 ± 1.1	40.0 ± 2.0	8.6	6.7	G8/K0V	–4.36	···	$8.36^{+0.30}_{-0.30}$	0.94
1E 0307.4+1424	03:10:12.55	+14:36:02.90	-4.0 ± 1.2	-25.3 ± 1.2	160.0 ± 80.0	10.5	8.8	G6V	···	···	7.75 ± 0.25	1.15
vB 1	03:17:26.39	+07:39:20.90	167.2 ± 1.3	-6.4 ± 1.4	43.1 ± 0.6	7.4	6.0	F8	–4.60	Hyades	$8.78^{+0.30}_{-0.30}$	1.18
HE 350	03:17:36.93	+48:50:08.50	23.2 ± 0.8	-23.0 ± 0.9	190.0 ± 11.0	11.1	9.3	G2	···	αPer	$7.90^{+0.30}_{-0.30}$	1.22
HE 373	03:18:27.39	+47:21:15.42	29.0 ± 0.7	-26.8 ± 2.0	190.0 ± 11.0	11.5	9.4	G8	···	αPer	$7.90^{+0.30}_{-0.30}$	1.21
HE 389	03:18:50.31	+49:43:52.19	22.5 ± 0.9	-23.9 ± 0.7	190.0 ± 11.0	11.2	9.5	G0	···	αPer	$7.90^{+0.30}_{-0.30}$	1.13
AP 93	03:19:02.76	+48:10:59.61	16.4 ± 4.0	-23.6 ± 1.4	190.0 ± 11.0	12.0	9.4	K2	···	αPer	$7.90^{+0.30}_{-0.30}$	1.00
1RXS J031907.4+393418	03:19:07.61	+39:34:10.50	27.3 ± 0.9	-25.3 ± 1.7	100.0 ± 50.0	11.7	9.5	K0V	···	···	7.75 ± 0.25	0.79
HE 622	03:24:49.71	+48:52:18.33	22.3 ± 0.9	-26.3 ± 0.7	190.0 ± 11.0	11.7	9.6	G7	···	αPer	$7.90^{+0.30}_{-0.30}$	1.06
HE 696	03:26:19.36	+49:13:32.54	19.8 ± 0.7	-25.0 ± 0.7	190.0 ± 11.0	11.6	9.7	G3	···	αPer	$7.90^{+0.30}_{-0.30}$	1.03
1E 0324.1–2012	03:26:22.05	–20:01:48.81	25.0 ± 1.6	7.4 ± 1.6	160.0 ± 80.0	10.4	8.9	G4V	···	···	7.75 ± 0.25	1.15
HE 699	03:26:22.22	+49:25:37.52	22.4 ± 0.8	-24.5 ± 0.7	190.0 ± 11.0	11.3	9.4	G3	···	αPer	$7.90^{+0.30}_{-0.30}$	1.12
HE 750	03:27:37.79	+48:59:28.78	22.0 ± 0.7	-25.6 ± 0.7	190.0 ± 11.0	10.5	9.1	F5	···	αPer	$7.90^{+0.30}_{-0.30}$	1.21

continued on next page

Table 2.2 – continued from previous page

Star	α (J2000.0)	δ (J2000.0)	$\mu_\alpha \cos\delta$ (mas yr^{-1})	$\mu_d elta$ (mas yr^{-1})	d (pc)	V or $V_{\rm T}$ (mag)	K_S (mag)	Sp.T.	R'_{HK}	Assoc.	Age (log Myr^{-1})	M ($M_\odot$)
HE 767	03:27:55.02	+49:45:37.16	21.1 ± 0.6	-26.0 ± 0.6	190.0 ± 11.0	10.7	9.2	F6	···	αPer	$7.90^{+0.30}_{-0.30}$	1.23
RX J0329.1+0118	03:29:08.06	+01:18:05.66	4.4 ± 1.3	-4.5 ± 1.3	100.0 ± 50.0	10.6	9.2	G0(IV)	···	···	7.75 ± 0.25	0.91
HE 848	03:29:26.24	+48:12:11.74	22.2 ± 0.6	-26.4 ± 0.6	190.0 ± 11.0	10.0	8.5	F9V	···	αPer	$7.90^{+0.30}_{-0.30}$	1.33
HE 935	03:31:28.99	+48:59:28.37	21.3 ± 0.9	-26.6 ± 0.6	190.0 ± 11.0	10.1	8.5	F9.5V	···	αPer	$7.90^{+0.30}_{-0.30}$	1.33
HE 1101	03:35:08.75	+49:44:39.59	20.9 ± 1.3	-28.5 ± 0.9	190.0 ± 11.0	11.3	9.3	G5	···	αPer	$7.90^{+0.30}_{-0.30}$	1.18
HD 22179	03:35:29.91	+31:13:37.45	42.6 ± 0.6	-46.0 ± 0.7	140.0 ± 70.0	9.0	7.4	G5IV	···	···	7.75 ± 0.25	1.26
HE 1234	03:39:02.91	+51:36:37.11	21.4 ± 0.8	-33.7 ± 0.7	190.0 ± 11.0	10.8	8.9	G4	···	αPer	$7.90^{+0.30}_{-0.30}$	1.27
HD 22879	03:40:22.08	–03:13:00.86	691.6 ± 1.1	-212.8 ± 1.1	24.0 ± 1.0	6.7	5.2	F7/8V	–4.71	···	$9.29^{+0.30}_{-0.30}$	0.79
HD 23208	03:42:39.80	–20:32:43.80	3.8 ± 1.4	24.1 ± 1.0	57.5 ± 4.7	9.2	7.2	G8V	–5.18	···	6.70 ± 0.30	0.61
HII 102	03:43:24.54	+23:13:33.30	17.1 ± 0.6	-43.7 ± 0.6	133.0 ± 6.0	10.5	8.7	G6	···	Pleiades	$8.08^{+0.30}_{-0.30}$	1.12
HII 120	03:43:31.95	+23:40:26.61	18.0 ± 0.7	-46.8 ± 0.6	133.0 ± 6.0	10.8	9.1	G5	···	Pleiades	$8.08^{+0.30}_{-0.30}$	1.05
HII 152	03:43:37.73	+23:32:09.59	19.5 ± 0.7	-46.9 ± 1.0	133.0 ± 6.0	10.7	9.1	G4	···	Pleiades	$8.08^{+0.30}_{-0.30}$	1.01
HII 174	03:43:48.33	+25:00:15.83	18.8 ± 1.1	-47.0 ± 0.9	133.0 ± 6.0	11.6	9.4	K1	···	Pleiades	$8.08^{+0.30}_{-0.30}$	0.90
HII 173	03:43:48.41	+25:11:24.19	20.4 ± 0.8	-48.4 ± 0.7	133.0 ± 6.0	10.9	8.8	K0	···	Pleiades	$8.08^{+0.30}_{-0.30}$	1.06
HII 250	03:44:04.24	+24:59:23.40	20.1 ± 1.0	-49.4 ± 0.7	133.0 ± 6.0	10.7	9.1	G3	···	Pleiades	$8.08^{+0.30}_{-0.30}$	1.04
HII 314	03:44:20.09	+24:47:46.16	18.2 ± 0.7	-49.8 ± 0.8	133.0 ± 6.0	10.6	8.9	G3	···	Pleiades	$8.08^{+0.30}_{-0.30}$	1.13
1RXS J034423.3+281224	03:44:24.25	+28:12:23.07	46.4 ± 0.7	-50.6 ± 0.6	100.0 ± 50.0	8.9	7.2	G7V	···	···	7.75 ± 0.25	1.30
HII 514	03:45:04.01	+25:15:28.23	17.3 ± 0.7	-46.3 ± 0.6	133.0 ± 6.0	10.7	9.0	G4	···	Pleiades	$8.08^{+0.30}_{-0.30}$	1.08
HII 571	03:45:15.35	+25:17:22.11	15.1 ± 0.9	-48.5 ± 0.9	133.0 ± 6.0	11.3	9.2	G9	···	Pleiades	$8.08^{+0.30}_{-0.30}$	0.96
HII 1015	03:46:27.35	+25:08:07.97	18.6 ± 0.7	-48.5 ± 0.9	133.0 ± 6.0	10.5	9.0	G1	···	Pleiades	$8.08^{+0.30}_{-0.30}$	1.08
HII 1101	03:46:38.78	+24:57:34.61	18.4 ± 0.8	-48.1 ± 0.7	133.0 ± 6.0	10.3	8.8	G4	···	Pleiades	$8.08^{+0.30}_{-0.30}$	1.10
HII 1182	03:46:47.06	+22:54:52.48	18.4 ± 0.6	-45.6 ± 0.7	133.0 ± 6.0	10.5	8.9	G1	···	Pleiades	$8.08^{+0.30}_{-0.30}$	1.09
HII 1200	03:46:50.54	+23:14:21.06	17.3 ± 0.6	-40.2 ± 0.7	133.0 ± 6.0	9.9	8.5	F6	···	Pleiades	$8.08^{+0.30}_{-0.30}$	1.25
HII 1348[†]	03:47:18.04	+24:23:27.00	14.1 ± 0.5	-48.8 ± 0.5	133.0 ± 6.0	12.1	9.7	K5	–5.18	Pleiades	$8.08^{+0.30}_{-0.30}$	0.86
HII 1776	03:48:17.70	+25:02:52.29	19.0 ± 1.0	-47.1 ± 1.0	133.0 ± 6.0	11.0	9.2	G5	···	Pleiades	$8.08^{+0.30}_{-0.30}$	1.02
HII 2106	03:48:58.49	+23:12:04.33	16.5 ± 1.3	-44.9 ± 1.1	133.0 ± 6.0	11.5	9.4	K1	···	Pleiades	$8.08^{+0.30}_{-0.30}$	0.91
RX J0348.9+0110	03:48:58.76	+01:10:53.99	35.1 ± 1.6	-22.1 ± 1.2	100.0 ± 50.0	10.6	8.3	K3(V)/E	···	···	$8.18^{+0.30}_{-0.30}$	1.05
HII 2147	03:49:06.11	+23:46:52.49	15.9 ± 0.9	-43.8 ± 0.8	133.0 ± 6.0	10.8	8.6	G7IV	···	Pleiades	$8.08^{+0.30}_{-0.30}$	1.11
HII 2278	03:49:25.70	+24:56:15.43	18.4 ± 0.9	-47.0 ± 0.8	133.0 ± 6.0	10.9	8.8	K0	···	Pleiades	$8.08^{+0.30}_{-0.30}$	1.09
HII 2506	03:49:56.49	+23:13:07.01	17.6 ± 0.7	-43.9 ± 0.6	133.0 ± 6.0	10.2	8.8	F9	···	Pleiades	$8.08^{+0.30}_{-0.30}$	1.15
HII 2644	03:50:20.90	+24:28:00.22	19.8 ± 0.8	-46.8 ± 0.9	133.0 ± 6.0	11.1	9.3	G5	···	Pleiades	$8.08^{+0.30}_{-0.30}$	0.98

continued on next page

Table 2.2 – continued from previous page

Star	α (J2000.0)	δ (J2000.0)	$\mu_\alpha \cos\delta$ (mas yr^{-1})	$\mu_d elta$ (mas yr^{-1})	d (pc)	V or $V_{\rm T}$ (mag)	K_S (mag)	Sp.T.	R'_{HK}	Assoc.	Age ($\log$ Myr^{-1})	M ($M_\odot$)
1RXS J035028.0+163121	03:50:28.40	+16:31:15.19	26.2 ± 1.3	-23.4 ± 2.1	138.0 ± 21.0	10.6	8.6	G5IV	···	···	7.75 ± 0.25	1.12
HII 2786	03:50:40.08	+23:55:58.94	17.6 ± 0.7	-45.2 ± 1.0	133.0 ± 6.0	10.3	8.9	F9	···	Pleiades	$8.08^{+0.30}_{-0.30}$	1.12
HII 2881	03:50:54.32	+23:50:05.52	17.7 ± 0.7	-46.9 ± 1.1	133.0 ± 6.0	11.6	9.1	K2	···	Pleiades	$8.08^{+0.30}_{-0.30}$	0.93
HII 3097	03:51:40.44	+24:58:59.41	17.5 ± 0.7	-46.1 ± 1.0	133.0 ± 6.0	11.0	9.1	G6	···	Pleiades	$8.08^{+0.30}_{-0.30}$	1.05
HII 3179	03:51:56.86	+23:54:06.98	19.2 ± 0.6	-46.5 ± 0.8	133.0 ± 6.0	10.0	8.6	F8	···	Pleiades	$8.08^{+0.30}_{-0.30}$	1.21
RX J0354.4+0535	03:54:21.31	+05:35:40.77	-1.4 ± 1.3	-7.6 ± 1.3	100.0 ± 50.0	10.2	8.7	G2(V)	···	···	8.25 ± 0.25	0.99
Pels 191	03:54:25.23	+24:21:36.38	17.1 ± 0.7	-46.8 ± 0.8	133.0 ± 6.0	11.1	9.1	G5IV	···	Pleiades	$8.08^{+0.30}_{-0.30}$	1.00
RX J0357.3+1258	03:57:21.39	+12:58:16.83	22.7 ± 1.8	-21.9 ± 1.5	149.0 ± 23.0	11.0	9.0	G0	···	···	7.75 ± 0.25	1.11
HD 285281	04:00:31.07	+19:35:20.70	2.7 ± 1.1	-12.9 ± 1.2	140.0 ± 70.0	10.2	7.6	K1	···	···	7.00 ± 0.50	1.11
HD 284135	04:05:40.58	+22:48:12.14	6.0 ± 0.6	-14.9 ± 0.6	140.0 ± 70.0	9.3	7.8	G3(V)	···	···	6.75 ± 0.25	1.11
HD 281691	04:09:09.74	+29:01:30.55	19.9 ± 0.7	-36.3 ± 1.0	140.0 ± 70.0	10.7	8.4	K1(V)	···	···	7.75 ± 0.25	1.13
HD 26182	04:10:04.69	+36:39:12.14	23.8 ± 0.7	-36.7 ± 0.7	100.0 ± 50.0	9.6	7.8	G0V	···	···	7.75 ± 0.25	1.20
HD 284266	04:15:22.92	+20:44:16.93	1.8 ± 1.0	-13.6 ± 0.7	140.0 ± 70.0	10.6	8.6	K0(V)	···	···	7.25 ± 0.25	1.20
HD 26990	04:16:16.50	+07:09:34.15	-85.6 ± 1.5	-52.1 ± 1.5	35.0 ± 2.0	7.6	5.9	G0(V)	–4.49	···	$8.92^{+0.30}_{-0.30}$	1.08
HD 27466	04:19:57.08	–04:26:19.60	-58.6 ± 1.2	-37.0 ± 1.2	36.0 ± 1.0	7.9	6.3	G5V	–4.64	···	$9.19^{+0.30}_{-0.30}$	1.01
vB 39	04:22:44.74	+16:47:27.56	-58.6 ± 1.2	-37.0 ± 1.2	39.3 ± 3.5	7.9	6.2	G4V	–4.51	Hyades	$8.78^{+0.30}_{-0.30}$	1.06
HD 285751	04:23:41.33	+15:37:54.87	8.2 ± 1.7	-15.8 ± 1.4	150.0 ± 75.0	11.3	8.8	K2(V)	···	···	6.75 ± 0.25	1.06
vB 49	04:24:12.78	+16:22:44.22	87.6 ± 1.3	-21.9 ± 1.2	57.5 ± 1.0	8.2	6.8	G0V	···	Hyades	$8.78^{+0.30}_{-0.30}$	1.14
vB 52	04:24:28.33	+16:53:10.32	113.1 ± 1.4	-23.3 ± 1.2	44.8 ± 0.8	7.8	6.3	G2V	–4.36	Hyades	$8.78^{+0.30}_{-0.30}$	1.12
vB 176	04:25:47.56	+18:01:02.20	102.6 ± 2.2	-29.9 ± 3.2	48.0 ± 1.0	9.0	6.8	K2V	–4.40	Hyades	$8.78^{+0.30}_{-0.30}$	0.95
vB 63	04:26:24.61	+16:51:11.84	106.7 ± 1.3	-24.5 ± 1.2	46.9 ± 1.0	8.0	6.4	G1V	–4.39	Hyades	$8.78^{+0.30}_{-0.30}$	1.09
vB 64	04:26:40.11	+16:44:48.78	107.0 ± 1.1	-26.8 ± 1.1	46.4 ± 0.9	8.1	6.5	G2+	–4.43	Hyades	$8.78^{+0.30}_{-0.30}$	1.07
vB 66	04:27:46.07	+11:44:11.07	110.1 ± 1.3	-13.2 ± 1.2	44.6 ± 0.9	7.5	6.2	F8	–4.39	Hyades	$8.78^{+0.30}_{-0.30}$	1.18
vB 73	04:28:48.29	+17:17:07.84	110.1 ± 1.1	-28.9 ± 1.0	44.5 ± 0.8	7.8	6.4	G2V	–4.47	Hyades	$8.78^{+0.30}_{-0.30}$	1.11
vB 79	04:29:31.61	+17:53:35.46	106.7 ± 1.1	-31.4 ± 1.1	45.6 ± 0.8	9.0	7.1	K0V	–4.43	Hyades	$8.78^{+0.30}_{-0.30}$	0.92
vB 180	04:29:57.73	+16:40:22.23	106.2 ± 1.1	-27.1 ± 1.1	46.0 ± 0.8	9.1	7.1	K1V	–4.46	Hyades	$8.78^{+0.30}_{-0.30}$	0.90
vB 88	04:31:29.35	+13:54:12.55	90.0 ± 1.2	-16.0 ± 1.2	53.1 ± 1.3	7.8	6.5	F9V	–4.55	Hyades	$8.78^{+0.30}_{-0.30}$	1.20
1RXS J043243.2–152003	04:32:43.51	–15:20:11.39	2.3 ± 1.1	14.2 ± 1.1	140.0 ± 70.0	10.6	8.6	G4V	···	···	6.58 ± 0.30	1.20
vB 91	04:32:50.12	+16:00:20.96	103.2 ± 1.0	-25.9 ± 1.0	45.9 ± 0.6	8.9	6.8	G7	···	Hyades	$8.78^{+0.30}_{-0.30}$	0.94
vB 92	04:32:59.45	+15:49:08.37	99.1 ± 1.2	-24.1 ± 1.2	47.8 ± 0.8	8.7	6.9	G7	–4.57	Hyades	$8.78^{+0.30}_{-0.30}$	0.98
vB 93	04:33:37.97	+16:45:44.96	99.0 ± 1.1	-22.9 ± 1.2	48.3 ± 0.7	9.4	7.4	G7	···	Hyades	$8.78^{+0.30}_{-0.30}$	0.87

continued on next page

Table 2.2 – continued from previous page

Star	α (J2000.0)	δ (J2000.0)	$\mu_\alpha \cos\delta$ (mas yr^{-1})	μ_delta (mas yr^{-1})	d (pc)	V or V_T (mag)	K_S (mag)	Sp.T.	R'_{HK}	Assoc.	Age ($\log$ Myr^{-1})	M ($M_\odot$)
vB 96	04:33:58.54	+15:09:49.04	101.9 ± 1.3	-29.4 ± 1.3	45.4 ± 0.8	8.5	6.5	G5	–4.53	Hyades	$8.78^{+0.30}_{-0.30}$	1.01
RX J0434.3+0226	04:34:19.54	+02:26:26.10	18.0 ± 2.0	-16.4 ± 1.9	161.0 ± 24.0	12.6	9.5	K4e	···	···	7.75 ± 0.25	0.90
vB 183	04:34:32.18	+15:49:39.23	91.0 ± 1.0	-20.0 ± 1.0	51.7 ± 0.8	9.7	7.6	G7	···	Hyades	$8.78^{+0.30}_{-0.30}$	0.86
vB 97	04:34:35.31	+15:30:16.56	98.1 ± 1.0	-26.7 ± 1.1	47.2 ± 0.9	7.9	6.4	F8:V:	–4.41	Hyades	$8.78^{+0.30}_{-0.30}$	1.12
vB 99	04:36:05.27	+15:41:02.60	95.0 ± 1.0	-23.1 ± 1.2	48.7 ± 0.7	9.4	7.4	G7	···	Hyades	$8.78^{+0.30}_{-0.30}$	0.88
vB 106	04:38:57.31	+14:06:20.16	99.5 ± 0.9	-24.4 ± 1.1	44.6 ± 0.9	8.0	6.4	G5	–4.50	Hyades	$8.78^{+0.30}_{-0.30}$	1.08
HD 282346	04:39:31.00	+34:07:44.43	31.3 ± 0.7	-53.8 ± 0.9	71.0 ± 14.0	9.8	7.4	G8V	···	···	$8.00^{+0.30}_{-0.30}$	1.04
RX J0442.5+0906	04:42:32.09	+09:06:00.86	28.9 ± 2.4	-22.3 ± 2.0	119.0 ± 21.0	11.2	9.1	G5(V)	···	···	7.75 ± 0.25	0.96
vB 142	04:46:30.38	+15:28:19.38	87.8 ± 1.1	-23.9 ± 1.1	48.2 ± 1.1	8.3	6.7	G5	–4.33	Hyades	$8.78^{+0.30}_{-0.30}$	1.05
vB 143	04:51:23.22	+15:26:00.45	66.7 ± 1.2	-17.2 ± 1.2	61.1 ± 1.9	7.9	6.7	F8	–4.62	Hyades	$8.78^{+0.30}_{-0.30}$	1.23
HD 286179	04:57:00.65	+15:17:53.09	-1.8 ± 1.5	-17.3 ± 1.4	140.0 ± 70.0	10.3	8.5	G3(V)	···	···	7.25 ± 0.25	1.23
HD 31950	05:00:24.31	+15:05:25.28	0.3 ± 1.1	-15.2 ± 1.1	100.0 ± 50.0	9.9	8.4	F8	···	···	7.75 ± 0.25	1.13
HD 286264	05:00:49.28	+15:27:00.68	20.0 ± 1.4	-59.0 ± 1.4	71.0 ± 11.0	10.9	7.6	K2IV	···	···	$7.30^{+0.30}_{-0.30}$	1.13
HD 32850	05:06:42.21	+14:26:46.42	282.8 ± 1.1	-239.9 ± 1.1	24.0 ± 1.0	7.7	5.7	G9V	–4.60	···	$9.12^{+0.30}_{-0.30}$	0.89
1RXS J051111.1+281353	05:11:10.53	+28:13:50.38	6.0 ± 0.8	-24.0 ± 0.7	199.0 ± 29.0	10.5	7.8	K0V	···	···	6.71 ± 0.30	0.89
HD 35850	05:27:04.77	–11:54:03.38	17.5 ± 0.7	-49.8 ± 0.8	27.0 ± 1.0	6.3	4.9	F7/8V	–4.10	···	7.50 ± 0.50	0.89
HD 36869	05:34:09.16	–15:17:03.20	23.9 ± 3.4	-21.8 ± 2.9	72.0 ± 21.0	8.5	6.9	G2V	–5.18	···	7.54 ± 0.54	1.20
1RXS J053650.0+133756	05:36:50.06	+13:37:56.22	4.9 ± 1.3	-108.8 ± 1.2	56.0 ± 28.0	10.6	8.1	K0V	···	···	8.25 ± 0.25	1.05
HD 245567	05:37:18.44	+13:34:52.52	7.5 ± 0.9	-33.2 ± 0.9	119.0 ± 21.0	9.6	7.6	G0V	···	···	$6.56^{+0.30}_{-0.30}$	1.05
HD 37216	05:39:52.33	+52:53:50.83	-10.0 ± 1.3	-141.4 ± 1.4	28.0 ± 1.0	7.9	6.0	G5	–4.46	···	8.83 ± 0.30	0.92
SAO 150676	05:40:20.74	–19:40:10.85	19.2 ± 1.2	-12.9 ± 1.2	78.0 ± 30.0	9.0	7.5	G2V	···	···	7.79 ± 0.29	1.14
HD 37006	05:46:11.89	+78:15:22.61	-45.9 ± 1.4	70.7 ± 1.4	35.0 ± 1.0	8.3	6.5	G0	–4.47	···	$8.87^{+0.30}_{-0.30}$	0.94
HD 38529	05:46:34.92	+01:10:05.31	-79.3 ± 0.9	-140.6 ± 1.0	42.0 ± 2.0	5.9	4.2	G8III/IV	–4.96	···	$9.68^{+0.30}_{-0.30}$	1.58
HD 38949	05:48:20.06	–24:27:50.04	-29.8 ± 1.1	-37.8 ± 1.2	43.0 ± 2.0	7.9	6.4	G1V	–4.36	···	$8.35^{+0.30}_{-0.30}$	1.09
HD 43989	06:19:08.05	–03:26:20.39	10.6 ± 0.9	-43.7 ± 1.0	50.0 ± 2.0	8.0	6.6	G0V	–4.15	···	7.75 ± 0.25	1.13
HD 49197	06:49:21.34	+43:45:32.87	-37.6 ± 0.6	-50.9 ± 0.6	45.0 ± 2.0	7.4	6.1	F5	–4.35	···	$8.70^{+0.20}_{-0.30}$	1.18
RE J0723+20	07:23:43.58	+20:24:58.64	-66.2 ± 1.8	-230.2 ± 2.6	24.0 ± 12.0	10.1	6.9	K3(V)	···	···	$8.13^{+0.37}_{-0.38}$	0.64
HD 60737	07:38:16.44	+47:44:55.34	-14.2 ± 1.0	-165.0 ± 1.0	38.0 ± 2.0	7.8	6.3	G0	–4.29	···	$8.17^{+0.30}_{-0.30}$	1.06
HD 61994	07:47:30.61	+70:12:23.97	-88.0 ± 1.0	-148.7 ± 1.1	28.0 ± 2.0	7.1	5.3	G6V	–4.51	···	$8.97^{+0.30}_{-0.30}$	1.07
HD 64324	07:54:48.47	+34:37:11.42	-120.5 ± 1.0	-173.4 ± 1.1	35.0 ± 1.0	7.8	6.2	G0	–4.58	···	$9.10^{+0.30}_{-0.30}$	1.01
HD 66751	08:10:20.51	+69:43:30.21	165.9 ± 1.0	116.1 ± 1.1	29.0 ± 1.0	6.6	5.1	F8V	–4.64	···	$9.18^{+0.30}_{-0.30}$	1.19

continued on next page

Table 2.2 – continued from previous page

Star	α (J2000.0)	δ (J2000.0)	$\mu_\alpha \cos\delta$ (mas yr^{-1})	$\mu_d elta$ (mas yr^{-1})	d (pc)	V or V_T (mag)	K_S (mag)	Sp.T.	R'_{HK}	Assoc.	Age ($\log$ Myr^{-1})	M ($M_\odot$)
HD 69076	08:15:07.73	−06:55:08.23	-11.6 ± 0.9	-159.3 ± 0.9	34.0 ± 1.0	8.3	6.4	K0V	–4.70	···	$9.27^{+0.30}_{-0.30}$	0.92
HD 70573	08:22:49.95	+01:51:33.58	-49.1 ± 1.1	-49.7 ± 1.1	46.0 ± 23.0	8.7	7.2	G1/2V	···	···	8.00 ± 0.50	0.95
HD 70516	08:24:15.66	+44:56:58.92	-63.1 ± 0.9	-178.4 ± 1.0	37.0 ± 3.0	7.7	6.1	G0	–4.30	αPer	$7.90^{+0.30}_{-0.30}$	1.06
HD 71974	08:31:35.05	+34:57:58.44	-5.9 ± 1.4	16.9 ± 1.5	29.0 ± 1.0	7.4	5.5	G5	–4.45	···	$8.94^{+0.30}_{-0.30}$	1.05
HD 72687	08:33:15.39	–29:57:23.66	-40.5 ± 1.3	19.8 ± 1.0	46.0 ± 2.0	8.3	6.7	G5V	···	···	$8.55^{+0.30}_{-0.30}$	1.04
HD 72760	08:34:31.65	–00:43:33.80	-194.3 ± 1.1	23.4 ± 0.8	21.8 ± 0.5	7.3	5.4	G5	–5.18	Hyades	$8.78^{+0.30}_{-0.30}$	0.91
HD 72905	08:39:11.62	+65:01:15.14	-28.9 ± 1.0	88.5 ± 1.0	14.0 ± 0.1	5.6	4.2	G1.5VB	–4.37	···	8.25 ± 0.25	1.04
HD 73668	08:39:43.81	+05:45:51.59	177.6 ± 1.5	-298.4 ± 1.6	36.0 ± 2.0	7.3	5.8	G1V	–4.75	···	$9.35^{+0.30}_{-0.30}$	1.13
HIP 42491	08:39:44.69	+05:46:14.00	173.9 ± 3.1	-297.2 ± 3.0	37.0 ± 8.0	8.6	6.5	G5	–4.63	···	$9.18^{+0.30}_{-0.30}$	0.93
HD 75302	08:49:12.53	+03:29:05.25	-147.8 ± 1.1	60.2 ± 1.1	30.0 ± 1.0	7.5	5.8	G5V	–4.60	···	$9.13^{+0.30}_{-0.30}$	1.01
HD 75393	08:49:15.35	–15:33:53.12	35.8 ± 1.4	-33.6 ± 1.2	42.0 ± 1.0	7.3	5.9	F7V	–4.36	···	$8.37^{+0.30}_{-0.30}$	1.20
HD 76218	08:55:55.68	+36:11:46.40	-25.4 ± 0.6	-12.4 ± 0.7	26.0 ± 1.0	7.8	5.8	G9–V	–4.42	···	$8.71^{+0.30}_{-0.30}$	0.92
HD 77407	09:03:27.08	+37:50:27.72	-80.2 ± 1.2	-168.0 ± 1.3	30.0 ± 1.0	7.1	5.4	G0(V)	–4.29	···	7.53 ± 0.30	1.10
HD 78899	09:12:28.27	+49:12:24.90	-49.7 ± 1.2	-176.5 ± 0.6	36.8 ± 1.4	7.6	5.8	K2V	–5.18	···	8.25 ± 0.25	1.11
HD 80606	09:22:37.56	+50:36:13.43	58.8 ± 1.5	13.2 ± 1.6	58.0 ± 20.0	9.1	7.3	G5	–4.94	···	9.66 ± 0.30	1.00
HD 82558	09:32:25.72	–11:11:05.00	-248.2 ± 1.2	35.1 ± 0.6	18.3 ± 0.3	7.8	5.4	K3V	–5.18	···	$8.00^{+0.30}_{-0.30}$	0.81
HD 82443	09:32:43.92	+26:59:20.76	-147.5 ± 0.9	-246.3 ± 0.5	17.7 ± 0.3	7.0	5.1	K0V	–5.18	···	$8.00^{+0.30}_{-0.30}$	0.90
HD 85301	09:52:16.77	+49:11:26.84	-213.7 ± 1.2	-68.9 ± 1.3	32.0 ± 1.0	7.8	6.1	G5	–4.58	···	$9.09^{+0.30}_{-0.30}$	0.98
SAO 178272	09:59:08.42	–22:39:34.57	-62.8 ± 1.4	-15.6 ± 1.7	58.0 ± 29.0	10.1	7.4	K2V	···	···	8.00 ± 0.50	0.88
HD 88638	10:14:35.76	+53:46:15.51	-270.9 ± 1.5	67.1 ± 1.5	38.0 ± 4.0	8.1	6.3	G5	–4.26	···	$9.50^{+0.30}_{-0.30}$	0.97
HD 90905	10:29:42.23	+01:29:27.82	-150.4 ± 0.8	-124.1 ± 0.8	32.0 ± 1.0	6.9	5.5	G1V	–4.35	···	$8.25^{+0.30}_{-0.30}$	1.15
HD 91782	10:36:47.84	+47:43:12.42	-71.4 ± 0.6	-81.7 ± 0.7	56.0 ± 3.0	8.1	6.8	G0	–4.34	···	$8.18^{+0.30}_{-0.30}$	1.15
HD 91962	10:37:00.02	–08:50:23.63	-94.1 ± 0.8	-48.8 ± 0.8	37.0 ± 2.0	7.0	5.4	G1V	–4.37	···	$8.39^{+0.30}_{-0.30}$	1.20
HD 92788	10:42:48.54	–02:11:01.38	-11.8 ± 1.2	-223.8 ± 1.3	32.0 ± 1.0	7.4	5.7	G6V	–4.94	···	9.65 ± 0.30	1.07
HD 92855	10:44:00.62	+46:12:23.86	-268.8 ± 1.1	-61.9 ± 1.2	36.0 ± 1.0	7.3	5.9	F9V	–4.34	···	$8.18^{+0.30}_{-0.30}$	1.12
HD 93528	10:47:31.20	–22:20:52.80	-122.7 ± 1.1	-29.4 ± 0.8	34.9 ± 1.2	8.4	6.5	K0V	–5.18	···	$8.00^{+0.30}_{-0.30}$	0.92
HD 95188	10:59:48.28	+25:17:23.65	-126.3 ± 1.4	1.7 ± 1.3	36.0 ± 1.0	8.5	6.6	G8V	–4.37	···	$8.42^{+0.30}_{-0.30}$	0.91
HD 98553	11:20:11.60	–19:34:40.54	69.1 ± 1.1	-68.9 ± 1.2	34.0 ± 1.0	7.6	6.1	G2/3V	–4.63	···	$9.17^{+0.30}_{-0.30}$	1.05
HD 99565	11:27:10.76	–15:38:55.05	1.6 ± 1.1	-197.2 ± 1.3	35.0 ± 3.0	7.6	5.8	G8V	–4.68	···	9.24 ± 0.30	1.08
HD 100167	11:31:53.92	+41:26:21.65	-42.7 ± 1.1	83.5 ± 1.1	35.0 ± 1.0	7.4	5.8	F8	–4.68	···	$9.25^{+0.30}_{-0.30}$	1.10
HD 101472	11:40:36.59	–08:24:20.32	-20.0 ± 0.8	-13.8 ± 0.8	39.0 ± 2.0	7.5	6.1	F7V	–4.37	···	$8.39^{+0.30}_{-0.30}$	1.13

continued on next page

Table 2.2 – continued from previous page

Star	α (J2000.0)	δ (J2000.0)	$\mu_\alpha \cos\delta$ (mas yr^{-1})	$\mu_d elta$ (mas yr^{-1})	d (pc)	V or $V_{\rm T}$ (mag)	K_S (mag)	Sp.T.	R'_{HK}	Assoc.	Age (log Myr^{-1})	M ($M_\odot$)
HD 101959	11:43:56.62	–29:44:51.80	-272.7 ± 1.6	37.4 ± 1.3	32.0 ± 1.0	7.0	5.6	G0V	–4.68	···	9.24 ± 0.30	1.13
HD 102071	11:44:39.32	–29:53:05.46	-71.9 ± 1.5	49.7 ± 1.4	30.0 ± 1.0	8.0	6.1	K0V	–4.70	···	$9.27^{+0.30}_{-0.30}$	0.93
BPM 87617	11:47:45.73	+12:54:03.31	-71.5 ± 1.9	-0.4 ± 1.8	50.0 ± 25.0	10.8	7.8	K5Ve	···	···	$8.13^{+0.37}_{-0.38}$	0.74
HD 103432	11:54:32.07	+19:24:40.44	-449.9 ± 1.0	-15.6 ± 0.8	37.0 ± 2.0	8.2	6.5	G6V	–4.72	···	$9.30^{+0.30}_{-0.30}$	0.96
HD 104576	12:02:39.46	–10:42:49.16	32.7 ± 1.0	-18.4 ± 0.9	49.0 ± 3.0	8.6	6.7	G3V	–4.34	···	$8.18^{+0.30}_{-0.30}$	1.02
HD 104860	12:04:33.71	+66:20:11.58	-56.1 ± 1.4	49.7 ± 1.4	48.0 ± 2.0	8.0	6.5	F8	–4.29	···	7.61 ± 0.30	1.12
HD 105631	12:09:37.26	+40:15:07.62	-314.3 ± 0.7	-51.3 ± 0.8	24.0 ± 1.0	7.5	5.6	G9V	–4.67	···	$9.23^{+0.30}_{-0.30}$	0.93
HD 106156	12:12:57.52	+10:02:15.62	210.5 ± 1.2	-357.6 ± 1.1	31.0 ± 1.0	7.9	6.1	G8V	–4.69	···	$9.27^{+0.30}_{-0.30}$	0.95
HD 106252	12:13:29.49	+10:02:29.96	24.2 ± 1.1	-280.3 ± 1.1	37.0 ± 1.0	7.4	5.9	G0	–4.83	···	$9.48^{+0.30}_{-0.30}$	1.11
HD 107146	12:19:06.49	+16:32:53.91	-175.6 ± 0.9	-149.5 ± 1.0	29.0 ± 1.0	7.0	5.5	G2V	–4.29	···	$8.00^{+0.30}_{-0.30}$	1.08
HD 108799	12:30:04.77	–13:23:35.14	-250.5 ± 2.1	-47.0 ± 2.2	25.0 ± 1.0	6.4	4.8	G1/2V	–4.36	···	$8.34^{+0.30}_{-0.30}$	1.15
HD 108944	12:31:00.74	+31:25:25.84	9.2 ± 1.1	25.1 ± 1.2	44.0 ± 2.0	7.3	6.0	F9V	–4.35	···	$8.24^{+0.30}_{-0.30}$	1.20
SAO 15880	12:43:33.36	+60:00:53.28	-125.2 ± 1.4	-66.4 ± 1.5	50.0 ± 25.0	9.4	7.3	K0	–5.18	···	$8.00^{+0.30}_{-0.30}$	0.88
SAO 2085	12:44:02.88	+85:26:56.40	-129.6 ± 0.8	43.2 ± 0.9	34.6 ± 17.3	8.8	7.3	G5	–5.18	···	$8.20^{+0.20}_{-0.20}$	0.85
HD 111456	12:48:39.46	+60:19:11.40	107.8 ± 3.1	-30.6 ± 2.6	24.2 ± 1.9	5.8	4.6	F5V	–5.18	···	8.50 ± 0.30	1.25
HD 112196	12:54:40.02	+22:06:28.65	52.1 ± 0.9	-33.9 ± 0.9	34.0 ± 2.0	7.1	5.6	F8V	–4.31	···	7.87 ± 0.30	1.16
HD 115043	13:13:37.01	+56:42:29.82	112.8 ± 0.9	-19.5 ± 1.0	26.0 ± 0.4	6.8	5.3	G1V	–4.48	···	$8.70^{+0.30}_{-0.30}$	1.08
HD 121320	13:54:28.20	+20:38:30.46	210.1 ± 1.0	-76.3 ± 1.0	33.0 ± 1.0	8.0	6.2	G5V	–4.69	···	$9.27^{+0.30}_{-0.30}$	0.97
HD 122652	14:02:31.63	+31:39:39.09	-94.5 ± 1.3	8.8 ± 1.3	37.0 ± 1.0	7.2	5.9	F8	–4.71	···	$9.29^{+0.30}_{-0.30}$	1.15
HD 129333	14:39:00.25	+64:17:29.94	-135.9 ± 1.1	-25.3 ± 1.2	34.0 ± 1.0	7.5	5.9	G5V	–4.11	αPer	$7.90^{+0.30}_{-0.30}$	1.05
HD 132173	14:58:30.51	–28:42:34.15	-99.9 ± 1.5	-93.0 ± 1.7	49.0 ± 2.0	7.7	6.2	G0V	–4.34	···	$8.18^{+0.30}_{-0.30}$	1.19
HD 133295	15:04:33.08	–28:18:00.65	40.1 ± 1.4	-51.9 ± 1.4	34.0 ± 1.0	7.2	5.8	G0/1V	–4.39	···	$8.53^{+0.30}_{-0.30}$	1.12
HD 134319	15:05:49.90	+64:02:50.00	-123.3 ± 1.1	110.1 ± 1.2	44.0 ± 1.0	8.4	6.8	G5(V)	–4.32	···	7.75 ± 0.25	0.99
HD 135363	15:07:56.31	+76:12:02.66	-130.5 ± 1.3	163.7 ± 1.3	29.0 ± 1.0	8.8	6.2	G5(V)	–4.17	···	7.79 ± 0.29	0.83
HD 136923	15:22:46.84	+18:55:08.31	-230.9 ± 1.1	77.2 ± 1.1	20.0 ± 0.4	7.1	5.3	G9V	–4.72	···	$9.30^{+0.30}_{-0.30}$	0.92
HD 138004	15:27:40.36	+42:52:52.82	-60.2 ± 0.8	-259.4 ± 0.8	32.0 ± 1.0	7.5	5.9	G2III	–4.73	···	9.32 ± 0.30	1.04
HD 139813	15:29:23.61	+80:27:01.08	-218.0 ± 1.2	105.8 ± 1.2	22.0 ± 0.3	7.3	5.5	G5	–4.35	···	$8.26^{+0.30}_{-0.30}$	0.92
HD 139498	15:39:24.40	–27:10:21.87	-21.8 ± 1.5	-28.1 ± 1.5	127.0 ± 10.0	9.6	7.5	G8(V)	···	ScoCen	$7.18^{+0.30}_{-0.30}$	0.92
RX J1541.1–2656	15:41:06.79	–26:56:26.33	-15.5 ± 5.5	-29.7 ± 1.6	145.0 ± 40.0	11.3	8.9	G7	···	USco	6.70 ± 0.30	0.92
HD 142229	15:53:20.02	+04:15:11.51	-24.4 ± 1.1	9.7 ± 1.0	41.0 ± 2.0	8.2	6.6	G5V	–4.44	Hyades	$8.78^{+0.30}_{-0.30}$	1.02
HD 142361	15:54:59.86	–23:47:18.26	-29.3 ± 1.1	-38.8 ± 1.1	101.0 ± 14.0	8.9	7.0	G3V	···	USco	6.70 ± 0.30	1.02

continued on next page

Table 2.2 – continued from previous page

Star	α (J2000.0)	δ (J2000.0)	$\mu_\alpha \cos\delta$ (mas yr^{-1})	$\mu_d elta$ (mas yr^{-1})	d (pc)	V or $V_{\rm T}$ (mag)	K_S (mag)	Sp.T.	R'_{HK}	Assoc.	Age ($\log$ Myr^{-1})	M ($M_\odot$)
HD 143006	15:58:36.92	–22:57:15.35	-10.6 ± 1.7	-19.5 ± 1.3	145.0 ± 40.0	10.2	7.1	G6/8	–4.03	USco	6.70 ± 0.30	1.02
(PZ99) J155847.8–175800	15:58:47.73	–17:57:59.58	-14.8 ± 3.5	-18.4 ± 2.8	145.0 ± 40.0	11.9	8.3	K3	···	USco	6.70 ± 0.30	1.02
RX J1600.6–2159	16:00:40.57	–22:00:32.24	-14.2 ± 1.7	-18.8 ± 1.7	145.0 ± 40.0	11.1	8.4	G9	···	USco	6.70 ± 0.30	1.02
ScoPMS 21	16:01:25.63	–22:40:40.38	-9.4 ± 2.8	-23.8 ± 1.7	145.0 ± 40.0	11.4	8.5	K1IV	···	USco	6.70 ± 0.30	1.02
(PZ99) J160302.7–180605	16:03:02.69	–18:06:05.06	-11.3 ± 2.9	-22.7 ± 1.7	145.0 ± 40.0	11.5	8.7	K4	···	USco	6.70 ± 0.30	0.87
ScoPMS 27	16:04:47.76	–19:30:23.12	-14.0 ± 2.3	-20.1 ± 3.1	145.0 ± 40.0	11.2	8.0	K2IV	···	USco	6.70 ± 0.30	0.87
(PZ99) J160814.7–190833	16:08:14.74	–19:08:32.77	-32.0 ± 7.3	-4.1 ± 7.7	145.0 ± 40.0	11.5	8.4	K2	···	USco	6.70 ± 0.30	0.87
HD 145229	16:09:26.63	+11:34:28.25	-99.5 ± 0.9	102.9 ± 1.2	33.0 ± 1.0	7.5	6.0	G0	–4.46	···	8.83 ± 0.30	1.05
ScoPMS 52	16:12:40.51	–18:59:28.31	-8.4 ± 2.4	-28.5 ± 4.1	145.0 ± 40.0	10.8	7.5	K0IV	···	USco	6.70 ± 0.30	1.05
(PZ99) J161318.6–221248	16:13:18.59	–22:12:48.96	-9.1 ± 1.2	-21.0 ± 1.4	145.0 ± 40.0	10.4	7.4	G9	···	USco	6.70 ± 0.30	1.05
(PZ99) J161329.3–231106	16:13:29.29	–23:11:07.56	-12.4 ± 2.0	-30.8 ± 2.5	145.0 ± 40.0	11.7	8.5	K1	···	USco	6.70 ± 0.30	1.05
(PZ99) J161402.1–230101	16:14:02.12	–23:01:02.18	-8.8 ± 1.7	-22.8 ± 1.7	145.0 ± 40.0	11.4	8.6	G4	···	USco	6.70 ± 0.30	1.05
(PZ99) J161411.0–230536	16:14:11.08	–23:05:36.26	-12.1 ± 1.6	-23.8 ± 1.9	145.0 ± 40.0	10.7	7.5	K0	···	USco	6.70 ± 0.30	1.05
(PZ99) J161459.2–275023	16:14:59.18	–27:50:23.06	-12.2 ± 1.6	-30.5 ± 5.0	145.0 ± 40.0	11.2	8.7	G5	···	USco	6.70 ± 0.30	1.05
(PZ99) J161618.0–233947	16:16:17.95	–23:39:47.70	-8.7 ± 2.0	-26.1 ± 1.7	145.0 ± 40.0	10.7	8.1	G7	···	USco	6.70 ± 0.30	1.05
HD 146516	16:17:31.39	–23:03:36.02	-13.2 ± 1.2	-17.3 ± 1.4	145.0 ± 40.0	10.1	8.0	G0IV	···	USco	6.70 ± 0.30	1.05
ScoPMS 214	16:29:48.70	–21:52:11.91	-5.6 ± 3.6	-22.1 ± 1.8	145.0 ± 40.0	11.2	7.8	K0IV	···	USco	6.70 ± 0.30	1.05
HD 150706	16:31:17.63	+79:47:23.15	95.1 ± 0.8	-89.2 ± 0.8	27.0 ± 0.4	7.0	5.6	G3(V)	–4.45	···	$8.81^{+0.30}_{-0.30}$	1.05
HD 150554	16:40:56.45	+21:56:53.24	-93.6 ± 1.0	5.2 ± 1.0	45.0 ± 2.0	7.7	6.3	F8	–4.76	···	$9.37^{+0.30}_{-0.30}$	1.14
HD 151798	16:50:05.17	–12:23:14.88	-72.8 ± 1.1	-104.1 ± 1.3	41.0 ± 2.0	8.0	6.5	G3V	–4.30	···	$7.75^{+0.30}_{-0.30}$	1.05
HD 152555	16:54:08.15	–04:20:24.89	-37.2 ± 1.2	-114.3 ± 1.3	48.0 ± 3.0	7.9	6.4	F8/G0V	–4.33	···	$8.10^{+0.30}_{-0.30}$	1.14
HD 153458	17:00:01.66	–07:31:53.93	97.3 ± 1.3	-20.2 ± 1.0	44.0 ± 2.0	8.1	6.4	G5V	–4.67	···	$9.23^{+0.30}_{-0.30}$	1.07
HD 154417	17:05:16.83	+00:42:09.18	-16.8 ± 0.9	-334.8 ± 0.9	20.0 ± 0.4	6.0	4.6	F9V	–4.57	···	9.08 ± 0.30	1.12
HD 155902	17:11:08.43	+56:39:33.10	-2.1 ± 1.2	-68.6 ± 1.3	28.0 ± 1.0	7.0	5.2	G5	–4.70	···	$9.27^{+0.30}_{-0.30}$	1.09
HD 157664	17:18:58.47	+68:52:40.61	32.0 ± 1.1	5.5 ± 1.1	84.0 ± 5.0	8.0	6.7	G0	···	···	$9.64^{+0.30}_{-0.30}$	1.44
HD 159222	17:32:00.99	+34:16:15.97	-240.0 ± 1.3	63.3 ± 1.5	24.0 ± 0.3	6.5	5.0	G1V	–4.75	···	$9.35^{+0.30}_{-0.30}$	1.10
HD 161897	17:41:06.70	+72:25:13.41	-121.8 ± 1.4	294.6 ± 1.4	29.0 ± 1.0	7.6	5.9	K0	–4.72	···	$9.30^{+0.30}_{-0.30}$	0.98
HD 165590	18:05:49.72	+21:26:45.60	-21.6 ± 1.0	-40.5 ± 0.9	37.7 ± 1.9	7.1	5.4	G0	–5.18	···	7.54 ± 0.54	1.19
HD 166181	18:08:15.67	+29:41:28.20	138.1 ± 1.9	-18.6 ± 1.7	32.6 ± 2.2	7.7	5.6	K0	–5.18	···	$8.00^{+0.30}_{-0.30}$	1.02
HD 166435	18:09:21.39	+29:57:06.08	71.4 ± 1.1	59.4 ± 1.1	25.0 ± 0.4	6.8	5.3	G1IV	–4.26	···	$9.50^{+0.30}_{-0.30}$	1.05
HD 167389	18:13:07.22	+41:28:31.33	51.4 ± 0.8	-128.1 ± 0.8	33.0 ± 1.0	7.4	5.9	F8(V)	–4.74	···	$9.34^{+0.30}_{-0.30}$	1.07

continued on next page

Table 2.2 – continued from previous page

Star	α (J2000.0)	δ (J2000.0)	$\mu_\alpha \cos\delta$ (mas yr^{-1})	$\mu_d elta$ (mas yr^{-1})	d (pc)	V or $V_{\rm T}$ (mag)	K_S (mag)	Sp.T.	R'_{HK}	Assoc.	Age ($\log$ Myr^{-1})	M ($M_\odot$)
HD 170778	18:29:03.94	+43:56:21.54	74.9 ± 0.9	155.1 ± 0.9	37.0 ± 1.0	7.5	6.0	G5	–4.41	···	$8.63^{+0.30}_{-0.30}$	1.09
HD 171488	18:34:20.10	+18:41:24.20	-20.7 ± 0.8	-50.9 ± 0.6	37.2 ± 1.2	7.4	5.8	G0V	–5.18	···	7.54 ± 0.54	1.12
HD 172649	18:39:42.11	+37:59:35.22	-26.6 ± 0.6	51.0 ± 0.7	47.0 ± 2.0	7.6	6.2	F5	–4.35	···	$8.24^{+0.30}_{-0.30}$	1.20
HD 175742	18:55:53.14	+23:33:26.40	130.8 ± 0.8	-283.1 ± 0.6	21.4 ± 0.5	8.2	6.1	K0	–5.18	···	9.50 ± 0.50	0.78
HD 179949	19:15:33.23	–24:10:45.61	116.6 ± 0.9	-101.7 ± 0.9	27.0 ± 1.0	6.2	4.9	F8V	–4.72	···	$9.30^{+0.30}_{-0.30}$	1.21
HD 187748	19:48:15.36	+59:25:21.36	15.8 ± 0.6	116.5 ± 0.5	28.4 ± 0.4	6.7	5.3	G0	–5.18	···	$8.00^{+0.30}_{-0.30}$	1.15
HD 187897	19:52:09.38	+07:27:36.10	133.6 ± 1.7	66.5 ± 1.6	33.0 ± 1.0	7.2	5.7	G5	–4.68	···	9.24 ± 0.30	1.11
HD 190228	20:03:00.77	+28:18:24.46	108.0 ± 1.1	-72.4 ± 1.1	62.0 ± 3.0	7.3	5.4	G5IV	–5.18	···	$10.0^{+0.30}_{-0.29}$	1.44
HD 191089	20:09:05.22	–26:13:26.63	39.3 ± 1.1	-68.2 ± 1.2	54.0 ± 3.0	7.2	6.1	F5V	···	···	8.25 ± 0.25	1.35
HD 193216	20:16:54.53	+50:16:43.55	-221.8 ± 1.1	-221.2 ± 1.1	31.0 ± 2.0	8.2	6.4	G5	–4.72	···	$9.31^{+0.30}_{-0.30}$	0.85
HD 193017	20:18:10.00	–04:43:43.23	-26.8 ± 1.0	-21.9 ± 1.2	37.0 ± 1.0	7.3	6.0	F6V	–4.63	···	$9.18^{+0.30}_{-0.30}$	1.13
HD 195034	20:28:11.81	+22:07:44.34	-23.3 ± 1.1	-243.4 ± 1.0	28.0 ± 1.0	7.2	5.6	G5	–4.70	···	$9.27^{+0.30}_{-0.30}$	1.06
HD 199019	20:49:29.30	+71:46:29.29	139.5 ± 1.0	100.3 ± 1.1	35.0 ± 1.0	8.3	6.5	G5	–4.37	···	$8.39^{+0.30}_{-0.30}$	0.94
HD 199143	20:55:47.68	–17:06:51.02	62.2 ± 1.5	-65.4 ± 1.3	48.0 ± 2.0	7.4	5.8	F8V	–4.02	···	7.20 ± 0.30	0.94
HD 199598	20:57:39.68	+26:24:18.40	266.6 ± 1.1	92.4 ± 1.1	33.0 ± 1.0	6.9	5.5	G0V	–4.65	···	$9.20^{+0.30}_{-0.30}$	1.16
HD 200746	21:05:07.95	+07:56:43.59	3.6 ± 1.1	-94.7 ± 1.7	44.0 ± 6.0	8.1	6.4	G5	–4.41	···	$8.64^{+0.30}_{-0.30}$	1.08
HD 201219	21:07:56.53	+07:25:58.47	189.0 ± 1.9	-11.5 ± 1.8	36.0 ± 2.0	8.1	6.4	G5	–4.54	···	$9.02^{+0.30}_{-0.30}$	0.98
HD 202108	21:12:57.63	+30:48:34.25	-20.1 ± 1.6	108.4 ± 1.6	27.0 ± 1.0	7.4	5.8	G3V	–4.67	···	$9.23^{+0.30}_{-0.30}$	0.99
HD 201989	21:14:01.80	–29:39:48.85	231.6 ± 1.2	-38.7 ± 1.2	30.0 ± 1.0	7.4	5.7	G3/5V	–4.53	···	$9.00^{+0.30}_{-0.30}$	1.03
HD 203030	21:18:58.22	+26:13:50.05	131.3 ± 1.6	8.6 ± 0.9	41.0 ± 2.0	8.5	6.7	G8V	–4.36	···	$8.60^{+0.18}_{-0.30}$	0.96
HD 204277	21:27:06.61	+16:07:26.85	-80.1 ± 1.1	-96.5 ± 1.1	34.0 ± 1.0	6.7	5.4	F8V	–4.43	···	$8.72^{+0.30}_{-0.30}$	1.21
HIP 106335	21:32:11.69	+00:13:17.90	415.3 ± 2.5	28.0 ± 1.4	49.4 ± 4.9	9.7	7.1	K3Ve+	–5.18	···	$8.70^{+0.30}_{-0.30}$	0.85
HD 205905	21:39:10.14	–27:18:23.59	386.9 ± 1.7	-84.8 ± 1.4	26.0 ± 1.0	6.7	5.3	G2V	–4.61	···	$9.14^{+0.30}_{-0.30}$	1.09
HD 206374	21:41:06.19	+26:45:02.25	343.4 ± 1.0	-90.0 ± 1.0	27.0 ± 1.0	7.5	5.8	G6.5V	–4.66	···	$9.22^{+0.30}_{-0.30}$	0.98
HD 209393	22:02:05.38	+44:20:35.47	38.7 ± 1.2	30.9 ± 1.2	34.0 ± 1.0	8.0	6.3	G5	–4.39	···	$8.56^{+0.30}_{-0.30}$	0.97
HD 209779	22:06:05.32	–05:21:29.15	160.4 ± 0.9	-59.3 ± 0.9	36.0 ± 1.0	7.7	5.9	G2V	–4.40	···	8.58 ± 0.30	1.07
V383 Lac	22:20:07.03	+49:30:11.67	93.4 ± 1.2	5.0 ± 1.2	50.0 ± 25.0	8.7	6.5	K0VIV	···	···	7.79 ± 0.29	1.04
HD 212291	22:23:09.17	+09:27:39.95	304.6 ± 1.3	33.6 ± 1.3	32.0 ± 1.0	7.9	6.3	G5	–4.69	···	$9.26^{+0.30}_{-0.30}$	0.96
HD 216275	22:50:46.34	+52:03:41.21	144.4 ± 1.0	170.0 ± 1.2	31.0 ± 1.0	7.3	5.8	G0	–4.74	···	$9.34^{+0.30}_{-0.30}$	1.07
HD 217343	23:00:19.29	–26:09:13.48	108.5 ± 1.3	-162.1 ± 1.4	32.0 ± 1.0	7.5	5.9	G3V	–4.29	···	$7.60^{+0.30}_{-0.30}$	1.04
HD 218738	23:09:57.23	+47:57:30.00	147.1 ± 6.8	12.4 ± 5.6	25.3 ± 4.9	7.9	5.7	dK2+dK2	–5.18	···	8.50 ± 0.30	0.90

continued on next page

Table 2.2 – continued from previous page

Star	α (J2000.0)	δ (J2000.0)	$\mu_\alpha \cos\delta$ (mas yr^{-1})	$\mu_d elta$ (mas yr^{-1})	d (pc)	V or $V_{\rm T}$ (mag)	K_S (mag)	Sp.T.	R'_{HK}	Assoc.	Age ($\log$ Myr^{-1})	M ($M_\odot$)
HD 218739	23:09:58.87	+47:57:33.90	154.2 ± 2.0	-1.1 ± 1.7	29.4 ± 2.0	7.1	5.7	G1V	–5.18	···	8.50 ± 0.30	1.07
RX J2312.0+2245	23:12:04.52	+22:45:26.28	23.7 ± 0.9	-16.5 ± 0.6	150.0 ± 75.0	9.9	8.3	G3	···	···	$8.70^{+0.30}_{-0.30}$	1.36
RX J2313.0+2345	23:13:01.24	+23:45:29.64	12.4 ± 0.9	-11.4 ± 0.6	150.0 ± 75.0	10.2	8.6	F8	···	···	$6.97^{+0.30}_{-0.30}$	1.36
HD 219498	23:16:05.02	+22:10:34.98	82.0 ± 0.9	-30.5 ± 1.0	60.0 ± 30.0	9.1	7.4	G5	···	···	8.35 ± 0.15	1.47
HD 221613	23:33:24.06	+42:50:47.88	243.2 ± 1.0	177.1 ± 1.0	33.0 ± 1.0	7.1	5.5	G0	–4.71	···	$9.30^{+0.30}_{-0.30}$	1.10

† HII 1348 was observed because it was a priori known to have a faint candidate companion. Hence the star is not part of the unbiased survey for sub-stellar companions.

CATALOGS.—*AP, HE*: α Per member (Heckmann et al., 1956); *BPM*: Bruce proper motion survey (Luyten, 1963); *1E, 2E*: *Einstein* satellite observations; *HII, Pels*: Pleiades member (Hertzspring, 1947; van Leeuwen et al., 1986); *(PZ99), ScoPMS*: Upper Scorpius member (Preibisch & Zinnecker, 1999; Walter et al., 1994); *1RXS*: *ROSAT* All-Sky Bright (Voges et al., 1999) and Faint Source Catalogs (Voges et al., 2000); *RE, 2RE*: *ROSAT* (2RE) Source Catalog of extreme ultra-violet sources (Pounds et al., 1993; Pye et al., 1995); *RX*: *ROSAT* satellite observations; *vB*: Hyades member (van Bueren, 1952);

2.4 Sample Biases and Discussion

Some of the sample selection criteria outlined in the previous section introduce obvious biases mostly against, and less often in favor of, miltiplicity in the survey. These are discussed below.

2.4.1 Examining the Biases

First of all, criteria (1–3), (11–12), and (14) do not introduce any multiplicity biases. The remainder may do so to varying extents.

Criterion (4): The requirement for good quality 2MASS photometry with no flags may exclude stars in binary pairs with separations of several arcseconds, as these could contaminate each other's photometry. However, because of criterion (5), such resolved (or de-blended) companions should not be present in the sample in the first place. Therefore, criterion (4) does not introduce bias beyond that already introduced by criterion (5).

Criterion (5): This requirement introduces an obvious bias against close stellar binary pairs. Given the range of heliocentric distances of stars in the sample, and assuming that $2.0''$ ($\approx$2 times the size of the 2MASS resolution element) is the minimum angular separation at which point sources in 2MASS can be resolved, companions in the 20–1000 AU projected separation range may be excluded. In practice, because of the limited dynamic range of 2MASS observations within $5''$ of bright stars ($\sim$4.5 mag at $5''$, $\sim$2.5 mag at $3''$; cf. Fig. 11 in Cutri et al., 2003), this criterion excludes mostly near-equal magnitude stellar companions. Sub-stellar companions will be too faint to be detected in such close proximity to bright stars in 2MASS, even at the youngest ages and even around the coolest (K5) stars in our sample.

Criterion (6): On one hand, similarly to the previous criterion, this selection criterion will exclude mostly equal-flux binaries, though over a wider range of projected physical separations (20–2500 AU). On the other hand, the criterion also excludes stars with projected faint red companions–potential brown dwarfs.

However, because the criterion is applied only to stars 100 Myr and older, and because of the limited dynamic range of the 2MASS Point Source Catalog within $12.8''$ ($\lesssim$ 6 mag), this criterion introduces a bias against sub-stellar companions in only a limited number of cases. The systems that may be excluded are late-type (K0–K5) dwarf primaries with massive (60–72$M_{\rm Jup}$) sub-stellar companions. These are expected to contribute a small fraction (<10%) of the existing solar analog/brown dwarf pairs and thus should not have a dramatic effect on the overall result.

Criterion (7): Given the unknown multiplicity selection criteria for these GTO programs, and the small number of discarded stars, the effect is likely unimportant. It is possible that the stars removed from the target list as a result of this criterion may be preferentially single.

Criterion (8): This criterion biases the sample against nearly equal-flux or equal-mass binary stars, with separations between 0 AU and 400 AU.

Criterion (9): Given that current observational evidence of the effect of stellar multiplicity on disk frequency does not support a correlation between the two phenomena (e.g., Bouvier et al., 1997), the effect of the addition of stars with known IR excesses on multiplicity is likely neutral. Indeed, one of the IR-excess stars added in this process, HD 134319, is a known triple system (Lowrance et al., 2005).

Criterion (10): Given that there is no clear evidence that extra-solar planets cannot exist in wide ($\gtrsim$10 AU) multiple systems, the addition of the few exo-planet host stars to the sample is not expected to affect the statistics of stellar and sub-stellar companions detectable in direct imaging.

Criterion (13): The application of this requirement hinders the discovery of faint companions in nearly equal-flux binary systems to the extent that such binaries were not removed already by criteria (5) and (6). It is therefore a bias against higher-order multiples. It does not bias against the detection of faint secondary companions to single stars.

Criterion (15): When open cluster stars *were* added to the deep sample, that

was done in an unbiased manner, without regard for the existence of previous high angular resolution observations.

2.4.2 Discussion

The complete set of target selection requirements outlined in §2.2.1–§2.2.3 and the subsequent exclusion criteria (1–14) are largely unbiased toward the detection of sub-stellar companions around most Sun-like stars, with the exception of 60–$75 M_{\rm Jup}$ brown dwarfs in orbit around K0–5 V stars and brown dwarfs orbiting near equal-flux ($\Delta K_S < 4$ mag) binaries. As already pointed out, the exclusion of the star/brown-dwarf combinations in the first case is not expected to have a large effect on the estimated brown-dwarf companion frequency. The bias has been ignored in the discussion of the survey incompleteness in §6. Similarly, the exclusion of binary systems from the deep sample will leave the analysis of the sub-stellar companion frequency around *single* stars unaffected.

The binary exclusion criteria will, on the other hand, strongly influence the observed stellar multiplicity, biasing the survey toward discovering a smaller fraction of binaries and multiples. Because of the complicated nature of the biases, an attempt to correct for them has not been made. Only a cursory discussion of stellar multiplicity is provided in §6.

2.5 Unique Advantages of the Present Survey in Comparison to Others

The distinctive features of the Palomar/Keck AO companion survey are: (1) its emphasis on young stars, (2) its focus on solar analogs, and (3) its use of high-order AO systems. We discuss the uniqueness and advantages of these characteristics in the following sections.

2.5.1 The Palomar/Keck AO Sample is Young

With a median age of 80 Myr and 101 stars in the deep imaging sample, the present survey targets the youngest and most comprehensive sample of young stars that has been scrutinized for sub-stellar companions. In comparison, previous high-contrast imaging surveys of similar size (>50 stars: Oppenheimer et al., 2001; Close et al., 2003; Beuzit et al., 2004; McCarthy & Zuckerman, 2004; Carson et al., 2005) have concentrated on nearby and typically older stars. Because of the lack of star-forming regions within 100 pc of the Sun, such surveys are dominated by stars with ages similar to that of the Sun (4.56 Gyr). The several dozen known members of young (10–35 Myr) kinematic groups within 100 pc from the Sun–Tucana/Horologium (Zuckerman & Webb, 2000; Torres et al., 2000), TW Hydra (Kastner et al., 1997; Torres et al., 2000), and β Pictoris (Zuckerman et al., 2001a))–have already been targeted, often repeatedly, by smaller high-contrast surveys (Chauvin et al., 2003; Neuhäuser et al., 2003; Masciadri et al., 2005; Lowrance et al., 2005). The limited number of known members of these groups, $\lesssim$40 altogether, precludes statistically significant conclusions. A notable exception to this trend is the work of McCarthy & Zuckerman (2004), which boasts the exploration of 178 stellar systems with a median age of 300 Myr, 90% of which lie within 25 pc of the Sun. However, a closer examination of this work reveals that the mean sample age has probably been under-estimated by a factor of $\sim$3. Hence, the sensitivity of the McCarthy & Zuckerman survey to sub-stellar companions is significantly poorer than claimed. This survey is given a more detailed consideration in §7.

Given the rapid decline in intrinsic luminosity of objects below the hydrogen-burning limit with age, surveys of solar neighborhood stars are often *less* sensitive to objects of sub-stellar mass than surveys concentrating on more distant, significantly younger stars. For example, a $0.05M_{\odot}$ brown dwarf is expected to decrease in brightness by 6.7 mag in the K band between the ages of 100 Myr and 5.0 Gyr (Baraffe et al., 2003). Lower-mass objects are expected to cool even faster: over the same period, a $0.01M_{\odot}$ object dims by 15.8 mag at K! Provided that such

young stars can be identified, allowing a corresponding increase (by a factor of 22 to 1400) in the mean heliocentric distance of the survey targets is justified, if sensitivity to low masses is the primary goal. Since a number of 1–100 Myr-old associations of young stars exist within 200 pc (distance modulus of 6.5 mag), imaging observations of them will likely produce brown dwarfs of much lower mass than any of the 1–10 Gyr-old brown dwrafs discovered in the solar neighborhood. Indeed, several brown dwarfs with estimated masses near and below the deuterium-burning limit ($\sim 13 M_{\rm Jup}$; Burrows et al., 1997) have been reported in the nearest (50–160 pc) associations of 1–15 Myr-old stars, both in isolation (e.g., Lucas et al., 2001; Briceño et al., 2002) and, more recently, as companions to more massive objects (Chauvin et al., 2004, 2005b; Neuhäuser et al., 2005).

Naturally, the ability to resolve such brown dwarfs and candidate giant planets in the vicinity of host stars decreases linearly with increasing heliocentric distance. Direct imaging surveys for companions to more distant young stars will be sensitive only to objects in correspondingly wider orbits. Therefore, while proximity to ths Sun was of secondary importance, after youth, in constructing the deep sample, among stars of the same age, the nearer ones were given preference whenever possible.

Figure 2.5 displays the complete (open circles) and the deep (filled circles) samples on an age vs. distance diagram. The horizontal dashed line in the Figure delimits the maximum age of stars included in the deep sample. Given the age vs. distance selection for stars in the deep sample, the final survey is most sensitive to 12–72 $M_{\rm Jup}$ companions at projected separations between approximately 20 and 1200 AU (§6.2.3).

2.5.2 The Palomar/Keck AO Sample Has a High Median Mass

The median primary spectral type for the Palomar/Keck survey is G5, which at the 80 Myr median sample age is equivalent to a mass of $\approx 1.0 M_{\odot}$ (Baraffe et al., 1998). The survey is focussed on solar-type stars in order to establish the low-mass multiplicity characteristics of stars similar to the Sun. On the other hand,

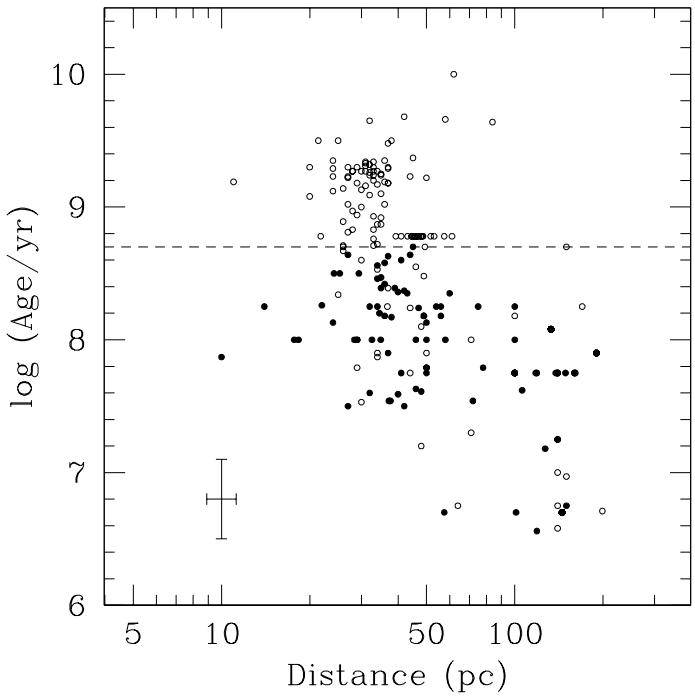

Figure 2.5: Age vs. heliocentric distance diagram for the complete survey sample (open circles) and for the deep sub-sample (filled circles). The errorbars at the bottom left denote the mean errors in age and distance. The horizontal dashed line delimits the maximum age for stars included in the deep sample.

sub-stellar companion surveys focussing on nearby stars are dominated by late K and M stars, as expected from volume-limited stellar samples. As a result, the mean primary mass in those surveys is smaller, $\sim 0.5 M_{\odot}$ (spectral type M0 V). Thus, the Palomar/Keck survey explores a distinct population of stars that is on average a factor of 2 more massive than that surveyed for sub-stellar companions previously.

The advantages of targeting more massive stars may not be immediately obvious. More massive stars are more luminous and hence require higher imaging contrast to achieve sensitivity to companions of sub-stellar masses. Several surveys have in fact deliberately focused on faint primaries, such as white dwarfs (Zuckerman & Becklin, 1992; Farihi et al., 2005), M dwarfs (Beuzit et al., 2004), and ultra-cool dwarfs (later than M7; Martin et al., 1999; Reid et al., 2001; Close et al., 2003; Burgasser et al., 2003; Bouy et al., 2003), as a way to reduce the need for high contrast in resolving faint close-in objects. These surveys do indeed probe for companion masses well below the hydrogen-burning limit. The resulting picture is that brown dwarfs and low-mass stars reside primarily in tight (< 15 AU) nearly equal-mass ($q \geq 0.7$) systems (Close et al., 2003). Examples to the contrary, as recently presented in Chauvin et al. (2005a) and Luhman (2004), are still considered exceptions. The most direct explanation for this is that low-mass multiples inhabit shallower potential wells and are therefore easily disrupted as a result of the frequent stellar encounters typical of star-forming regions. Hence, low-mass binaries in tight orbits survive preferentially. Conversely, higher-mass stars can maintain gravitationally bound companions at larger orbital semi-major axes, which can survive dynamical perturbations by passing stars.

The first advantage of looking for sub-stellar companions around more massive stars is that the companions can be expected to exist at wider separations. Indeed, all of the directly imaged brown dwarf companions to $\gtrsim 0.3 M_{\odot}$ stars (i.e., excluding the ultra-cool binaries) reside at projected separations between 14 AU and 3600 AU. This is a particularly important feature of companions to more massive systems in the context of the Palomar/Keck young stars survey because of the

greater median heliocentric distance of the sample. That is, by concentrating the Palomar/Keck effort on more massive and younger (and by necessity, more distant) stars, we can hope to resolve some of the least massive sub-stellar companions to solar-type stars. The detection limits of the survey are such that this allows us to probe, albeit only partially (§6.2.3) for objects with masses below the deuterium burning limit–potential extrasolar giant planets.

The second advantage of having a relatively massive sample of stars is that, absolute mass estimates aside, the sub-stellar secondaries in systems are more prominent at a fixed mass ratio q. For example, a 500 Myr-old $1M_{\odot}$ star orbited by a $0.05M_{\odot}$ brown dwarf ($q = 0.05$) has an expected K-band flux ratio of 7.8 mag (Baraffe et al., 1998, 2003). On the other hand, a $0.6M_{\odot} + 0.03M_{\odot}$ system (also $q = 0.05$) at the same age has a projected K-band flux ratio of 8.5 mag and thus requires higher contrast for detection. The effect is more pronounced at even lower mass ratios. Hence, high-contrast imaging surveys of appropriately selected samples of young massive stars allow the opportunity to study the dynamical survival of low mass ratio ($q < 0.1$) systems with unprecedented sensitivity and statistics. This fact is exemplified by recent AO surveys of B (Shatsky & Tokovinin, 2002) and A (Kouwenhoven et al., 2005) stars in the 5–20 Myr-old Scorpius OB2 association (de Zeeuw et al., 1999; Mamajek et al., 2002). With only minor (0–25%) corrections for incompleteness, the authors of the two surveys find that $\gtrsim 20\%$ of all multiple systems with B and A primaries have mass ratios $q \leq 0.1$. The result is not unexpected in view of radial-velocity and direct imaging multiplicity surveys of lower-mass FGK dwarfs (e.g., Duquennoy & Mayor, 1991; Mazeh et al., 2003; Patience et al., 2002). However, the latter are severely (80–100%) incomplete at these low mass ratios. Hence, the combination of a relatively massive sample of young stars and high-contrast imaging allows the opportunity to explore low-mass ratio systems to a high level of completeness. A high-contrast survey of the multiplicity of young solar analogs similar to those of young B and A stars has not been performed. The present survey fills this gap.

2.5.3 The Palomar/Keck Survey Uses a High-Order AO System

The PALAO system (Troy et al., 2000) employs a 349-element deformable mirror (DM) behind a Shack-Hartmann wavefront sensor. A similar DM is used in the Keck AO system (Wizinowich et al., 2000). They are considered high-order AO systems as they are able to correct a larger number of modes in the Zernicke polynomial expansion of the incoming wavefront than "curvature" AO systems, which employ deformable mirrors with smaller numbers (20–50) of active elements. In broad terms, the result is improved dynamic range in the vicinity of bright ($R \lesssim 10$ mag) stars though compromised performance at the faint ($R \gtrsim 12$ mag) end. Given that the survey targets are all brighter than $R = 12$, the PALAO and Keck AO systems are optimally suited for this study.

The majority of the large ground-based surveys discussed above have either not used AO (McCarthy & Zuckerman, 2004) or used only low-order tip-tilt or curvature AO (Oppenheimer et al., 2001; Close et al., 2003; Beuzit et al., 2004). They thus suffer from 2–5 mag poorer contrast in the vicinity of bright stars, compared to the present Palomar/Keck survey, effectively preventing the discovery of close-in sub-stellar companions. Recent exceptions to this rule are the Carson et al. (2005) survey of old solar neighborhood stars, which also used PALAO, but focused on older stars and thus lacks comparable companion sensitivity, and the VLT/NACO (Masciadri et al., 2005) and *HST*/NICMOS (Lowrance et al., 2005) surveys, which reach approximately 1 mag deeper.

2.5.4 Comparison to Recent, Higher-Contrast Surveys and Summary

Since the Palomar/Keck AO survey began in 2002, the complete results from one medium-sized (45 stars; Lowrance et al., 2005) and one small (28 stars; Masciadri et al., 2005) high-contrast surveys have been announced. In addition, discoveries of sub-stellar companions from two other such surveys in progress have been published (Chauvin et al., 2005a,b; Neuhäuser et al., 2005). The rate of detection

of sub-stellar companions from these has been markedly higher in comparison to previous surveys, with a total of 5 discovered.

All of these surveys have attained $\sim$1 mag higher contrast than the present Palomar/Keck survey, by virtue of their use of *HST*/NICMOS (Lowrance et al.) or of the novel high-order AO system NAOS (Rousset et al., 2000) on the VLT (Masciadri et al.; Chauvin et al.; Neuhäuser et al.). Most of these, with the exception of the *HST* survey, focus on southern stars ($\delta < -30°$), inaccessible from Palomar. Partially as a result of this, all 5 of the bona fide sub-stellar companions reported in these surveys orbit stars with declinations $\delta < -30°$. The reason for this north-south asymmetry in survey focus and success rate, in addition to the concentration of technology at the southern latitude of the VLT, is the larger concentration of known nearby young stellar moving groups in the southern hemisphere. Consequently, the northern hemisphere remains relatively unexplored for sub-stellar companions to young stars. The Palomar/Keck AO survey fills this niche by taking advantage of the recent vast compilation of young solar analogs over the entire sky, made available to us through the FEPS team.

Therefore, the Palomar AO survey of young solar analogs presented here is unique in its scale, sensitivity, and focus on young stars at northern declinations.

Chapter 3

Observations and Methodology

3.1 Overview

This Chapter presents two examples of the observational and analytical steps that we followed in: (1) searching for low-mass companions to young stars, (2) confirming their physical association with the respective stars, and (3) establishing their mass.

Section §3.2 presents a pilot study for sub-stellar companions to the nearby (7.8 pc) ∼300 Myr-old (Barrado y Navascués, 1998; Song et al., 2001) star α Lyr (Vega) conducted at the beginning of the observing campaign. Because of its early spectral type (A0), Vega was not included in the solar analog survey. The study, published in Metchev et al. (2003), is included here as an introduction to the near-IR high-contrast imaging possibilities with the Palomar AO system and as a demonstration that planetary-mass companions to nearby stars are potentially detectable in direct imaging with ground-based telescopes.

Section §3.2 also presents the principal approach that we have employed for deciding the physical association between a star and a candidate companion: establishing common proper motion through differential astrometry. Although a gravitational bond between two celestial bodies can be claimed unambiguously only after solving for a common orbit, for resolved stellar systems this typically requires multiple observations over many years. In the meantime, however, the

common space motion of a nearby binary system sets it apart from background stars, which, because of their much higher heliocentric distances, appear stationary. Therefore, by establishing common space motion between a pair of high-proper-motion stellar or sub-stellar objects with respect to background objects, one can infer that the pair is gravitationally bound. This requires only two observations taken over a period of time generally much shorter than the orbital period. The required time-span is inversely proportional both to the apparent proper motion of the stars and to the precision of the astrometric measurements. In the case of Vega, owing to the high proper motion of the star (351 mas yr^{-1}; Perryman et al., 1997), adequate astrometric follow-up with PALAO was possible within two months of the first-epoch observations. For the smaller apparent proper motions of the stars in the companion survey ($\lesssim$100 mas yr^{-1}), time-spans of 1–3 years and a more accurate astrometric calibration of the PHARO pixel scale (§4) were required.

Section §3.3, published in Metchev & Hillenbrand (2004), contains a detailed description of the observing strategy (§3.3.2) in seeking and confirming candidate companions to solar analogs with the Palomar and Keck AO systems. It also presents the three principal approaches that we have used to estimate companion masses: (i) near-IR colors and absolute magnitudes (§3.3.3.1), (ii) near-IR spectroscopy (§3.3.3.3), and (iii) orbital motion (§3.3.4.3.1). These are applied to the newly-discovered and confirmed companions to stars in the survey: a sub-stellar companion to HD 49197 and stellar companions to HD 129333, V522 Per, and RX J0329.1+0118. Methods (i) and (ii) rely on empirical relations to estimate the luminosities and temperatures of the companions (assuming the same distance and age as those of the respective primary), which are then compared to theoretical predictions for cool and ultra-cool dwarfs. The third approach, applied only to the HD 129333A/B system, demonstrates the power of combining high angular resolution imaging and radial velocity monitoring in solving for dynamical masses in binary systems. Finally, we show that in cases of candidate binary systems where physical association may not be conclusively decided through relative astrome-

try, statistical arguments, based on a comparison between the spectroscopically-determined temperature and luminosity of the companion and the known space density of similar objects, offer a powerful tool in constraining the likelihood for physical association (§3.3.4.1).

3.2 Adaptive Optics Observations of Vega: Eight Detected Sources and Upper Limits to Planetary-mass Companions

[†]Stanimir A. Metchev, Lynne A. Hillenbrand, & Russel J. White

California Institute of Technology, Division of Physics, Mathematics & Astronomy, MC 105–24, Pasadena, California 91125

Abstract

From adaptive optics observations with the Palomar 5-meter telescope we place upper limits on the masses of any planetary companions located between ∼30–230 AU away from Vega, where our data are sensitive to depths ranging from $H = 12.5$ mag to $H = 19.0$ mag fainter than Vega itself. Our observations cover a plus-shaped area with two $25'' \times 57''$ elements, excluding $7'' \times 7''$ centered on the star. We have identified 2 double and 4 single point sources. These projected companions are 14.9–18.9 mag fainter than Vega and if physically associated would have masses ranging from 4 to 35 M_{Jup} and orbital radii 170–260 AU. Recent simulations of dusty rings around Vega predict the presence of a perturbing body with mass <2–3 M_{Jup} and orbital radius ∼40–100 AU, though more massive ($\lesssim$10 M_{Jup}) planets cannot be excluded. None of the detected objects are this predicted planet. Based on a color-magnitude, spectroscopic, and proper motion analysis, all objects are consistent with being background sources. Given the glare of Vega, a 2 M_{Jup} object near the expected orbital radii would not have been visible at the 5σ level in our data, though any >10 M_{Jup} brown dwarf could have been seen at separation >80 AU.

[†]A version of this Section was published in *The Astrophysical Journal*, vol. 582, 1102

3.2.1 Introduction

The A0V star Vega is famously known since the early days of data return from IRAS as a young main sequence star surrounded by dust (Aumann et al., 1984). Its age (270–380 Myr; Song et al., 2001) combined with the large fractional excess luminosity at infrared wavelengths ($L_{\rm excess}/L_* \approx 10^{-5}$ or $M_{\rm dust} \approx 1/2 M_{\rm moon}$; Backman & Paresce, 1993) imply that dust is being generated at the current epoch by either grinding collisions between larger rocky bodies, a.k.a. planetesimals (Harper et al., 1984; Weissman, 1984; Zuckerman & Becklin, 1993), or in cometary ejecta (Beust et al., 1989, 1990, and references therein). If the dust is not continuously regenerated it will be depleted by a combination of Poynting-Robertson drag and radiation pressure on a time-scale much shorter than the age of Vega. Discovery of the infrared excess around Vega and other main sequence stars too old to possess the so-called primordial dust and gas disks that are commonly found around 1–10 Myr-old stars, led to coining of the term "debris disk." Searches for other examples of "the Vega phenomenon" have led to the cataloging of a mere tens of objects (see, e.g., Mannings & Barlow, 1998; Silverstone, 2000), mostly early-type stars whose dust was detectable with *IRAS* or *ISO*, or observable from the ground with mid-infrared instrumentation on large telescopes.

The mid- and far-infrared (25–850 μm) emission from Vega is extended over tens of arcseconds (Aumann et al., 1984; Harvey et al., 1984; Zuckerman & Becklin, 1993; Heinrichsen et al., 1998; Holland et al., 1998). Aperture synthesis imaging at 1.3 mm (Koerner et al., 2001; Wilner et al., 2002) resolved several dust clumps located $\sim$8–14$''$ from the central source (60–110 AU, assuming the Hipparcos parallax of 128.9 milli-arcsec). One interpretation is that these clumps trace the densest portions of the already inferred face-on circumstellar ring (Dent et al., 2000). Additional support for a ring interpretation comes from Vega's spectral energy distribution, which is close to photospheric at shorter wavelengths ($\lesssim$20 μm; Heinrichsen et al., 1998), and suggests an inner gap in the density distribution that may or may not be entirely devoid of hot dust. At 11.6 μm extensions larger than 1/4$''$ are ruled out by the imaging of Kuchner et al. (1998). Interferometric

work by Ciardi et al. (2001), however, did suggest extended emission at 2.2 μm.

Observations of structure in the circumstellar dust around Vega have spawned detailed models for a planetary perturber (Gorkavyi & Taidakova, 2001; Wilner et al., 2002). Resonance trapping and gravitational scattering induced by a body of mass 2–3 $M_{\rm Jup}$ are consistent with the Holland et al. (1998) map and with the interferometric observations of Koerner et al. (2001) and Wilner et al. (2002). Due to degeneracies in dynamical models (e.g., Wilner et al., 2002), more massive planets ($\sim$10 $\rm M_{Jup}$) also cannot be ruled out. Modeling to date assumes a face-on orientation of the presumed dust disk or ring. Evidence for this geometry comes both from a ring-shaped (e.g., Heinrichsen et al., 1998) albeit clumpy (Koerner et al., 2001; Wilner et al., 2002) dust distribution and from detailed analysis of stellar line profiles (assuming parallel disk and stellar rotation axes; Gulliver, Hill, & Adelman, 1994).

Our experiment was designed to search for low-mass companions within 4–30″ of Vega, in part to test the aforementioned planetary perturber predictions. Imaging observations close to this bright source are usually "burned out" in survey data such as POSS or 2MASS. Ground-based coronagraphic observations (Smith et al., 1992; Kalas & Jewitt, 1996) have also lacked sufficient sensitivity. Except for NICMOS images (Silverstone et al., 2002) with sensitivity comparable to ours, high dynamic-range observations have not been previously reported.

3.2.2 Observations

Data were obtained with the Palomar adaptive optics (PALAO; Troy et al., 2000; Bloemhof et al., 2000) system in residence at the Palomar 5-m telescope. PALAO employs PHARO, the Palomar High Angular Resolution Observer (Hayward et al., 2001), a 1024^2 pix HgCdTe HAWAII detector with imaging (25″ or 40″ field of view) and spectroscopic (R =1500–2500) capabilities. Broad- and narrow-band filters throughout the JHK atmospheric windows are available, as well as a choice of coronagraphic spot sizes and Lyot masks.

Vega was observed on the night of 2002 June 22 with additional follow-up

observations obtained on August 28 and 29 (UT), all under photometric sky conditions. The observing strategy was to take deep images in H-band to maximize the detection likelihood of faint low-mass objects (see e.g., Burrows et al., 1997). The point spread function (PSF) was 0.6–0.9″ uncorrected at H-band and improved to <0.1″ with adaptive correction. A neutral density filter (1%) manually placed in front of the wave front sensor (WFS) enabled AO lock on such a bright object. AO performance was very good during most of the observing, with Strehl ratios up to 20% in H. We did not employ the coronagraphic mode of PALAO for these observations since scattered light suppression was not sufficient enough to prevent saturation on the array outside the boundaries of the largest coronagraph ($0.97'' = 12\lambda/D$ in H) in the shortest possible integration time (1897 milli-sec).

On June 22, a total of 26 minutes on-source integration was obtained with the 25″ field of view in H-band at each of 4 pointings: north, south, east, and west around Vega (henceforth: Vega N, S, E, and W fields), with Vega itself located 3.5″ off of the imaging field at each positioning of the telescope. Due to field overlaps, ∼13% of the area covered (2210 arcsec^2) was observed for 52 minutes. Dithering at the 0.25–1.00″ level was performed for the on-source frames. More widely dithered sky frames were taken at locations ∼2′ farther away from Vega with source-to-sky time split 2:1. The integration time for individual exposures was 10.9 seconds. For the eastern field in which several objects were noticed in real time, we also obtained J, H, and K_s data with 2.5 minutes total on-source integration time taken as 5 separate frames, with Vega offset 22–28″ to the west. The airmass range was 1.03–1.30 for the entire observing sequence.

Photometric calibration was achieved via immediate observation of 2MASS 183726.28+385210.1 (GSC 03105-00679, a G8V star) located ∼7.7′ from Vega with 2MASS magnitudes $K_s = 8.296 \pm 0.033$, $H = 8.365 \pm 0.022$, and $J = 8.745 \pm 0.028$. This source, although not a photometric standard, is sufficient as a local calibrator and was observed at airmass 1.35. Two other much fainter 2MASS sources are also present in the image.

During the second epoch observations, resolution $R = 1500$ and 2400 K-band

spectra of the brightest discovered object were obtained (August 28) through a $0.52''$ slit and a K grism for a total of 100 minutes on-source integration. The object was dithered $10''$ along the slit for sky-subtraction. Spectra of scattered light from Vega were used as a telluric standard. Short-exposure (5 minutes per filter) dithered JHK_s images were taken (August 29) as follow-up to the June 22 data to test for common proper motion with Vega. The airmass of Vega for the second epoch observations varied between 1.01 and 1.13.

We also observed a binary system (HD 165341) with a well-determined orbit in the Sixth Catalog of Orbits of Visual Binary Stars[1] in order to determine precisely the plate-scale and orientation of the PALAO system. We derive for the $25''$ field a plate-scale of 0.025168 ± 0.000034 arcsec/pixel.

3.2.3 Data Processing

Our image reduction steps, written in IDL and IRAF, include the standard procedures of flat-fielding, sky-subtracting, interpolating/masking bad pixels, and mosaicking the dither pattern. This last step required correcting for image drift (likely caused by change in the direction of the gravity vector in PHARO over the duration of the observing sequence), the rate of which varied between 0.5 and 1.2 arcsec/hour.

Image stacks from each of the four deep pointings (June 22) were registered to the first image in the series. For the east field in which several point sources were detected, each image was registered by centroiding on the brightest object. For the north field, centroiding was possible on the bright reflection artifact due to Vega. For the other two fields registration was accomplished by first averaging sets of 9 consecutive exposures, extrapolating the position of Vega from the intersection of 6 scattered light "rays" in the image halo, and combining the 16 registered averages. In this manner, the location of the star could be constrained to within ± 5.0 pix $= \pm 0.13''$ (c.f. ± 0.10 pix for our mean centroiding precision in the north and east fields). We did attempt cross-correlation techniques for dither pattern

[1] Available at http://ad.usno.navy.mil/wds/orb6.html.

correction but these were not as successful as the above procedures. The final step was to orient the images with north–up and east–left. Astrometric calibration was established assuming the plate-scale derived from the binary star observations and by reference to the Hipparcos (J2000.0) coordinates of Vega. Our final image of the Vega vicinity is presented in Figure 3.1a.

Various methods to reduce the large halo from Vega were attempted, including reflections, rotations, and data smoothing. Shown in Figure 3.1b is a difference image, for which a Gaussian-smoothed ($\sigma = 5$ pix, FWHM = 12 pix; c.f. FWHM = 4 pix for the point sources) version of the original image has been subtracted. This procedure effectively removes large scale gradients. Strong artifacts do remain, however, and contribute to our limited sensitivity to point sources within $\sim 10''$ of Vega.

Spectra of the brightest point source were extracted using the APALL task within IRAF. A quadratic polynomial was fit to all pixels with values >10% of the peak flux along an aperture. Local background was estimated from a region 0.50–1.25$''$ from the aperture center. The extracted spectra were divided by that of the telluric standard (with the 2.166 μm Brγ absorption feature interpolated over) to correct for instrumental response and atmospheric transmission. Wavelength calibration was done by fitting a dispersion relation to sky OH emission lines. Finally, the wavelength-calibrated spectra were co-added.

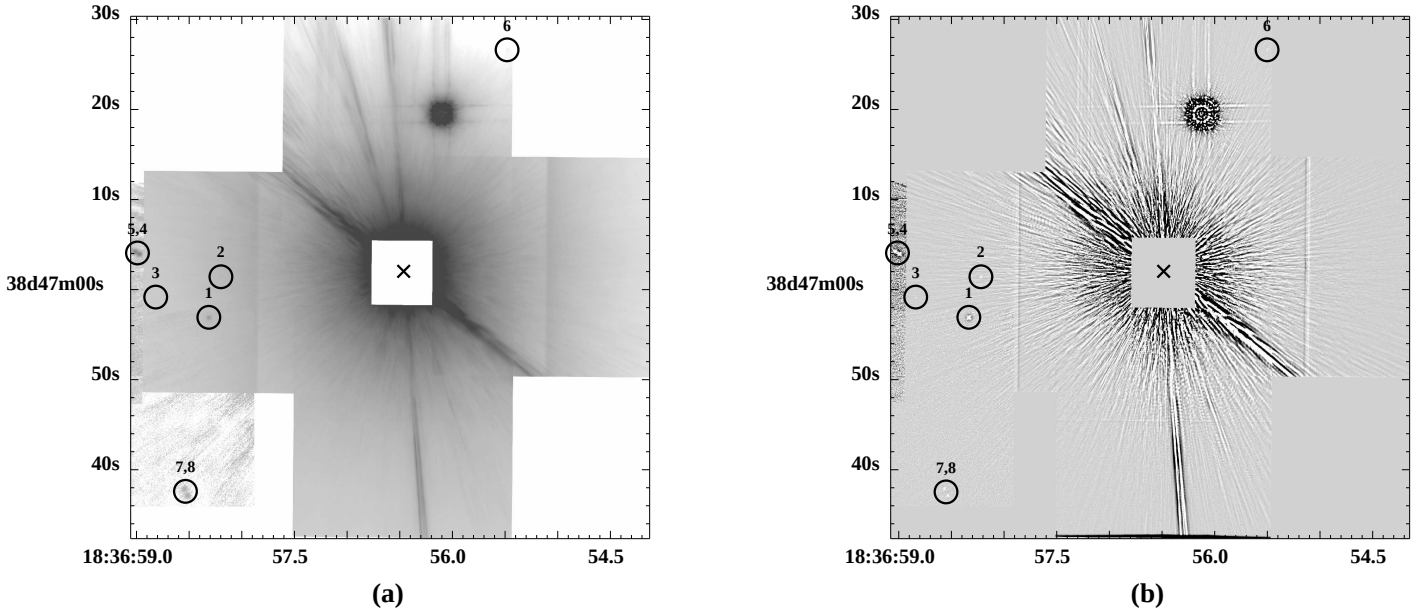

Figure 3.1: (a) Composite H-band mosaic of the Vega region obtained with PALAO. Eight point sources are detected, 5 to the east, 2 to the south-east, and 1 to the north of Vega. The two close, eastern-most objects are just off the edge of the deep exposure of the Vega E field, but have been pasted in from our shallower JHK_s images, obtained for photometry purposes, to show their location. Similarly, the double source to the south-east was discovered only in the follow-up shallow JHK_s observations. A bright "ghost" reflection of Vega is also visible in the north field. (b) The same image, with a smoothed ($\sigma = 5$ pix) version of itself subtracted, to enhance faint sources in the wings of Vega's halo.

3.2.4 Photometry of Detected Sources

The positions of identified sources are indicated in Figure 3.1. During the first epoch of observations we detected 6 point sources, 5 of which were to the east of Vega. Four of these are single while two are a close ($0.6''$) double, which is $0.7''$ off the east edge of our deep Vega E image, and were observed only in the short JHK_s exposures. The sixth point source is in the north field. During the follow-up observations we detected another double ($0.8''$) source south-east of Vega. PSF fitting techniques suggest these are in fact all stellar point sources and not partially resolved galaxies.

We performed photometry using both aperture and PSF techniques. First, we used the IRAF/PHOT task in the short exposures with aperture radii of 10 (K_s), 18 (H), and 32 (J) pixels ($0.50'', 0.90''$, and $1.5''$ diameters on the sky) chosen to correspond to $2 \times$ FWHM of the image core and to include the first Airy ring. The mode of the counts in a 30–40 pixel annulus provided local sky that was critical for subtracting residual scattered light from Vega. For sources 1–6, magnitudes in each of the bands were obtained by comparing the measured aperture flux to that of the 2MASS standard in the same aperture. The magnitudes and positions of sources 7 and 8 were boot-strapped from those of source 1, with its error added in quadrature. Airmass corrections were applied using extinction coefficients for Palomar as previously determined by L.A.H. (0.114, 0.029, and 0.065 magnitudes per airmass in J, H, and K, respectively). We also used the PSF, PEAK, and ALLSTAR tasks in IRAF/DAOPHOT for PSF fitting photometry. PSF fitting worked best at K_s-band but required a large number of iterations at H and J for convergence in part because the stellar profiles are not diffraction limited. Differences between the aperture and PSF-fitting magnitudes are 0.2–0.3 mag (much larger than the formal errors), and the scatter of the PSF magnitudes is 50% larger than that of the aperture magnitudes at J and H.

Our photometry (Table 3.1) is from apertures, except for sources 4 and 5, for which we simultaneously fit PSF profiles to each of the components of the double source to determine their magnitude difference. A larger aperture ($2.5''$ diameter—

to include the PSFs of both sources at all bands) is used to measure a combined flux, and individual magnitudes are obtained from the large-aperture magnitude and the magnitude difference from PSF fitting. The photometry for these two sources is less precise due to a more uneven background.

Repeatability of the photometry from frame to frame was assessed using aperture photometry on the calibration field, which is free of the bright background present in the Vega fields. We find 0.04 mag r.m.s. scatter between the 5 frames. For the shallow JHK_s exposures near Vega, frame-to-frame differences are larger due to background variations induced by dithering that placed Vega closer to the image area for some frames than for others. We have included this scatter in our errors.

We do not include a Strehl term in our calibration, as the implied corrections were larger than the uncorrected frame-to-frame scatter. The Strehl ratio changed from ∼15% in the deep H exposures to 2–3% in the subsequent shallow ones, but was relatively stable between the short exposures of the object and the calibration fields.

3.2.5 Analysis

3.2.5.1 Sensitivity Limits

In the absence of the bright glare from Vega, our deep observations should nominally detect point sources at $S/N = 5$ to $H = 20.8$ (21.2, for 13% of the image), while the shorter JHK_s exposures should reach $J = 20.8$, $H = 20.1$, and $K_s = 18.9$. However, the star adds substantial scattered light background and makes point source detection a function of position with respect to Vega.

We have assessed our H-band detection limits using artificial star experiments, both in the direct image mosaic and in the halo-subtracted image. IRAF/PSF was used to fit the two brightest single objects in the processed Vega E image, and artificial stars were added to the same image with ADDSTAR. A single experiment consisted of adding sources of constant magnitude at $1''$ intervals along 9 radial

Table 3.1: Near-infrared Point Sources in the Vicinity of Vega

ID	Coordinates (J2000.0)	J (mag)	H (mag)	K_S (mag)	Separation From Vega (arcsec)	P.A. (degree)	Mass If Associated ($M_{\rm Jup}$)
1	18:36:58.19 +38:46:56.2	15.64 ± 0.07	14.78 ± 0.05	14.53 ± 0.06	22.26 ± 0.03	103.4 ± 0.1	13–35
2	18:36:58.08 +38:47:00.7	$> 18.5 \pm 0.1$	17.20 ± 0.07	16.55 ± 0.06	22.33 ± 0.03	91.8 ± 0.1	7–24
3	18:36:58.70 +38:46:58.4	$> 19.3 \pm 0.1$	18.92 ± 0.12	18.23 ± 0.12	27.70 ± 0.03	96.0 ± 0.1	4–18
4	18:36:59.35 +38:47:05.5	17.15 ± 0.13	16.25 ± 0.14	15.98 ± 0.12	29.41 ± 0.05	86.2 ± 0.1	8–27
5	18:36:59.39 +38:47:05.7	16.76 ± 0.20	16.29 ± 0.16	16.27 ± 0.12	29.93 ± 0.05	85.8 ± 0.1	8–27
6	18:36:55.36 +38:47:25.9	$\cdots$	17.43 ± 0.07	$\cdots$	27.05 ± 0.05	335.0 ± 0.1	6–22
7	18:36:58.43 +38:46:37.9	17.12 ± 0.12	16.50 ± 0.06	16.20 ± 0.07	33.87 ± 0.06	133.8 ± 0.1	8–27
8	18:36:58.40 +38:46:37.2	17.18 ± 0.12	16.48 ± 0.09	16.29 ± 0.09	34.11 ± 0.06	135.1 ± 0.1	8–27

[a]Minimum value interpolated from the Burrows et al. (2001) models for 300 Myr; maximum value from the Chabrier et al. (2000) models for 500 Myr.

(originating from Vega) directions, offset by 15° from each other. We observed the minimum separation from Vega, at which a source would be considered "detected" by eye: at $S/N \gtrsim 5$ according to formal S/N calculations assuming Gaussian noise statistics. Since the primary source of noise (scattered light from Vega) does not behave in a Gaussian manner, however, the S/N statistic does not carry the correct information about the significance of a detection and is only used as an approximate measure of the local contrast.

The experiments were repeated at 0.5 mag steps. For a given radial distance, there are thus up to 9 independent measurements of the limiting magnitude (fewer for larger distances, where some artificial sources fall beyond the array), as shown in Figure 3.2. Our average sensitivity ranges from $\Delta H = 12.5$ mag at $4''$ to $\Delta H = 19$ mag at $\geq 26''$, 1.8 magnitudes brighter than for low-background observations.

Extensive artificial star experiments were not performed for the less well-registered parts of the mosaic: the Vega S and Vega W fields. However, after applying the registration method used for these fields (ray intersection) to the Vega E field, for which centroiding provided the best registration among our fields, we observe that the faintest object in Vega E ($H = 18.9$) is at the detection limit ($S/N = 4.7$). The detection limit is thus 0.3 mag brighter than the $H = 19.2$ found at that location using centroiding. Since smearing of point sources due to improper registering is uniform across the image (there being only translational and no rotational degrees of freedom), we estimate limiting magnitudes in Vega S and W ∼0.3 mag brighter than in Vega E and N.

3.2.5.2 Comparisons to Models

Figures 3.3 and 3.4 show the photometric measurements from Table 3.1 for the detected point sources assuming a common distance modulus with Vega, along with a 300 Myr isochrone for 1–30 $M_{\rm Jup}$ objects (Burrows et al., 2001) and known field L and T dwarfs (whose ages may range from 0.5–10 Gyr). Given their colors, all sources detected by us in the vicinity of Vega are too red compared to the expected locus of planetary-mass companions (from Table 3.1) and too faint to be

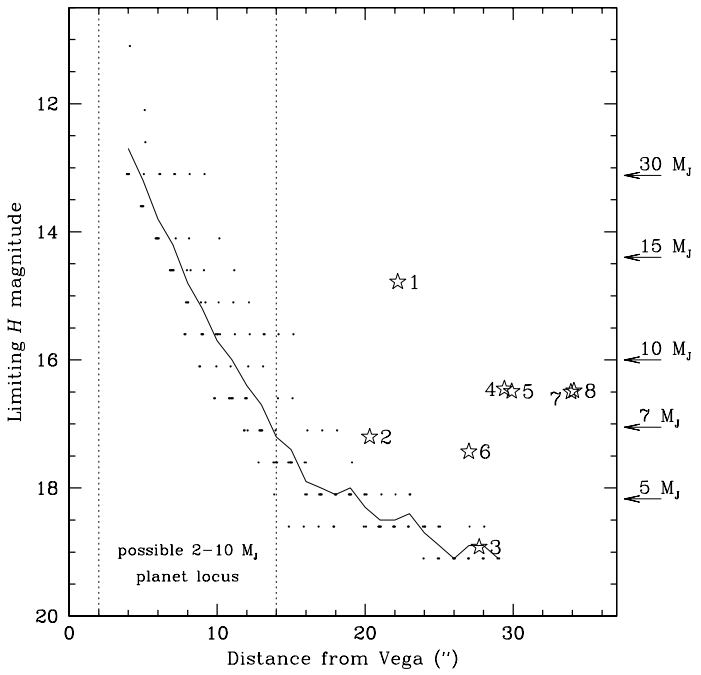

Figure 3.2: H-band sensitivity of our deep images to faint objects as a function of radial distance from Vega, analyzed for the case of the east field. Solid points represent individual measurements of the limiting magnitude at different position angles and angular separations from Vega (a slight offset has been applied between points along the abscissa for clarity). The solid line delineates the azimuthal average as a function of separation. Numbered stars indicate detected point sources. Horizontal arrows indicate the corresponding planetary mass at a given H magnitude (for 300 Myr, Burrows, priv. comm.). The area between the vertical dotted lines marks the locus of the inferred planet (Gorkavyi & Taidakova, 2001; Wilner et al., 2002). Thirteen per cent of the total area imaged has twice the integration time and hence $\sim$0.4 mag better sensitivity, which is not accounted for in this analysis. The limiting magnitude along the brightest ray at P.A. = 50° (see Figure 3.1) is $\sim$1 mag poorer (as realized in the uppermost points in the graph) than along directions with no bright artifacts. No limiting magnitudes are inferred for the $\sim 4'' \times 4''$ area covered by the "ghost" in the north field.

brown dwarfs. Hence, they are most likely background stars. This was confirmed for objects 1–5 by a relative proper motion test, with the positions of objects 2–5 (measured from PSF fits) compared to that of object 1. None changed by more than 17 ± 15 milli-arcseconds (mas) $= 0.68 \pm 0.60$ pix between the two epochs. The proper motion for Vega over the period (67 days) was 64.4 ± 0.8 mas $= 2.56 \pm 0.03$ pix (Hipparcos), and hence any projected companion that is gravitationally bound to Vega should have moved by this amount (barring all 5 being associated).

No colors or proper motion information are available for source 6, hence we can only estimate its likelihood of association with Vega from the expected frequency of field stars. To assess background contamination, we used the SKY model of Wainscoat et al. (1992), which for the position of Vega ($l = 67.45°, b = 19.24°$) gives a 7.6% probability that 4 or more stars of the specified magnitudes (for objects 1–3 and 6) are seen in the deep image. Thus, our detections are statistically consistent with being background stars.

Our results, nevertheless, demonstrate that detection of planetary-mass companions to nearby stars with ground-based telescopes is a real possibility. Based on their H magnitudes, we list the predicted masses of the candidate companions in the last column of Table 3.1, assuming a common distance modulus with Vega and using models from Burrows (private communication) and Chabrier et al. (2000) for a 300 Myr-old star. In using the Chabrier et al. models, linear interpolation has been applied between the values for 100 Myr and 500 Myr. Both sets of models include internal heating processes only and no, e.g., irradiation of the planetary atmosphere by the star or reflected light from the star, but are appropriate given the large orbital separation of our candidate companions and the wavelength regime in which we are working. We should have detected any planets/brown dwarfs >10 $M_{\rm Jup}$ at separations $>12''$ (90 AU), and >5 $M_{\rm Jup}$ at $>20''$ (160 AU) from Vega.

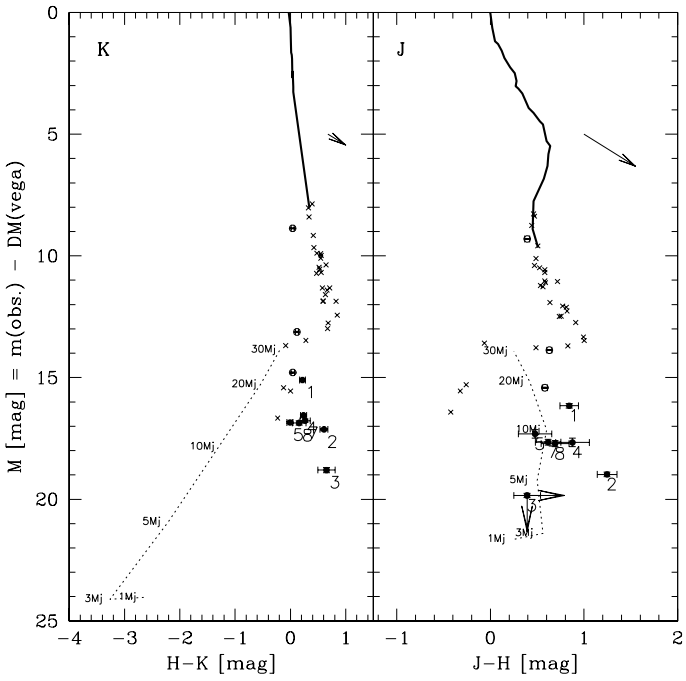

Figure 3.3: JHK_s color-magnitude diagrams in the CIT photometric system. Heavy solid line is the main sequence relation for spectral types A0–M6, and the crosses are M4–T6 dwarfs from Leggett et al. (2002). Dotted line is the Burrows et al. 300 Myr isochrone for masses 1–30 $M_{\rm Jup}$, as labeled. The arrow corresponds to 5 magnitudes of interstellar reddening. Filled circles with error bars represent our Vega field data, while open circles are the calibration field data.

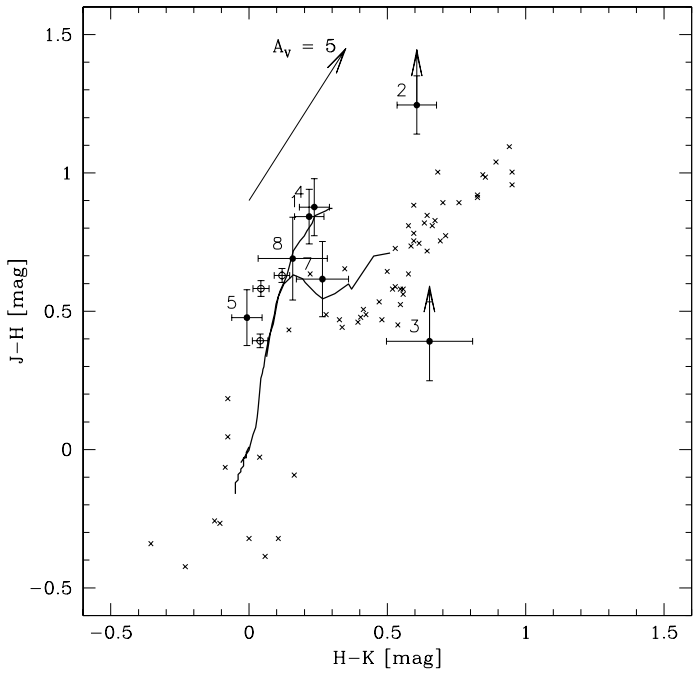

Figure 3.4: JHK_s color-color diagram, in the CIT photometric system. See Figure 3.3 for description of symbols.

3.2.6 Discussion

Based on proper motion, colors, and field star considerations, it is unlikely that the newly discovered objects are sub-stellar companions to Vega. Yet their existence in close proximity to Vega is heretofore unappreciated.

With respect to the predicted 2–3 $M_{\rm Jup}$ planetary perturber to Vega's dust distribution, Gorkavyi & Taidakova (2001, see also Ozernoy et al. (2000)) quote exact positions of a possible planet, with orbital radius ∼100 AU. We find no $H < 16.5$ objects (>8 $M_{\rm Jup}$; Burrows et al. models) at either of their quoted positions, or along the line connecting them, which may also be solutions to the model. Point sources are found neither along the Wilner et al. planetary orbit, nor anywhere within the 14″ sub-millimeter emission (albeit at lower sensitivity limits: $H <$ 17–13; >7–30 $M_{\rm Jup}$).

How do our upper limits compare to others in the literature for Vega? Gatewood & de Jonge (1995) find no astrometric evidence for planets >12 $M_{\rm Jup}$ at 1.5–5.0 AU (1.2–7 year period). Holland et al. (1998) place an upper limit of 12 $M_{\rm Jup}$ on companions based on null result observations with Keck/NIRC, though no details are given. The NICMOS images of Silverstone et al. (2002) have similar sensitivity to ours (to within 0.5 mag at 1.10 μm and 2.05 μm), yet cover an area too small to see any of the objects detected by us. The Oppenheimer (1999) survey of stars within 8 pc, which just barely included Vega, found no companions at the positions of our detections. Based on their sensitivity curves, objects brighter than r =16–17 mag should have been detected around Vega from 20–30″. Given the $R - H$ colors of low-mass stars for which $H - K = 0.1$–0.3 (K2–M5 spectral types: $R - H$ >2.0), the Oppenheimer survey may have just missed detecting our brightest projected companion to Vega if it is a background star as early as K2. Our spectrum ($S/N \approx 15$) of object 1 indeed places it in the K5V–M5V spectral type range.

Our imaging data can also be used to test a possible cosmological origin of the sub-millimeter dust clumps around Vega. Spectral energy distributions of (sub-)millimeter galaxies (Dannerbauer et al., 2002; Goldader et al., 2002; Klaas

et al., 2001) suggest $z \gtrsim 1$ for any responsible background galaxy, given our non-detection at H band. However, deep searches for K-band counterparts to several sub-millimeter galaxies have reached $K \approx 22$ mag (e.g., Dannerbauer et al., 2002) with no counterpart detection, suggesting that our data may be too insensitive (by 6–7 magnitudes at these locations) to put a sensible limit on this hypothesis.

3.2.7 Conclusions

We find 8 faint objects within 35″ of Vega that are 15–19 mag fainter than the star at H-band. If associated, at the 330 Myr age for Vega, current brown-dwarf cooling models (Burrows et al., 2001; Chabrier et al., 2000) set their masses at 5–35 $M_{\rm Jup}$. The number of detected objects is however consistent with estimates of field star density, and their colors and proper motion indicate that they are not associated with Vega.

We thus exclude the possibility of a distant (80–220 AU; ∼83% of this area is imaged), massive (>10 $M_{\rm Jup}$; >6 $M_{\rm Jup}$ for 120–220 AU) planetary/brown-dwarf companion causing the observed dust distribution around Vega. We also detect nothing at the positions of the predicted planetary perturbers, with upper mass limits 7–15 $M_{\rm Jup}$ (H<17–13), well above the 2–3 $M_{\rm Jup}$ predictions. We detect nothing at the position of the mid-infrared dust clumps, placing limits on the possibility of their extragalactic interpretation.

3.3 Initial Results from the Palomar Adaptive Optics Survey of Young Solar-type Stars: A Brown Dwarf and Three Stellar Companions

[†]Stanimir A. Metchev & Lynne A. Hillenbrand

California Institute of Technology, Division of Physics, Mathematics & Astronomy, MC 105–24, Pasadena, California 91125

Abstract

We present first results from the Palomar Adaptive Optics Survey of Young Stars conducted at the Hale 5 m telescope. Through direct imaging we have discovered a brown dwarf and two low-mass stellar companions to the young solar-type stars HD 49197, HD 129333 (EK Dra), and V522 Per, and confirmed a previously suspected companion to RX J0329.1+0118 (Sterzik et al., 1997), at respective separations of 0.95″ (43 AU), 0.74″ (25 AU), 2.09″ (400 AU), and 3.78″ (380 AU). Physical association of each binary system is established through common proper motion and/or low-resolution infrared spectroscopy. Based on the companion spectral types, we estimate their masses at 0.06, 0.20, 0.13, and 0.20 $M_{\odot}$, respectively. From analysis of our imaging data combined with archival radial velocity data, we find that the spatially resolved companion to HD 129333 is potentially identical to the previously identified spectroscopic companion to this star (Duquennoy & Mayor, 1991). However, a discrepancy with the absolute magnitude suggests that the two companions could also be distinct, with the resolved one being the outermost component of a triple system.[2] The brown dwarf HD 49197B is a new member of a growing list of directly imaged sub-stellar companions at 10–1000 AU

[†]A version of this Section was published in *The Astrophysical Journal*, vol. 617, 1330

[2]More detailed radial-velocity and direct-imaging monitoring of HD 129333, subsequently published in (König et al., 2005), has shown that the system is a binary. The dynamical masses of the components are $0.9 \pm 0.1 M_{\odot}$ and $0.5 \pm 0.1 M_{\odot}$. The secondary mass reported in König et al. is consistent with the one inferred in the present work (Metchev & Hillenbrand, 2004). The am-

separations from main sequence stars, indicating that such brown dwarfs may be more common than initially speculated.

3.3.1 Introduction

High-contrast imaging searches for low-mass companions to nearby and/or young stars have increased dramatically in number since the initial discovery of a brown-dwarf companion to a main sequence star (Gl 229) through direct imaging (Nakajima et al., 1995). One particularly powerful technique is adaptive optics (AO), which provides the high angular resolution ($\lesssim 0.1''$) achievable at the diffraction limit of large ground-based telescopes. The widening niche of high-contrast imaging opened by recent developments in AO technology implies that not only brown dwarfs but exo-solar planets may be within the realm of direct imaging. Nowadays nearly every ground-based telescope equipped with an AO system hosts an imaging companion-search project. The sudden explosion in interest in this topic has been fueled by the success of the radial velocity (r.v.) method in detecting solar system analogs (e.g., Marcy & Butler, 1998). Through longer time-lines of observation and higher precision, the sensitivity of r.v. surveys has now extended outwards to include planets at semi-major axes $\gtrsim$3 AU (Carter et al., 2003; Naef et al., 2004), i.e., near the Jovian region in the Solar System. While the sensitivity of direct imaging to "planetary-mass" (1–13 Jupiter masses (M_J); Burrows et al., 1997) objects at such separations from Sun-like stars is still extremely limited due to contrast requirements, several higher-mass brown-dwarf companions have been discovered at wider separations (see compilation in Reid et al., 2001), some at projected distances as small as 14–19 AU (Els et al., 2001; Liu et al., 2002). High-resolution spectroscopic monitoring and direct imaging are thus complementary in searching for sub-stellar companions to stars. Future development of both methods

biguity in the multiplicity in the present case is rooted in the assumption of a fixed mass for the primary (§3.3.4.3.1)–a necessary step given the insufficient number of orbital constraints. The adopted fixed mass ($1.05 M_\odot$) was too large, compared to the one found from König et al.'s better constrained orbital solution.

promises to narrow, and eventually close, the sensitivity gap between them.

Young stars are the most suitable targets for direct imaging of sub-stellar companions. At ages of 10–100 million years (Myr) the expected brightness ratio in the near IR between a 10 $M_{\rm Jup}$ object and a solar-type star is 10^{-3}–10^{-5} (Burrows et al., 1997; Baraffe et al., 2003). Modern AO systems can routinely achieve comparable dynamic range at $1''$ separations from bright stars. Hence, for young stars within 40 pc of the Sun we can probe for massive planets at separations comparable to the giant planet region in our own Solar System. However, few young stars are known at such small heliocentric distances. These are constrained to several tens of members of young moving groups: TW Hya (Rucinski & Krautter, 1983; de La Reza et al., 1989), Tucana/Horologium (Zuckerman & Webb, 2000; Zuckerman et al., 2001a), and β Pic (Zuckerman, Song, & Webb, 2001b), and have already been targeted with sensitive space-based and ground-based AO surveys, which have uncovered 3–4 brown-dwarf companions (Lowrance, 2001; Lowrance et al., 2003; Neuhäuser & Guenther, 2004), but no planetary-mass ones.

Because contrast and projected separation are the limiting factors in detectability of sub-stellar companions, brown dwarfs, being more luminous than planets, are detectable at greater heliocentric distances and at smaller angular separations from their host stars. At the same physical separation from the primary (e.g., 50–100 AU), brown-dwarf companions should be detectable around older (several gigayears [Gyr]) and/or more distant ($\lesssim$200 pc) stars compared to planets, allowing a larger sample of targets. With regard to this, we have commenced a survey of young (<500 Myr) solar-type (F5–K5) stars within 200 pc using the AO system on the Palomar 5-m telescope. Our survey sample is largely a subset of the sample targeted by the Formation and Evolution of Planetary Systems (FEPS) *Spitzer* Legacy Team (Meyer et al., 2004). Although faint primary stars, such as M dwarfs or white dwarfs, offer more favorable contrast for imaging sub-stellar companions, we have chosen to limit our sample to solar analogs because of interest in determining the multiplicity statistics of sub-stellar objects around other suns. Furthermore, several recent large surveys have already explored the multiplicity

of nearby ($\lesssim$50 pc) cool stars (Close et al., 2003; Carson et al., 2003; McCarthy & Zuckerman, 2004) or white dwarfs (Zuckerman & Becklin, 1992; Green, Ali, & Napiwotzki, 2000), while a large sample of F–G stars has not been studied because of comparatively small numbers in the immediate solar neighborhood.

Preliminary results from our survey were reported in Metchev, Hillenbrand, & Meyer (2002). Here we present the strategy of the survey, and the discovery and confirmation of resolved low-mass companions to HD 49197, HD 129333 (EK Dra), V522 Per, and RX J0329.1+0118. We shall refer to these throughout the paper as HD 49197B, HD 129333B, V522 PerB, and RX J0329.1+0118B. For convenience of notation, a second candidate companion to HD 49197 found to be an unrelated background star will be denoted as HD 49197"C". The full sample and further results from the survey will be discussed in a later paper.

3.3.2 Observing Strategy

The observations described in this section are representative of our general survey observing strategy. Table 3.2 details the imaging and spectroscopic observations specifically for the four objects presented here. The properties of the observed primaries are given in Table 3.3.

3.3.2.1 Imaging

3.3.2.1.1 First-Epoch Imaging and Survey Sample Subdivision

First epoch observations are obtained with the Palomar AO system (PALAO; Troy et al., 2000) in residence at the Cassegrain focus of the Palomar 5-m telescope. Since the summer of 2003 the wavefront sensor runs at frame rates up to 2 kHz, and the system routinely produces diffraction-limited images ($0.09''$ at K_S) with Strehl ratios[3] in the 30–50% range at 2μm on $V < 12$ guide stars and up to 75% on $V < 7$ mag guide stars. PALAO employs the Palomar High Angular Resolution

[3]The Strehl ratio is an empirical measure of the quality of an image, equal to the ratio of the peak of the observed PSF to the peak of the ideal, diffraction-limited, telescope PSF. High-order AO systems nowadays routinely achieve Strehl ratios >50% at K-band.

Table 3.2: Observations

Target	First Epoch/Telescope	Mode	Second Epoch/Telescope	Mode
HD 49197	2002 Feb 28/Palomar	JHK_S coronagraphic imaging	2003 Nov 9–10/Keck II	JHK_S coronagraphic imaging, K spectroscopy
HD 129333	2003 Jan 12/Palomar	JHK_S non-coronagraphic imaging, JK spectroscopy	2003 May 13/Palomar	Brγ non-coronagraphic imaging
V522 Per	2003 Sep 20/Palomar	JHK_S non-coronagraphic imaging	2003 Nov 10/Keck II	K_SL' non-coronagraphic imaging, JK spectroscopy
RX J0329.1+0118	2003 Sep 21/Palomar	JHK_S coronagraphic imaging	2003 Nov 10/Keck II	K spectroscopy

Table 3.3: Properties of the Observed Stars

	Proper Motion (mas yr^{-1})		Parallax		$K_S^{\rm a}$	Age^{rmb}	
Object	$\mu_\alpha \cos\delta$	μ_δ	(mas)	Spectral Type	(mag)	(Myr)	Notes
HD 49197	-35.12 ± 1.05	-48.59 ± 0.63	22.41 ± 0.87	F5 V	6.067 ± 0.024	$260 - 790$	1,3
HD 129333	-138.61 ± 0.61	-11.92 ± 0.68	29.46 ± 0.61	G0 V	5.914 ± 0.021	$10 - 100$	1,4
V522 Per	17.6 ± 3.0	-26.9 ± 2.7	5.46 ± 0.20	$\cdots$	9.352 ± 0.024	90 ± 10	2,5
RX J0329.1+0118	5.4 ± 1.1	-5.8 ± 1.1	$\lesssim 10$	G0 IV	9.916 ± 0.019	≈ 120	2,6,7

NOTES.— 1. Proper motion and parallax from *Hipparcos* (Perryman et al., 1997). 2. Proper motion from Tycho 2 (Høg et al., 2000). 3. Spectral type from *Hipparcos* (Perryman et al., 1997). 4. Spectral type from Buscombe & Foster (1997). 5. Assumed to be at the mean *Hipparcos* distance (van Leeuwen, 1999) of the α Per cluster. 6. A distance of at least 100 pc can be inferred for this young ($\sim$100 Myr; Frink et al., 1997) star from its small proper motion and its location toward the Taurus star-forming region. 7. Spectral type from Buscombe (1998).

[a] From the 2MASS Point Source Catalog (Cutri et al., 2003).

[b] See §3.3.4.2.

Observer (PHARO; Hayward et al., 2001), a 1024×1024 pix HgCdTe HAWAII detector with imaging (25 mas/pix and 40 mas/pix pixel scale) and spectroscopic (R=500–2000) capabilities in the near IR. A set of coronagraphic spots, Lyot masks and neutral density (ND) filters are available to achieve the desired dynamic range.

Our program entails K_S-band (2.15μm) imaging in the 25 mas/pix mode ($25'' \times 25''$ field of view) both with and without a $0.97''$-diameter coronagraphic stop. For high dynamic range, long (1 min) coronagraphic images are taken to identify fainter (potentially sub-stellar) companions at separations $>0.5''$. Twenty-four such exposures are taken, for a total of 24 min integration per target, with 6 min spent at each of 4 different orthogonal detector orientations (obtained by rotating the Cassegrain ring of the telescope). For every 6 min of on-target imaging (i.e., at each detector orientation), separate 1-min coronagraphic exposures are taken at five dithered sky positions 32–60$''$ from the star. For high angular resolution (but with lower dynamic range), short (1.4–9.8 sec) non-coronagraphic exposures are taken to look for close companions of modest flux ratio and to establish relative photometric calibration. The images are taken in a 5-point dither pattern at the vertices and center of a box $6''$ on a side. A 1%-transmission ND filter is used if necessary to avoid saturation[4]. On occasion, a narrow-band (1%) Brackett-γ (2.17μm) filter is used for higher throughput, instead of the ND 1% filter.

To avoid detector saturation and/or decreased sensitivity over a substantial fraction of the image area, stars with bright ($\Delta K_S < 4$) projected companions in the PHARO field of view (FOV) were not observed with deep coronagraphic exposures. However, binaries with separation $\leq 0.5''$ were included, as both components of the binary could then be occulted by the coronagraph. This naturally splits our survey sample in two groups: the "deep" subsample, consisting of essentially single stars and close binaries, and the "shallow" subsample encompassing the remaining stars. Membership to one of the two subsamples was assigned at

[4]The ND 1% filter was calibrated photometrically through repeated (17–20 per band) observations of 3 program stars with and without the filter, and its extinction was measured at 4.753±0.039 mag at J, 4.424±0.033 mag at H, and 4.197±0.024 mag at K_S.

the telescope, when their multiplicity and approximate flux ratio was revealed during the short exposures. The shallow subsample was further expanded to include stars out to 200 pc and/or older than 500 Myr to cover the entire FEPS sample accessible from the Northern hemisphere.

Short dithered exposures were taken of all stars, while long coronagraphic exposures were taken only of stars in the deep subsample at K_S band. In addition, short J- (1.22μm) and H-band (1.65μm) exposures were taken of all candidate binaries (all stars in the shallow survey, and the $< 0.5''$ systems in the deep survey) to allow approximate photospheric characterization of the components.

In accordance with the above distinction, HD 49197 was observed for a total of 24 min with the coronagraph as a part of the deep survey, while HD 129333 and RX J0329.1+0118 (with bright candidate companions), and V522 Per (α Per member, 190 pc from the Sun; van Leeuwen, 1999) were observed only with short exposures. Conditions were photometric during the first epoch observations of HD 49197, V522 Per, and RX J0329.1+0118, and unstable during those of HD 129333.

3.3.2.1.2 Follow-Up Imaging

We obtain second-epoch imaging observations of all candidate companions to check for common proper motion with their corresponding stars. Such were taken for HD 129333 with PALAO/PHARO, and for HD 49197, V522 Per, and RX J0329.1+0118 with NIRC2 (Matthews et al., in prep.) and the Keck II AO system (diffraction limit $0.05''$ at K_S; Wizinowich et al., 2000). Conditions were not photometric during follow-up, and only the best images (Strehl ratio $S \gtrsim 40\%$) were selected for astrometry. HD 129333 was followed up in the narrow-band Brackett γ filter, which allowed higher throughput than the ND 1% filter in the shortest (1.4 sec) PHARO exposures. Given the unstable atmospheric conditions during the second-epoch imaging of HD 129333, this allowed us to take high signal-to-noise (S/N) exposures on time-scales that would most finely sample the variations in the seeing and to select only the ones with the best imaging quality.

Keck follow-up is done at JHK_S, or at K_SL' if the candidate companion is expected to be bright enough to be seen at L' (given $0.7 < K_S - L' < 2.5$ for L and T dwarfs; Leggett et al., 2002). Sequences of short (up to 20 sec from multiple co-adds) dithered non-coronagraphic and long (1 min) target-sky-target exposures are taken with a $1''$- or $2''$-diameter coronagraph in the same manner as with PHARO, though without detector rotations. The candidate companions are exposed until a S/N ratio comparable to that in the first-epoch PHARO observation is achieved (for similar positional accuracy), up to 6 min per filter in J, H, and K_S. The total integration time at L' is up to 10.5 min, which allows the detection of $L' \lesssim 15.0$ objects. We mainly use the 40 mas/pix (wide) NIRC2 camera ($41''$ FOV), which severely under-samples the Keck AO point-spread function (PSF), but is known to suffer from less distortion than the 20 mas/pix (medium) camera over the same field (Thompson, Egami, & Sawicki, 2001). Although we also have the option of using the 10 mas/pix (narrow) camera ($10''$ FOV) in NIRC2, it does not allow follow-up of distant candidate companions, and we avoid using it for consistency with the other NIRC2 observations.

3.3.2.1.3 Imaging Data Reduction

All imaging data are reduced in a standard fashion for near IR observations. Flat fields are constructed either from images of the twilight sky (for the Palomar data) or from images of the lamp-illuminated dome interior (for the Keck data). A bad pixel mask is created from the individual flats, based on the response of each pixel to varying flux levels. Pixels whose gain deviates by more than 5 sigma from the mode gain of the array are flagged as bad. Sky frames for the dithered, non-coronagraphic exposures are obtained by median-combining four of the five exposures in the dither pattern (excluding the central pointing) and rejecting the highest pixel value in the stack. The coronagraphic-mode sky frames are median-combined using an average sigma clipping algorithm to remove pixels deviant by more than 5 sigma. The sky-subtracted images of each target are divided by the flat field, then registered and median-combined to create a final high signal-to-

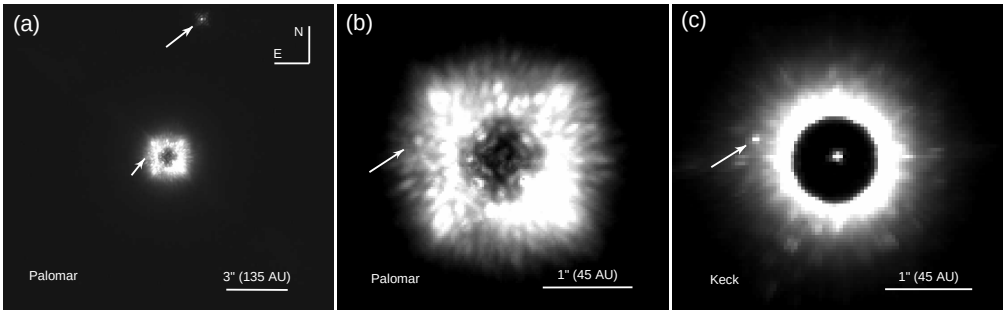

Figure 3.5: K_S-band (2.15μm) first (a, b) and second (c) epoch images of HD 49197. Panel (a) shows both candidate companions to HD 49197; panels (b) and (c) are zoomed in to point out only the close-in, bona fide companion (HD 49197B). The first-epoch image is the result of 24 median-combined 60 sec exposures with Palomar/PHARO, whereas the second-epoch image was formed by median-combining six 60 sec exposures with Keck/NIRC2. A 1.0″-diameter coronagraph occults the primary in both cases; in the Keck image the coronagraph shows a residual ≈0.16% transmission. HD 49197B was initially unnoticed in the first-epoch image, where its detection was hindered by the presence of equally prominent AO speckles.

noise (S/N) image (Figures 3.5 and 3.6). However, photometric and astrometric measurements are performed on the individual reduced images.

No PSF stars are observed at either Palomar or Keck. With PHARO at Palomar, median-combined images from all 4 detector orientations can be used to reproduce an approximate PSF. This approach was chosen to emulate the observation of separate PSF stars of identical brightness and color, while optimizing the time spent on science targets. However, we have found that a simple 180° rotation and subtraction technique works equally well, and we use that on both the Palomar and Keck data. While neither approach eliminates telescopic speckle noise (as could be the case if actual PSF stars were observed), both significantly reduce point-symmetric structure in the PSF.

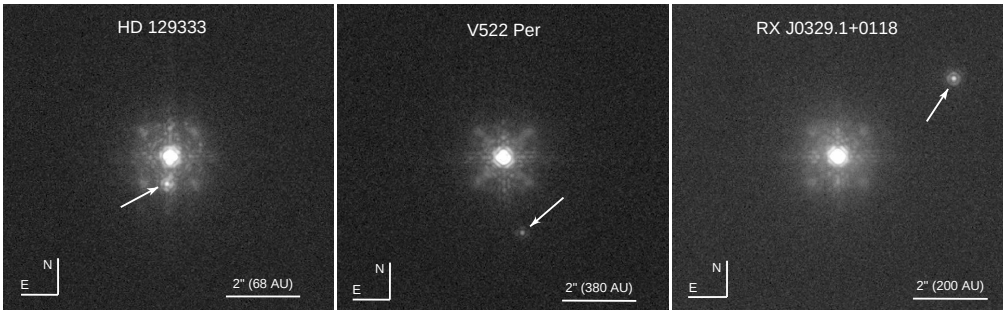

Figure 3.6: Palomar images of the stellar companions. The HD 129333 image is taken through a narrow-band (1%) Brγ (2.166 μm) filter, while the V522 Per and RX J0329.1+0118 images are taken at K_S. Five dithered 1.4 sec exposures were aligned and median-combined to obtain each of the displayed images.

3.3.2.2 Astrometric Calibration

The exact pixel scale of the 25 mas PHARO camera was determined using known binary stars from the Sixth Orbit Catalog (Hartkopf, Mason, & Worley, 2001; Hartkopf & Mason, 2003): WDS 09006+4147 (grade 1; Hartkopf, Mason, & McAlister, 1996), WDS 16147+3352 (grade 4; Scardia, 1979), WDS 18055+0230 (grade 1; Pourbaix, 2000), and WDS 20467+1607 (grade 4; Hale, 1994). These "calibration binaries" are observed throughout our campaign at Palomar at all four detector orientations. The combination of grade 1 (accurately determined, short-period) orbits and grade 4 (less accurately known, longer-period) orbits was selected from the list of astrometric calibrators recommended by Hartkopf & Mason (2003). Despite the lower quality of the solution for binaries with grade 4 orbits, their periods are generally much longer (889 and 3249 years for WDS 16147+3352 and WDS 20467+1607 vs. 21.78 and 88.38 years for WDS 09006+4147 and WDS 18055+0230, respectively), so their motions are predicted with sufficient accuracy for many years into the future. The mean pixel scale of PHARO was measured to be 25.22 mas/pix with a 1 sigma scatter of 0.11 mas/pix among measurements of the individual binaries at different detector orientations. This measurement is consistent with, though less precise than, our previous determination (25.168 $\pm$ 0.034 mas/pix; Metchev,

Hillenbrand, & White, 2003), which was obtained from only one calibration binary at a single Cassegrain ring orientation. The larger scatter of our more recent measurement is indicative of the systematics involved in choosing different calibration binaries and in observing at more than one detector orientation.

The pixel scale of the wide NIRC2 camera was calibrated using the binary WDS 15360+3948 (grade 1; Söderhjelm, 1999). The obtained value of 39.82±0.25 mas/pix is consistent with the pre-ship measurement of 39.7±0.5 max/pix[5]. Because only one binary was used for calibrating NIRC2, a 0.63% error term corresponding to the uncertainty in the semi-major axis of the binary has been added in quadrature to the uncertainty of our measurement.

3.3.2.3 Spectroscopy

3.3.2.3.1 Observations

Spectroscopy of faint targets in the halos of bright objects is more challenging than spectroscopy of isolated targets. Care needs to be taken to achieve optimum suppression of the scattered light of the bright stars either by using a coronagraph (in a manner similar to coronagraphic imaging) or by aligning the slit so as to minimize light admitted from the halo. Since neither PHARO nor NIRC2 allow coronagraphic spectroscopy, when taking spectra of faint companions we orient the slit as close as possible to 90° from the primary-companion axis. Spectra of brighter companions, for which the signal from the halo is negligible compared to that from the target, are obtained by aligning the binary along the slit. Given that we often use the F5–K5 IV–V primaries in our sample as telluric standards, such alignment improves our observing efficiency. Sky spectra are obtained simultaneously with the target spectra by dithering the targets along the slit.

Promising candidate companions are observed at medium resolution ($R = 1000 - 3000$) at K and (AO correction permitting) at J. In PHARO we use the corresponding grism and filter combination (K or J) and the 40 mas/pix cam-

[5]See http://www2.keck.hawaii.edu/inst/nirc2/genspecs.html.

era, while in NIRC2 we use the K or J filter with the "medres" grism, and the wide (40 mas/pix) camera. For K-band spectroscopy in first order with PHARO and in fifth order with NIRC2 we achieve complete coverage of the 2.2μm atmospheric window. For J-band spectroscopy in first order with PHARO the coverage is limited by the size of the detector to a 0.16μm bandwidth. J-band spectroscopy with NIRC2 can cover the entire 1.2μm window, but the spectrum is split between the fifth and the sixth dispersion orders. To allow simultaneous data acquisition from both orders, we fit both onto the wide camera by clipping the fifth (longer-wavelength) order shortward of 1.22μm and the sixth (shorter-wavelength) order longward of 1.28μm. The combined J-band spectrum has complete coverage between 1.16–1.35μm.

We took J and K-band spectra with PHARO of HD 129333A/B, J and K spectra with NIRC2 of V522 PerA/B, and K-band NIRC2 spectra of HD 49197A/B and RX J0329.1+0118A/B. For the observations of HD 129333 with PHARO and of RX J0329.1+0118 with NIRC2, the binary was aligned along the slit, whereas spectra of the other two binaries (with fainter companions) were obtained by placing each component in the slit individually. A 0.26″ (6.5 pix) slit was used in PHARO, and a 0.08″ (2 pix) slit was used in NIRC2, resulting in spectral resolutions of 1200 at J and 1000 at K with PHARO, and 2400 at fifth-order J (1.22–1.35μm), 2900 at sixth-order J (1.15–1.28μm), and 2700 at K with NIRC2.

Flat fields with the dispersive grisms in place were not obtained for any of our spectroscopic observations. Instead, the raw spectra were divided by an imaging flat field, constructed in the same manner as for the imaging observations. The flat-fielded spectra were corrected for bad pixels, using the same bad pixel mask as in the imaging case. Strong positive deviations due to cosmic ray hits were then eliminated using the L.A. Cosmic Laplacian filter algorithm (van Dokkum, 2001). Fringing was at a noticeable level ($\approx$15%) only in spectra obtained with PHARO (of HD 129333) and was reduced to below 5% by dividing the target spectrum by that of the telluric standard, taken at a nearby position on the detector.

3.3.2.3.2 Spectroscopic Data Reduction

Extraction of the spectra is performed using IRAF/APEXTRACT tasks. To reduce contamination from the halo of the primary in the companion spectra, the local background (arising mostly from the halo) is fit by a first-order polynomial along the direction perpendicular to the dispersion axis and subtracted during extraction. In addition, the aperture width for the companion spectrum is conservatively set to the full width at half maximum of the profile so as to include only pixels with maximum signal-to-noise. Pixels within the aperture are summed along detector columns (which are nearly perpendicular to the dispersion axis), and the resulting "compressed" spectrum is traced along the dispersion axis by fitting a high order (8 to 15) Legendre polynomial. The tracing step is approximately equal to the slit width, where at each step the data point is obtained as the sum of 3–10 adjacent pixels (1.5–3 slit widths; the spectra of fainter objects being more heavily averaged) in the compressed spectrum. This procedure is found to produce consistent results for extractions of multiple dithered spectra of the same companion, indicating that scattered light contamination from the primary has been reduced to a small level. Nevertheless, in some cases of very faint close-in companions, the continuum shape is still found to vary noticeably among the individual extractions. We therefore avoid classifying the spectra of the companions based on their continuum shapes, but rely on the relative strengths of narrow absorption features (discernible given our resolution) instead (§3.3.3.3).

A dispersion solution for each spectrum is obtained from night sky lines in non-sky-subtracted images, using the task IDENTIFY and OH emission-line lists available in IRAF. For the spectra of primaries observed separately (e.g., HD 49197 and V522 Per), whose shallower (10–120 sec) exposures do not contain telluric emission lines at a high enough S/N to allow the fitting of a dispersion solution, such is derived after registration with deeper (10–15 min long) companion spectra taken immediately after those of the primaries. The tasks FXCOR and SPECSHIFT are used to cross-correlate and align the individual wavelength-calibrated spectra for a given object. The individual primary and companion spectra are then median-

combined using SCOMBINE.

Since the primaries (when earlier than K0) double as telluric standards, their spectra are first corrected for photospheric absorption from atomic hydrogen (H Pβ at 1.282μm and H Brγ at 2.166μm) by hand-interpolating over the absorption with the task SPLOT. Weaker absorption features due to Na I, Ca I, Si I, Al I, and Fe I, although present in the spectra of our telluric standards, are left uncorrected because of blending (at our resolution) with various OH absorption lines in the Earth's atmosphere. After thus correcting the telluric spectra, the spectra of the companions are divided by those of the telluric standards. Finally, the spectra of the companions are multiplied by black bodies with temperatures corresponding to the spectral types of the telluric standards (based on effective temperature vs. spectral type data from Cox, 2000) and boxcar-smoothed by the width of the slit.

The above reduction procedure applies in exact form for NIRC2 spectra, which do not suffer from fringing. For PHARO data, which are noticeably affected by fringing, we divide the individual target spectra by those of the telluric standard before median-combining and wavelength calibration, since fringing depends on detector position, not on the dispersive element.

Reduced spectra for the objects reported here are presented in Figure 3.7 and 3.8. The mismatch in the continuum slopes between the fifth- and sixth-order J-band spectra of the companion to V522 Per may be due to our use of imaging, instead of spectroscopic flats.

3.3.3 Analysis

3.3.3.1 Photometry

Broad-band near-IR photometry of the companions is presented in Table 3.4. The measured quantity in each case is the relative flux (ΔJ, ΔH, ΔK_S, $\Delta L'$) of the companion with respect to that of the primary. When the companions were visible without the coronagraph (in all cases except for the close-in companion to HD 49197), the fluxes of both components were measured directly from the short-

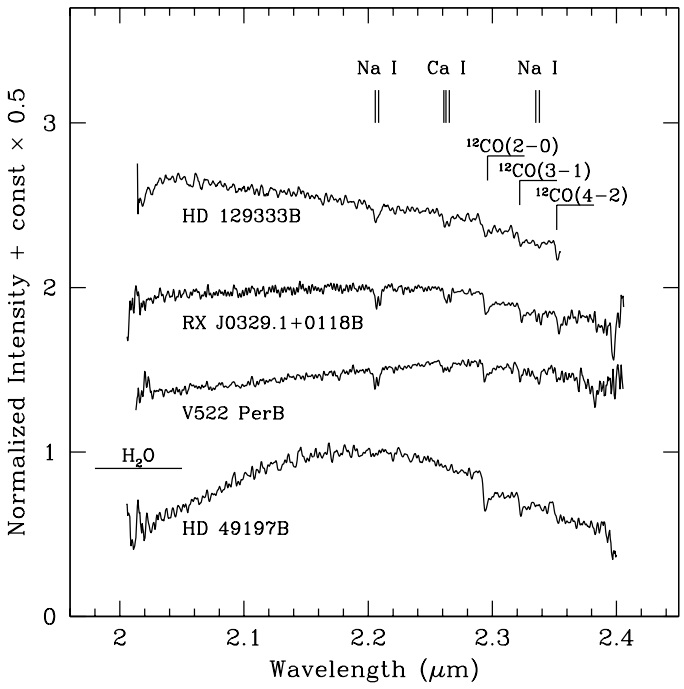

Figure 3.7: K-band spectra of the low-mass companions from Palomar (HD 129333B; $R \approx 1000$) and Keck (RX J0329.1+0118B, V522 PerB, and HD 49197B; $R \approx 2700$). All spectra have been normalized to unity at 2.20μm and offset by 0.5 in the vertical axis.

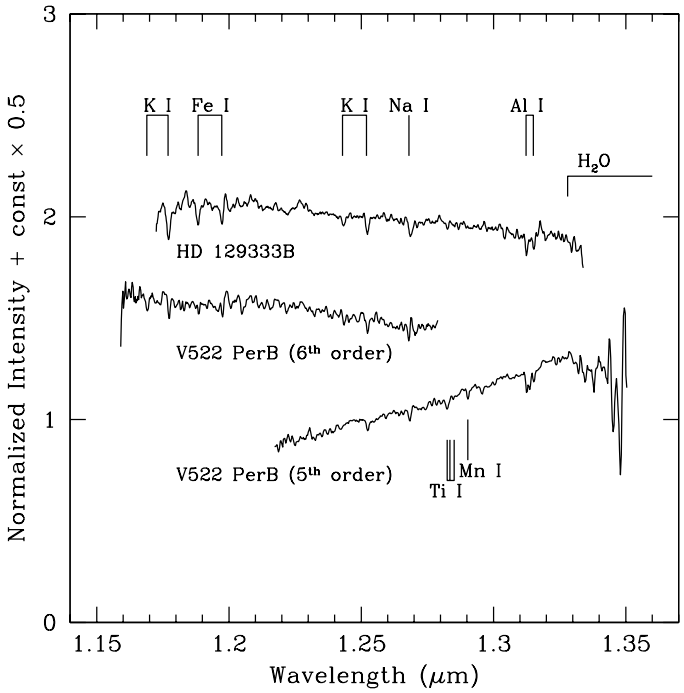

Figure 3.8: J-band spectra of two of the low-mass companions from Palomar (HD 129333B; $R \approx 1200$) and Keck (V522 PerB; $R \approx 2400$ in the fifth order and $R \approx 2900$ in the sixth). All spectra have been normalized to unity at 1.25μm and offset by 0.5 in the vertical axis.

exposure non-coronagraphic images. Flux ratios for the HD 129333, V522 Per, RX J0329.1+0118, and HD 49197A/"C" systems were obtained from the Palomar images in apertures of radii of $0.2''$ ($2\lambda/D$ at K_S). For the photometry of HD 129333B we subtracted the halo of the nearby ($0.74''$) primary (as detailed in §3.3.2.1.3) to minimize its contribution to the flux of the secondary. In the case of the HD 49197A/B system, the $0.95''$ companion is not seen in PHARO images taken without the coronagraph, and only coronagraphic exposures were obtained with NIRC2. The magnitude of the companion was obtained with respect to the residual flux of the primary seen through the $1''$ NIRC2 coronagraphic spot. The flux measurements were performed on the PSF-subtracted NIRC2 images in a $0.16''$-radius ($3.2\lambda/D$ at K_S) aperture. The transmission of the spot was established from photometry of another program star in images taken with and without the $2''$ coronagraph: its extinction was measured at 9.27 ± 0.07 mag at J, 7.84 ± 0.03 mag at H, and 7.19 ± 0.03 mag at K_S. The companion was seen in all 6 one-minute coronagraphic exposures at K_S, but because of varying photometric conditions and proximity of diffraction spikes, it was detected in only 3 out of 6 PSF-subtracted exposures at H, and 1 out of 6 at J.

Sky values for each of the observed objects were determined as the centroid of the flux distribution in a $0.1''$-wide annulus with an inner radius larger by λ/D than the distance at which the radial profile of the object fell below the level of the local background. For the primaries observed with PHARO this inner radius was $2.0''$ ($20\lambda/D$ at K_S), while for HD 49197A, the flux of which was measured through the NIRC2 coronagraph, the inner radius was $0.2''$ ($5\lambda/D$). For the companions, the inner radius of the sky annulus varied from 2.25–4 times the K_S diffraction limit, depending on whether the local background was strongly influenced by the halo of the primary (as near HD 49197 and HD 129333), or not. Experiments with varying sky annulus sizes in the two more detached systems (V522 Per and RX J0329.1+0118) showed that the relative photometry between two objects in the same image is preserved to within 0.08 mag for annuli ranging between 2.25–$20\lambda/D$ in inner radius.

Table 3.4: IR Magnitudes and Colors of the Companions

Object	ΔJ	ΔH	ΔK_S	$J-H$	$H-K_S$	K_S	K_S-L'
HD 49197B	9.6 ± 1.2	8.52 ± 0.12	8.22 ± 0.11	1.2 ± 1.2	0.33 ± 0.20	14.29 ± 0.14	$\cdots$
HD 49197"C"	6.86 ± 0.10	6.82 ± 0.09	6.68 ± 0.10	0.27 ± 0.14	0.17 ± 0.14	12.75 ± 0.10	$\cdots$
HD 129333B	3.38 ± 0.10	3.13 ± 0.09	3.04 ± 0.08	0.55 ± 0.14	0.19 ± 0.12	8.95 ± 0.08	$\cdots$
V522 PerB	5.69 ± 0.09	5.44 ± 0.09	5.16 ± 0.09	0.63 ± 0.13	0.38 ± 0.13	14.51 ± 0.09	0.15 ± 0.18
RX J0329.1+0118B	4.22 ± 0.12	3.86 ± 0.08	3.65 ± 0.08	0.59 ± 0.15	0.31 ± 0.13	12.85 ± 0.09	$\cdots$

The $J-H$ and $H-K_S$ colors and K_S magnitudes are derived from the measured relative photometry by adopting the Two-Micron All Sky Survey (2MASS; Cutri et al., 2003) magnitudes for the primaries. The $K_S - L'$ color of the companion to V522 Per was calculated assuming $K_S - L' = 0.04$ for the F5 V primary (Bessell & Brett, 1988). A near-IR color-color diagram of the detected companions is presented in Figure 3.9. Extinction corrections of $A_J = 0.087$, $A_H = 0.055$, $A_K = 0.033$, and $A_L = 0.016$ have been applied to the colors of V522 PerB, based on $E(B-V) = 0.10$ toward the α Per cluster as measured by Pinsonneault et al. (1998). We have adopted $A_V = 3.1E(B-V)$, and the interstellar extinction law of Cardelli, Clayton, & Mathis (1989).

Based on the colors and the ΔK_S magnitudes, we can infer that HD 49197"C" is a likely F–G background star, whereas the remaining companions are consistent with being late-type stars associated with their primaries.

3.3.3.2 Astrometry

Three of the four systems were observed at two different astrometric epochs. RX J0329.1+0118 was observed only once, though prior-epoch astrometric data for it exist from Sterzik et al. (1997). Table 3.5 details for each binary the observed offset and position angle of the companion from the primary during the first and second epochs of observation, as well as the estimated offset and position angle during the first epoch, had the system not been a common proper motion pair. The estimates are extrapolated backwards in time from the second-epoch astrometry, which for all except HD 129333 was obtained with NIRC2 on Keck and was more accurate, assuming proper motions from *Hipparcos* (Perryman et al., 1997) for HD 49197 and HD 129333, and from Tycho 2 (Høg et al., 2000) for V522 Per and RX J0329.1+0118. Parallactic motions were also taken into account, as they are significant for stars $\lesssim 200$ pc at our astrometric precision (several milli-arcsec). The assumed proper motions and parallaxes for all stars are listed in Table 3.3. To ensure the correct propagation of astrometric errors, the epoch transformations were performed following the co-variant treatment of the problem, as detailed in

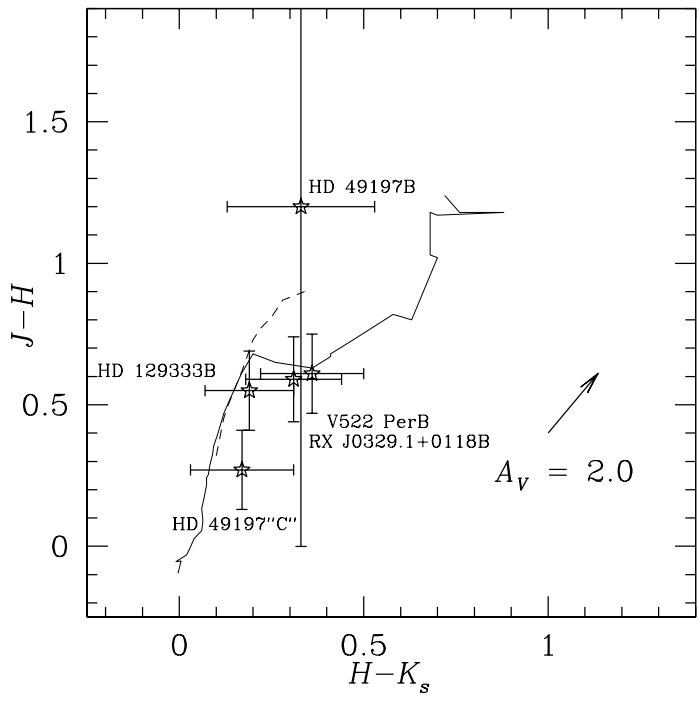

]

Figure 3.9: Near-IR color-color diagram of the detected companions. The solid line represents the B2V–L8V main sequence, with data compiled from Cox (2000, B2V–M6V) and Kirkpatrick et al. (2000, M8V–L8V). The dashed line shows the G0–M7 giant branch (Cox, 2000). The Cox and the Kirkpatrick et al. colors are converted from the Johnson-Glass (Bessell & Brett, 1988) and 2MASS (Cutri et al., 2003) systems, respectively, to the CIT system using relations from Carpenter (2001). HD 49197"C" is too blue to be a bona fide low-mass companion to HD 49197. The near IR colors of the remainder of the companions agree well with their inferred spectral types (Table 3.7).

Table 3.5: Astrometry of the Companions

	Epoch 1		Epoch 2		Epoch 1 if Non-common Proper Motion	
	Offset	P.A.	Offset	P.A.	Offset	P.A.
Object	(arcsec)	(degrees)	(arcsec)	(degrees)	(arcsec)	(degrees)
HD 49197B	0.9499±0.0054	78.25±0.40	0.9475±0.0022	77.60±0.25	0.9029±0.0037	81.87±0.31
HD 49197"C"	6.971±0.030	346.13±0.34	7.016±0.008	346.50±0.10	6.950±0.009	346.10±0.10
HD 129333B	0.7343±0.0032	173.19±0.35	0.7363±0.0032	173.37±0.35	0.7221±0.0033	180.68±0.37
V552 PerB	2.0970±0.0090	194.02±0.34	2.0937±0.0032	193.91±0.11	2.0991±0.0032	193.93±0.11
RX J0329.1+0118B	3.75±0.05	303±5	3.781±0.016	303.85±0.34	3.714±0.070	303.7±1.1

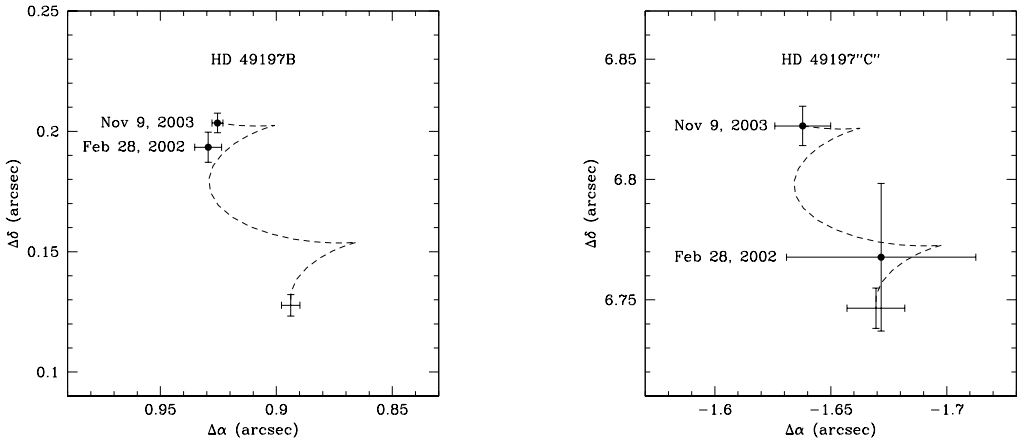

Figure 3.10: Proper motion diagram for the two companions to HD 49197. The offsets from the primary at each observational epoch are plotted as solid points with errorbars. The inferred offsets at the first epoch (assuming non-common proper motion) are shown just with errorbars. The dashed lines reflect the proper and parallactic motions of the primary between the two epochs. HD 49197B is a common proper motion companion within the 1 sigma errors, while HD 49197"C" is more consistent with being a background object.

Lindegren (1997).

Proper motion diagrams for each object are presented in Figures 3.10–3.12. The first- and second-epoch measurements are shown as solid points with error bars, and the inferred first-epoch position (assuming non-common proper motion) is shown only with errorbars. The dashed line reflects the combined proper and parallactic motion of the primary over the period between the two epochs. Below we discuss the evidence for common proper motion in each system.

3.3.3.2.1 HD 49197

The existence of the close (0.95″) companion to HD 49197 was unappreciated prior to the second-epoch imaging: the star was followed up because of the more distant (6.8″) candidate companion (HD 49197"C"). Upon its discovery in the

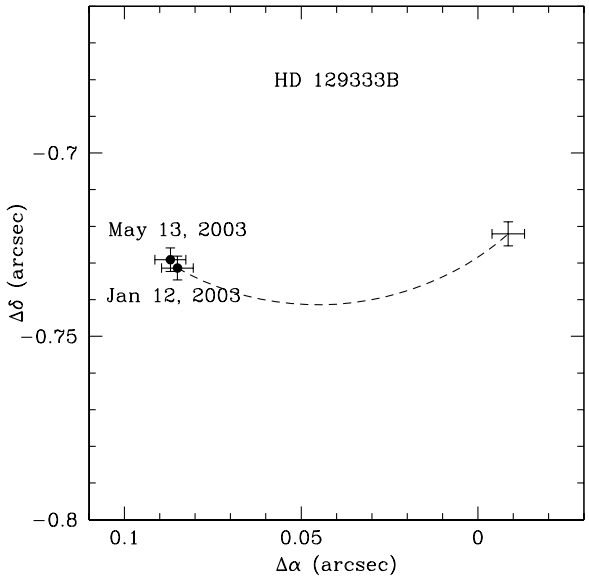

Figure 3.11: Same as Figure 3.10 for the companion to HD 129333. Within the 1 sigma errors, the companion shares the proper motion of the primary.

Keck image (Figure 3.5c), the close companion was recovered in the earlier Palomar image, where a dark circular ring around the core at the radial distance of the first Airy null ($\approx 0.1''$) distinguishes it from the telescopic speckles (Figure 3.5b).

As is evident from Figure 3.10, HD 49197B (left panel) is much more consistent with being a proper motion companion of the primary, than with being an unrelated background star projected along the same line of sight, whereas the reverse holds for HD 49197"C" (right panel). Therefore, we claim that the close-in HD 49197B is a bona fide companion, whereas the more widely separated HD 49197"C" is not.

The astrometry for HD 49197B from the two observational epochs is not in perfect agreement, perhaps because of its orbital motion around component A. At a projected separation of 43 AU, the orbital period will be >240 years (assuming a circular face-on orbit and a mass of $1.16 M_{\odot}$ for the F5 V primary; Allende Prieto & Lambert, 1999), resulting in a change in position angle of $<2.6^{\circ}$ between the

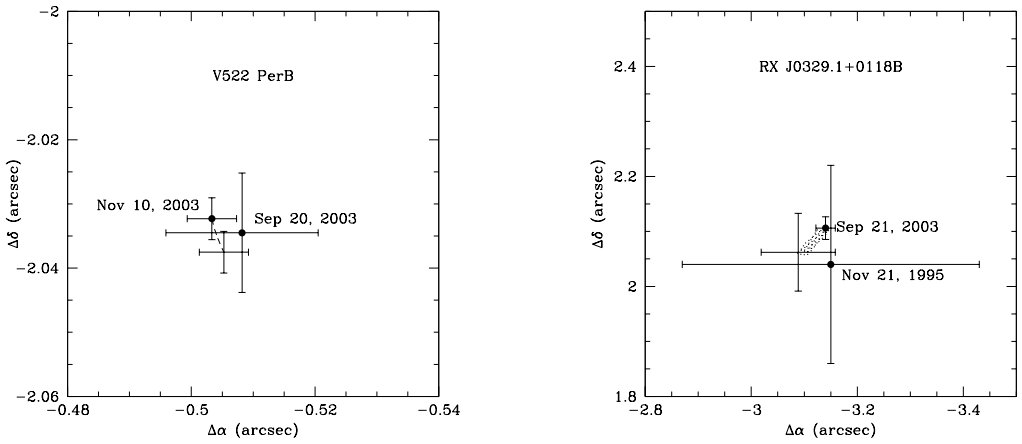

Figure 3.12: Same as Figure 3.10 for the companions to V522 Per (*left*) and RX J0329.1+0118 (*right*). The November 21, 1995, data point for the companion to RX J0329.1+0118 is from Sterzik et al. (1997) and is set to be at the mean epoch of their observations (November 19–23, 1995). The proper motion of the primaries between the observation epochs are too small to decide the physical association of the companions within the astrometric errors. The probability of association in each system is estimated from near IR spectroscopy (§3.3.4.1).

two epochs. This may explain the observed discrepancy of $0.64^\circ \pm 0.47^\circ$ in position angle between the two observations, while the change in separation (2.4±5.8 mas) is consistent with being zero. Future observations spanning a sufficiently long time-line may be used to determine the dynamical mass of the HD 49197A/B system.

3.3.3.2.2 HD 129333

The offset positions of the companion to HD 129333 in the two observations taken 16 months apart are fully consistent with each other and are inconsistent with the object being a background star (Figure 3.11). HD 129333B thus shares the proper motion of the primary and is a bona fide companion.

3.3.3.2.3 V522 Per and RX J0329.1+0118

The astrometry for these two systems (Figure 3.12) is inconclusive because of their smaller proper motions, insufficient time-span between the observations, and/or less accurate astrometry. The likelihood of physical association of the companions with the primaries is investigated from low-resolution spectroscopy in §3.3.4.1 below.

3.3.3.3 Spectroscopy

Infrared spectral classification of M–L dwarfs is done most successfully in the J and H bands, where a suite of indices based on the relative strengths of H_2O, FeH, K I, and Na I absorption have been developed to characterize their effective temperatures (Slesnick, Hillenbrand, & Carpenter, 2004; Geballe et al., 2002; Gorlova et al., 2003; McLean et al., 2003) and surface gravities (Gorlova et al., 2003). However, spectroscopy of cool companions in the bright halos of their primaries is often more difficult at J and H than at K because of larger flux contrast and poorer quality of the AO correction at shorter wavelengths. Here we present J-band spectra of the two brighter companions: HD 129333B and V522 PerB.

Cool dwarfs can be classified at K band based on the strength of their H_2O absorption shortward of 2.05μm, the depth of the CO 2.29μm bandhead, and the equivalent width (EW) of the Na I 2.21μm doublet (Kleinmann & Hall, 1986; Ali et al., 1995; McLean et al., 2003; Slesnick et al., 2004). Even cooler, late-L and T dwarfs are best characterized by the strength of their CH_4 absorption at >2.20μm (Burgasser et al., 2002; McLean et al., 2003). We present K-band spectra of all four companions discussed in this paper.

Spectral types of the detected companions have been determined following infrared absorption line classification systems at K-band (for Na I Ca I CO) from McLean et al. (2003, spectral types M6V–T8) and Ali et al. (1995, F3V–M6V), and at J-band (for K I and Ti I from Gorlova et al. (2003, M4V–L8) and Wallace et al. (2000, O7–M6)). Luminosity classes are based on the relative strengths of Na I, Ca I, and CO absorption at K band (Kleinmann & Hall, 1986) and on the strengths of Mn I and K I absorption at J (Wallace et al., 2000; Gorlova et al., 2003).

We have avoided the use of temperature-sensitive H_2O indices that span large fractions of the spectrum ($\gtrsim$4% total band width, e.g., the H_2OD index of McLean et al. (2003), or the H_2O-2 index of Slesnick et al. (2004)) because of their strong dependence on the overall continuum shape of the spectrum and because of the uncertainties in the spectral shapes of faint companions extracted from the halos of bright objects (§3.3.2.3). We have used the J-band 1.34 μm H_2O index of Gorlova et al. (2003), however, which measures only the onset of H_2O absorption at that wavelength and is narrow (1.4% band width).

Below we analyze the K- and J-band spectra of the companions to HD 49197, HD 129333, V522 Per, and RX J0329.1+0118. The inferred effective temperatures and spectral types are provided in Tables 3.6 and 3.7.

*3.3.3.3.1 **K**-band Spectroscopy of HD 49197B*

Our spectrum of HD 49197B (Figure 3.7) shows strong CO and H_2O bands characteristic of ultra-cool dwarfs, but lacks a CH_4 absorption feature, indicating

Table 3.6: Spectroscopic Measurements for the Companions

Star	EW(Na I[a] (Å)	EW(Ca I)[a] (Å)	EW(CO)[a] (Å)	EW(K I)[b] (Å)	H_2O index[b]	$T^{c}_{\rm eff,Ca}$ (K)
HD 49197B	-0.3 ± 0.6	0.2 ± 0.4	0.82 ± 0.05[d]	···	···	<3000
HD 129333B	5.17 ± 0.59	4.79 ± 0.64	7.26 ± 0.57	2.18 ± 0.11	···	3660
V522 PerB	5.87 ± 0.58	3.11 ± 0.50	5.67 ± 0.38	1.07 ± 0.16	0.91 ± 0.01	3200
RX J0329.1+0118B	6.76 ± 0.60	3.81 ± 0.39	8.63 ± 0.17	···	···	3300

[a] At K band as defined by Ali et al. (1995).

[b] At J band as defined by Gorlova et al. (2003).

[c] Calculated from empirical relations relating $T_{\rm eff}$ to EW(Ca I) (Table 4 in Ali et al., 1995). The sign of the linear coefficient in the Ca I "cool" relation of Ali et al. has been changed from '–' (as erroneously listed in their paper) to '+' to match the slope of their empirical data. Ali et al. quote an error of ±300 K for this index.

[d] The CO index for HD 49197B is not in Å, but as defined by McLean et al. (2003).

Table 3.7: Estimated Properties of the Companions

Objects	Spectral Type	Mass ($M_\odot$)	Projected Separation (AU)	Probability of Chance Alignment
HD 49197B	L4 $\pm$ 1[a]	$0.060^{+0.012}_{-0.020}$	43	3×10^{-6}
HD 129333B	M2 $\pm$ 1[b]	$0.20^{+0.30}_{-0.08}$	25	3×10^{-6}
V522 PerB	M4 $\pm$ 1[b]	0.125 ± 0.025	400	2×10^{-3}
RX J0329.1+0118B	M3 $\pm$ 2[b]	$0.20^{+0.30}_{-0.10}$	380	9×10^{-4}

[a] Inferred from the K-band spectrum and from the absolute magnitude of the object (§3.3.3.3.1).

[b] Based on the estimate of the Ca I-derived effective temperature (Table 3.6) and on the J-band K I and H_2O absorption (if available). A MK spectral type vs. $T_{\rm eff}$ classification for dwarfs is adopted from Bessell (1991).

that it is earlier than L8 (Geballe et al., 2002). On the other hand, Na I absorption is also absent from the spectrum, pointing to a spectral type of L3 or later (McLean et al., 2003), independent of gravity (cf. Figure 8 in Gorlova et al., 2003). Following the analysis of $R{\sim}2000$ K-band spectra of M6–T8 dwarfs in McLean et al. (2003), we form a CO absorption index from the ratio of the median flux in an absorbed (2.298–2.302 μm) vs. an unabsorbed (2.283–2.287 μm) region of the spectrum. We find CO=0.80±0.03 (where the error has been estimated as the quadrature sum of the relative uncertainties of the median in the two spectral regions), which indicates a spectral type of L7 or later. However, the CO index is not very sensitive to L-dwarf temperatures and varies by up to 0.15 (60% of its total range of variation between spectral types M5 and T2) within the same spectral type (Figure 13 in McLean et al., 2003).

Alternatively, we can also use the absolute K_S-band magnitude of HD 49197B to estimate its spectral type, following the empirical relation of Kirkpatrick et al. (2000), based on a sample of 24 M and L dwarfs with measured parallaxes:

$$M_{K_S} = 10.450 + 0.127(\text{subclass}) + 0.023(\text{subclass})^2, \tag{3.1}$$

where subclass = −1 for M9 V, 0 for L0 V, 1 for L1 V, etc. The scatter about the fit is approximately 1 subclass. From the inferred apparent K_S magnitude of HD 49197B, and from the parallax of the primary, we obtain $M_{K_S} = 11.04 \pm 0.24$ for the secondary, which corresponds to a spectral type of L3±1.5.

We assign a final spectral type of L4 with an uncertainty of 1 subclass. This is based on the intersection of the results from our spectroscopic analysis, suggesting L3–L7, and from the K_S-band absolute magnitude, pointing to L1.5–L4.5. A spectral type of L4±1 for HD 49197B is also consistent with a by-eye comparison of its K-band spectrum with the grid of L-dwarf standards from Leggett et al. (2001).

*3.3.3.3.2 **K**-band Spectroscopy of HD 129333B, RX J0329.1+0118B, and V522 PerB*

We classify the K-band spectra of these companions following the analyses of Ali et al. (1995) and Kleinmann & Hall (1986), whose data are taken at similar resolutions to ours (R=1380–3900 and 2500–3100, respectively), and span the F8–M7 spectral type range. We employ the spectral classification sequence of Ali et al., whose empirically-derived indices are based on a larger sample of dwarf stars than in Kleinmann & Hall.

Our reduced spectra were first shifted to 0 km s^{-1} heliocentric velocity, where the shift was determined by fitting Gaussian profiles to the Na I doublet, and comparing the fitted line centers to their values in the solar spectrum (Mohler, 1955). For consistency with the Ali et al. (1995) spectral classification, we have chosen the same bands for integrating the Na I (2.21μm), Ca I (2.26μm), and ^{12}CO(2–0) (2.29μm) absorption. The continuum in the target spectra was fit to three regions devoid of absorption lines: 2.0907–2.0951μm, 2.2140–2.2200μm, and 2.2873–2.2925μm. These have been selected as a combination of the continuum regions used by Ali et al. (1995) and Kleinmann & Hall (1986), so as to constrain the fit on both sides of the Na I doublet (as in Kleinmann & Hall, 1986, where the continuum-fitting regions are widely separated from the Na I lines), as well as near it (as in Ali et al., 1995, where the continuum is constrained only on the long-wavelength side of the Na I lines).

The absorption strength in each band was obtained as an equivalent width, by integrating the profile of the spectrum in the band with respect to a global continuum level defined by the three continuum bands. The only exception is the EW of the ^{12}CO(2–0) first overtone bandhead, for which we have adopted the mean continuum level of the third continuum band (as in Kleinmann & Hall, 1986 and Ali et al., 1995). The one-sigma errors in the EWs were calculated by propagating the r.m.s. noise of the spectrum in the nearest continuum band, assuming independent pixel variances. The EWs of Na I and Ca I were corrected for corresponding absorption in the spectra of the telluric standards, the EW of

which (0.84±0.57 Å for Na I and 1.14±0.36 Å for Ca I in G stars; Ali et al., 1995) was added to that measured for the companions. The final EWs are listed in Table 3.6.

To infer effective temperatures for the companions to HD 129333, RX J0329.1+0118, and V522 Per, we employ empirical relations between the strength of K-band Na I, Ca I, and CO absorption and effective temperature ($T_{\rm eff}$), as determined by Ali et al. (1995, their Table 4). Na and CO produce the most characteristic K-band features of cool stars. However, their absorption strengths are inaccurate tracers of temperature for stars cooler than 4000 K, and are, in addition, gravity-sensitive (Kleinmann & Hall, 1986; Gorlova et al., 2003). On the other hand, Ca I transitions in the K-band require the population of higher energy states and hence are more temperature-sensitive. However, their absorption strength is degenerate with the stellar effective temperature: Ca I absorption at 2.26μm peaks at ∼3500 K, and decreases for higher and lower effective temperatures (Kleinmann & Hall, 1986; Ali et al., 1995). This behavior is fit via two separate $T_{\rm eff}$ vs. EW(Ca I) relations in Ali et al. (1995). By combining the information from Ca I with that from Na I and ^{12}CO(2–0), we can break this degeneracy and use the more temperature-sensitive Ca I index to constrain the effective temperature for each star to within ∼300 K (the quoted uncertainty of the Ca I index in Ali et al., 1995). For HD 129333B, with a Ca I absorption strength near the breaking point between the "hot" and "cool" relations, we take the average of the two estimates. For V522 PerB and RX J0329.1+0118B, whose Na I and CO absorption is indicative of temperatures $T_{\rm eff} < 3400$ K, we use only the "cool" relation. The effective temperatures inferred from Ca I absorption are listed in Table 3.6. As in Ali et al. (1995), we adopt a spectral type vs. effective temperature classification for M dwarfs from Bessell (1991) and obtain spectral types of M1, M3, and M4 for HD 129333B, RX J0329.1+0118B and V522 PerB, respectively, with an uncertainty of 2 spectral subtypes. A visual inspection and comparison of the strengths of the various absorption features with K-band spectral sequences from Leggett et al. (2001) and Wallace & Hinkle (1997) confirm these results. Given the comparable

values of their Na I and ^{12}CO(2–0) EWs, all stars have likely dwarf gravities (cf. Figure 7 in Kleinmann & Hall, 1986).

*3.3.3.3.3 **J**-band Spectroscopy of HD 129333B and V522 PerB*

We further constrain the spectral types of HD 129333B and of V522 PerB from their J-band spectra. These show the characteristic absorption features of M stars: K I lines at 1.169μm, 1.177μm, 1.243μm, and 1.252μm, Fe I at 1.188μm and 1.197μm, Na I at 1.268μm, Al I at 1.312μm and 1.315μm, and H_2O absorption at $\lambda > 1.34\mu$m (Figure 3.8). The spectrum of V522 PerB exhibits also Ti I and Mn I absorption over 1.282–1.298 μm. Spectral classification at J band was done based on the depth of the H_2O and K I absorption, following the index definitions of Gorlova et al. (2003). After re-sampling our data to match the $R\approx350$ spectral resolution of Gorlova et al., we form the 1.34μm water index as the ratio of the mean fluxes (in a 0.004 μm wide region) at 1.336μm and at 1.322μm, and we measure the K I EW by integrating the absorption over the region 1.2375–1.2575μm. Because K I absorption in the solar-like photospheres of the telluric standards is small ($EW(\text{K I}\lambda1.14\mu\text{m}) \approx 0.1 \times EW(\text{Na I}\lambda2.21\mu\text{m}) = 0.08$ Å for the Sun; Mohler, 1955; Ali et al., 1995), the K I EW measurements of the companions were not corrected for it.

For HD 129333B, we cannot estimate the strength of the 1.34μm water absorption because of insufficient spectral coverage. The EW of K I indicates a spectral type of M2–M4. Averaging this with our K-band estimate of M1±2, we assign a spectral type of M2±1 for HD 129333B. Given the youth of HD 129333 (<120 Myr; see §3.3.4.2), the companion may have lower-than-dwarf gravity. The effect of this on alkali absorption lines in the near IR is degenerate with temperature (Gorlova et al., 2003; McGovern et al., 2004) and could be compensated by a later spectral type. However, spectral types later than M3 are inconsistent with the depth of the strongly temperature-sensitive Ca I absorption in this star (§3.3.3.3.2). In addition, HD 129333B lacks noticeable Mn I absorption, which is weak in M dwarfs but grows deeper with decreasing surface gravity in M stars (Fig. 9 in Wallace

et al., 2000). Hence, we conclude that HD 129333B is a M2±1 dwarf.

For V522 PerB, both the K I EW and the water absorption index point to a spectral type of M3–M5, in agreement with our K-band estimate (M4±2). The stronger Ti I absorption than in HD 129333B is also consistent with a cooler photosphere. We thus assign a spectral type of M4±1 to V522 PerB. The strength of the Mn I transition indicates a potentially subgiant surface gravity, though as noted in §3.3.3.3.2, the effect is not seen at K band.

3.3.4 Discussion

3.3.4.1 Likelihood of Physical Association

Our astrometric follow-up of HD 49197B and HD 129333B confirmed common proper motion between these two companions and their respective primaries. However, the smaller proper motions of V522 Per and RX J0329.1+0118 prevented us from concluding the same for their respective companions, given the time-span of our observations. The probability of physical association in these systems can be inferred from the spectroscopically determined spectral types and absolute magnitudes of the companions. If the absolute magnitude inferred from the spectral type of a companion agrees with its measured apparent magnitude at the heliocentric distance of the respective primary, then the companion is likely to be a bona fide one (modulo the space density of stars of similar spectral type as the companion).

Figure 3.13 presents a comparison of the spectroscopic vs. photometric absolute magnitudes. The correspondence is good for the four companions followed up via near IR spectroscopy, indicating that they are at similar heliocentric distances as their primaries and are thus likely to be physically bound to them. The location of the remaining candidate companion (HD 49197"C") along the ordinate is inferred from its near-IR colors. As mentioned in §3.3.3.1, HD 49197"C" is a likely F–G star ($2.0 \leq M_K \leq 4.0$; Cox, 2000), i.e., it is intrinsically too bright to be associated with HD 49197 (F5 V) given its faint apparent magnitude.

A robust statistical analysis of the likelihood of chance alignment in the four

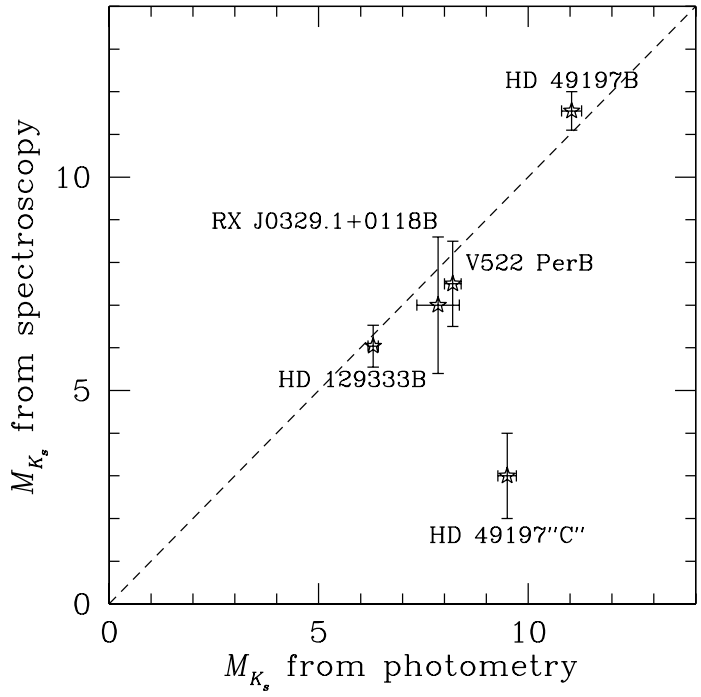

Figure 3.13: Comparison of the photometrically derived absolute K_S-band magnitudes of the companions (assuming the heliocentric distances of the corresponding primaries) to the spectroscopically inferred ones. The dashed line has a slope of unity. The location of HD 49197"C" (of which no spectra were taken) along the vertical axis is based on a spectral type (F–G) inferred from its near IR colors (§3.3.3.1). HD 49197"C" is intrinsically too bright to be at the same heliocentric distance as HD 49197, whereas the remainder of the companions are consistent with being at the distances of their respective primaries.

systems discussed here is not yet possible at this stage of the survey. They are only a fraction of the ones discovered to have candidate companions. With follow-up observations still in progress, the exact number of bound systems is unknown. We defer a discussion of the companion chance alignment probability based on the full ensemble statistics until a later paper. Here we consider these probabilities only on a per system basis. To give an approximate idea of the limited statistics from which these preliminary results are extracted, we point out that to date we have analyzed multi-epoch astrometric data for approximately 15 stars (mostly from the deep survey) with faint ($\Delta K_S > 3$, i.e., expected to be of spectral type M or later) companions within $4''$.

We base our calculation of the probability of false association in each system on the empirically determined spatial density of cool objects (M–T spectral types) in the solar neighborhood. There are 112 such known objects in the northern ($\delta > -20^\circ$) 8 pc sample (Reid et al., 2003). The northern 8 pc sample covers 65% of the sky and is estimated to be ∼15% incomplete. The total number of cool objects and white dwarfs within 8 pc of the Sun is therefore expected to be 198, with a volume density of 0.10 pc^{-3}. This estimate is based on a small fraction of the thin disk population (scale height 325 pc; Bahcall & Soneira, 1980) of the Galaxy and hence should not vary substantially as a function of galactic latitude.

We then calculate the number of cool dwarfs expected to be seen in projection toward each system within a conical volume of radius $4''$ centered on the star, with the observer at the apex of the cone. We truncate the radial extent of the conical volume by requiring that the apparent K magnitude of a projected companion falls within the limits allowed by the spectral type (and hence, absolute magnitude) of the detected one. Absolute K magnitudes for the M2–4 dwarfs discussed here have been adopted from Bessell (1991). Although Bessell's M dwarf classification system pre-dates the discovery of ultra-cool dwarfs (later than M5), it remains valid for early M dwarfs. For L4±1 spectral types we adopt absolute K magnitudes from Dahn et al. (2002).

The expected number μ of unrelated cool dwarfs within the relevant volume

around each star is listed in the last column of Table 3.7. Given that for all stars $\mu \ll 1$, we can assume that the event of seeing an unrelated field object in the vicinity of one of our program stars is governed by Poisson statistics. Hence, the probability of finding one or more such dwarfs near any given star (i.e., the probability of chance alignment) is $1 - e^{\mu} \approx \mu$. As seen from Table 3.7, after having followed up the companions spectroscopically, we can claim with $\geq$99.99% certainty in each case that the companion is physically associated with its respective primary. As discussed above, such probabilities need to be regarded in the context of the ensemble statistics. Within our sample of 4 spectroscopically confirmed companions, the probability that at least one is a false positive is 3×10^{-3}. This exemplifies the power of spectroscopic follow-up as an alternative to multi-epoch astrometry in constraining the likelihood of physical association in a system.

3.3.4.2 Stellar Ages and Companion Masses

We estimate the ages of the primaries (Table 3.3) from published data on their chromospheric activity, Li I equivalent width, and kinematic association with young moving groups. Masses for each of the companions (Table 3.7) were determined either from the low-mass pre-main sequence evolutionary models of Baraffe et al. (1998) or from the brown-dwarf cooling models of Chabrier et al. (2000, "DUSTY") and Burrows et al. (1997). We have not used the dust-free "COND" models of Baraffe et al. (2003), since they are more appropriate for temperatures $\lesssim$1300 K (i.e., for T dwarfs) when all grains are expected to have gravitationally settled below the photosphere.

HD 49197B. From the strength of Ca H & K core emission in Keck/HIRES spectra of the primary, Wright et al. (2004) determine an age of 525 Myr for HD 49197, which we assume accurate to within $\approx$50%, given the variation in chromospheric activity of solar-type stars (Henry et al., 1996). No other age-related indicators exist in the literature for this F5 star. From our own high-resolution optical spectra, we measure EW(Li λ6707.8) = 80 mÅ (White et al., in preparation), consistent with a Pleiades-like (120 Myr; Stauffer, Schultz, & Kirkpatrick, 1998)

or older age. Hence, we adopt an age of 260–790 Myr for the primary. Assuming co-evality, the mass of the secondary is $0.060^{+0.012}_{-0.025} M_{\odot}$ (Burrows et al., 1997; Chabrier et al., 2000), where the range of masses accomodates the one sigma error in the inferred absolute magnitude of the secondary and the allowed age range for the primary. HD 49197B is thus a brown dwarf.

HD 129333B. The primary is a well-known young star, kinematically belonging to the Local Association (Pleiades moving group, 20–150 Myr; Soderblom & Clements, 1987; Montes et al., 2001b). Results from the Mount Wilson spectroscopic survey (Soderblom, 1985) and from the Keck/Lick r.v. program (Wright et al., 2004) show strong Ca II H & K emission, indicating high levels of chromospheric activity and youth. Wright et al. list an age of <10 Myr for this star, though the chromospheric activity-age relation is not reliable for stars that young, in part because of the large variance in rotation rates of stars younger than 50–80 Myr (e.g., Soderblom et al., 1993) and because the relation is not calibrated at such young ages. Montes et al. (2001a) report strong Li I absorption (EW(Li I) = 198 mÅ) and conclude that the star is "significantly younger" than the Pleiades (120 Myr; Stauffer et al., 1998). Assuming an age of 10–100 Myr for the system, we estimate the mass of the secondary at $0.20^{+0.30}_{-0.08} M_{\odot}$ (from models of Baraffe et al., 1998).

V522 PerB. The primary is a member of the α Per open cluster, confirmed by photometry, kinematics, and spectroscopy (Prosser, 1992). From high-resolution spectroscopy and determination of the lithium depletion boundary in the cluster, Stauffer et al. (1999) determine an age of 90±10 Myr, consistent with a recent age estimate from upper main-sequence turn-off fitting (Ventura et al., 1998). Using the Lyon group stellar evolution models (Baraffe et al., 1998), we determine a mass of 0.085–0.15 $M_{\odot}$ for the secondary. However, from their sub-stellar "DUSTY" code (Chabrier et al., 2000), the treatment of dust opacity in which may be more appropriate for this cool (∼3200 K) star, we find that its mass is ≥0.10 $M_{\odot}$. We thus estimate 0.10–0.15 $M_{\odot}$ for the mass of V522 PerB.

RX J0329.1+0118B. Neuhäuser et al. (1995) list RX J0329.1+0118 (G0 IV) as a fast-rotating ($v \sin i$ = 70 km/s) X-ray source south of Taurus, with a Li I equivalent width of 110 mÅ: all indicators of relative youth. Assuming a common origin and distance with the stars in the Taurus molecular cloud (140 pc; Kenyon, Dobrzycka, & Hartmann, 1994), the authors claim that its bolometric luminosity is higher than that of a zero-age main-sequence star, and the star is therefore likely in the pre-main sequence (PMS) phase. From a proper-motion survey of PMS stars in Taurus-Auriga, however, Frink et al. (1997) find that the young stars south of Taurus discussed in Neuhäuser et al. (1995) are kinematically unrelated to those in Taurus, and that star formation in the two complexes must have been triggered by different events. From the Pleiades-like Li I equivalent width of RX J0329.1+0118, we assign an age of ≈120 Myr for this star. Given the spectral type of the secondary, its mass is $0.20^{+0.30}_{-0.10} M_{\odot}$ (Baraffe et al., 1998).

3.3.4.3 HD 129333: Binary or Triple?

The existence of a stellar companion to HD 129333 has already been inferred in the r.v. work of Duquennoy & Mayor (1991, DM91), who find that the star is a long-period single-lined spectroscopic binary (SB1). From their derived orbital parameters, the authors determine a secondary mass $M_2 \geq 0.37 M_{\odot}$ and suggest that the star be targeted with speckle interferometry to attempt to resolve the companion. We should therefore consider whether the companion that we have resolved (and named HD 129333B) is identical to the spectroscopically inferred one.

3.3.4.3.1 The Combined Radial Velocity and Astrometric Solution

Combining r.v. and astrometric data presents a powerful approach to fully constrain all the orbital elements of a binary system. In this Section we test the hypothesis that the DM91 and the imaged companions are identical by attempting to solve for the parameters of the relative orbit and checking for consistency with all available data.

The orbital parameters that can be determined through r.v. monitoring of an SB1 are the eccentricity e, the period P, the epoch T_0 of periastron, the longitude ω of periastron, the systemic radial velocity $v_{\rm rad,0}$, and the primary velocity semi-amplituide K_1. K_1 is related to the other orbital parameters through the mass function:

$$f(M) = \frac{(M_2 \sin i)^3}{(M_1 + M_2)^2} = \frac{(1-e^2)^{3/2} P K_1^3}{2\pi G}, \tag{3.2}$$

where $M_{1,2}$ are the component masses, i is the inclination of the orbit with respect to the observer, and π and G are constants (e.g., Heintz, 1978, p.80). The orbital inclination i cannot be constrained from r.v. monitoring; hence the masses and the semi-major axes $a_{1,2}$ of the binary components are degenerate with i.

From astrometric observations we can fit for e, P, T_0, ω, i, $a_{1,2}$ (and hence, $M_{1,2}$), and for the only remaining parameter—the longitude of the ascending node Ω. Therefore, by performing a least-squares fit to the combined and appropriately-weighted r.v. and astrometric data, one can fully determine the orbit of a binary and attain greater precision in estimating the orbital elements (Morbey, 1975).

We first list the orbital parameters that have been already determined. Based on the r.v. measurements shown in Figure 3.14, DM91 find $e = 0.665 \pm 0.023$, $T_0 =$ JD 2446932$\pm$20 = year 1987.37, $\omega = 188.0 \pm 5.2^\circ$, $K_1 = 5.09 \pm 0.20$ km s^{-1}, and $P = 4575$ days = 12.53 years. DM91 state, however, that the period is probably accurate only "to the nearest unit of $\log P$" (i.e., $10^{3.5} < P < 10^{4.5}$ days, or between 8.7 and 87 years) and calculate the uncertainties in e, T_0, ω, and K_1 for a fixed P. Nevertheless, because of the high eccentricity of the orbit and because of their adequate observational coverage of the star near r.v. minimum, the final values of these three parameters are not expected to be significantly different. Assuming that the r.v. and the resolved companions are the same, we impose the additional constraints derived from our astrometric observations, namely, the separation ρ and position angle ϕ between the binary components on 2003 May 13 ($T =$ JD 2452772 = year 2003.36). Given the long (multi-year) orbital period and the small change (insignificant within the error bars) between our two relative as-

trometric observations taken four months apart, we only use one of the astrometric measurements. Finally, we adopt a mass of 1.05 $M_{\odot}$ for the G0 V primary, based on an estimate from Dorren & Guinan (1994).

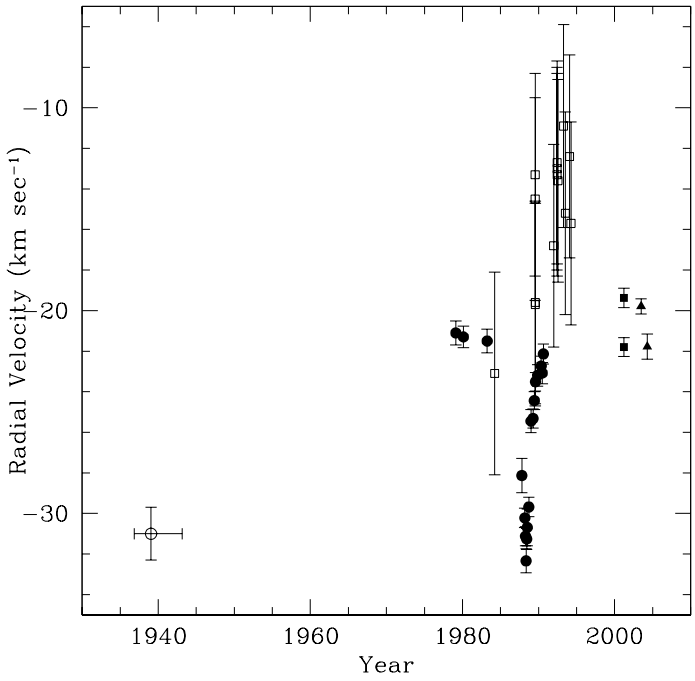

Figure 3.14: Radial velocity data for HD 129333 from the literature. Data from DM91 are plotted as filled circles, from Dorren & Guinan (1994) as open squares, from Montes et al. (2001a) as filled squares, and from Wilson & Joy (1950) as an open circle. Our own unpublished r.v. data are shown as solid triangles. The exact epoch of the Wilson & Joy observation is unknown. Given the DM91 orbital solution and the current phase coverage, periods <16 years can be excluded.

The equation that determines the binary orbit is Kepler's equation:

$$E - e \sin E = \frac{2\pi}{P}(T - T_0), \tag{3.3}$$

where the eccentric anomaly E is related to the true anomaly θ through:

$$\tan\frac{\theta}{2} = \left(\frac{1+e}{1-e}\right)^{1/2} \tan\frac{E}{2}. \tag{3.4}$$

The remaining equations are:

$$P = 2\pi\sqrt{\frac{a^3}{G(M_1+M_2)}} \tag{3.5}$$

$$r = a(1 - e\cos E) \tag{3.6}$$

$$\rho^2 = r^2(1 - \sin^2(\theta+\omega)\sin^2 i) \tag{3.7}$$

$$\tan\Omega = \frac{\tan\phi - \tan(\theta+\omega)\cos i}{1 + \tan\phi\tan(\theta+\omega)\cos i}. \tag{3.8}$$

Because the orbital period of HD 129333 is poorly constrained by DM91, we choose to treat P as a free parameter. Thus, the unknown parameters are eight: P, M_2, i, a (the semi-major axis of the relative orbit), Ω, E, the radius vector $r(T-T_0)$, and the true anomaly $\theta(T-T_0)$ of the companion in the relative orbit at time $T-T_0$. From the combined imaging and r.v. data we have imposed seven constraints: $\rho(T-T_0)$, $\phi(T-T_0)$, e, ω, M_1, K_1, and $T-T_0$. Given that the number of unknowns is greater than the number of constraints, we cannot solve unambiguously for the parameters, let alone use a least-squares approach to determine their best-fitting values. However, by stepping through a grid of constant values for one of the parameters, we can determine the rest.

We choose M_2 as our step parameter for the grid, treating it as a known parameter. In principle we can use Equations 3.4–3.7 to express P in terms of M_2, E, and the known variables, and then substitute this expression in Equation 3.3, which can be solved for E. However, because of the complexity of the general functional form $P(M_2, E, \rho, \phi, e, \omega, M_1, K_1, T-T_0)$ and because Kepler's equation cannot be solved analytically, we employ a two-stage iterative approach. In the outer iteration, for a given value of M_2 we converge upon a solution for P, and in the inner iteration we use the Newton-Raphson method to solve Kepler's equation for E. The iterative Newton-Raphson method has been described in detail else-

where (e.g., Press et al., 1992), so we do not discuss it further. The convergence of the outer iteration loop however merits a brief description.

We take an initial estimate P_0 for the period and invert Equation 3.2 to obtain a numerical value for $\sin i$ as a function of P and M_2. From Equations 3.4–3.7 we then express P in terms of the known parameters plus M_2, E, and $\sin i$, and plug that expression in Equation 3.3, which is then easier to solve for E. Once E is obtained, we invert Kepler's equation to find a solution $P = P_1$ for the orbital period that depends on the initial guess P_0. We repeat the above procedure by substituting P_1 for P_0, and so forth until the values P_j converge. We stop when the value of P is constrained to better than 0.1%, which usually occurs after 3–4 iterations. Because of the monotonic dependence of the orbital elements i, a, and E on P, we can be certain that the thus-obtained solution for P is unique.

Following the above procedure and adopting the DM91 values for e, T_0, and K_1, we find that if the resolved companion is identical to the r.v. one, its mass is at least $0.68 M_\odot$, with a corresponding period of 50.0 years, $a = 16.3$ AU, and $i = 85°$. Values as small as $M_2 = 0.58 M_\odot$ ($P = 42.8$ years, $a = 14.4$ AU, $i = 84°$) are possible if all parameters are set at their one-sigma deviations that minimize M_2.

However, a minimum mass of $\approx 0.58 M_\odot$ for HD 129333B does not agree with the constraint from our IR spectroscopy, $M_2 \leq 0.50 M_\odot$ (§3.3.3.3, §3.3.4.2), obtained from comparison to theoretical evolutionary tracks from Baraffe et al. (1998). Moreover, a companion with mass $M_2 \geq 0.58 M_\odot$ (spectral type K8 or earlier; Cox, 2000) would be too bright in absolute magnitude ($M_K \leq 5.1$; Bessell, 1991) to be identified with HD 129333B ($M_{K_S} = 6.30 \pm 0.12$, from its apparent magnitude and from the *Hipparcos* distance to HD 129333). It is therefore likely that the r.v. and the spectroscopic companion are not identical.

The inconsistency between the masses could be explained by noting that a recent study of low-mass binaries by Hillenbrand & White (2004) has shown that most modern stellar evolutionary models tend to underestimate dynamical masses of main and pre-main sequence stars. According to the authors, the Baraffe et al.

(1998) models underestimate the mass of a $0.5M_{\odot}$ main sequence star by ≈20%. This could reconcile the limits on the mass of HD 129333B obtained from near IR spectroscopy with those from the orbital solution. However, the problem of the companion being sub-luminous remains.

3.3.4.3.2 Comparison to Other Radial Velocity Data

The DM91 set of r.v. data are the most accurate and deterministic for the orbit of HD 129333. Other data exist from Wilson & Joy (1950), Dorren & Guinan (1994), Montes et al. (2001a), and our own high-resolution spectroscopic observations[6] (Figure 3.14); however, they do not improve the orbital phase coverage greatly. Although Dorren & Guinan (data plotted as open squares) appear to have captured the binary near an r.v. maximum around 1993, their data are less restrictive because of their large uncertainties. In addition, the Dorren & Guinan data for 1990 systematically overestimate the r.v. of the primary with respect to DM91 data taken over the same period. We therefore choose to disregard the Dorren & Guinan data set. The remaining data are very limited, and we do not attempt to use them to re-fit the DM91 orbital solution. However, they are of some utility in constraining the orbital period.

Because no other r.v. minimum is observed for HD 129333 between 1987.37 and 2003.36, we conclude that $P > 16$ years. The Wilson & Joy data point (based on three measurements) is consistent with an r.v. minimum and is thus critical in constraining the orbital period. However, the authors do not list an epoch for the observations. The Wilson & Joy data were taken in the course of the Mt. Wilson stellar spectroscopic survey and are kept in the Ahmanson Foundation Star Plates Archive[7]. After consultation with the original plates, we retrieve the dates of the individual observations: 1936 March 10 (year 1936.19), 1936 Jun 4 (year 1936.42), and 1942 Jun 24 (year 1942.48). We adopt the mean date of these

[6] $v_{\rm rad} = -19.79 \pm 0.37$ km s^{-1} and -21.77 ± 0.62 km s^{-1} on 2002 April 18 and 2003 February 10, respectively (Hillenbrand et al., in prep.).

[7] Maintained at the Carnegie Observatories of Washington, Pasadena, California.

observations, the year $1938.4^{+4.1}_{-2.2}$, as the epoch for the Wilson & Joy measurement $v_{\rm rad} = -31.0 \pm 1.3$ km s^{-1}, where the errors in the epoch correspond to the interval between their first and last observation. Because of its highly eccentric orbit, the star must have been within 1 year of r.v. minimum at this epoch. Given the r.v. minimum in 1987.37 and $P > 16$ years, we infer that the r.v. companion has a likely orbital period equal to the interval between the two observed minima, or to some integer fraction thereof: $49.0^{+2.4}_{-4.2}$ years, $24.5^{+1.2}_{-2.1}$ years, or $16.3^{+0.8}_{-1.4}$ years (all consistent with the DM91 estimate).

The 49-year orbital period agrees with the one obtained in §3.3.4.3.1 and supports the evidence that the r.v. and the resolved companion may be identical. If the r.v. companion was on a 24.5-year period ($a = 9.8$ AU, from the DM91 orbital elements), it would have been $\gtrsim 0.33 - 0.44''$ from the primary during our imaging in 2003, with mass $M_2 \geq 0.47 M_\odot$. Such a companion should have been at least as bright as the resolved one ($\Delta K_S = 3.0$), although could have fallen just below our detection limits ($\Delta K_S \approx 3.0$ at $0.4''$) if it was at the lower limit of the allowed mass range. Given $q = M_2/M_1 \geq 0.46$ in this case, the star should be easily detectable as a double-lined spectroscopic binary (SB2) through high-resolution spectroscopy in the near IR, where the contrast favors detecting SB2 systems with mass ratios as small as 0.2 (Prato et al., 2002). A 16.3-year period can most probably be excluded, since the 2003 data point does not indicate an approaching r.v. minimum (Figure 3.14) in late-2003–2004, as would be expected at this periodicity.

Therefore, even after consideration of additional archival r.v. data, the question about the multiplicity of HD 129333 remains open. The system can be either a binary with a 14–16 AU semi-major axis (but a discrepancy in the inferred mass of the secondary) or a triple with a 10 AU inner (spectroscopic) and ∼25 AU outer (resolved) components. Indeed, SIMBAD does list HD 129333 as a BY Dra variable, which may indicate that the high level of chromospheric activity arises from close binarity, rather than extreme youth. However, the high photospheric Li I abundance of HD 129333 and its kinematic association with the Pleiades moving group (§3.3.4.2) confirm its young age. Moreover, at 10 AU semi-major

axis the inferred spectroscopic companion is too distant to be synchronized with the rotation period of the primary (2.7 days; Dorren & Guinan, 1994) and to thus affect its chromospheric activity. An additional close-in component would be required that should produce a short-period SB1 or SB2 spectroscopic signature, as in binary BY Dra systems. Such is not reported by DM91, however.

In deciding whether a triple system with a 24.5-year period for the r.v. (inner) companion is a likely state for HD 129333, it is worth considering the dynamical stability of such a system. We adopt masses of 1.05 $M_{\odot}$, 0.5 $M_{\odot}$, and 0.2 $M_{\odot}$ for the primary, the inner, and the outer (resolved) companion, respectively, and apply a dynamical stability criterion from the numerical analysis of Donnison & Mikulskis (1995). Assuming prograde orbits, the Donnison & Mikulskis condition for stability as applied to HD 129333 states that the distance of closest approach of the outer companion to the barycenter of the system should be >27 AU. Variations in the masses of the two companions within the determined limits do not change this requirement by more than 3–5 AU. At a projected separation of 25.0 ± 1.5 AU from the primary, the resolved companion is fully consistent with this requirement. Hence, the system can be a dynamically stable triple.

3.3.4.4 HD 49197B: A Rare Young L Dwarf

Our empirical knowledge of the photospheres of young (<1 Gyr) L dwarfs is currently very limited. The only confirmed such dwarfs are all companions to main sequence stars: G 196–3B (L2, 20–300 Myr; Rebolo et al., 1998), Gl 417B[8] (L4.5, 80–300 Myr; Kirkpatrick et al., 2001), the pair HD 130948B/C (L2, 300–600 Myr; Potter et al., 2002), and now HD 49197B (L4, 260–790 Myr). It is useful to expand the sample of young L dwarfs in order to study gravity-sensitive features in their spectra and to provide constraints for evolutionary models of ultra-cool dwarfs.

Younger L dwarfs have been reported in several open clusters: σ Ori (1–8 Myr; Zapatero Osorio et al., 1999), the Trapezium (∼1 Myr; Lucas et al., 2001), and

[8]Gl 417B is itself considered to be resolved by Bouy et al. (2003) into two components with a 70 mas separation, equal to the diffraction limit of their *HST/WFPC2* observations.

Chameleon I (1–3 Myr; López Martí et al., 2004). However, these results have not been independently confirmed. The youth of σ Ori 47 (L1.5), and hence its association with the cluster, has been recently brought into question by McGovern et al. (2004), who find that the object shows strong K I absorption at J band, characteristic of several Gyr old field dwarfs. Lucas et al. (2001) determine M1–L8 spectral types for their objects in the Trapezium, using water indices defined for the $R \approx 30$ H-band spectra. They also use Burrows et al. (1997) sub-stellar evolutionary tracks to infer masses from IJH photometry. However, the deduced spectral types and the masses correlate very poorly—a result potentially traceable to the anomalous continuum shapes of their spectra (their Figure 4), some of which appear to contain residual telluric or instrument-transmission features (as seen in their Figure 1) that the authors interpret as photospheric water absorption. Finally, in their analysis of photometrically-identified brown dwarfs toward Chameleon I, López Martí et al. (2004) acknowledge that the classification of their early L dwarfs is uncertain, because their locus overlaps with that of extincted M-type objects on their color-magnitude diagram (Figure 8 in that paper).

Therefore, because of its association with a young star, HD 49197B is one of only five known young L dwarfs whose age can be determined with reasonable certainty. All five span a narrow range in spectral type: L2–L5. A program of uniform spectroscopic observations of these young L dwarf companions, undertaken in a manner similar to the NIRSPEC brown dwarf spectroscopic survey of McLean et al. (2003), promises to establish gravity-sensitive standards (as in Kleinmann & Hall, 1986, for F8–M7 stars) to use in determining the ages of isolated L dwarfs.

3.3.4.5 Sub-Stellar Companions to Main-Sequence Stars

Until recently, only a handful of brown dwarf companions to nearby A–M stars were known from direct imaging, all at angular separations $>4''$ (see compilation in Reid et al., 2001). With AO technology still in its early developing stages, ground-based direct imaging observations of main-sequence stars were sensitive mostly to massive, widely separated sub-stellar companions. From the observed dearth

of brown dwarf companions to main sequence stars at separations comparable to those in main sequence binaries, it was inferred that the radial-velocity "brown dwarf desert" (for separations $\lesssim$3 AU; Campbell et al., 1988; Marcy & Benitz, 1989; Marcy & Butler, 2000) extended to at least 120 AU (Oppenheimer et al., 2001) or 1200 AU (McCarthy, 2001; McCarthy & Zuckerman, 2004), with estimates for the brown dwarf companion frequency around 1% within this separation range. From 2MASS data, however, Gizis et al. (2001) found that the brown dwarf companion fraction was much higher ($\sim$18%) at separations >1000 AU from F–M0 dwarfs and was consistent with that of stellar companions to G stars (Duquennoy & Mayor, 1991). Though the Gizis et al. result is based on only 3 bound companions out of 57 then known field L and T dwarfs (a fourth bound companion, GJ 1048B, has now been confirmed in the same sample by Seifahrt, Neuhäuser, & Mugrauer, 2004), they exclude a brown dwarf companion fraction of 1.5% at the 99.5% confidence level. Such an abrupt change in the frequency of bound brown dwarfs at 1000 AU from main-sequence stars is not predicted by any of the current brown dwarf formation scenarios. More likely would be a continuously varying sub-stellar companion fraction from inside the r.v. brown dwarf desert at <3 AU out to distances >1000 AU.

Recent results from more sensitive space- and ground-based surveys point to a somewhat higher frequency of sub-stellar companions. In a survey of 45 young stars within $\sim$50 pc, the NICMOS Environments of Nearby Stars team has reported the discovery of 2 confirmed brown dwarfs, TWA 5B (Webb et al., 1999; Lowrance et al., 1999) and HR 7329B (Lowrance et al., 2000), and a probable third one: the binary companion Gl 577B/C, whose components likely span the stellar/substellar boundary (Lowrance et al., 2003). A similar survey of twenty-four 5–15 Myr old stars in the more distant ($\approx$150 pc) Scorpius-Centaurus association does not detect any plausible sub-stellar companions (Brandner et al., 2000). Even so, the fraction of stars with sub-stellar companions detected with NICMOS (2–3 out of 69) is markedly higher than the one reported from the two initial large-scale ground-based surveys (2 out of $\approx$390; Oppenheimer et al., 2001; McCarthy &

Zuckerman, 2004) and is inconsistent with the incompleteness-corrected estimate ($\leq$2%) of McCarthy & Zuckerman (2004). Furthermore, as a result of improvements in existing AO technology and the equipping of several large telescopes with newly-designed high-order AO systems, recent ground-based direct imaging efforts have been more successful in detecting close-in brown dwarf companions to Sun-like primaries: Gl 86B (Els et al., 2001), HD 130948B/C (Potter et al., 2002), HR 7672B (Liu et al., 2002), and HD 49197B (this paper). All of these are at angular separations $<3''$ and at projected distances $<$50 AU from their primaries and hence are inaccessible for imaging by McCarthy & Zuckerman (2004), whose survey targeted the 75–1200 AU separation range. Finally, with the natural guide star limit of AO systems being pushed to ever fainter magnitudes using curvature sensors (down to $\sim$16 mag at 0.8μm; Siegler et al., 2003), a number of very low-mass (VLM) binaries has become known, with separations as small as 1 AU. The components in these VLM binaries often straddle the stellar-substellar boundary (for a compilation, see Table 4 in Close et al., 2003).

The emergent picture from these recent discoveries is that of potential deficiency of brown dwarfs at 10–1000 AU separations from main sequence stars, though not as pronounced as in the r.v. brown dwarf desert (frequency $<$0.5%; Marcy & Butler, 2000). Based on one detection (of a binary brown dwarf companion) among 31 stars, Potter et al. (2002) set a lower limit of 3.2$\pm$3.2% for the frequency of brown dwarfs at 10–100 AU from main sequence stars. At separations $>$50 AU from the NICMOS discoveries (Lowrance et al., 1999, 2000) and from their newly-reported brown dwarf companion to the star GSC 08047–00232 in Horologium, Neuhäuser & Guenther (2004) report that brown dwarfs are found around 6$\pm$4% of stars. The outer scale for the Neuhäuser & Guenther (2004) estimate is not specified, but is probably limited to 1000–2000 AU by the FOV of high angular resolution IR detectors (up to $40''\times40''$; e.g., NICMOS, or ones used behind AO) and by the distances out to which young stars are probed for sub-stellar companions (out to 100–200 pc). By combining these estimates with the Gizis et al. (2001) estimate of 18$\pm$14% at separations $>$1000 AU, we can conclude that,

despite the small number statistics involved, there possibly exists a continuum in the frequency distribution of brown dwarf companions at separations ranging from within the r.v. brown dwarf desert ($\leq$3 AU) out to >1000 AU (where brown dwarf companions are as common as stellar ones). The observed decline in the rate of occurrence of directly imaged brown dwarf companions at small separations is likely at least partially an effect of the limited sensitivity of imaging surveys to close-in low-mass brown dwarfs. New, sensitive surveys for sub-stellar companions, such as the Palomar AO Survey of Young Stars, are poised to explore this regime in the next few years.

3.3.5 Conclusion

We have presented the observing strategy and first results from the Palomar Adaptive Optics Survey of Young Stars, aimed at detecting sub-stellar companions to <500 Myr solar analogs within 200 pc of the Sun. We have discovered low-mass (0.04–0.5 $M_{\odot}$) companions to 4 young nearby stars. The L4$\pm$1 brown dwarf HD 49197B and the M2$\pm$1 V star HD 129333B have been confirmed as companions to their corresponding primaries through follow-up astrometry and spectroscopy. Physical association in the V522 Per and RX J0329.1+0118 systems, containing respectively M4$\pm$1 and M3$\pm$2 secondaries, has been established with >99.95% confidence from spectroscopy and from the expected space density of objects of similar spectral type.

The astrometry for the resolved stellar companion to HD 129333 is found to be consistent with archival r.v. data for this single-lined spectroscopic binary, indicating that the resolved and the r.v. companions may be identical. Given the inferred mass constraints on the secondary, however, the companion is then underluminous by at least 1 mag at K_S. A solution in which the star is a triple is also likely. It does not suffer from similar inconsistencies and could be dynamically stable. Because the expected mass ratio between the inner two companions of the triple is $\geq$0.46, they should be resolved as a double-lined spectroscopic binary from high resolution infrared spectroscopy. In either case HD 129333 is confirmed to

be a multiple star and hence not a true analog of the young sun, as previously considered (e.g., Dorren & Guinan, 1994; Strassmeier & Rice, 1998).

The newly-discovered brown dwarf HD 49197B is one of a very few confirmed young (<1 Gyr) L dwarfs. It is also a member of a small number of brown dwarf companions imaged at projected separations of <50 AU from their host stars, i.e., at distances comparable to the giant-planet zone in the Solar System. The number of such companions, albeit small, has been growing steadily in recent years with the results of more sensitive imaging surveys coming on-line. Longer duration radial velocity surveys and improvements in AO techniques are expected to further push the detection limits of each method to the point where their sensitivities overlap. Although the true extent and depth of the so-called "brown dwarf desert" will not be revealed until that time, increased sensitivity to sub-stellar companions at small separation has already resulted in upward revisions of their estimated frequency.

Chapter 4

Pixel Scale and Orientation of PHARO

Abstract

I determine the pixel scale distortion of the PHARO array as a function of array pixel coordinates, telescope pointing (hour angle and declination), and orientation of the Cassegrain ring rotator. The solution is based on an astrometric experiment using an astrometric mask in the light path of PALAO/PHARO and on observations of known calibration binary systems. The attained accuracy is 0.09–0.15%, depending on whether observations at one or several diffrent Cassegrain ring orientations are considered. This is the most comprehensive and final determination of the PHARO pixel scale and supersedes the previous two estimates outlined in White (2002, Memo I) and Metchev (2003, Memo II).

4.1 Pre-amble

The astrometric results in §3 were obtained under the assumption that the pixel scale and orientation of the PHARO detector is well-established from measurements taken near the center of the array, ignoring possible distortion of the focal plane. Because the science observations discussed until now were either of high proper motion stars (Vega: 350 mas yr^{-1}; §3.2) or were also obtained near the center of the array (HD 49197, HD 129333, V522 Per, and RX J0329.1+0118; §3.3), this assumption was adequate. However, the PHARO beam is known to be

distorted (Hayward et al., 2001), by up to 0.4% at f/29 (25 mas pix^{-1}) and 0.8% at f/18 (40 mas pix^{-1}). Accurate characterization of this distortion was necessary before considering the results from my survey, which focused on stars with smaller (10–100 mas yr^{-1}) proper motions and which revealed candidate companions over the full extent of the PHARO chip. This chapter addresses this issue by describing an experiment that I designed to measure the spatial variations of the pixel scale of the PHARO 25 mas pix^{-1} camera, with a field of view of $25.6'' \times 25.6''$. A calibration of the 40 mas pix^{-1} camera is not discussed, as it was not used for my companion survey.

A similar experiment has already been performed for all three NIRC2 cameras during its pre-ship testing (Thompson et al., 2001), the results of which have been implemented in my astrometric analysis of candidate companions.

4.2 Introduction

Accurate astrometry requires detailed knowledge of the focal plane distortion and of the detector placement therein. Often, the dominant source of astrometric error is not the centroiding or the point-spread-function (PSF) fitting accuracy, but the limitation of our knowledge of detector pixel scale variations. For example, the centers of high signal-to-noise point sources on PHARO can be measured to better than 1/10 of a pixel, and the pixel scale at the center of the detector is, by design, known to 4 significant digits: 25.10 mas pix^{-1}. In principle, therefore, one should be able to measure object positions with $\lesssim$2 mas precision and to obtain relative astrometry accurate to a few parts times 10^{-4}. In practice, because of unknown focal plane distortion at the detector location, imaging observations often fall short of this target by up to 1.5 orders of magnitude. Thus, images of binary stars dithered over the entire $25'' \times 25''$ array show systematic pixel scale distortion of up to 0.25 mas pix^{-1} from one detector edge the another (White, 2002; Metchev, 2003, Memos I and II). The corresponding distortion relative to the array center (512,512) is up to 3–4 pix (75–100 mas) near the edges. The problem is com-

pounded when comparing images obtained at different orientations of the PHARO focal plane with respect to the horizon: at different Cassegrain ring (CR) angles, telescope hour angles, and declinations (Metchev, 2003, Memo II). The reason for these dependencies lies in the placement of PHARO and of the PALAO system at the Cassegrain focus of the Palomar $200''$ telescope. The overall orientation of the AO + camera system follows that of the telescope, and, as a result, they experience changing gravity vectors. Without fitting for the observed trends with telescope pointing, the achieved r.m.s. astrometric precision with PHARO as a fraction of the angular separation between point sources is $\lesssim$0.9%. In comparison, the astrometric precision with NIRC2 AO on Keck II is much higher. The distortion of the approximately equivalent in spatial sampling (20 mas pix^{-1}) and coverage ($20'' \times 20''$) medium camera in NIRC2 is known to $\approx$9 mas r.m.s. or 0.09% at the edge of the field. NIRC2 and the Keck AO system are mounted at the Nasmyth focus on Keck II, and thus the direction of the gravity vector on the instruments is independent of telescope pointing.

The drive for high-angular precision astrometry has been motivated in recent years by direct imaging (usually with AO) and astrometric searches for extrasolar planets. In the direct imaging approach, the astrometric accuracy reflects directly on the significance with which a candidate common proper motion pair of objects can be confirmed or rejected as such. Since more distant stars have smaller proper motions, more accurate astrometry is needed for the timely confirmation of candidate orbiting sub-stellar companions. In practice, 0.9% astrometric precision translates into a 100 mas 1σ error on the relative position of a candidate companion at the edge of the PHARO $25'' \times 25''$ FOV, if the primary is placed at the field center. Thus, a direct imaging campaign with a typical 2-year time span can test (at the 3σ level) the physical association of candidate stellar pairs with proper motions higher than 150 mas yr^{-1} only. Given the mean random motions of stars in the solar neighborhood, this limits the radius of a direct imaging survey with PALAO to stars within 30–40 pc from the Sun. The factor of $\sim$10 higher astrometric precision attained with Keck allows a proportionately greater survey

radius, resulting in a ∼1000 times larger number of potential planet-host stars, and including stars in the nearest star-forming regions—prime targets for the direct imaging of warm young giant planets. Given the heliocentric distances (up to 200 pc) of the young stars in my survey for sub-stellar companions to young solar analogs, such higher astrometric accuracy is mandatory.

In this final memo (Memo III), I present the results from a much more comprehensive pixel scale experiment than discussed in the previous two memos and characterize the dependence of the PHARO pixel scale on telescope declination, hour angle, and orientation of the CR. The derived functional solution allows me to improve the astrometric precision with PALAO/PHARO to between 0.09% and 0.15%, i.e., to a level comparable to the one achieved with Keck AO/NIRC2. The experimental set-up and observations are presented in §4.3, and the fitted parametric relations in §4.4. For quick reference, the relevant equations and tables are: Eqns. 4.1–4.4 and 4.7–4.11, and Tables 4.4 and 4.5. The accompanying computer code, written in the IDL language, is available at
http://www.astro.caltech.edu/~metchev/AO/PHARO_25mas_distortion/ .

4.3 Experiment Description

The pixel scale experiment consisted of two parts. In the first part, I used a custom-made astrometric mask to determine the (high-order) distortion of the focal plane at the location of PHARO. Because the mask was not inserted in the main telescope beam, possible non-common path effects meant that the results from this part of the experiment were not expected to fully characterize the dependence of the PHARO pixel scale on telescope pointing. The dominant term arising in the non-common path, a tilt, was measured in the second part of the experiment, in which a number of binary stars with well-known orbits were observed to test and to correct the pixel scale solution. The description of the two experiments follows.

4.3.1 Astrometric Mask Experiment

Astrometric masks are primary calibrators of focal plane scale. Given optimal placement in the optical train, they can allow absolute measurement of pixel scales of detectors.

4.3.1.1 Assembly

In my case, the location of the mask needed to be chosen to maximize the number of telescope, AO, and camera optics in the beam path between the mask and the detector, without interfering with the regular science operations of the telescope and of the AO system. The latter requirement excluded the use of the available large Shack-Hartmann screen made to fit the size of the primary and allowed intervention only after all telescope optics (primary and secondary mirrors). I chose to place the astrometric mask on the PALAO optical bench, preceding all of the PALAO optics. I mounted the mask in the path of the "white light" beam—the internal PALAO light source used for nightly calibration of the AO system wavefront sensor (WFS). The beam path of the astrometric experiment thus coincided with the beam path of science light modulo a reflection off a 45° flat mirror located ≈15 cm behind the $f/15.9$ Cassegrain focus of the telescope (Fig. 4.1). This placement encompassed all of the PALAO and PHARO optics between the mask and the detector, and minimized the non-common path between the telescope beam and the mask experiment beam (Fig. 4.2). Because the mask was mounted onto the PALAO stage, which resides on the CR, rotations of the CR did not affect the overall image orientation during this experiment.

The astrometric mask itself was a 40.6×45.7×0.5 mm reticle made of fused silica with evenly spaced holes, initially designed to measure the pixel scale and distortion of the NIRC2 detector on Keck II, and taken on loan from K. Matthews for the present experiment. The reticle had two grids of pinholes: a coarse grid of 43×43 8μm-diameter holes at 0.70 mm intervals and a fine grid of 21×21 4μm-diameter pinholes at 0.35 mm intervals (Fig. 4.3). For the $f/29.91$ (25.10 mas pix^{-1}) PHARO beam, I used the coarse grid, expected to produce 1.32 mm spacing be-

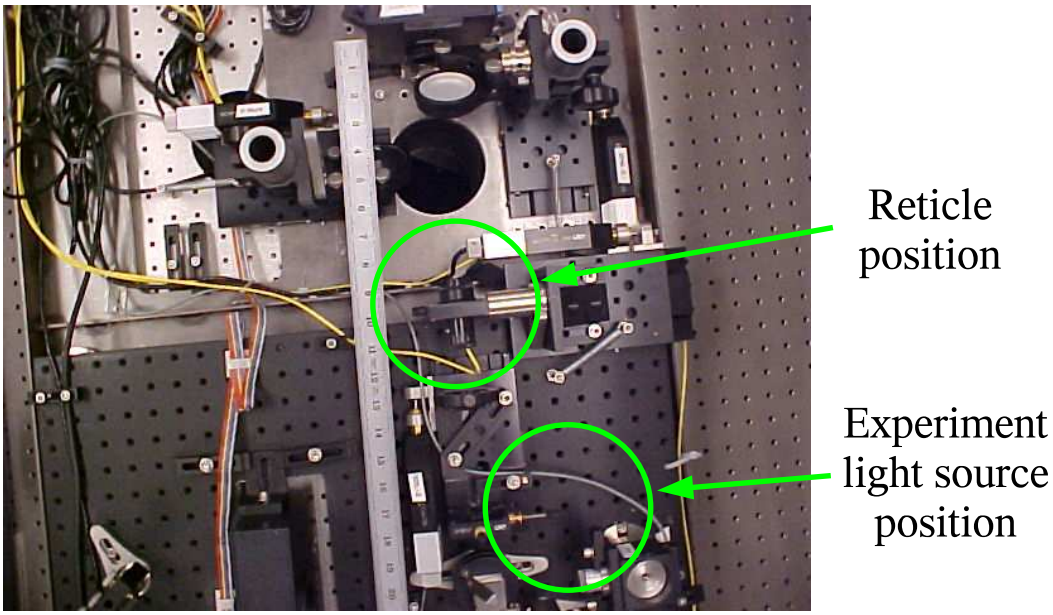

Figure 4.1: A view from above onto the PALAO bench. A ruler with inch-marks is overlayed for scale. The dark 3-inch-diameter circular hole near the top of the image is where the beam from the telescope enters PALAO, the main optics of which are underneath the shown breadboard. Off the bottom of the image is the location of the white light source. During WFS calibration and during the reticle experiment, the beam from the light source is reflected off the 45° flat mirror (above the dark hole, near the top of the image), which is moved in the telescope beam path. The locations of the astrometric mask (the reticle) and of the experiment light source, which I installed after this picture was taken, are marked with circles. The pre-existing light source seen in the reticle circle was pushed out of the beam path with the moving stage onto which it is attached (seen to the right of it). Image courtesy of Rick Burress.

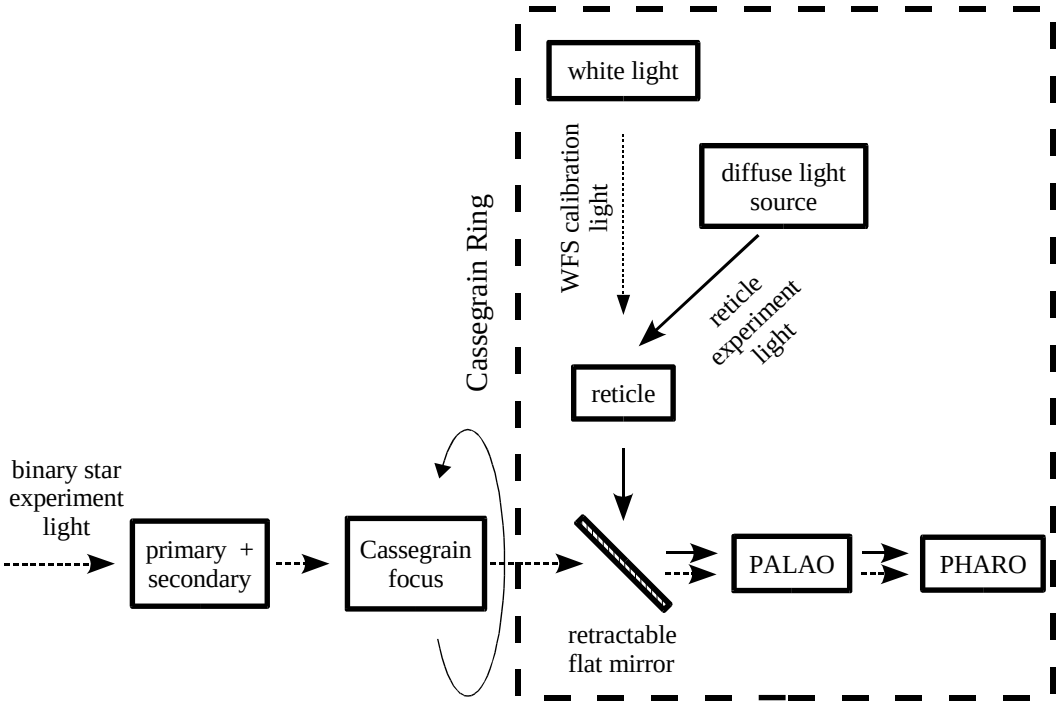

Figure 4.2: A diagram of the set-up for the pixel scale experiment. The beam paths followed during the reticle and binary star experiments are traced by thick continuous and dashed arrows, respectively. The additional beam path used for WFS calibration is traced by a dotted arrow. The long-dashed box delimits the part of the system mounted on, and rotating with, the Cassegrain ring. The sense of rotation of the Cassegrain ring is marked by the thin continuous line. The reticle is confocal with the Cassegrain focus, modulo a 45° flat mirror. This flat mirror and the primary + secondary telescope mirrors are the three non-common path optics between the experimental set-up and regular science operations.

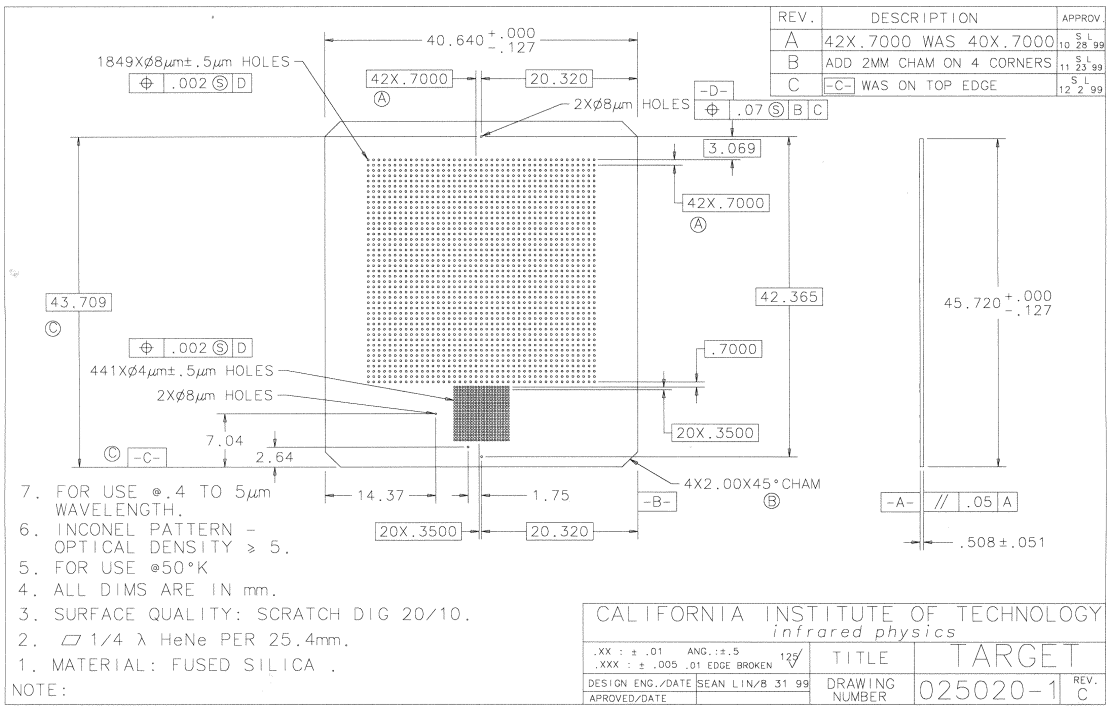

Figure 4.3: A sketch of the reticle used in the experiment. All dimensions are in mm, except where specified.

tween the images of the individual pinholes on the detector. Given the 18.5μm pixel pitch (Hayward et al., 2001), the corresponding pixel distance is 71.2 pix.

The reticle was securely enclosed in a custom-made steel frame mounted onto the top of the PALAO optical bench using a P100–A–1 Newport optical mount. The optical mount allowed fine angular adjustments of the mounted optic along the axes normal to the optical axis. I used the fine-tuning knobs to maximize the amount of light transmitted through the pinholes, ensuring that the reticle is within 0.5° of being perpendicular to the white light beam. The optical mount itself was placed on a translation stage that allowed me to position the reticle in focus. As an internal light source I used a 4 W light bulb firmly mounted onto the optical bench. The bulb provided adequately uniform illumination of the reticle. I did not use the already built-in white light: it is a point source used for calibration and its beam is too narrow to illuminate sufficient area on the reticle.

4.3.1.2 Tests

I assembled the experiment in the Palomar AO laboratory on 2 March 2004, while PALAO was off the telescope. PHARO was cooled to its cryogenic temperature to allow the recording of imaging data. I took test images in the laboratory to check and optimize the alignment of the system. These were taken in series of ten 1.4 s exposures with the lightbulb switched on. At the end of the experiment I took ten 1.4 s "background" exposures with the light bulb off to subtract from the test images and minimize the effect of bad and hot pixels. Figure 4.4 shows an example background-subtracted image taken in the K_S band. The image displays the characteristic grid pattern of point sources corresponding to individual pinholes in the reticle. The rotated appearance of the grid on the detector reflects the orientation of the science beam as it comes into PALAO at the nominal orientation of the CR.

Upon successful installation and testing of the pinhole mask in the laboratory, PALAO and PHARO were mounted on the telescope on 3 March 2004. I conducted the remainder of the experiment under a dark, closed dome, with settings similar to those used during regular science operations. In PHARO, I performed tests with the broad J, H, and K_S filters, and the narrow CO-bandhead and Brackett γ filters, with the 25 mas pix^{-1} and the 40 mas pix^{-1} cameras, with the standard and medium cross Lyot masks, and with and without the ND1% filter. I did not experiment with different slit wheel settings. Due to a temporary mechanical failure in PHARO, the slit wheel was stuck in the $0.4''$-diameter coronagraphic spot setting.

To test for flexure dependence of the PHARO pixel scale, I directed the telescope to a series of pointings at various hour angles and declinations within the allowed telescope limits. The pointings ranged from 6 h west to 6 h east in hour angle, and from $-30°$ south to $88°$ north in declination, at steps of 1.5 h in hour angle and $15°$ in declination. During most of the experiment, the CR rotator angle was maintained near $333.5°$, placing the y-axis on PHARO within $\approx 1.5°$ of north. Limited experiments with rotating the CR in steps of $90°$ were also performed at

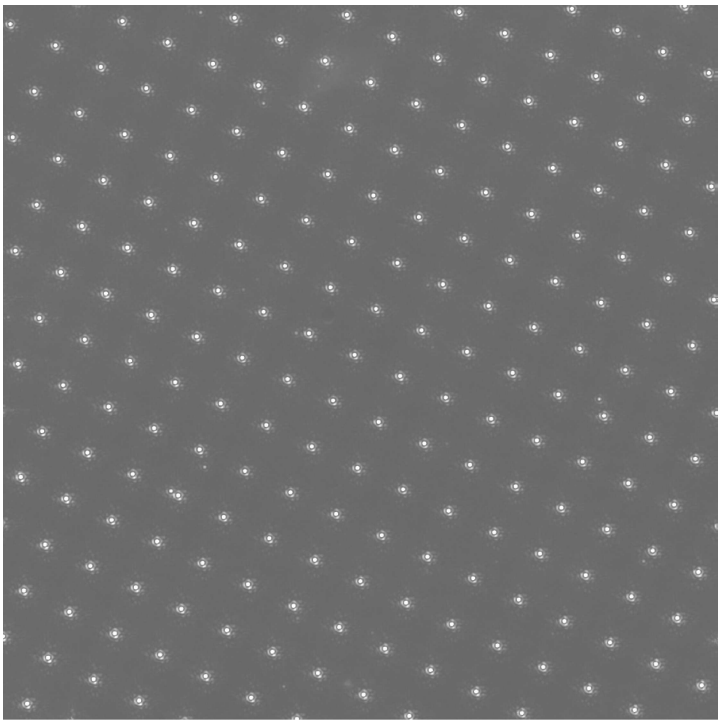

Figure 4.4: A background-subtracted image of the reticle pattern, taken with the 25 mas pix^{-1} PHARO camera on 2 March 2004. The detector is 1024×1024 pix, corresponding to an area of $25.6'' \times 25.6''$ on the sky. The evenly-spaced grid of point sources maps the holes in the reticle and allows a precise determination of the pixel scale. The occasional point sources in between the grid points are due to manufacturing defects in the mask and are filtered out in the subsequent astrometric analysis. The $\approx 25^\circ$ angle of the pattern with respect to the y-axis of the detector corresponds to the rotation of the telescope beam with respect to the orientation of the CR.

zenith and at -30° declination on the meridian. For the flexure test I employed the K_S filter in PHARO, which is the one used in most scientific AO observations with the $200''$ and allows fine sampling of the 90 mas (FWHM) diffraction-limited PALAO PSF with the 25 mas pix^{-1} camera. The remaining wheel settings for the flexure experiment were: "$0.4''$ coronagraph" (slit wheel), "medium cross" (Lyot wheel), and "open" (grism wheel).

Throughout the experiment the tip-tilt (TT) and the deformable mirror (DM) loops remained open. Because of the small spacing between the pinholes in the reticle, wave-front sensing on any particular pinhole would have been complicated by stray light contamination from neighboring holes. Although the practice of leaving the TT and DM off is in contrast with normal science operations, it was not expected to affect the final result. Changes in the detector pixel scale are expected to be induced by distortions in the geometrical figures (e.g., because of changing gravity vectors) of the optics. If the TT and DM mirrors suffer such distortions, they would be relayed along the beam path regardless of whether their actuators are active (i.e., as in closed loop operation) or not.

4.3.1.3 Astrometric Measurements

A total of 450 PHARO images were taken during the course of the experiment. The pixel coordinates of the evenly-spaced points sources in each of the images were measured with an automated procedure to fit Gaussian profiles. The width of the Gaussian profiles was set to match the PSF FWHM: 3.4 pix at K_S and Brackett γ, 2.6 pix at H and 2.1 pix at J. Extraneous sources in between the grid points were ignored, as they were caused by manufacturing defects in the reticle substrate. Point sources near the coronagraphic spot or near bad pixels on the detector were also removed from the subsequent analysis. Given the spot brightness and shape of the PSF, the spot coordinates were obtained to a mean precision of ± 0.026 pix in x and ± 0.030 pix in y.

I calculated the distances between each spot and its closest neighbors on the grid to look for variation with detector position. Figure 4.5 shows the obtained

inter-spot distances along the two grid axes for a case in which the telescope was pointed at zenith, and the CR angle was set to 333.5°. Circles mark distance measurements in the direction of the continuous-line vector, and squares mark measurements along the dashed-line vector. Each point is located in the middle of two neighboring grid spots (not shown) and its size is linearly proportional to the distance between the spots. The shortest and the longest inter-spot pixel distance along each direction is labeled above the corresponding dot. The lack of data near $(x, y) = (340, 230)$ is caused by an area of bad pixels on the detector.

It is immediately evident from Figure 4.5 that the pixel scale across the array is not uniform. Along the position angle (PA) of the continuous-line vector the inter-spot distance is smallest (71.65 pix) in the top left corner of the array and largest (72.38 pix) in the bottom right corner. The variation of the pixel scale along the PA of the dashed-line vector follows an approximately vertical direction, with the shortest inter-spot distance (72.25 pix) near the bottom left corner of the array and the longest (72.73 pix) near the top.

To first order, the measurements of the inter-spot distances point to a tilt in the optical system. Indeed, the plane of the PHARO detector is known to be tilted by 0.1° with respect to the $f/29.91$ focal plane by design. In §4.4.1 I will also discuss probable apparent beam tilt that was induced by my imperfect alignment of the reticle perpendicularly to the beam. A further comparison with the expected inter-spot pixel distance of 71.2 pix also reveals possible direction-dependent magnification. Both effects, tilt and magnification, are typical of focal plane distortion patterns, such as pincushion or barrel.

4.3.2 Binary Star

Binary stars and various rich stellar fields are secondary astrometric calibrators. Accurate positions of each of the stars in the field need to have been established a priori with the use of a primary astrometric calibrator. Such measurements are available in the literature, and I have used binary stars with well-characterized orbital solutions from the Sixth Catalog of Orbits of Visual Binary Stars (Hartkopf

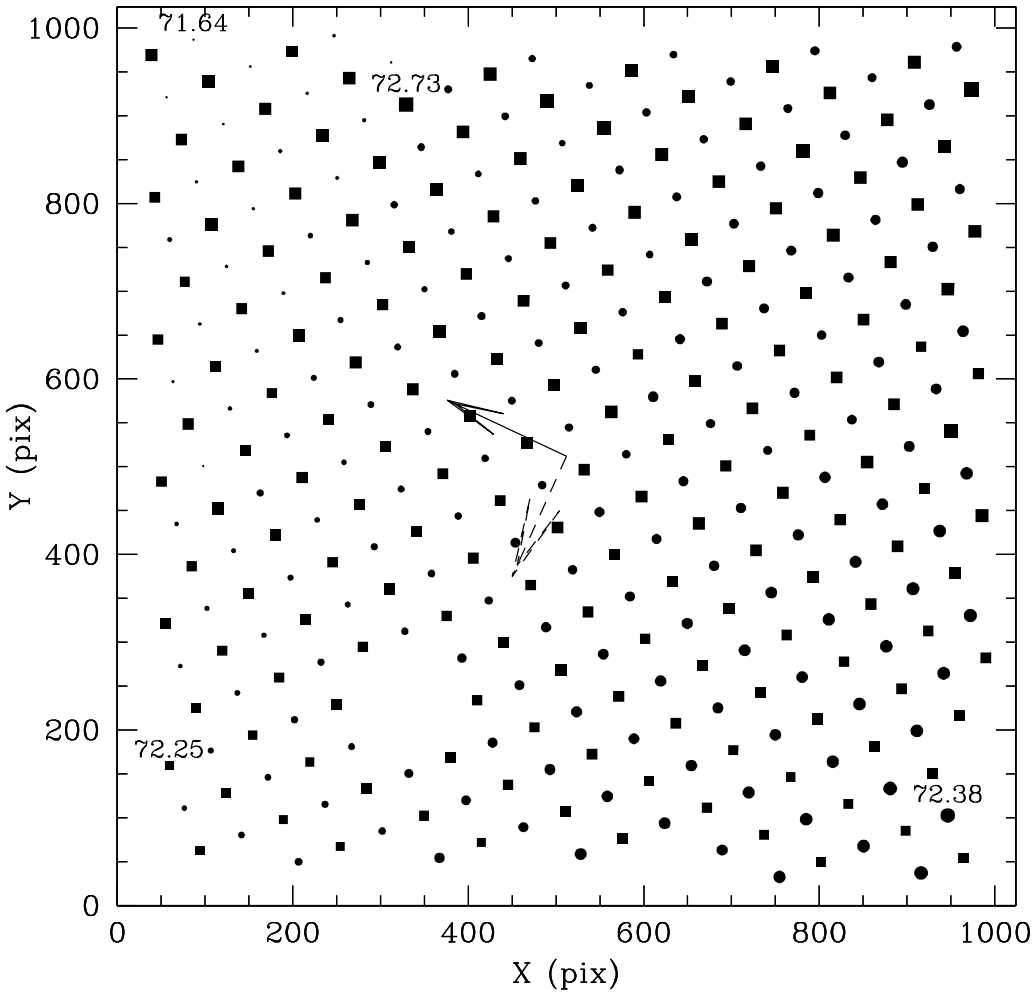

Figure 4.5: Pixel distances between neighboring grid spots in the reticle image. Circles denote distances along the continuous-line vector, and squares mark distances along the dashed-line vector. Each point is located in the middle of two neighboring grid spots (not shown), and its diameter is linearly proportional to the distance between the spots. The minimum and maximum inter-spot pixel distances along each direction are marked above the corresponding point.

& Mason, 2005). Binary star observations can be performed in identical manner to science observations, and therefore astrometric measurements based on binary stars do not suffer from the non-common path errors associated with the use of the pinhole mask described in §4.3.1.

4.3.2.1 Observations

Observations of binaries for pixel scale calibration were conducted on most observing runs during the course of my three-year survey for sub-stellar companions to young solar analogs (Metchev & Hillenbrand, 2004). The binaries were selected from the subset of "calibration candidates" recommended by Hartkopf & Mason (2003). These have either well-known "grade 1" orbits, with minimal uncertainties of the orbital elements, or less well-known (grade 4–5) orbits with long orbital periods ($\gtrsim$1000 yr), resulting in negligible systematic errors in the predicted binary configuration over tens of years. The list of the calibration binaries that I have used, along with their relevant orbital parameters, is given in Table 4.1. All binary systems in the Table are named using their Washington Double Star (WDS) Catalog (Mason et al., 2001) identifiers.

Table 4.2 gives the dates on which each calibration binary was observed and details the telescope orientation during each observation. The calibration observations were conducted under a broad range of atmospheric conditions, from calm and clear to windy and with heavy cirrus. The natural seeing varied from $0.5''$–$2''$ at K_S band, and the airmass between 1.0 and 2.0. The AO loop rate for these bright ($V = 3 - 6$ mag) stars was set between 500 Hz and 1500 Hz. The Strehl ratios were estimated to be between 10% and 70%, sometimes varying on a timescale of minutes. All binaries were observed with the H, K_S, or Brγ filters in PHARO with an ND 0.1% or ND 1.0% filter inserted in front of the array to keep the stars from saturating in the shortest (1.4 s) exposures.

Because of unstable atmospheric conditions, the AO correction was sometimes inadequate, resulting in isolated poor (not diffraction-limited) images. Less often, entire sequences of observations were of low quality, such as those of WDS 18055+

Table 4.1: Observed Calibration Binaries and Parameters of Their Relative Orbits

Binary (WDS)	a (arcsec)	P (years)	T_0 (year)	e (degrees)	i (degrees)	Ω (degrees)	ω (degree)	WDS grade	Ref.
09006+4147	0.6472 ± 0.0010	21.776 ± 0.017	1993.725 ± 0.023	0.1507 ± 0.0008	131.26 ± 0.13	204.39 ± 0.19	32.52 ± 0.36	1	1
15232+3017	0.8676 ± 0.0012	41.585 ± 0.013	1933.721 ± 0.057	0.2620 ± 0.0031	59.03 ± 0.15	203.19 ± 0.20	38.42 ± 0.51	1	2
16147+3352	5.927	888.989	1826.949	0.7605	31.795	16.889	72.201	4	3
18055+0230	4.5540 ± 0.0052	88.38 ± 0.02	1895.94 ± 0.02	0.4992 ± 0.0004	121.16 ± 0.08	302.12 ± 0.10	14.0 ± 0.1	1	4
20467+1607	10.22	3249	2305	0.88	148.78	88.06	331.16	4	5
23052−0742	0.2026 ± 0.0007	21.840 ± 0.019	1983.108 ± 0.022	0.3878 ± 0.0025	48.01 ± 0.042	204.87 ± 0.50	82.83 ± 0.45	1	1
23322+0705	0.173	30.73	1987.47	0.263	31.0	126.8	57.0	1	6

References.—1. Hartkopf et al. (1996); 2. Mason et al. (1999); 3. Scardia (1979); 4. Pourbaix (2000); 5. Hale (1994); 6. Hartkopf & Mason (2000).

Notes.—Explanation of orbital parameters: a—semi-major axis; P—period; T_0—epoch of periastron; e—eccentricity; i—inclination; Ω—longitude of periastron; ω—longitude of the ascending node.

Table 4.2: Observations of Calibration Binaries

Date	Epoch	Binary	Ephemerides		CR Angle	Hour Angle	DEC	Note
(UT)	(year)	(WDS)	$\rho(''$)	P.A.($^\circ$)	(degrees)	(degrees)	(degrees)	
Jun 23, 2002	2002.476	18055+0230	4.3351	142.8677	63.5	···	2.50	
May 10, 2003	2003.356	09006+4147	0.7219	13.0340	63.5	34.0 – 37.9 W	41.78	
May 11, 2003	2003.359	20467+1607	9.2023	265.7002	243.5	19.9 – 17.5 E	16.12	
Jul 15, 2003	2003.537	16147+3352	7.0780	236.4879	63.5, 153.5, 243.5, 333.5	11.9 – 49.0 W	33.86	
Jul 16, 2003	2003.539	18055+0230	4.5697	140.8363	63.5, 153.5, 243.5, 333.5	5.3 E – 15.7 W	2.50	
Sep 20, 2003	2003.720	23322+0705	0.1936	6.3602	63.5, 333.5	15.0 – 32.5 W	7.08	
Sep 21, 2003	2003.723	18055+0230	4.6168	140.4406	63.5	16.4 – 18.8	2.50	
		23052–0742	0.1223	230.8686	63.5	19.0 – 15.0 E	−7.70	
Dec 9, 2003	2003.939	09006+4147	0.7072	7.8751	243.2	39.8 – 41.3 W	41.78	
Feb 5, 2004	2004.099	09006+4147	0.7018	6.4283	243.5, 333.5	11.6 – 16.2 W	41.78	
		18055+0230	4.6881	139.8472	333.5	48.3 – 45.9 E	2.50	poor
Feb 6, 2004	2004.101	09006+4147	0.7018	6.4104	333.5	15.5 – 21.5 W	41.78	
		18055+0230	4.6885	139.8438	333.5	41.4 – 39.1 E	2.50	
Feb 7, 2004	2004.104	18055+0230	4.6891	139.8386	333.5	38.3 – 35.1 E	2.50	
Jun 26, 2004	2004.486	18055+0230	4.7681	139.1897	62.9, 152.9, 242.9, 332.9	9.6 – 15.6 W	2.50	
		20467+1607	9.1805	265.6374	152.9	25.4 – 26.5 W	16.12	
Jun 27, 2004	2004.489	18055+0230	4.7685	139.1864	152.9	66.6 – 66.9 W	2.50	poor
		20467+1607	9.1805	265.6373	152.9	29.0 – 29.4 W	16.12	
Jun 28, 2004	2004.491	15232+3017	0.5092	105.0731	152.9	3.8 – 5.5 W	30.29	
		16147+3352	7.0953	236.6373	152.9	6.4 – 6.0 E	33.86	
		18055+0230	4.7689	139.1832	62.9	25.9 – 26.2 W	2.50	
Oct 4, 2004	2004.759	09006+4147	0.6744	0.1452	332.9	39.4 – 38.5 E	41.78	
Oct 5, 2004	2004.762	18055+0230	4.8243	138.7337	242.9, 332.9	21.2 – 23.3 W	2.50	
		20467+1607	9.1751	265.6219	242.9, 332.9	15.1 – 13.1 E	16.12	

0230 on 5 February 2004 and 27 June 2004 (Table 4.2). Poor images were excluded from the subsequent analysis, for which I have chosen only images in which a diffraction-limited core of FWHM = 3.6–4.0 pix was clearly visible.

4.3.2.2 Tests

Each binary star was dithered to the center and vertices of a 6″ on a side box dither pattern for the purpose of sky-subtraction. The five-point dither patterns were performed generally near the center of the array to allow quick comparison among different binaries and observing runs. On the nights of 15 and 16 July 2003 I performed extensive tests of the variation of the pixel scale across the entire PHARO array at four orthogonal orientations of the CR rotator: 333.5°—N-up, E-left (nominal); 63.5°—N-left, E-down; 153.5°—N-down, E-right; and 243.5°—N-right, E-up (Fig. 4.6).

4.3.2.3 Astrometric Measurements

The pixel coordinates of the binary star components were obtained in a manner similar to the point source coordinates in the reticle experiment (§4.3.1.3). I fitted Gaussian profiles to the diffraction-limited PSF cores, with FWHM=3.5–3.7 pix for the K_S and Brγ images and FWHM=2.7 pix for the H-band images.

I compared the measured separation and orientation for all binaries to the values predicted from their orbital solutions. Figure 4.7 shows the result of this comparison for the case of WDS 16147+3352, which was dithered over the entire area of the detector at four different CR angles. As in Fig. 4.5, the dots in Fig. 4.7 mark the midway points for the binary at each detector location. The sizes of the dots are proportional to the magnitude of the pixel scale, ranging from 25.19 mas pix^{-1} in the top right corner of the array at CR angle of 243.5° to 25.54 mas pix^{-1} in the top left corner at CR angle of 153.5°.

It is immediately evident that the pixel scale is a strong function of array coordinates and CR angle. In the past, a mean pixel scale of 25.22 mas pix^{-1} with an r.m.s. scatter of 0.11 mas pix^{-1} (0.44% relative error; Memo II) was

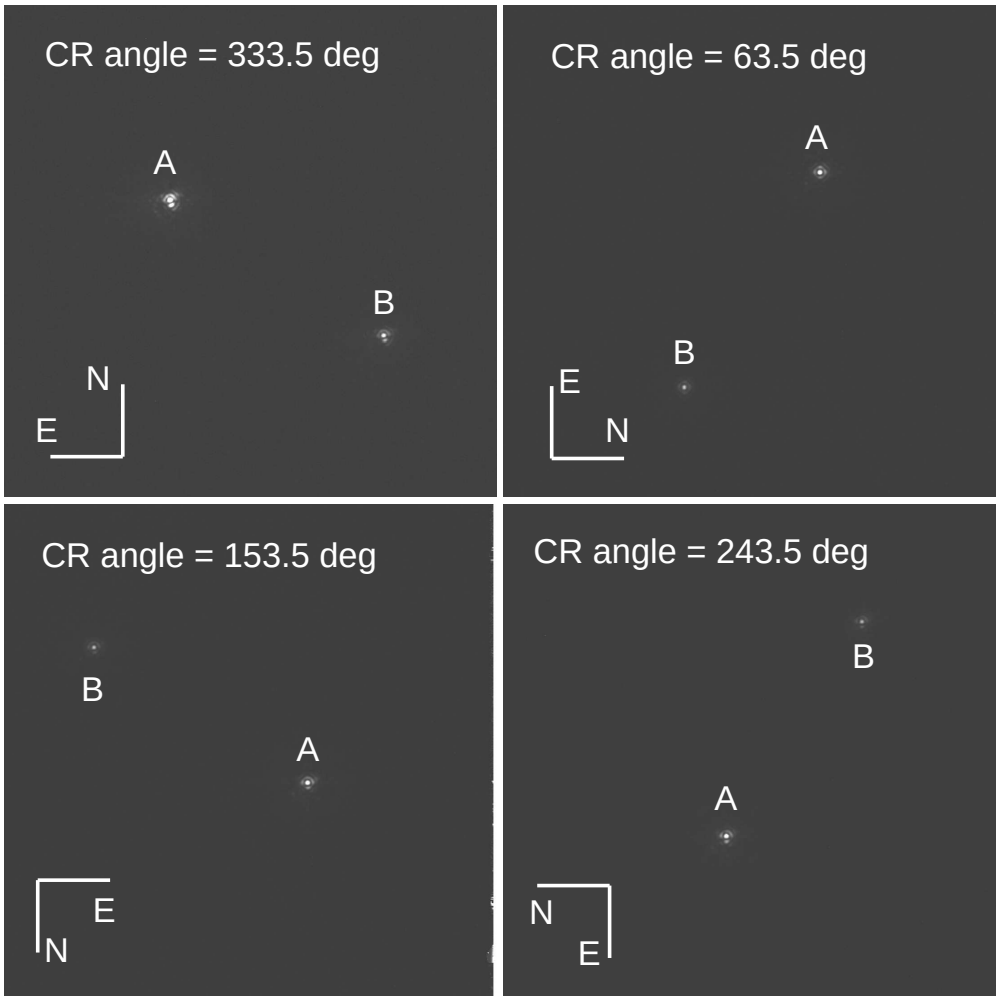

Figure 4.6: Images of the calibration binary WDS 16147+3352 taken in the K_S band on 15 July 2003 at four mutually orthogonal orientations of the CR rotator. The binary separation on that date was predicted to be $7.0780''$ and the position angle $236.4879°$.

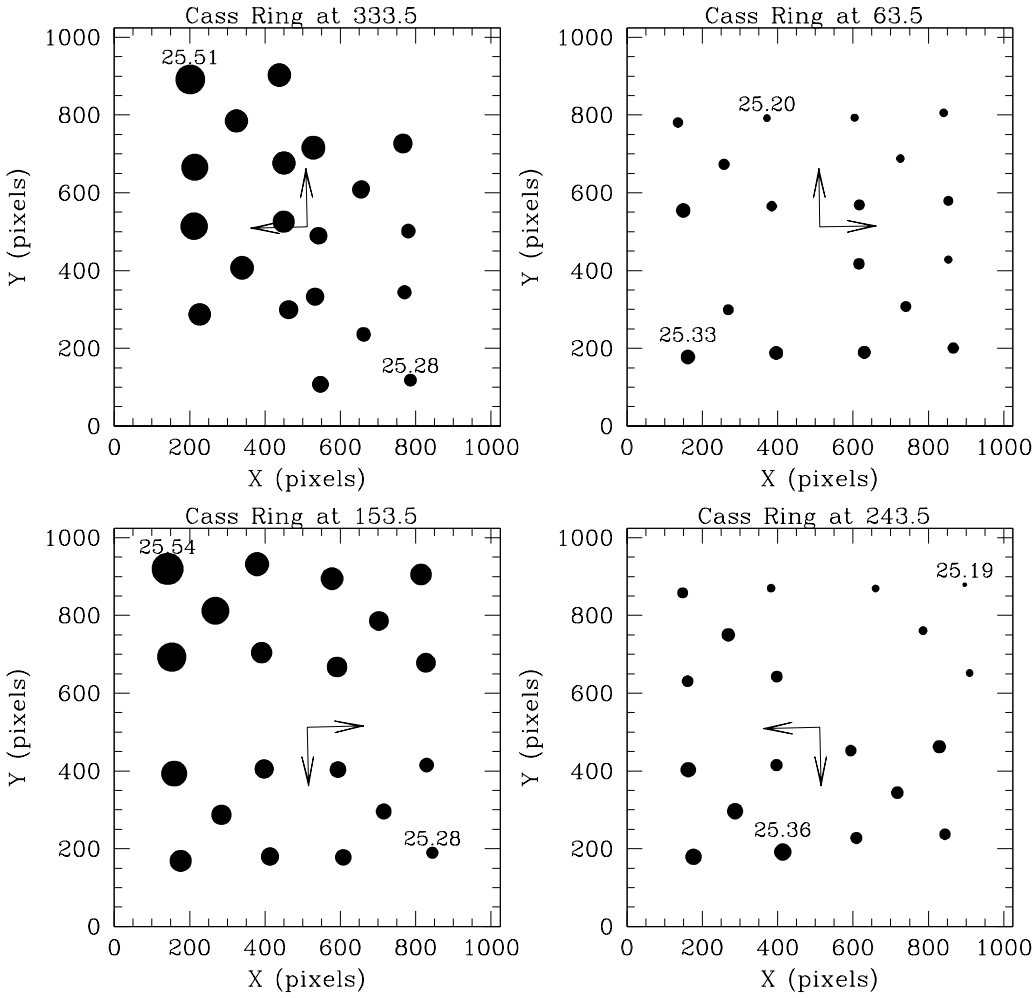

Figure 4.7: Positional and CR dependence of the pixel scale of PHARO based on observations of the WDS 16147+3352 calibration binary on 15 July 2003. The dot size indicates the pixel scale, decreasing linearly from the largest value (25.54 mas pix^{-1}) to the smallest one (25.19 mas pix^{-1}). The arrow hands point to north and east, with East being 90° counter-clockwise from north. The binary orientation in each panel is the same as in the corresponding panel of Fig. 4.6.

adopted. However, because the pixel scale measurements are not randomly distributed around the mean, the r.m.s. scatter conceals the full range of variation of the pixel scale: up to 0.7% between the center and edge of the detector. Adding to this the 0.34° (0.0059 radians) uncertainty in the absolute detector orientation found in Memo II, the overall relative astrometric precision at the edge of the array becomes $\sqrt{0.007^2 + 0.0059^2} = 0.0092 = 0.92\%$. This is the effective limit on the astrometric accuracy at the edge of the PHARO detector, if distortion effects are not accounted for.

4.4 Analysis and Results

In this section I examine the pixel scale of the PHARO detector in the $f/29.91$ (25.10 mas pix^{-1}) mode as a function of detector coordinates, telescope pointing, and CR rotation. For the first two factors I will use the results from the reticle experiment. For the last I will use the data from the calibration binary observations. Eventually, I also discuss the effect of changing camera optics and detector read-out.

4.4.1 Pixel Scale Distortion as a Function of Detector Position

In principle, I can calculate the exact distortion at each location on the array by comparing the measured inter-spot distance to the expected one (71.2 pix) from the reticle experiment set-up. In practice, because of the inability to align the pinhole mask exactly at 90° to the optical axis of the experiment, the reticle may have an unknown tilt that would result in a skewed appearance of the imaged pinhole pattern. Hence, the axes of the imaged grid are not expected to be perpendicular to each other, and the ratio of the mean inter-spot distances along the two axes may not be unity.

To characterize the intrinsic (i.e., without the complications induced by telescope pointing) distortion of the PHARO pixel scale, I examine the set of reticle images taken with the telescope pointed at zenith (declination $\delta = +33.356°$) and

with the CR angle set to 333.5°. This I will consider the nominal setting for the telescope. The distortion at any other telescope pointing will be expressed relative to the pixel scale solution at this setting. I parameterize the distortion in terms of four quantities: θ_1, θ_2, d_2, and d_2. The first two parameters are the PAs of the grid axes with respect to the detector (x, y) coordinate system, with PA=0° along the y axis. The latter two parameters are the distances between neighboring spots along the corresponding PAs. As already stated, generally $|\theta_1 - \theta_2| \neq 90°$ and $d_1/d_2 \neq 1$. If the observed distortion in the reticle images was caused only by reticle and detector tilt, θ_1, θ_2, d_1, and d_2 would attain constant values regardless of detector position. Higher-order image distortion will induce x- and y-dependent variation of these parameters.

I fit for the measured angles and spacings (Fig. 4.5) between neighboring grid points along both grid axes, using first-degree linear two-dimensional (2D) polynomials for the angles and for the inter-spot distances. At the center (512,512) of the array, I obtain:

$$\theta_1(512, 512) = 64.8455° \pm 0.0025°$$

$$\theta_2(512, 512) = 155.0740° \pm 0.0051°$$

$$d_1(512, 512) = 72.0099 \pm 0.0051 \text{ pix}$$

$$d_2(512, 512) = 72.4521 \pm 0.0068 \text{ pix}.$$

The errors represent the r.m.s. scatter of 15 independent measurements and fits.

Assuming that the image distortion vanishes at the center of the array in the nominal telescope setting, I use $\mathbf{d_1}$ and $\mathbf{d_2}$ as two separate unit vectors (with directions along θ_1 and θ_2, and lengths d_1 and d_2, respectively) to measure the pixel scale along either direction relative to the center of the array. Without being able to change the orientation of the reticle image on the array, the lengths of the two unit vectors cannot be compared. However, an absolute determination of the pixel scale will be possible when I consider binary star images taken at mutually perpendicular CR angles in §4.4.3.

I create an array of the expected spot positions, provided that tip and tilt are the only distortions in the beam, i.e., assuming that each spot is an integer number of $\mathbf{d_1}$ and $\mathbf{d_2}$ vector lengths away from the spot nearest the detector center. The coordinate residuals between the actual and the expected spot positions reveal the intrinsic pixel scale distortion of the PHARO $f/29.91$ beam. Panels (a) and (b) of Figure 4.8 show the direction and the magnitude of the distortion. Letting (x', y') be the distortion-corrected pixel coordinates, I find that the intrinsic pixel scale distortion is well fit by the following polynomials:

$$x'(x_c, y_c) = 512 + a_0 + a_1 y_c + a_2 y_c^2 + a_3 x_c + a_4 x_c y_c + a_5 x_c^2 \tag{4.1}$$

$$y'(x_c, y_c) = 512 + b_0 + b_1 y_c + b_2 x_c, \tag{4.2}$$

where $x_c = x - 512$ and $y_c = y - 512$. The values of the individual parameters are tabulated in Table 4.3. The reduced χ^2 values of the fits for each of the 15 reticle images taken at the nominal telescope setting vary from 0.74 to 1.01 for x' and from 0.54 to 1.54 for y'. There is thus no need for $x_c y_c$ cross-term dependence in either x' or y'.

Expressions 4.1 and 4.2 with the parameter values tabulated in Table 4.3 describe the intrinsic pixel scale distortion of the PHARO 25 mas pix^{-1} camera when the telescope is pointed at zenith.

4.4.2 Pixel Scale Variation with Hour Angle and Declination

Having established the intrinsic PHARO distortion, I pursue a more general solution of the pixel scale for arbitrary telescope hour angle and declination, though still at a fixed CR angle. Because of limited experimentation with varying the CR angle during the reticle experiment, these observations had insufficient phase-space coverage to characterize its effect on the pixel scale. Nevertheless, CR-angle dependent variations were measured from the binary star observations and will be discussed in §4.4.3.

Here I present a solution based on 300 reticle images taken in the 6 h west to 6 h

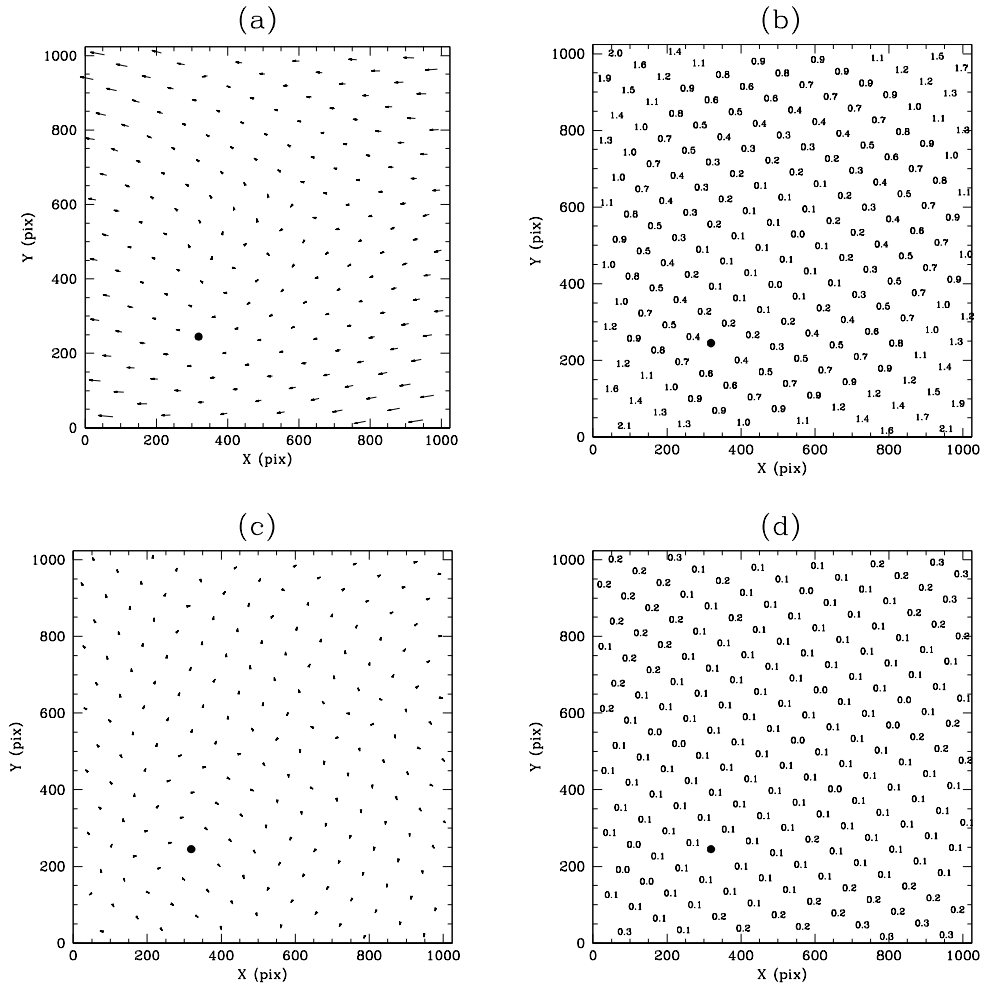

Figure 4.8: The intrinsic geometric distortion of the $f/29.91$ (25 mas pix^{-1}) PHARO camera with the telescope pointed at zenith. The large dot in all panels denotes the location of an area of bad pixels on the detector. (a) The direction and length of an arrow indicate the direction and magnitude of the distortion at the position of the tail of the arrow. The arrow length was set to 20 times that of the actual image distortion in pixels. (b) The actual size of the image distortion in pixels (i.e., 1/20 of the arrow length). (c, d) Same as (a, b), after applying the distortion correction from Eqns. 4.1 and 4.2.

Table 4.3: Preliminary Distortion Coefficients for the 25 mas PHARO Camera with the Telescope Pointed at Zenith

Parameter	Value	Error	Unit
a_0	0.0275	0.0032	pix
a_1	-8.9×10^{-5}	1.0×10^{-5}	pix^0
a_2	-4.513×10^{-6}	1.3×10^{-8}	pix^{-1}
a_3	1.000147	0.000017	pix^0
a_4	0	$\cdots$	pix^{-1}
a_5	-4.250×10^{-6}	1.3×10^{-8}	pix^{-1}
b_0	0.0162	0.0047	pix
b_1	1.000307	0.000028	pix^0
b_2	-9.0×10^{-5}	1.3×10^{-5}	pix^0

east ($-90°$ to $+90°$) hour angle range and between $-30°$ and $+88°$ in declination, with the CR angle fixed at 333.5°. I find that the effect of telescope pointing on the pixel scale is systematic and is reflected in the values of the a_1 and b_2 coefficients in Eqns. 4.1 and 4.2 above. Their variation with hour angle and declination is illustrated in Figure 4.9 and is described by the following functional dependences:

$$a_1(\kappa,\delta) = \alpha_0 + \alpha_1\delta + \alpha_2\delta^2 + \alpha_3\delta^3 + \alpha_4\kappa + \alpha_5\kappa\delta + \alpha_6\kappa\delta^2 + \alpha_7\kappa^2 + \\ + \alpha_8\kappa^2\delta + \alpha_9\kappa^3 \qquad (4.3)$$

$$b_2(\kappa,\delta) = \beta_0 + \beta_1\delta + \beta_2\delta^2 + \beta_3\delta^3 + \beta_4\kappa + \beta_5\kappa\delta + \beta_6\kappa\delta^2 + \beta_7\kappa^2 + \\ + \beta_8\kappa^2\delta + \beta_9\kappa^3 \qquad (4.4)$$

where κ denotes hour angle and δ denotes declination, both in units of degrees. The values for α_i and β_i are tabulated in Table 4.4. The reduced χ^2 values for all three fits are high: 2.5 and 4.7, respectively. However, fitting through singular value decomposition shows that higher numbers of parameters are unjustified. The high value of χ^2 thus indicates the possible presence of other factors that I have failed

to take into account in the parameterization. Nevertheless, the r.m.s. deviations of the three fits are $\lesssim 8 \times 10^{-5}$—a factor of 2 smaller than the scatter in the coefficients in front of the remaining two linear terms in Eqns. 4.1 and 4.2, a_3 and b_1, which show no significant trends with hour angle and declination (Fig. 4.9). Therefore, I do not pursue more complex functional expressions for a_1 and b_2. Table 4.5 lists the adopted values or functional dependencies for the coefficients a_i and b_i, and their scatter. These are now based on the data from the 300 reticle images taken over the entire range of hour angles and declinations sampled in the pinhole experiment. The mean r.m.s. of the difference between the fitted and the measured coordinates of the pinhole images is 0.13 pix, compared to 0.67 pix under the assumption of a constant pixel scale.

4.4.3 Absolute Calibration of the Pixel Scale Distortion

The parametric fit derived in §4.4.1 and §4.4.2 is based on data from an internal light source and is incomplete because of unknown beam tilt. The pixel scale distortion is known only modulo the ratio of the lengths of the $\mathbf{d_1}$ and $\mathbf{d_2}$ unit vectors. Because the mounting of the astrometric mask did not allow for rotation along the beam axis, I could not sample the pixel scale with different reticle orientations to determine the beam tilt. Here I have used observations of binary stars at different CR angles to determine this tilt and to transform the partially distortion-corrected pixel coordinates (x', y') (Eqns. 4.1 and 4.2) to a fully distortion-corrected coordinate system (x'', y'').

4.4.3.1 Additional Parameterization: Beam Tilt

In principle, the reticle beam tilt can be readily calculated from the values of θ_1, θ_2, d_1, and d_2, obtained during the reticle experiment (§4.4.2). However, because of the non-common path between the reticle and the science beams (Fig. 4.2), the reticle beam tilt will, in general, be different from the tilt of the science beam. I will therefore proceed with an independent parameterization of the science beam tilt. The higher-order distortion of the science beam may also be different from

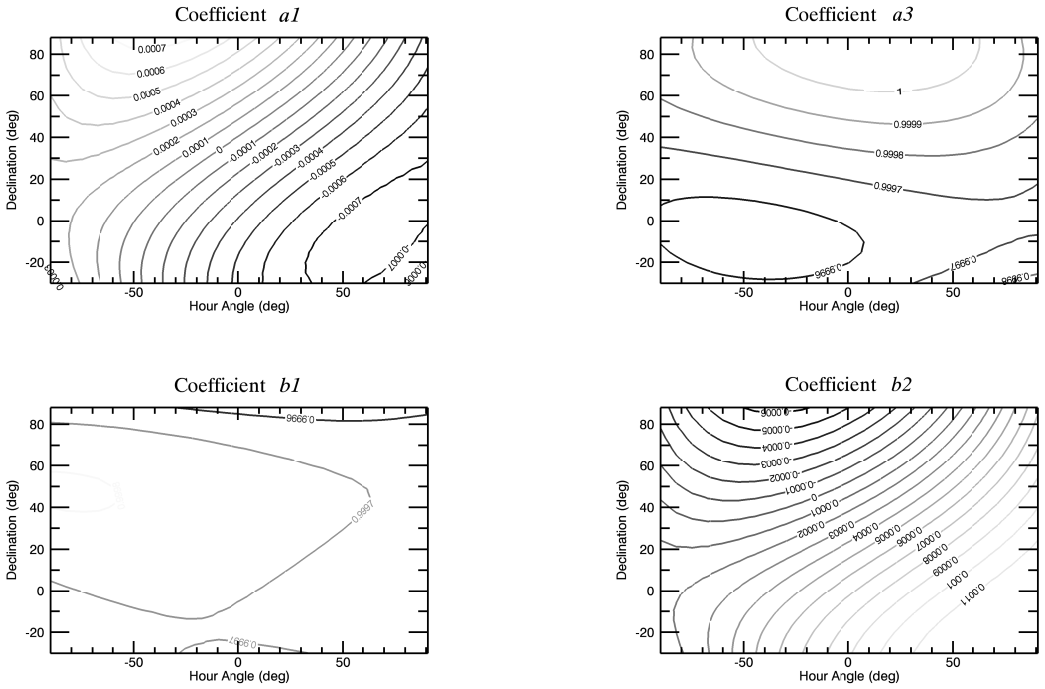

Figure 4.9: Third-degree 2D polynomial fits to the dependence of the linear expansion coefficients in Eqns. 4.1 and 4.2 on hour angle (west is negative, east is positive) and declination. The contour spacing is 0.0001 pix pix^{-1}. Coefficients a_1 and b_2 show significant variation, while the variation of a_3 and b_1 is negligible. The -0.0006 and -0.0007 contour levels in the bottom right corner of the *top left* panel are artifacts due to the polynomial fitting of the data: no measurements were taken at this extreme (and unattainable) combination of hour angle and declination.

Table 4.4: Coefficients in the Expansions of a_1 (Eqn. 4.3) and b_2 (Eqn. 4.4)

Parameter	Value	Error	Unit
α_0	-2.496×10^{-4}	5.4×10^{-6}	degree^0
α_1	7.22×10^{-6}	1.5×10^{-7}	degree^{-1}
α_2	9.16×10^{-8}	6.5×10^{-9}	degree^{-2}
α_3	-5.47×10^{-10}	6.5×10^{-11}	degree^{-3}
α_4	-8.14×10^{-6}	1.1×10^{-7}	degree^{-1}
α_5	0	$\cdots$	degree^{-2}
α_6	0	$\cdots$	degree^{-3}
α_7	2.14×10^{-8}	1.7×10^{-9}	degree^{-2}
α_8	-1.031×10^{-9}	3.1×10^{-11}	degree^{-3}
α_9	3.66×10^{-10}	1.7×10^{-11}	degree^{-3}
β_0	1.997×10^{-4}	5.3×10^{-6}	degree^0
β_1	-1.054×10^{-5}	1.5×10^{-7}	degree^{-1}
β_2	-7.41×10^{-8}	6.4×10^{-9}	degree^{-2}
β_3	5.37×10^{-10}	6.4×10^{-11}	degree^{-3}
β_4	7.58×10^{-6}	1.0×10^{-7}	degree^{-1}
β_5	0	$\cdots$	degree^{-2}
β_6	0	$\cdots$	degree^{-3}
β_7	1.07×10^{-8}	1.7×10^{-9}	degree^{-2}
β_8	8.87×10^{-10}	3.1×10^{-11}	degree^{-3}
β_9	-2.83×10^{-10}	1.7×10^{-11}	degree^{-3}

Table 4.5: Final Distortion Coefficients and Expressions at Arbitrary Telescope Hour Angle and Declination

Coefficient	Value or Equation	R.M.S. Scatter	Unit
a_0	0.018	0.035	pix
a_1	Eqn. 4.3	6.8×10^{-5}	pix^0
a_2	-4.51×10^{-6}	1.1×10^{-7}	pix^{-1}
a_3	0.99983	1.7×10^{-4}	pix^0
a_4	0	$\cdots$	pix^{-1}
a_5	-4.37×10^{-6}	1.2×10^{-7}	pix^{-1}
b_0	0.019	0.046	pix
b_1	1.00001	1.4×10^{-4}	pix^0
b_2	Eqn. 4.4	8.5×10^{-5}	pix^0

that of the reticle beam (described by Eqns. 4.1–4.4). However, the binary star observations will show (§4.4.4) that the high-order parameterization obtained from the reticle experiment is adequate for the science beam. This implies that most of the high-order distortion in the science beam arises in PALAO and PHARO, after the primary and secondary telescope mirrors, in agreement with the larger number of optics at that point in the optical train.

A tilted plane can be parameterized by two angle variables in the detector coordinate system: one, ζ, to specify the tilt between the two planes, and another, ϕ, to specify the orientation of their intersection (a line). Figure 4.10 demonstrates this parameterization for the detector (x', y') and tilted beam (x_b, y_b) planes, which intersect along the line AB. The projection (x_t, y_t) of the (x_b, y_b) coordinate system on the detector is a suitable one to use for images of the sky, since the x_t and y_t axes are orthogonal. The projections of any other pairs of orthonormal (x_b, y_b) axes, where neither of the vectors $\mathbf{x_b}$ or $\mathbf{y_b}$ lie along AB, would not be mutually orthogonal and would require an extra parameter for their description.

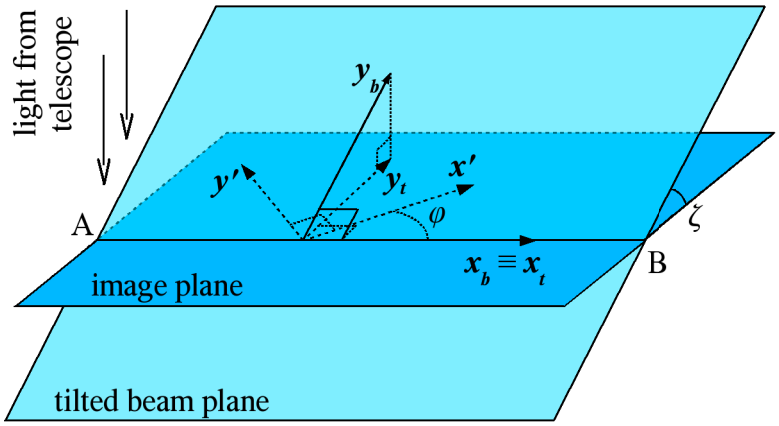

Figure 4.10: A diagram of the intersection between the detector image plane (x', y') and the tilted beam plane (x_b, y_b). The two planes intersect along the line AB at an angle ζ. The orientation of AB with respect to the detector x axis in the image plane is ϕ. The projections of the $\mathbf{x_b}$ and $\mathbf{y_b}$ unit vectors onto the image plane are denoted as $\mathbf{x_t}$ and $\mathbf{y_t}$. Right angles are marked with square corners.

Because the x_t and y_t unit vectors do not have the same length ($\mathbf{x_b}$ and $\mathbf{y_b}$ do), distances along the x_t direction will be magnified by $|\mathbf{x_t}|/|\mathbf{y_t}| = 1/\cos\zeta$ with respect to distances along the y_t direction. Furthermore, a 90° rotation of a vector in the telescope beam plane (x_t, y_t; e.g., via a CR rotation) will, in general, result in a $90° + \epsilon$ rotation of the projection of the vector on the detector. For small values of ζ, $-\zeta^2/4 \leq \epsilon \leq \zeta^2/4$. This is precisely the effect that limited the absolute determination of the plate scale in §4.4.2. By taking images of a single binary star at two different orientations of the CR, from the two independent measurements of the binary separation and position angle, I can determine the direction ϕ of the tilt and the magnification factor $1/\cos\zeta$. I was unable to do this with the reticle because the orientation of the reticle beam was fixed with respect to the detector.

To this end, I transform the detector (x', y') coordinates of each of the binary components to the (x_t, y_t) coordinate system, apply a magnification of $1/\cos\zeta$ along the y_t axis, and transform back to the detector system. The final coordinates (x'', y''), obtained in this manner, are the fully distortion-corrected pixel

coordinates. Using the center of the detector (512,512) as the origin, the exact coordinate transformations are:

$$\begin{pmatrix} x_t \\ y_t \end{pmatrix} = \begin{pmatrix} \cos\phi & \sin\phi \\ -\frac{\sin\phi}{\cos\zeta} & \frac{\cos\phi}{\cos\zeta} \end{pmatrix} \begin{pmatrix} x' - 512 \\ y' - 512 \end{pmatrix} \tag{4.5}$$

$$\begin{pmatrix} x'' \\ y'' \end{pmatrix} = \begin{pmatrix} \cos\phi & -\sin\phi \\ \sin\phi & \cos\phi \end{pmatrix} \begin{pmatrix} x_t \\ y_t \end{pmatrix} + \begin{pmatrix} 512 \\ 512 \end{pmatrix}. \tag{4.6}$$

Therefore:

$$\begin{pmatrix} x'' \\ y'' \end{pmatrix} = \begin{pmatrix} \frac{\sin^2\phi}{\cos\zeta} + \cos^2\phi & \sin\phi\cos\phi - \frac{\sin\phi\cos\phi}{\cos\zeta} \\ \sin\phi\cos\phi - \frac{\sin\phi\cos\phi}{\cos\zeta} & \sin^2\phi + \frac{\cos^2\phi}{\cos\zeta} \end{pmatrix} \begin{pmatrix} x' - 512 \\ y' - 512 \end{pmatrix} + + \begin{pmatrix} 512 \\ 512 \end{pmatrix} \tag{4.7}$$

4.4.3.2 Solving for the Beam Tilt

I solved Eqn. 4.7 using observations of the calibration binaries WDS 16147+3352 and WDS 18055+0230 taken at four orthogonal CR orientations: 333.5° (nominal), 63.5°, 153.5°, and 243.5°. Detailed observations of these two binaries were conducted on July 15 and 16 2003 (Table 4.2), where the binaries were dithered over the entire array at each CR angle, with the purpose of mapping the pixel scale distortion. Because of the 90° step between CR orientations, the final distortion-corrected coordinates x'' and y'' should map onto each other from one CR orientation to the next. That is,

$$\Delta x''_{333.5} = \Delta y''_{63.5} = \Delta x''_{153.5} = \Delta y''_{243.5} \tag{4.8}$$

$$\Delta y''_{333.5} = \Delta x''_{63.5} = \Delta y''_{153.5} = \Delta x''_{243.5}, \tag{4.9}$$

where $\Delta x''_\psi$ and $\Delta y''_\psi$ are the x'' and y'' components of the distortion-corrected binary separation at a CR angle of ψ. Eqns. 4.8 and 4.9 can be solved for each

pair of mutually perpendicular CR orientations, yielding four distinct solutions per binary star for the orientation ϕ of the beam tilt and for the magnification factor $1/\cos\zeta$. Combining the results for the two binaries, I find

$$\phi = 83.3^\circ \pm 2.5^\circ \tag{4.10}$$

$$\frac{1}{\cos\zeta} = 1.0069 \pm 0.0006, \tag{4.11}$$

where the uncertainties represent the r.m.s. scatter of the 8 solutions. The beam tilt angle is thus $\zeta = 6.7^\circ$. This is too large compared to the 0.1° detector tilt from the PHARO design specifications. It is also unrelated to the possible tilt of the reticle beam because the reticle is not in the science beam. The observed science beam tilt may be due to the fact that the detector is likely offset from the center of the focal plane, in which case the dominant term of the pincushion or of the barrel distortion may be tilt.

After adding beam tilt, parameterized by ϕ and $1/\cos\zeta$ to the overall distortion correction, the astrometric measurements of the calibration binaries become randomly distributed around the mean value and have their r.m.s. scatter reduced by a factor of 4. Figure 4.11 shows the improvement in the pixel scale uniformity, as calculated using WDS 16147+3352 after applying the full distortion correction. For this calibration binary, the astrometric precision was 0.44% (r.m.s.) without applying any beam tilt or distortion tilt correction (Fig. 4.7). The r.m.s. scatter improves to 0.25% after applying the beam tilt correction and further decreases to 0.11% after applying both the beam tilt and the higher-order distortion correction. The largest astrometric r.m.s. scatter, 0.15%, is observed in the case of the binary WDS 18055+0230. This I set as the overall limit on the precision with the PHARO 25 mas pix^{-1} camera.

4.4.3.3 Complete Characterization of the Detector Distortion

The complete distortion solution for the 25 mas pix^{-1} PHARO pixel scale is thus based on Eqns. 4.1–4.4 and 4.7–4.11, with the relevant polynomial coef-

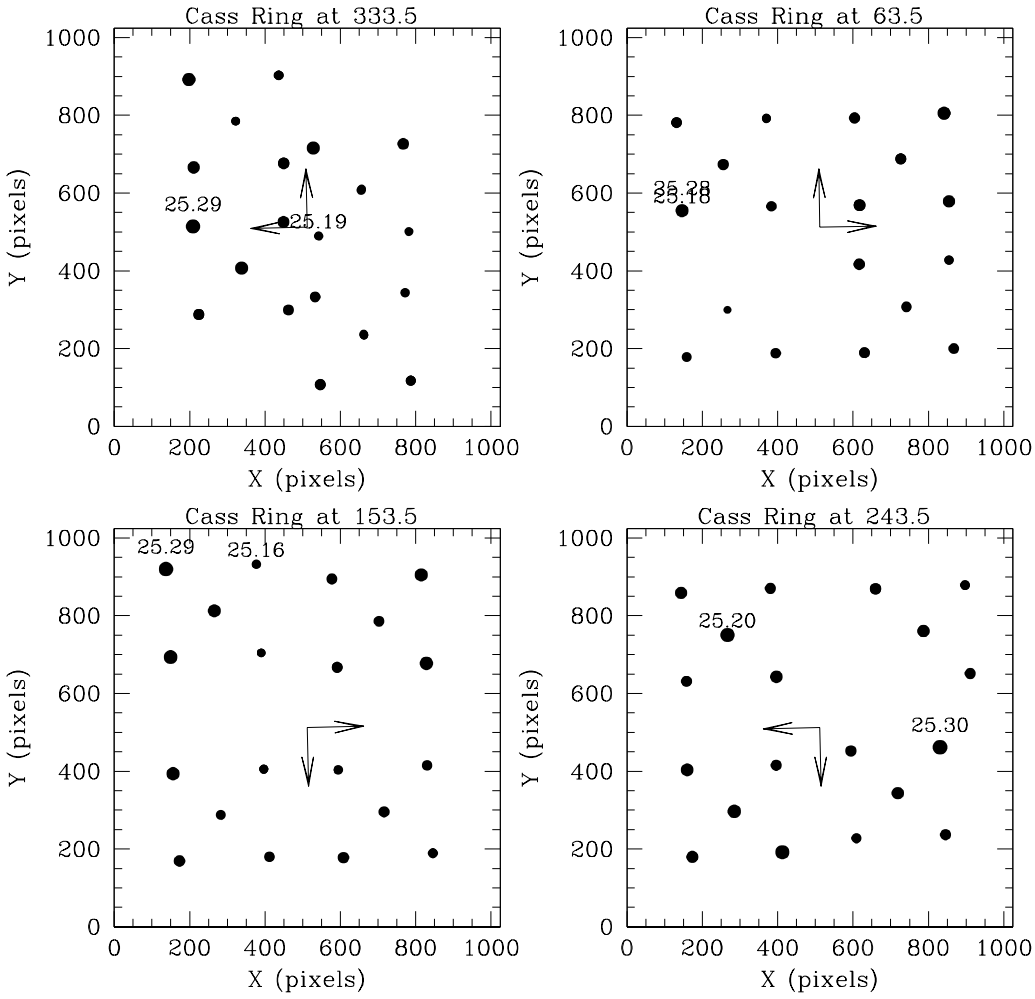

Figure 4.11: Same as Fig. 4.7, but after applying the full distortion correction (§4.4.2 and §4.4.3). The pixel scale values are randomly distributed and have a decreased range of variation.

ficients tabulated in Tables 4.4 and 4.5. A suite of IDL programs that corrects the PHARO distortion using these mathematical relations can be found at http://www.astro.caltech.edu/~metchev/AO/PHARO_25mas_distortion/.

Figure 4.12 illustrates the total amount of distortion (arrows) present on the array with the telescope pointed at zenith and the CR rotator at two mutually perpendicular orientations: 333.5° (nominal; panels a, b) and 63.5° (panels c, d). The dashed lines in Fig. 4.12a,c indicate the high-order distortion component only. In the case of the nominal CR setting, the dashed lines are identical to the arrows in Fig. 4.8a. Figure 4.12 clearly demonstrates that beam tilt is the dominant source of pixel scale distortion and that it is a strong function of the CR angle.

4.4.4 Absolute Pixel Scale of the 25 mas pix^{-1} PHARO Camera

Having achieved a quantitative understanding of the distortion of the PHARO camera, I can now accurately determine its mean pixel scale and orientation with respect to the celestial compass rose. For the purpose, I use the results from the calibration binary observations. The derived pixel scale and CR angle $\mathrm{CR_N}$ at which the detector is aligned with the celestial axes are given in Table 4.6. The table lists the individual values for each calibration binary observation at each CR angle, the mean values for each star from all (N) measurements on a given date at each CR angle, and the overall mean values from all stars. In calculating the mean values I have excluded binaries with angular separations $\lesssim 0.5''$ (WDS 15232+3017, WDS 23052–0742, and WDS 23322+0705) because of partial PSF overlap that brings the measured centroids closer together and overestimates the pixel scale. In addition, I excluded observations taken in poor seeing conditions, as these displayed complex PSF structure that could not be adequately fit by Gaussian functions. All excluded observations have been correspondingly marked in the last column of Table 4.6.

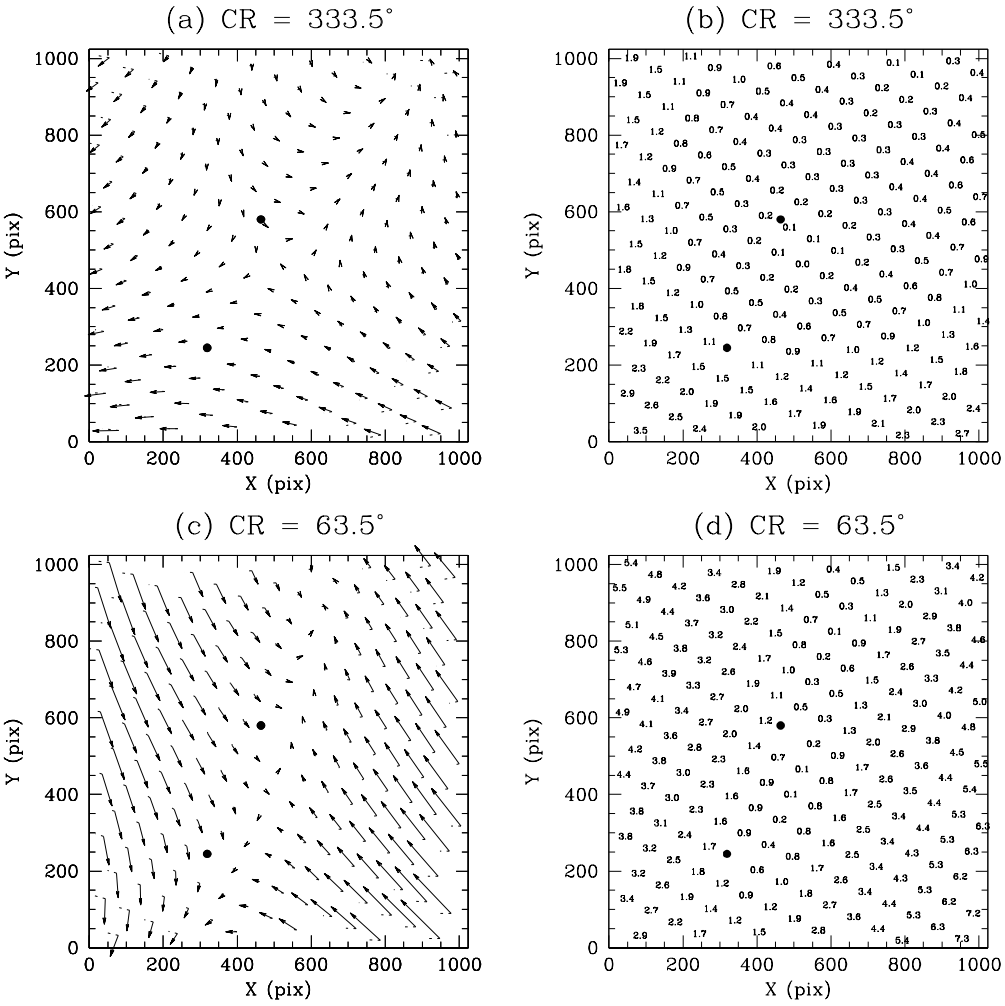

Figure 4.12: Distortion of the PHARO 25 mas pix^{-1} camera with the telescope pointed at zenith and at CR angles of 333.5° (nominal orientation; panels a, b) and 63.5° (c, d). The arrows in panels (a, c) denote the total distortion, while the dashed lines denote the high-order distortion component only. The length of the arrows corresponds to the pixel magnitude of the distortion (panels c, d) multiplied by a factor of 10. A comparison to a distortion-corrected map of the array, as in Figure 4.8, is not possible, because a finely-spaced grid of measurements of the calibration binaries was not obtained. Instead, the accuracy of the distortion correction is inferred from the small scatter in the pixel scale across the array (Fig. 4.11).

Table 4.6: Pixel Scale and Orientation of the 25 mas pix^{-1} PHARO Camera

Binary (WDS)	Date (UT)	CR Angle (degrees)	Pixel Scale[a] (mas pix^{-1})	CR_N^a (degrees)	N	Note
09006+4147	May 10, 2003	63.5	25.154 ± 0.028	334.497 ± 0.040	25	
	Dec 9, 2003	243.2	25.161 ± 0.028	334.629 ± 0.102	10	
	Feb 5, 2004	333.5	25.121 ± 0.059	334.622 ± 0.108	25	
		243.5	25.150 ± 0.054	334.580 ± 0.082	10	
	Feb 6, 2004	333.5	25.162 ± 0.079	334.514 ± 0.105	20	
		243.5	25.196 ± 0.040	334.520 ± 0.066	14	
	Oct 4, 2004	332.9	25.091 ± 0.034	334.559 ± 0.059	10	
	mean		$\mathbf{25.138 \pm 0.031}$	$\mathbf{334.564 \pm 0.060}$	**5**	
15232+3017	Jun 28, 2004	152.9	24.027 ± 0.017	331.368 ± 0.049	13	excl.
16147+3352	Jul 15, 2003	333.5	25.235 ± 0.020	334.767 ± 0.033	87	
		63.5	25.236 ± 0.021	334.768 ± 0.030	62	
		153.5	25.234 ± 0.025	334.744 ± 0.025	60	
		243.5	25.242 ± 0.026	334.814 ± 0.040	55	
	Jun 28, 2004	152.9	25.230 ± 0.014	334.641 ± 0.055	5	
	mean		$\mathbf{25.235 \pm 0.004}$	$\mathbf{334.747 \pm 0.064}$	**5**	
18055+0230	Jul 16, 2003	333.5	25.023 ± 0.029	334.262 ± 0.054	25	
		63.5	25.026 ± 0.025	334.281 ± 0.048	25	
		153.5	25.037 ± 0.018	334.334 ± 0.028	5	
		243.5	25.028 ± 0.025	334.334 ± 0.058	25	
	Sep 21, 2003	63.5	25.077 ± 0.025	334.427 ± 0.047	25	
	Feb 5, 2004	333.5	25.069 ± 0.054	334.199 ± 0.099	25	excl.
	Feb 6, 2004	333.5	25.036 ± 0.028	334.203 ± 0.079	15	
	Feb 7, 2004	333.5	25.025 ± 0.011	334.223 ± 0.023	10	
	Jun 26, 2004	332.9	25.032 ± 0.019	334.184 ± 0.044	5	
		62.9	25.003 ± 0.016	334.169 ± 0.042	5	
		152.9	25.030 ± 0.016	334.209 ± 0.045	5	
		242.9	25.007 ± 0.026	334.214 ± 0.023	5	
	Jun 27, 2004	152.9	25.034 ± 0.087	334.143 ± 0.196	5	excl.
	Jun 28, 2004	62.9	25.005 ± 0.010	334.165 ± 0.029	5	
	Oct 5, 2004	332.9	25.023 ± 0.009	334.167 ± 0.028	5	
		242.9	25.022 ± 0.012	334.190 ± 0.032	5	
	mean		$\mathbf{25.028 \pm 0.018}$	$\mathbf{334.240 \pm 0.078}$	**14**	
20467+1607	May 11, 2003	243.5	25.198 ± 0.014	335.086 ± 0.025	20	
	Jun 26, 2004	152.9	25.188 ± 0.029	335.084 ± 0.039	10	

continued on next page

Table 4.6 – continued from previous page

Binary (WDS)	Date (UT)	CR Angle (degrees)	Pixel Scale[a] (mas pix^{-1})	CR_N^a (degrees)	N	Note
	Jun 27, 2004	152.9	25.191 ± 0.008	335.045 ± 0.022	5	
	Oct 5, 2004	332.9	25.209 ± 0.017	335.027 ± 0.014	5	
		242.9	25.187 ± 0.004	335.075 ± 0.012	5	
	mean		$\mathbf{25.195 \pm 0.009}$	$\mathbf{335.063 \pm 0.026}$	**5**	
23052−0742	Sep 21, 2003	63.5	26.834 ± 0.646	332.078 ± 1.538	8	excl.
23322+0705	Sep 20, 2003	333.5	27.265 ± 0.439	333.830 ± 0.392	22	excl.
		63.5	27.275 ± 0.300	332.919 ± 0.991	19	excl.
	mean		27.270 ± 0.007	333.375 ± 0.644	2	excl.
overall unweighted mean			$\mathbf{25.149 \pm 0.090}$	$\mathbf{334.654 \pm 0.344}$	**4**	
corrected for binary systematics			$\mathbf{25.001 \pm 0.039}$	$\mathbf{334.92 \pm 0.12}$	**3**	
predicted			**25.10**[b]	**335.8**[c]		

[a] The errors listed represent only the 1σ measurement scatter. They are not the errors of the means, which would be a factor of $\sqrt{N-1}$ smaller for N measurements. They also do not include the errors in the ephemerides of the binaries.

[b] Hayward et al. (2001).

[c] Day crew setting before 2003.

An unweighted average of the mean measurements of the 4 calibration binaries produces a distortion-free pixel scale of 25.149 ± 0.090 mas pix^{-1} and $CR_N = 334.65 \pm 34°$. The quadrature sum of the r.m.s. scatter of the two indicate that the achieved astrometric accuracy is 0.76%—not a big improvement on the initially determined value (§4.2). However, a closer inspection of the mean pixel scales derived from each binary reveals that the results from the same binary are very self-consistent—to within 0.15%—over the course of 2 years. A comparison of the mean results among the different binaries, on the other hand, shows that they are significantly (5–10σ) discrepant. Thus, the scatter in the final values of the pixel scale and CR_N angle are dominated by systematic differences in the orbital solutions for the four calibration binaries: WDS 09006+4147, WDS 16147+3352, WDS 18055+0230, and WDS 20467+1607. These differences are confirmed from independent and concurrent (2002 and 2003) interferometric observations of three of the binaries, WDS 16147+3352, WDS 18055+0230, and WDS 20467+1607 (Mason et al., 2004a,b), which demonstrate that the orbital solutions mis-predict the binary separation and position angle by as much as 0.8% (WDS 16147+3352) and

0.7° (WDS 18055+0230), respectively. The discrepancies between the observations and the derived orbits are such that they make the mean pixel scales and orientations of the individual binaries more consistent, and the fractional astrometric accuracy considering all 3 of these binaries improves to 0.32% (penultimate line in Table 4.6). To take advantage of the even higher accuracy characteristic of repeated measurements of the same binary, the entire astrometric calibration can be tied to that binary. However, the astrometry in that case will not be correct in absolute terms.

After correcting for systematics in the calibration binaries, the final distortion-free pixel scale of the PHARO 25 mas pix^{-1} camera is 25.001 ± 0.039 mas pix^{-1} (Table 4.6). This value is marginally (2.5σ) consistent with the optical design prediction of 25.10 mas pix^{-1}. The orientation of the CR rotator at which celestial north is aligned with the detector y-axis is $\mathrm{CR_N} = 334.92 \pm 0.12°$ and is 6σ discrepant from the previous setting. The setting has been updated as a result of our orientation measurements.

As a final note, it is important to observe that the distortion-corrected pixel scale is lower than all previous determinations: both the one design value and all of the binary star measurements. This is a result of the fact that the mean value of the magnification factor $1/\cos\zeta$ is greater than unity. $1/\cos\zeta$ was defined as the magnification of one of the beam tilt axes with respect to the other. That is, physical scales are normalized to measurements along one of the two tilt axes (y_t; Fig. 4.10). If, instead, an average magnification value of $1/\bar{\cos}\,\zeta = (1 + 1/\cos\zeta)/2 = 1.0034$ was used, the distortion-corrected pixel scale would become fully consistent (25.09 ± 0.04 mas pix^{-1}) with the design value. Either pixel scale can be used to obtain the exact same astrometric result, as long as the overall distortion solution is adjusted for the adopted value of the magnification.

4.4.5 Other Sources of Pixel Scale Variations

4.4.5.1 Cassegrain Ring Orientation

The solution for the pixel scale distortion in §4.4.2 includes terms linearly dependent on the hour angle and declination of the telescope. These are most probably associated with the changing direction of the gravity vector on PALAO and PHARO. Rotations of the CR are expected to have a similar effect, especially at high zenith angles. This expectation was confirmed through a comparison of two sets of reticle images taken at zenith and at -30° declination on the meridian, with the CR angle stepped through the 4 mutually orthogonal orientations used for binary star observations (§4.3.2 and §4.4.3.2). Similarly to the dependence on hour angle and declination, the dependence on CR angle is also concentrated in the linear terms of Eqns. 4.1 and 4.2, and the range of parameter variation is comparable—within 0.0007 pix pix^{-1} of the mean value.

Exploring this dependence would have required four times as much engineering time as already devoted (6 hours) to the observations for this experiment, which was unavailable considering the schedule of science operations with the $200''$ telescope. As discussed in §4.4.4, the achieved astrometric precision as a result of the experiments described here has already reached the desired goal of 0.15%. Given that, other than during my sub-stellar companion survey, the telescope is rarely used with extensive CR rotations in imaging mode, the necessity for a further calibration of this dependence is marginal. If only the observations taken near the nominal CR setting (333.5°) are considered in the current set of calibration binary data, the astrometric precision for the calibration binary with largest r.m.s. scatter (WDS 18055+0230) further improves to 0.09%. This may be the hard limit, beyond which random effects, such as non-simultaneous read-out of the detector quadrants (§4.4.5.3) may dominate.

4.4.5.2 Choice of Intermediate Optics

In addition to determining the distortion of the pixel scale across the PHARO detector and its variation with telescope pointing, the pinhole mask experiment was also aimed at establishing the dependence of the pixel scale on the selection of intermediate camera optics. Such dependence may be present because of variations in the thickness and indices of refraction within individual transmissive optics.

I find that the various settings of the filter, Lyot, and grism wheels affect (by up to 2 pix) the absolute positions of the pinhole images on the array. However, they do not affect their relative placement with respect to each other, indicating that the optics are uniform within the measurement errors.

4.4.5.3 Detector Readout

Unexpectedly, I discovered an occasional shear by up to 0.6 pix in x and 0.4 pix in y among the relative positions of the pinhole images in different detector quadrants. The shear is $>$0.1 pix in magnitude in approximately 20% of all images taken with the reticle. Such sheared images have been excluded from the parameterization of the pixel scale in §4.4.1 and §4.4.2. The reason for this probably lies in non-simultaneity of the charge transfer and/or read-out of the 4 detector quadrants. Because this effect is constant in magnitude between a pair of PHARO quadrants, its fractional significance increases at shorter separations: e.g., for a binary with a pixel separation of 10 pix ($\approx$0.25″), the relative astrometric error may be as high as 7%, and may completely foil any attempts at, for example, measuring orbital motion. However, the likelihood that such a close binary will span detector quadrant boundaries in more than one of a series of images is small. Nevertheless, future users of PALAO/PHARO should bear this effect in mind and avoid imaging close multiple systems near the center of the array, where the likelihood that the individual stellar components are in different detector quadrants is higher.

4.5 Conclusion of the PHARO Pixel Scale Experiment

I designed and implemented a pinhole mask astrometric experiment, which revealed with superior accuracy, compared to previous binary star experiments, the distortion on the array. By combining the results from this experiment with observations of binary stars with known orbits, I arrived at a full formulaic description of the PHARO 25 mas pix^{-1} pixel scale as a function of telescope hour angle, declination, and Cassegrain ring orientation. As a result, the precision of astrometric measurements with PHARO was improved over the previously determined pointing-independent limit of $\lesssim$0.9% (Memo II) by a factor of 3–10. Although measurable discrepancies between the orbital predictions for the calibration binaries precluded a calibration of the pixel scale to better than 0.32% ($10^{-2.5}$), I showed that multi-epoch observations of the same calibration binary at different CR angles are consistent to within 0.15% ($10^{-2.8}$). Furthermore, if observations obtained only at a single CR angle were compared, the self-consistency improved to 0.09% ($10^{-3.1}$). This accuracy was maintained throughout the two-year period over which the measurements were taken.

Given the use of multiple CR orientations in my survey, I adopt 0.15% as the calibration limit of my astrometric accuracy. This allows me to test at the $\sim 3\sigma$ confidence level the physical association of candidate pairs of stars with proper motions as small as 50 mas yr^{-1}, after only a year of observations, and nearly out to the edges of the PALAO/PHARO $25'' \times 25''$ field.

4.6 Astrometry with PHARO and NIRC2: Errors and Accuracy

When investigating changes in the relative positions between objects with small proper motions, a thorough identification of the sources of astrometric error and a careful propagation of such errors is crucial. While performing the error analysis for my companion survey, I have kept track of random and systematic uncertainties

arising from the following sources: (1) object pixel centering, (2) centering of the primary behind the coronagraph, (3) pixel scale distortion, (4) knowledge of the ephemeris of the binary standards used for astrometric calibration, and (5) knowledge of the heliocentric distance and proper motion of the primary. The errors from these various sources are carefully propagated through any rotations, such as when aligning Palomar images taken at different detector orientations, while also carrying over the resulting covariances.

For all but the faintest candidate companions, error (1) is of order $<$0.1 pix (2.5 mas for PHARO, 4.0 mas for NIRC2) and contributes negligibly to the overall error budget.

The errors associated with (2) are significant only for Palomar astrometry because the PHARO coronagraphic spot is opaque, and only when the relative position of a companion could not be bootstrapped with respect to that of another object visible in both the coronagraphic and non-coronagraphic images. In such cases I determined the position of the primary behind the PHARO coronagraph by cross-correlating the coronagraphic images with 180°-rotated versions of themselves, using the image center (pixel 512,512) as the rotation origin. This is, in effect, an auto-correlation technique. The calculated x, y pixel shift between the two versions of the same image was twice the magnitude of the $\Delta x, \Delta y$ pixel offset of the star from the center of the array. I was thus able to retrieve the absolute pixel position of the star within an error circle of radius 0.50 pix (12.5 mas). For NIRC2, which has coronagraphic spots that are partially transmissive and thus allow accurate object centering, the error from (2) has the same magnitude as the object centering error (1).

Detector distortion errors (3) are significant in both PHARO and NIRC2. My preceding analysis of the PHARO pixel scale distortion showed that it is known to a fractional accuracy of 0.15% across the array for images taken at multiple CR orientations. The corresponding distortion-related error reaches a maximum of 19 mas at the outer radius (12.5″) of my survey. For NIRC2, the overall r.m.s. residual of the distortion-corrected pixel coordinates in the wide (40 mas pix^{-1})

camera is 0.64 pix (26 mas), though a factor of $\sim$2 smaller within $4''$ of the array center (Thompson et al., 2001).

The fourth source of error is significant when the systematic differences between the orbital predictions of the various calibration binaries are unknown. I have strived to minimize this effect by using a limited number of calibration binaries at all observing epochs. The astrometry for all 2003–2005 Palomar and 2004 Keck observations is tied to the separation and orientation of a single calibration binary, WDS 18055+0230, allowing astrometric accuracy of 0.15%. Because of the consistency of the PHARO pixel scale during 2003 and 2004, I have adopted this accuracy also for PHARO data taken in 2002, when the need for repeated astrometric calibration was unappreciated. Comparisons with Keck 2003 astrometry are more problematic, as a systematic effort to observe the same calibration binaries at both telescopes was made only in 2004. Furthermore, while the PHARO orientation has remained constant with respect to the Cassegrain ring within the measurement errors, consecutive observing campaigns with NIRC2 show that the detector orientation changes by up to 0.7°, though it remains approximately constant over consecutive nights during the same observing run. On three NIRC2 nights (16–18 May, 2003) during which I did not observe one of the three calibration binaries used for the absolute determination of the PHARO pixel scale, the absolute orientation of NIRC2 was not known to better than $\approx 0.3^\circ$. I have attempted to minimize the associated uncertainties by relying on Palomar astrometry in the relevant cases.

Finally, the effect of (5) was negligible in all cases, given that the parallaxes and yearly proper motions of all stars are known to (generally much) better than $\sim$10 mas, i.e., at least to a factor of 2 smaller than the dominant sources of error (2–4).

By averaging the measured change in the positions of stationary background sources discovered over the 3-year period of my survey (§5), I find that the overall attained astrometric precision is: 0.16% ($10^{-2.8}$) for Palomar non-coronagraphic observations, 0.38% ($10^{-2.4}$) for Palomar coronagraphic observations, and 0.40%

($10^{-2.4}$) for Keck (coronagraphic) observations. My non-coronagraphic astrometry with Palomar is therefore limited to the level at which astrometric observations at different CR angles can be calibrated. With more regular monitoring, I expect that the precision of the Keck NIRC2 wide-camera astrometry can be improved at least to the same level. Even greater gains in astrometric accuracy with NIRC2 should be possible by using the finer pixel scale (10 and 20 mas pix^{-1}) cameras, which at minimum provide Nyquist sampling of the $\approx$50 mas Keck K-band PSF.

Chapter 5

Complete Survey: Observations, Detection, and Association of Candidate Companions

In §3 we described the observing strategy and presented the basic analytical methodology of the Palomar/Keck survey for companions to young solar analogs. In §5.1 of the present chapter we list the full set of observations and provide further pertinent details of the Palomar and Keck imaging campaigns. Recommendations for future high-contrast imaging campaigns with PALAO are also discussed in this §5.1.1 and §5.1.3). Then, in §5.2, we discuss the object detection approach and the empirically-constrained detection limits. The complete list of candidate companions detected in first-epoch imaging is given in §5.3, Tables 5.6 and 5.7. Section §5.4 presents a discussion of the various methods employed for constraining physical association of the companions with the respective primaries.

5.1 Observations

The full sample of 266 stars, selected as discussed in §2, was observed with AO at Palomar and Keck II over the course of 3 years, between Jan 31, 2002, and Jan 24, 2005. Tables 5.1 and 5.2 list the epochs and atmospheric conditions during each night of observations. The Palomar campaign was conducted with the PALAO system (Troy et al., 2000) and the PHARO near-IR camera (Hayward et al., 2001) in its 25 mas pix^{-1} mode providing a $25.6'' \times 25.6''$ field of view. At Keck, we used

the facility AO system (Wizinowich et al., 2000) on Keck II and the NIRC2 near-IR camera (Matthews et al., in preparation) in its 40 mas pix^{-1} mode, offering a field of view of $40.6'' \times 40.6''$. A detailed description of the observing approach was provided in §3.3.2.

Throughout the remainder of this work, we will consider only candidate companions detected with a radius of $12.5''$ from each star. This we set as the outer working angle (OWA) of the survey. The limit is $0.3''$ (12 pix) smaller than the half-width of the PHARO camera in 25mas pix^{-1} mode, thus excluding pixels on the edges of the PHARO array, which have a higher incidence of being bad or having high dark current. The OWA excludes any candidate companions detected in the corners of the PHARO chip or at $>12.5''$ separations with NIRC2 on Keck. In any case, the positions of such widely-separated objects generally suffer from appreciable astrometric uncertainties (§4), and thus little can be inferred about their physical association with the respective candidate primaries over the time span of the survey. Conversely, the use of a single OWA for the Palomar and Keck components of the survey allows the data to be considered as an ensemble. In addition, a fixed OWA, rather than a survey region matched to the rectangular of the PHARO detector, allows a simple centrally symmetric analysis.

We define the inner working angle (IWA) of the survey to be $0.55''$. This is $0.065''$ and $0.05''$ larger than the radii of the respective PHARO and NIRC2 coronagraphic spots that we used. The difference corresponds approximately to the half-width at half-maximum ($0.05''$) of the Palomar K_S-band PSF, following the idea that the entire PSF core of a point source would have to be visible outside the coronagraphic for it to be identified as a candidate companion.

Table 5.1: Palomar Observations

Date (UT)	V-band Seeing (arcsec)		Cloud Cover
	start	end	
2002 Jan 31	2.0	2.5	clear
2002 Feb 01	1.5	2.0	clear
2002 Feb 28	<1.0	<1.0	cirrus
2002 Mar 01	1.2	3.0	clear, fog
2002 Mar 02	3.5	2.0	clear
2002 Mar 03	3.0	4.0	clear
2002 Jun 21	1.0	1.0	clear, then cloudy
2002 Jun 22	0.8	1.0	clear
2002 Jun 23	1.2	1.0	clear
2002 Aug 27	1.3	1.1	clear
2002 Aug 28	1.0	1.0	clear
2002 Aug 29	1.2	1.0	mostly clear
2002 Aug 30	1.0	1.0	clear
2002 Aug 31	1.2	1.2	scattered cirrus to cloudy
2002 Nov 16	1.9	1.4	some cirrus, then clear
2002 Nov 17	1.3	1.2	variable cirrus, clear at end
2002 Nov 18	1.8	1.2	scattered cirrus
2003 Jan 11	1.2	1.5	cloudy, then clear
2003 Jan 12	1.2	1.0	mostly clear

continued on next page

Table 5.1–continued from previous page

Date (UT)	V-band Seeing (arcsec)		Cloud Cover
	start	end	
2003 Jan 13	1.1	1.1	mostly clear
2003 Jan 14	1.0	1.1	variable cirrus
2003 May 10	1.4	1.1	clear
2003 May 11	1.5	2.0	clear, then scattered cirrus
2003 May 13	1.5	1.5	cloudy
2003 Jul 14	0.9	1.2	variable cirrus
2003 Jul 15	0.9	1.4	cirrus, then clear
2003 Jul 16	1.1	1.2	variable clouds
2003 Sep 20	1.0	1.0	clear
2003 Sep 21	1.2	1.9	clear
2003 Dec 09	3.0	2.0	clear
2003 Dec 10	1.3	2.2	clear, fog
2004 Feb 05	1.4	2.0	clear
2004 Feb 06	3.0	2.3	variable cirrus
2004 Feb 07	0.9	1.5	thin cirrus, then clear
2004 Jun 04	1.0	0.8	clear
2004 Jun 26	1.2	1.1	mostly clear
2004 Jun 27	1.4	1.0	clear
2004 Jun 28	1.2	1.1	clear
2004 Oct 03	0.9	0.9	clear
2004 Oct 04	1.0	1.0	clear
2004 Oct 05	1.0	1.0	clear
2005 Jan 24	1.6	1.6	clear for 0.5 hrs, then closed

Observations of the 101 stars in the deep sample were obtained at Palomar and/or Keck, with a total of 48 of these observed at Keck. The Keck observations were generally conducted to follow-up candidate companions from prior-epoch imaging at Palomar. However, 7 stars were observed coronagraphically only

Table 5.2: Keck Observations

Date (UT)	V-band Seeing (arcsec)	Cloud Cover
2003 May 16	0.7	clear, then cirrus
2003 May 17	1.0	partly cloudy
2003 May 18	1.0	cirrus
2003 Nov 09	0.7	some cirrus
2003 Nov 10	0.5	cirrus, then clear
2004 Jun 05	1.0	clear
2004 Jun 06	0.8	clear
2004 Oct 07	0.8	some cirrus
2004 Oct 08	1.2	cirrus, sometimes thick

at Keck. The 165 stars in the shallow sample were observed only at Palomar. Tables 5.3 and 5.4 list the epochs and mode of imaging observations for all stars in the deep and shallow samples. Stars determined to be single during the first ("discovery") imaging epoch were not followed up. Stars showing candidate companions were re-imaged at later epochs, where multiple follow-up visits were paid to stars with small proper motions to better constrain the likelihood of association between any of the field objects and the primary.

The Palomar coronagraphic observations nominally amounted to 24 min of on-source integration time at K_S band during the discovery epoch. When the brightness of the candidate companions allowed it, subsequent imaging at Palomar was shallower. For Keck observations the total K_S exposure time was 6 min, which resulted in similar or greater depth of imaging, compared to Palomar. In cases when the depth of the Palomar discovery epoch images was inadequate because of insufficient exposure time or poor weather, a repeated deep image was attempted at a later epoch, at either Palomar or Keck. Thus, most of the targets in the deep sample were imaged to the nominal depth of the survey. This was not achieved

only for 11 deep-sample stars, which were observed only at Palomar for less than 24 min each and/or in poor weather. Such stars have entries in the 'Notes' column of Table 5.3, where we have specified the length of the total exposure (if <24 min) at each epoch of observations, and whether the imaging quality was poor.

Additional limitations on the imaging depth of the Palomar observations dependent on the choice of Lyot stop and attenuating optic are discussed in §5.1.1. Section §5.1.2 discusses the corresponding details for the Keck observations. The two sections also present calibrations of the near-IR transmissivities of relevant attenuating optics: the PHARO ND 1% filter and the NIRC2 coronagraphic spots. Tables 5.1 and 5.2 list the observation epochs at Palomar and Keck, respectively, along with notes on the atmospheric conditions for each night of observations.

In the final part (§5.1.3) of this section, we discuss in greater detail than addressed in §3.3.2.1.1 the benefits and limitations of the CR rotation approach to imaging at Palomar.

Table 5.3: Deep Sample Observations

Star	UT Date	Observatory	Optic	Lyot Stop	Notes
HD 377	2002-08-28	Palomar	corona	Medium cross	
	2003-11-09	Keck	corona		deepest
	2004-10-07	Keck	corona		
HD 691	2002-08-31	Palomar	corona	Medium cross	
	2002-11-18	Palomar	corona	Medium cross	deepest
HD 984	2002-08-29	Palomar	corona	Medium cross	deepest
	2003-09-20	Palomar	corona	Medium cross	
	2004-10-04	Palomar	corona	Medium cross	
HD 1405	2004-06-06	Keck	corona		deepest
QT And	2002-08-29	Palomar	corona	Medium cross	
	2003-11-10	Keck	corona		deepest

continued on next page

Table 5.3–continued from previous page

Star	UT Date	Observatory	Extra Optic	Lyot Stop	Notes
	2004-10-07	Keck	corona		
HD 7661	2002-08-30	Palomar	corona	Medium cross	
	2002-11-09	Keck	corona		deepest
HIP 6276	2002-08-30	Palomar	corona	Medium cross	deepest
	2004-10-08	Keck	corona		
HD 8907	2002-08-27	Palomar	corona	Medium cross	deepest
HD 12039	2002-08-28	Palomar	corona	Medium cross	13 min, deepest
HD 15526	2003-09-20	Palomar	corona	Medium cross	deepest
1RXS J025216.9+361658	2002-11-18	Palomar	corona	Medium cross	
	2003-11-10	Keck	corona		deepest
	2004-02-07	Palomar	corona	Medium cross	
HD 17925	2003-09-21	Palomar	corona	Medium cross	deepest
1RXS J025751.8+115759	2002-11-16	Palomar	corona	Medium cross	deepest
RX J0258.4+2947	2002-02-28	Palomar	corona	Big cross	deepest
1RXS J030759.1+302032	2002-11-18	Palomar	corona	Medium cross	deepest
HD 19668	2002-08-27	Palomar	corona	Medium cross	
	2003-11-09	Keck	corona		deepest
1E 0307.4+1424	2003-01-12	Palomar	corona	Medium cross	deepest
AP 93	2003-09-20	Palomar		Medium cross	
	2004-10-03	Palomar		Medium cross	
	2004-10-08	Keck	corona		deepest
1RXS J031907.4+393418	2002-08-29	Palomar	corona	Medium cross	
	2003-11-10	Keck	corona		deepest
	2004-10-08	Keck	corona		
HE 622	2003-09-20	Palomar		Medium cross	
	2004-10-08	Keck	corona		deepest
1E 0324.1–2012	2003-01-12	Palomar	corona	Medium cross	poor
	2004-02-07	Palomar	corona	Medium cross	
	2004-10-08	Keck	corona		deepest
RX J0329.1+0118	2003-09-21	Palomar	corona	Medium cross	deepest
HE 1101	2003-09-20	Palomar		Medium cross	
	2004-10-03	Palomar		Medium cross	
	2004-10-07	Keck	corona		deepest

continued on next page

Table 5.3–continued from previous page

Star	UT Date	Observatory	Extra Optic	Lyot Stop	Notes
HD 22179	2002-11-16	Palomar	corona	Medium cross	
	2003-11-09	Keck	corona		deepest
	2004-02-07	Palomar	corona	Medium cross	
	2004-10-08	Keck	corona		
HD 23208	2004-10-05	Palomar	corona	Medium cross	deepest
HII 120	2003-09-20	Palomar		Medium cross	
	2004-10-04	Palomar		Medium cross	
	2004-10-08	Keck	corona		deepest
HII 2147	2003-01-13	Palomar	corona	Medium cross	deepest
1RXS J035028.0+163121	2002-11-17	Palomar	corona	Medium cross	deepest
RX J0354.4+0535	2003-01-13	Palomar	corona	Medium cross	
	2004-02-07	Palomar		Medium cross	
	2004-10-07	Keck	corona		deepest
Pels 191	2002-11-18	Palomar	corona	Medium cross	10 min, deepest
RX J0357.3+1258	2003-01-11	Palomar	corona	Medium cross	
	2003-11-09	Keck	corona		deepest
	2004-02-07	Palomar	corona	Medium cross	
HD 285751	2002-01-31	Palomar	corona	Big cross	deepest
RX J0442.5+0906	2003-01-11	Palomar	corona	Medium cross	deepest
	2004-02-07	Palomar		Medium cross	
HD 286179	2002-01-31	Palomar	corona	Big cross	
	2004-02-07	Palomar		Medium cross	
	2004-10-07	Keck	corona		deepest
HD 31950	2002-11-16	Palomar	corona	Medium cross	
	2003-11-09	Keck	corona		deepest
	2004-02-07	Palomar	corona	Medium cross	
	2004-10-08	Keck	corona		
HD 35850	2002-02-01	Palomar	corona	Big cross	deepest
HD 36869	2003-01-14	Palomar	corona	Medium cross	deepest
	2004-10-05	Palomar	ND1	Medium cross	
1RXS J053650.0+133756	2002-02-28	Palomar	corona	Big cross	
	2003-01-14	Palomar	corona	Medium cross	
	2003-11-10	Keck	corona		deepest

continued on next page

Table 5.3–continued from previous page

Star	UT Date	Observatory	Extra Optic	Lyot Stop	Notes
HD 245567	2002-11-16	Palomar	corona	Medium cross	
	2003-11-09	Keck	corona		
	2004-02-07	Palomar	corona	Medium cross	
	2004-10-08	Keck	corona		deepest
SAO 150676	2002-11-17	Palomar	corona	Medium cross	
	2004-02-07	Palomar	corona	Medium cross	
	2004-10-08	Keck	corona		deepest
HD 38949	2002-11-18	Palomar	corona	Medium cross	16 min, poor, deepest
HD 43989	2004-02-07	Palomar	corona	Medium cross	8 min, poor, deepest
HD 49197	2002-02-28	Palomar	corona	Big cross	
	2003-11-09	Keck	corona		deepest
	2004-02-07	Palomar	corona	Medium cross	
RE J0723+20	2002-02-28	Palomar	corona	Big cross	deepest
	2003-01-13	Palomar		Medium cross	
	2004-02-05	Palomar		Medium cross	
HD 60737	2002-01-31	Palomar	corona	Big cross	
	2003-01-11	Palomar	corona	Medium cross	
	2003-11-10	Keck	corona		deepest
HD 70573	2002-02-01	Palomar	corona	Big cross	deepest
HD 70516	2002-01-31	Palomar	corona	Big cross	
	2002-11-16	Palomar	corona	Medium cross	deepest
HD 72905	2002-02-28	Palomar	corona	Big cross	deepest
HD 75393	2002-11-17	Palomar	corona	Medium cross	deepest
HD 82558	2003-12-09	Palomar	corona	Medium cross	18 min, deepest
HD 82443	2004-02-07	Palomar	corona	Medium cross	20 min, deepest
SAO 178272	2003-01-13	Palomar	corona	Medium cross	19 min, poor, deepest
	2004-02-07	Palomar	corona	Medium cross	6 min, poor
HD 90905	2002-02-01	Palomar	corona	Big cross	
	2003-01-12	Palomar	corona	Medium cross	
	2004-02-05	Palomar	corona	Medium cross	
	2004-06-05	Keck	corona		deepest
HD 91782	2002-03-02	Palomar	corona	Big cross	
	2003-01-11	Palomar	corona	Medium cross	

continued on next page

Table 5.3–continued from previous page

Star	UT Date	Observatory	Extra Optic	Lyot Stop	Notes
	2003-05-10	Palomar	corona	Medium cross	
	2004-02-05	Palomar	corona	Medium cross	
	2004-06-05	Keck	corona		
	2004-06-06	Keck	corona		deepest
HD 92855	2002-02-01	Palomar	corona	Big cross	
	2003-01-13	Palomar	corona	Medium cross	
	2004-02-06	Palomar	corona	Medium cross	
	2004-06-06	Keck	corona		deepest
	2004-06-26	Palomar	corona	Medium cross	
HD 93528	2004-02-07	Palomar	corona	Medium cross	deepest
HD 95188	2002-03-02	Palomar	corona	Big cross	poor, deepest
HD 101472	2002-03-02	Palomar	corona	Big cross	poor
	2003-01-14	Palomar	corona	Medium cross	12 min, deepest
BPM 87617	2003-01-12	Palomar	corona	Medium cross	deepest
	2003-07-16	Palomar		Medium cross	
	2004-02-05	Palomar		Medium cross	
HD 104576	2002-06-22	Palomar	corona	Medium cross	deepest
HD 104860	2002-06-23	Palomar	corona	Medium cross	
	2003-05-11	Palomar	corona	Medium cross	
	2004-06-05	Keck	corona		deepest
HD 107146	2002-01-31	Palomar	corona	Big cross	
	2003-01-14	Palomar	corona	Medium cross	deepest
SAO 15880	2004-02-06	Palomar	corona	Medium cross	
	2004-06-06	Keck	corona		deepest
SAO 2085	2004-02-07	Palomar	corona	Medium cross	deepest
HD 111456	2004-02-06	Palomar	corona	Medium cross	deepest
HD 132173	2002-02-28	Palomar	corona	Big cross	
	2004-02-07	Palomar	corona	Medium cross	deepest
HD 139813	2002-02-01	Palomar	corona	Big cross	
	2003-05-17	Keck	corona		
	2003-05-18	Keck	corona		deepest
HD 139498	2003-07-15	Palomar		Medium cross	
	2004-06-26	Palomar	corona	Medium cross	deepest

continued on next page

Table 5.3–continued from previous page

Star	UT Date	Observatory	Extra Optic	Lyot Stop	Notes
HD 142361	2002-06-21	Palomar	corona	Medium cross	18 min, deepest
	2003-07-16	Palomar	ND1	Medium cross	
	2004-06-27	Palomar	ND1	Medium cross	
HD 143006	2002-06-23	Palomar	corona	Medium cross	
	2003-05-18	Keck	corona		
	2004-06-05	Keck	corona		deepest
(PZ99) J155847.8–175800	2004-06-06	Keck	corona		deepest
ScoPMS 21	2002-06-22	Palomar	corona	Medium cross	
	2004-06-05	Keck	corona		deepest
(PZ99) J160302.7–180605	2003-05-18	Keck	corona		
	2004-06-06	Keck	corona		deepest
ScoPMS 27	2004-06-28	Palomar	corona	Medium cross	deepest
ScoPMS 52	2002-08-31	Palomar	corona	Medium cross	deepest
	2004-06-26	Palomar		Medium cross	
(PZ99) J161318.6–221248	2002-06-21	Palomar	corona	Medium cross	
	2003-05-18	Keck	corona		
	2004-06-05	Keck	corona		deepest
(PZ99) J161402.1–230101	2003-07-15	Palomar		Medium cross	
	2004-06-05	Keck	corona		deepest
(PZ99) J161411.0–230536	2002-06-21	Palomar	corona	Medium cross	6 min
	2004-06-05	Keck	corona		deepest
(PZ99) J161459.2–275023	2003-07-15	Palomar		Medium cross	
	2004-06-05	Keck	corona		deepest
(PZ99) J161618.0–233947	2004-06-27	Palomar	corona	Medium cross	deepest
HD 146516	2003-05-10	Palomar		Medium cross	
	2004-06-05	Keck	corona		deepest
ScoPMS 214	2002-08-30	Palomar	corona	Medium cross	
	2004-06-05	Keck	corona		deepest
	2004-06-27	Palomar	corona	Medium cross	
HD 151798	2002-06-21	Palomar	corona	Medium cross	12 min
	2003-05-16	Keck	corona		deepest
	2004-06-26	Palomar	corona	Medium cross	12 min
HD 165590	2004-06-28	Palomar	corona	Medium cross	deepest

continued on next page

Table 5.3–continued from previous page

Star	UT Date	Observatory	Extra Optic	Lyot Stop	Notes
HD 166181	2004-06-06	Keck	corona		deepest
HD 170778	2004-06-27	Palomar	corona	Medium cross	deepest
HD 171488	2004-06-06	Keck	corona		deepest
	2004-10-08	Keck	corona		
HD 172649	2002-06-21	Palomar		Medium cross	
	2002-08-31	Palomar	corona	Medium cross	deepest
	2003-05-13	Palomar		Medium cross	
	2003-05-18	Keck	corona		
	2004-06-05	Keck	corona		
HD 187748	2004-06-27	Palomar	corona	Medium cross	deepest
HD 191089	2003-09-20	Palomar	corona	Medium cross	
	2004-06-26	Palomar	corona	Medium cross	deepest
HD 199019	2002-08-29	Palomar	corona	Medium cross	deepest
HD 200746	2003-09-21	Palomar	corona	Medium cross	6 min
	2004-06-26	Palomar	corona	Medium cross	4 min, deepest
HD 203030	2002-08-28	Palomar	corona	Medium cross	deepest
	2003-07-16	Palomar	corona	Medium cross	
	2004-06-26	Palomar	corona	Medium cross	
HD 209393	2002-11-17	Palomar	corona	Medium cross	deepest
	2003-09-20	Palomar	corona	Medium cross	
	2004-10-07	Keck	corona		
HD 209779	2002-11-16	Palomar	corona	Medium cross	deepest
V383 Lac	2002-08-27	Palomar	corona	Medium cross	
	2003-07-16	Palomar	corona	Medium cross	
	2003-11-09	Keck	corona		deepest
HD 217343	2003-09-21	Palomar	corona	Medium cross	deepest
HD 218738	2003-12-10	Palomar	corona	Medium cross	
	2004-10-04	Palomar	corona	Medium cross	deepest
HD 218739	2003-12-10	Palomar	corona	Medium cross	
	2004-10-04	Palomar	corona	Medium cross	deepest
HD 219498	2002-08-30	Palomar	corona	Medium cross	deepest
	2003-09-20	Palomar	corona	Medium cross	
	2004-10-05	Palomar	corona	Medium cross	

Table 5.4: Shallow Sample Observations

Star	UT Date	Observatory	Optic	Lyot Stop	Notes
HD 224873	2002-08-31	Palomar	ND1	Medium cross	
	2003-09-21	Palomar	ND1	Medium cross	
HD 9472	2002-11-18	Palomar	ND1	Medium cross	
	2003-09-20	Palomar	ND1	Medium cross	
	2004-10-05	Palomar	ND1	Medium cross	
RE J0137+18A	2002-01-31	Palomar		Big cross	
	2003-09-20	Palomar	ND1	Medium cross	
HD 13507	2002-08-28	Palomar	corona	Medium cross	18 min
HD 13531	2002-08-28	Palomar	ND1	Medium cross	
	2003-09-21	Palomar	ND1	Medium cross	
	2004-10-05	Palomar	ND1	Medium cross	
1RXS J025223.5+372914	2003-09-21	Palomar		Medium cross	
	2004-10-05	Palomar		Medium cross	
2RE J0255+474	2002-02-28	Palomar		Big cross	
	2004-10-05	Palomar		Medium cross	
HD 18940	2002-08-29	Palomar	ND1	Medium cross	
HD 19632	2002-08-30	Palomar		Medium cross	
vB 1	2002-08-29	Palomar	ND1	Medium cross	
HE 350	2003-09-20	Palomar		Medium cross	
	2004-10-04	Palomar		Medium cross	
HE 373	2003-09-20	Palomar		Medium cross	
	2003-11-10	Keck			
	2004-10-05	Palomar		Medium cross	
HE 389	2003-09-20	Palomar		Medium cross	
	2004-10-04	Palomar		Medium cross	
HE 696	2003-09-20	Palomar		Medium cross	
HE 750	2003-09-20	Palomar		Medium cross	

continued on next page

Table 5.4–continued from previous page

Star	UT Date	Observatory	Optic	Lyot Stop	Notes
HE 767	2003-09-20	Palomar		Medium cross	
HE 848	2003-09-20	Palomar		Medium cross	
HE 935	2003-09-20	Palomar		Medium cross	
HE 1234	2003-09-20	Palomar		Medium cross	
HII 102	2003-09-20	Palomar		Medium cross	
	2004-10-04	Palomar		Medium cross	
HII 152	2003-09-21	Palomar		Medium cross	
HII 174	2003-09-21	Palomar		Medium cross	
HII 250	2003-12-10	Palomar		Medium cross	
HII 314	2003-12-10	Palomar		Medium cross	
1RXS J034423.3+281224	2002-11-17	Palomar	ND1	Medium cross	
	2004-10-05	Palomar	ND1	Medium cross	
HII 514	2003-12-10	Palomar		Medium cross	
HII 571	2003-12-10	Palomar		Medium cross	
	2004-10-03	Palomar		Medium cross	
HII 1015	2003-12-10	Palomar		Medium cross	
HII 1101	2003-12-10	Palomar		Medium cross	
	2004-10-05	Palomar		Medium cross	
HII 1182	2003-12-10	Palomar		Medium cross	
	2004-10-03	Palomar		Medium cross	
	2005-01-24	Palomar		Medium cross	
HII 1348†	2004-10-03	Palomar		Medium cross	
HII 1776	2003-12-10	Palomar		Medium cross	
HII 2106	2003-12-10	Palomar		Medium cross	
	2005-01-24	Palomar		Medium cross	
RX J0348.9+0110	2003-12-10	Palomar		Medium cross	
	2005-01-24	Palomar		Medium cross	
HII 2278	2003-12-10	Palomar		Medium cross	
	2005-01-24	Palomar		Medium cross	
HII 2644	2003-12-10	Palomar		Medium cross	
HII 2786	2003-12-10	Palomar		Medium cross	
HII 2881	2003-12-10	Palomar		Medium cross	
	2005-01-24	Palomar		Medium cross	
HII 3097	2003-12-10	Palomar		Medium cross	

continued on next page

Table 5.4–continued from previous page

Star	UT Date	Observatory	Optic	Lyot Stop	Notes
HII 3179	2003-12-10	Palomar		Medium cross	
HD 285281	2002-02-01	Palomar		Big cross	
	2004-02-07	Palomar		Medium cross	
HD 284135	2002-01-31	Palomar		Big cross	
	2004-02-07	Palomar	ND1	Medium cross	
HD 281691	2002-11-18	Palomar		Medium cross	
	2004-02-07	Palomar		Medium cross	
HD 26182	2003-12-10	Palomar		Medium cross	
HD 284266	2002-01-31	Palomar		Big cross	
	2003-12-10	Palomar		Medium cross	
HD 26990	2003-12-10	Palomar	ND1	Medium cross	
	2005-01-24	Palomar	ND1	Medium cross	
vB 39	2003-01-12	Palomar		Medium cross	
vB 49	2003-01-12	Palomar		Medium cross	
vB 52	2003-01-12	Palomar		Medium cross	
	2004-10-05	Palomar	ND1	Medium cross	
vB 176	2003-12-10	Palomar		Medium cross	
	2004-10-03	Palomar	ND1	Medium cross	
vB 63	2003-01-12	Palomar		Medium cross	
vB 66	2002-11-17	Palomar	corona	Medium cross	
vB 73	2003-01-12	Palomar		Medium cross	
vB 180	2003-12-10	Palomar		Medium cross	
vB 88	2003-12-10	Palomar		Medium cross	
1RXS J043243.2–152003	2003-01-12	Palomar		Medium cross	
vB 91	2003-12-10	Palomar		Medium cross	
	2004-10-03	Palomar	ND1	Medium cross	
vB 96	2003-12-10	Palomar		Medium cross	
RX J0434.3+0226	2003-01-12	Palomar		Medium cross	poor
vB 106	2003-12-10	Palomar		Medium cross	
	2004-10-05	Palomar	corona	Medium cross	
HD 282346	2002-11-18	Palomar		Medium cross	
	2004-10-04	Palomar	ND1	Medium cross	
vB 142	2002-11-17	Palomar	corona	Medium cross	
	2003-11-10	Keck	corona		

continued on next page

Table 5.4–continued from previous page

Star	UT Date	Observatory	Optic	Lyot Stop	Notes
	2004-02-07	Palomar	corona	Medium cross	
HD 286264	2003-12-10	Palomar		Medium cross	
1RXS J051111.1+281353	2002-02-28	Palomar		Big cross	
	2003-01-14	Palomar		Medium cross	
	2003-12-10	Palomar		Medium cross	
HD 37006	2003-01-11	Palomar		Medium cross	
	2003-12-10	Palomar		Medium cross	
HD 61994	2002-11-18	Palomar	ND1	Medium cross	
HD 66751	2002-11-18	Palomar	ND1	Medium cross	
HD 69076	2002-11-18	Palomar	ND1	Medium cross	
	2003-05-11	Palomar	ND1	Medium cross	
	2004-02-06	Palomar		Medium cross	
HD 71974	2002-03-03	Palomar		Big cross	
HD 72687	2003-12-09	Palomar	ND1	Medium cross	
HD 72760	2002-11-16	Palomar	ND1	Medium cross	
HD 73668	2002-05-11	Palomar	corona	Medium cross	
	2004-02-06	Palomar		Medium cross	
HD 77407	2002-01-31	Palomar		Big cross	
	2003-01-13	Palomar	ND1	Medium cross	
	2003-05-10	Palomar	ND1	Medium cross	
HD 78899	2003-12-09	Palomar	ND1	Medium cross	
HD 88638	2002-01-31	Palomar	corona	Big cross	17 min
HD 91962	2002-03-02	Palomar		Big cross	
	2003-05-10	Palomar	ND1	Medium cross	
	2004-02-05	Palomar	ND1	Medium cross	
HD 98553	2003-01-11	Palomar		Medium cross	
HD 99565	2003-01-11	Palomar	ND1	Medium cross	
	2003-05-11	Palomar	ND1	Medium cross	
	2004-02-05	Palomar	ND1	Medium cross	
HD 100167	2002-03-03	Palomar	corona	Big cross	poor
HD 101959	2002-02-28	Palomar		Big cross	
HD 102071	2002-02-28	Palomar		Big cross	
HD 108799	2003-05-10	Palomar	ND1	Medium cross	
	2003-07-16	Palomar	ND1	Medium cross	

continued on next page

Table 5.4–continued from previous page

Star	UT Date	Observatory	Optic	Lyot Stop	Notes
	2004-02-05	Palomar	ND1	Medium cross	
	2004-06-26	Palomar	ND1	Medium cross	
HD 108944	2002-03-03	Palomar		Big cross	
	2002-06-21	Palomar		Medium cross	
	2003-01-13	Palomar	ND1	Medium cross	
	2003-05-11	Palomar	ND1	Medium cross	
	2004-02-05	Palomar	ND1	Medium cross	
	2004-06-27	Palomar	ND1	Medium cross	
HD 112196	2002-02-01	Palomar		Big cross	
	2003-01-13	Palomar	ND1	Medium cross	
	2003-05-11	Palomar	ND1	Medium cross	
	2004-02-05	Palomar	ND1	Medium cross	
	2004-06-26	Palomar	ND1	Medium cross	
HD 115043	2003-12-09	Palomar	ND1	Medium cross	
	2004-06-27	Palomar	ND1	Medium cross	
HD 129333	2003-01-11	Palomar	ND1	Medium cross	
	2003-01-12	Palomar	ND1	Medium cross	
	2003-05-13	Palomar		Medium cross	
	2004-02-05	Palomar	ND1	Medium cross	
HD 133295	2002-02-28	Palomar		Big cross	
HD 134319	2002-03-02	Palomar		Big cross	poor
	2003-01-14	Palomar	ND1	Medium cross	
	2004-06-27	Palomar	ND1	Medium cross	
HD 135363	2002-02-01	Palomar		Big cross	
	2003-01-14	Palomar	ND1	Medium cross	
	2004-06-27	Palomar	ND1	Medium cross	
RX J1541.1–2656	2003-07-15	Palomar		Medium cross	
	2004-06-27	Palomar		Medium cross	
RX J1600.6–2159	2003-07-15	Palomar		Medium cross	
(PZ99) J160814.7–190833	2002-08-31	Palomar		Medium cross	
(PZ99) J161329.3–231106	2003-05-10	Palomar		Medium cross	
	2004-06-26	Palomar		Medium cross	
HD 150554	2003-05-10	Palomar	ND1	Medium cross	
	2003-07-16	Palomar	ND1	Medium cross	

continued on next page

Table 5.4–continued from previous page

Star	UT Date	Observatory	Optic	Lyot Stop	Notes
HD 152555	2002-08-31	Palomar	ND1	Medium cross	
	2003-07-16	Palomar	ND1	Medium cross	
	2004-06-26	Palomar	ND1	Medium cross	
HD 155902	2003-09-21	Palomar	ND1	Medium cross	
HD 157664	2003-05-10	Palomar	corona	Medium cross	
	2004-10-04	Palomar	ND1	Medium cross	
HD 166435	2002-06-23	Palomar	corona	Medium cross	
	2002-08-30	Palomar	corona	Medium cross	
	2003-05-16	Keck	corona		
	2004-06-26	Palomar	corona	Medium cross	
HD 167389	2003-05-13	Palomar	ND1		
HD 175742	2004-06-28	Palomar	corona	Medium cross	
HD 193216	2003-07-16	Palomar	corona	Medium cross	12 min, poor
	2004-06-27	Palomar	corona	Medium cross	12 min
HD 199143	2002-06-23	Palomar	ND1	Medium cross	
	2003-09-21	Palomar	ND1	Medium cross	
	2004-10-05	Palomar	ND1	Medium cross	
HD 201989	2003-07-16	Palomar	ND1	Medium cross	
HIP 106335	2004-06-28	Palomar	corona	Medium cross	
HD 205905	2003-07-16	Palomar		Medium cross	
HD 206374	2003-07-16	Palomar		Medium cross	
RX J2312.0+2245	2002-08-30	Palomar	ND1	Medium cross	
	2003-09-20	Palomar		Medium cross	
	2004-10-05	Palomar		Medium cross	
RX J2313.0+2345	2002-08-30	Palomar		Medium cross	
HD 221613	2002-11-18	Palomar	ND1	Medium cross	
	2003-09-21	Palomar	ND1	Medium cross	

[†]HII 1348 is not a part of the unbiased survey for sub-stellar companions.

5.1.1 Choice of PHARO Lyot Stop and the Use of a Neutral Density Filter

The coronagraphic observations at Palomar were conducted using two different undersized Lyot stops to block the secondary obscuration and the telescope spiders:

the "medium" and the "big" cross, obscuring 40% and 76% of the total telescope aperture, respectively (Hayward et al., 2001). The use of a Lyot stop of the correct size is expected to noticeably improve the dynamic range achievable in high-order AO coronagraphy by suppressing signal with high spatial frequency near the edge of the coronagraph (Sivaramakrishnan et al., 2001). Early experiments with the PALAO/PHARO system by Oppenheimer et al. (2000a) had suggested that the big cross provided the best contrast in single exposures of several seconds, outperforming the medium and "standard" (no undersizing) Lyot masks by up to 0.5 mag between $0.5''$–$2.0''$ from bright stars. However, our experience from observing each star in multiple longer exposures was that the less oversized Lyot stops allowed better real-time monitoring of the star-coronagraph alignment and more accurate post-processing image registration. With the medium and the standard Lyot stops, the position of the star behind the coronagraph could be monitored by the location of a Poisson-like spot within the dark area of the coronagraph (Fig. 5.1): the result of constructive interference of high spatial frequency light pushed to the periphery of the Lyot plane by the coronagraph. The big Lyot stop likely shutters that too aggressively to allow the formation of a sufficiently bright Poisson spot. Because image registration of multiple exposures was crucial for obtaining greater overall exposure depth, we stopped using the big cross after the March 2002 observing run. Given the adopted technique of rotating the Cassegrain ring to 4 mutually orthogonal orientations during the imaging of each star (§3.3.2), the medium cross provided the best compromise between registration ability for the final images and consistency with which it would obscure the telescope spiders at each Cassegrain ring orientation. Column 5 in Tables 5.3 and 5.4 indicates which Lyot stop was used for each star.

As a result of the use of two different Lyot stops during the first epoch of Palomar imaging and because of the alignment issue for images taken with the big cross, the dynamic range achieved in the two cases is somewhat different. While in most cases when the medium cross was used, image alignment accurate to $\lesssim 0.1$ pix could be performed on the Poisson spot, for all images of stars taken with the big

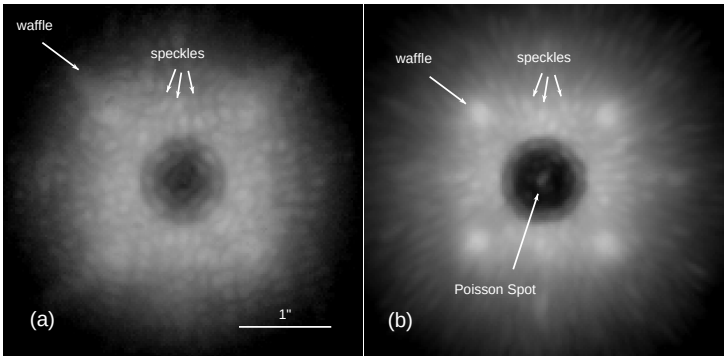

Figure 5.1: Close-up sample images with the big (a) and medium (b) Lyot stops, using the $0.97''$ coronagraph. Characteristic features of the PALAO PSF are indicated with arrows. The medium Lyot stop allows the formation of a Poisson spot at the location of the star, enabling consistent image registration.

cross, and for few taken with the median cross, this was not possible. Instead, when other point sources in the field of a star obscured by the coronagraph were visible in the individual short exposures, these sources were used as references for registration. However, for 17 stars (17% of the sample) showing no candidate companions, we had to rely on cross-correlation techniques, which had poorer positional accuracy (0.5 pix; §4.6). As a result, these 17 images are, on average, 0.23 mag shallower. This factor has been taken into account in the calculation of the ensemble survey detection limits (§5.2).

The non-coronagraphic observations at Palomar were also performed with two different settings: with and without a 1% neutral density (ND) filter in the beam path. The ND filter was used for imaging stars brighter than $K_S = 7 - 8$ mag (depending on atmospheric transparency) to prevent detector saturation. This is noted accordingly with an "ND1" entry in column 4 of Tables 5.3 and 5.4. Fainter stars were observed without the filter. The use of the ND filter does not have a measurable effect on the overall contrast. However, it further limits the depth of non-coronagraphic exposures. We calibrated the near-IR extinction of the ND 1% filter from relative photometric measurements of three program stars with and without the ND filter. The calibration results are tabulated in Table 5.5. The Lyot

Table 5.5: Magnitude Extinction due to PHARO and NIRC2 Optics

Transmissive Optic	ΔJ	ΔH	ΔK_S
PHARO ND 1% filter	4.753 ± 0.039	4.424 ± 0.033	4.197 ± 0.024
NIRC2 $1''$ coronagraph	8.36 ± 0.28	7.78 ± 0.15	7.10 ± 0.17
NIRC2 $2''$ coronagraph	9.26 ± 0.09	7.79 ± 0.22	7.07 ± 0.22

stop setting for the non-coronagraphic exposures was left as in the coronagraphic observations.

5.1.2 Choice of NIRC2 Coronagraphs and Pupil Mask

Images with NIRC2 were obtained only in coronagraphic mode, using predominantly the $1''$-diameter spot, though the $2''$-diameter spot was used during the May 16–18, 2003, observing run. Unlike the PHARO coronagraphic spots, the NIRC2 spots are transmissive, offering the possibility to obtain accurate relative positioning and approximate photometry with respect to the primary. A measurement of the throughput of the $2''$ spot was already presented in §3.3.3.1. Subsequent observations showed that such measurements are dependent on the quality of the AO correction, possibly because of the amount of spill-over light behind the edge of the coronagraph. Thus, approximate relative photometry with the NIRC2 coronagraph is likely feasible only with good AO correction (usually at H and K band), when spill-over behind the coronagraph is minimized. Table 5.5 lists the measured near-IR extinction in magnitudes for the $1''$ and $2''$ NIRC2 coronagraphs. The large apparent difference in the J-band transmissivity of the two coronagraphic spots is a probable effect of spillover, aggravated by poorer AO performance at J.

Similarly to PHARO, NIRC2 offers a selection of undersized hexagonal and circular pupil masks to occult the mirror edges, though not the telescope spiders. Among those we chose the "inscribed circle" mask, which corresponds to the largest circular aperture inscribed in the telescope mirror. This mask has a 90.7% clear area and provides round, rather than hexagonal, PSFs—a factor that was deemed

important for aperture photometry and centering.

5.1.3 Rotating the Cassegrain Ring at Palomar: The Cons Outweigh the Pros

Identifying faint objects in the haloes of bright stars is one of the principal directions of modern astronomy. The main challenge is to remove the contribution of the PSF as close to the star as possible, and bring down the residual noise as close to the photon noise limit as possible. Various experimental techniques of PSF subtraction with advanced AO systems are currently being tested, such as simultaneous differential imaging (Racine et al., 1999; Close, 2004; Marois et al., 2005) and differential polarimetry (Kuhn et al., 2001; Apai et al., 2004). With conventional AO, the best approaches involve either image rotation followed by "roll-angle" subtraction, or the observation of a suitable PSF standard star. Both in principle allow the subtraction of the PSF to within a factor of $\sim$3–5 of the photon noise limit, beyond which imperfect elimination of speckles dominates the noise. The former is the method of choice for altitude-azimuth (alt-az) telescopes (e.g., Keck), as the sky can by allowed to rotate in between exposures while keeping the PSF fixed with respect to the detector (i.e., when imaging in "vertical angle" mode). The difference of two images taken at different sky position angles provides nearly as good a subtraction of the PSF as is possible with conventional AO. The PSF standard star approach is better suited to telescopes on equatorial mounts, where, if no additional image plane rotation capability exists, the position angle of the sky is constant. Observing separate PSF stars is often undesirable, however, as it adds 100% overhead.

We initially saw the ability to rotate the Hale telescope CR ring as an opportunity to mimic alt-az behavior at Palomar and thus maintain high observing efficiency, without needing to observe PSF stars. Because the CR carries both PALAO and PHARO (containing most of the intermediate optics), most of the PSF artifacts induced in the optical train were expected to retain a constant orientation on the detector, while the sky position angle changes. The only difference

with a true alt-az telescope would be the fact that the telescope primary and secondary mirrors, and the secondary support spiders, *will* rotate with respect to the detector. We believed that the use of an aggressive Lyot stop, such as the medium or big cross, to cover the mirror edges and the spiders, would adequately limit this undesirable effect. By rotating through 90°, we planned to ensure constant alignment of the support spiders with the Lyot stop mask. Discussions with Tom Hayward and Stephen Eikenberry, both extensive users of the PALAO system at the time, suggested that this may be a viable, albeit previously unexplored approach.

The procedure was adopted without extensive testing, and because of the four-cornered symmetry of the characteristic Shack-Hartmann "waffle" pattern of the PALAO PSF (Fig. 5.1), it appeared that the approach could provide good cancelation at least of the corner waffle speckles. However, we subsequently discovered that this method does not offer noticeable improvement over a technique based on a simple rotation (or mirror flipping) of the image around the primary, followed by a subtraction of the rotated image. As it turned out, the PSF speckles rotated *with* the detector, indicating that most of the wavefront aberration was incurred by the primary and secondary telescope mirrors. The 180°-rotation and subtraction technique quickly became the method of choice for PSF subtraction for all of the coronagraphic data. Nevertheless, the CR rotation strategy during observations was maintained, partially for survey self-consistency, and partially to mitigate the effect of a large-scale ($\sim 15''$) low surface brightness ghost reflection of the telescope pupil, visible in most of the deep coronagraphic exposures. The ghost image did not follow the rotations of the array and could thus be effectively removed by median-combining data from different CR orientations.

The most negative effect of the CR rotations, which went unnoticed for a large fraction of the survey duration, had to do with the non-uniformity of the PHARO pixel scale (§4). The use of CR rotations limited the imaging depth because when objects were rotated to different parts of the array images of identical parts of the sky suffered different amounts of focal plane distortion. Thus, images

taken at CR angles differing by 90° were not related by a simple 90° rotation, but rather by a rotation by $90° + \epsilon$ and by a position-dependent magnification (§4.4.3). The result was a noticeable smearing of the PSF in the final, un-rotated, median-combined images beyond 4″–7″ from the central star. This smearing was initially erroneously attributed to anisoplanatism. However, in later images taken under excellent atmospheric conditions, when high (>50%) Strehl ratio PSFs of point sources were obtained out to the edge of the array (indicating that the isoplanatic angle was much larger than the PHARO field), stars in the array corners appeared as distinct binaries in the final un-rotated image.[1] Therefore, in practice, CR rotations limited the imaging depth at large ($\gtrsim 10''$) separations by a factor of ≈2 (0.75 mag). At smaller angular separations the decrease in image depth was marginal and was close to 0 mag inwards of ≈4″, where the differential field distortion between CR orientations was <2 pix—less than half of the PSF FWHM.

In addition to the negative effect on image depth, because of the sparse detector coverage in the calibration of the pixel scale dependence on the CR angle, the use of CR rotations also limits the astrometric precision to a factor of $\gtrsim$1.6 from what is optimally attainable when observing only at a single CR angle (§4.4.4).

Finally, CR rotations incur some amount of overhead, related to re-acquiring AO lock at each new CR angle. This was about 3 min per rotation, or 38% of the total on-source exposure time, for 3 rotations in between 4 distinct CR orientations.

To summarize, the use of CR rotations for deep AO imaging over the entire field of the PHARO detector offers fewer benefits than set-backs. While it does allow the elimination of large-scale ghost reflections from the telescope pupil, it overall decreases exposure depth at >5″ separations, has a negative effect on astrometric precision, and adds overhead when compared to simple staring-mode (i.e., without the use of a standard star) observations. The recommended approach, as a result of our experience with PALAO, is to chose pairs of science targets that are closely

[1] Although 4 distinct images of the same star should be expected, given that images were taken at 4 separate CR orientations, diametrically opposite CR orientations seemed to produce similar overall distortions (cf. Fig. 4.7), resulting in pair-wise combination of the 4 expected images.

separated ($\lesssim 10^\circ$) on the sky and that are mutually suitable (i.e., have similar brightness and color) to serve as PSF standards for each other. The technique is appropriate for coronagraphic surveys of young open clusters, where the density of stars is higher than in the field. Upon our recommendation, the approach was successfully implemented for the purpose of the *Space Interferometry Mission* Planets around Young Stars (PLAYS) key project (P.I. C. Beichman). The PSF-subtracted images showed an improvement in contrast by 0.5–1.0 mag over $0.5''$–$3''$ from the host star, compared to the simple rotation and subtraction method. Unfortunately, this approach may not be adequate for surveys of widely-separated sample targets, such as the present one.

5.2 Object Detection—Limits

5.2.1 Automatic Source Detection Is Not Well-suited to High-Contrast AO Imaging

Object detection is a straightforward matter to automate in images, in which the PSF is radially symmetric, approximately constant in time, and has a well-characterized dependence on image location. This is the case with the majority of ground-based seeing-limited and space-based observations. Various approaches are available, such as matched-filtering, localized signal-to-noise calculation, and image deconvolution, to name a few of the most popular ones. These have been implemented in a wide variety of programs, such as DAOPHOT (Stetson, 1987), SExtractor (Bertin & Arnouts, 1996), WAVDETECT (Freeman et al., 2002), findobs in the ECLIPSE package (Devillard, 2001), StarFinder (Diolaiti et al., 2000), idac (Jefferies & Christou, 1993), etc. These programs are best suited, and often essential, for the detection of point sources in crowded fields. These often contain objects of similar brightness and have a well-characterized spatial PSF behavior. The automated programs are less adequate for fields that are scarce in sources and where high-contrast is required. In addition, they are not applicable to coronagraphic imaging, where the main (and frequently only) point

source is occulted. The above limitations describe well the sparsely populated, high-contrast, coronagraphic images in the present survey.

High-contrast AO imaging presents great difficulties for automated source finding because of the large number of speckles in the vicinity of the star (Fig. 5.1). The speckles are individual images of the star, that form from uncorrected and/or induced (by the telescope optics) aberrations in the wavefront and appear indistinguishable from point sources to automated detection routines. A vivid example of this is the close-up of the Palomar image of the $\Delta K_S = 8.2$ mag HD 49197A/B system (Fig. 3.5b), where the companion is drowned in speckle noise. The existence of the companion, hinted by a dark ring around one of the speckles with a radius corresponding to that of the first Airy null radius, was appreciated only after it was discovered in a later-epoch higher-contrast Keck AO image. As a result, even though some of the source detection algorithms listed above have been developed (StarFinder), or adapted (DAOPHOT, idac), for AO image restoration, they did not produce satisfactory results on our images. Our experiments with DAOPHOT, WAVDETECT, and StarFinder produced large numbers of spurious detections, the vast majority of which could be identified with speckles around the coronagraph. If the signal-to-noise threshold in the source-finding algorithms was adjusted to a correspondingly higher level, the algorithms would miss the bona fide point sources in the field. The character of the result did not change whether we used various methods of PSF subtraction or not. Similar experiences and conclusions are drawn in Carson et al. (2005), who also used the PALAO/PHARO system for their sub-stellar companion search. Therefore, after some experimentation, despite an understanding that automated source detection has the potential to offer greater repeatability and conceptual clarity, we abandoned the approach.

The remaining option is visual identification. It has been our experience during this survey that, barring subjective factors, visual inspection of images for candidate companions always produces superior results, compared to automated detection. A glance through the high-contrast AO literature re-affirms this. The

vast majority of researchers, including the authors of the first successful imaging survey for sub-stellar companions (Oppenheimer et al., 2001), have (sometimes grudgingly) ultimately resorted to by-eye identification of candidate companions (Tokovinin et al., 1999; Brandner et al., 2000; Luhman & Jayawardhana, 2002; McCarthy & Zuckerman, 2004; Masciadri et al., 2005; Luhman et al., 2005). Few examples to the contrary exist, in addition to the experiments of Carson et al. (2005). One exception is the study of Lowrance et al. (2005), who apply a rigorous custom-made automated detection scheme to their NICMOS data. However, the Lowrance et al. survey benefits from the well-behaved PSF of space-borne *HST* imaging. In a separate instance, Shatsky & Tokovinin (2002) use DAOPHOT II (Stetson, 1992) for their non-coronagraphic AO data. DAOPHOT II allows additional cleaning around the PSF and is thus potentially more appropriate for AO data, where the PSF consists of a narrow core and a broad halo. However, the authors do not discuss an application of the approach to their set of coronagraphic data. Finally, Schroeder et al. (2000) concede that, after spending several man *months* in investigating different automated source detection approaches, simple by-eye inspection is most reliable. Therefore, having found no better alternative, we adopted visual inspection as the method of choice for identifying candidate companions.

5.2.2 Visual Source Detection and Limits

We carefully inspected all of the final coronagraphic images for candidate companions and measured their positions and fluxes with the PHOT task in IRAF. The visual inspection was repeated multiple times during image reduction, photometry, and astrometry; hence subjective factors were brought down to a minimum. We examined the images both prior to, and after PSF subtraction. At small angular separations PSF subtraction facilitates the detection of faint objects embedded in the bright halo of the star, while at larger separations (in the background-limited regime) it induces noise and limits their visibility. When a candidate point source was detected, the individual 1 min images and the 6 min median-combined images

taken at the same CR angle were inspected to check for the object at the corresponding locations. In most cases, this was sufficient to distinguish artifacts from bona fide point sources. Still, because of the greater depth of the final image (despite some PSF smearing at $>4''$ separations), very faint objects were sometimes not visible in <24 min sub-sets of images. Such candidate companions, less than a dozen overall near the detection limit, were treated as real objects and followed up with further imaging. Only 3 such objects turned out to to be real, as evidenced by deeper Keck images, though the existence of several still remains undecided.

We attempted various methods of PSF removal on the final images, including: (1) subtracting a median-combined PSF of the star formed from the individual images taken at all 4 CR angles, (2) 180° rotation centered on the star and subtraction of the image from itself (§5.1.3), (3) high-pass filtering, in which a Gaussian-smoothed (Gaussian FWHM $= 1 - 3\times$ PSF FWHM) version of the image was subtracted from the original, and (4) simple subtraction of an azimuthally medianed radial profile. We found that (1–3) gave comparable results, while (4) did not perform as well as the rest because of the four-cornered shape of the PSF. Even though (3) is arguably the most widely used method for PSF subtraction when separate PSF observations are not available, we found that, because of the central symmetry of the brightest AO speckles (Boccaletti et al., 2002; Bloemhof, 2003), method (2) worked similarly well. Method (2) also did not alter the photon statistics of the PSF-subtracted image in the spatially correlated manner incurred by Gaussian smoothing. We therefore relied on method (2) for the most.

We quantified the ability to detect faint objects as a function of angular separation from the star, by randomly introducing artificial point sources of constant (modulo random Poisson noise) brightness, in a manner analogous to the one described in §3.2.5.1. We performed the experiment on the reduced coronagraphic and non-coronagraphic survey images of the star HD 172649, for which the data were taken under good observing conditions with Strehl ratios of ≈50%. We introduced 1000–5000 artificial point sources of constant brightness at random locations over the entire area of the images and counted the fraction of them that were re-

trievable in 0.25″–1.0″-wide concentric annuli centered on the star. We repeated the experiment for a range of artificial star magnitudes, at steps of 0.5 mag. The PSF for the artificial stars in the unocculted image was obtained from a fit to the primary, whereas in the coronagraphic image it was obtained from a fit to the brightest field object ($\Delta K_S = 6.4$ mag).

Figure 5.2 presents the results from the artificial star experiments, where the contrast limits from coronagraphic observations at Palomar and Keck are shown with solid and long-dashed lines, respectively, and the non-coronagraphic limits for Palomar are shown with a short-dashed line. The slow upturn in the Palomar limits (decrease in contrast) at >5″ separations is due to an additive parameter to model the decreasing exposure depth toward the edge of the PHARO field, because of image mis-registration among the different CR angles (§5.1.3). The parameter is set to vary linearly between 0 mag and 0.75 mag in the 4–12.5″ separation range. As is evident from Figure 5.2, under good observing conditions, the 6 min long Keck AO coronagraphic images offered 0.5–1.5 mag higher contrast and depth than the 24 min PALAO images, with the highest difference being in the 1.0″–1.5″ separation range, where the presence of waffle-mode distortion in the PSF limits the contrast at PALAO.

5.2.3 R.M.S. Noise Detection Limits

Often instead of performing artificial star experiments, a seemingly more analytically appealing and straightforward approach is taken, in which the contrast limits are determined in a purely statistical manner from the r.m.s. deviation σ of the pixel counts in the PSF halo in concentric annuli centered on the star. Five to ten σ is generally regarded as a sufficiently conservative level in approximating realistic detection limits.

We implement this approach by constructing an azimuthally-symmetric radial profile of the PSF, equal at each radius to the r.m.s. scatter of the pixel values in 4 pixel wide (0.1″) annuli. Instead of treating the pixels independently, we normalize their r.m.s. scatter to an aperture of radius equal to the FWHM of the PSF, to

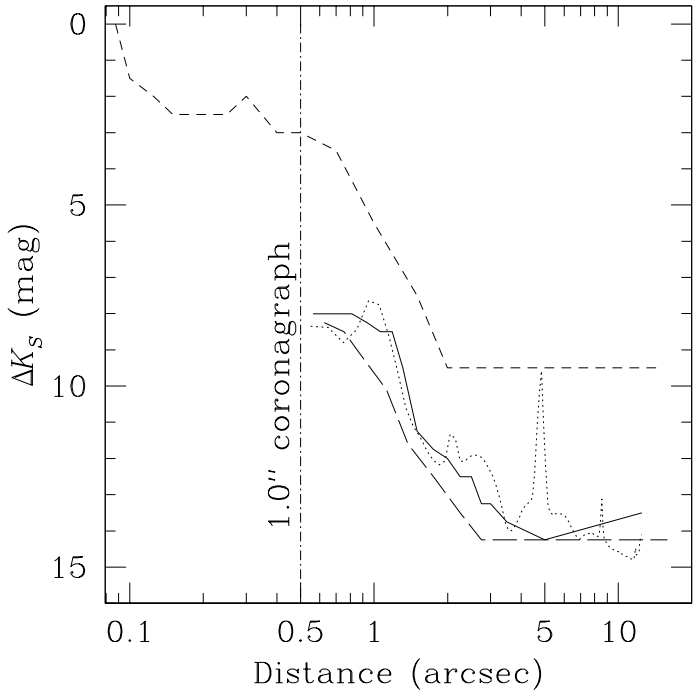

Figure 5.2: Empirical detection limits for the survey at K_S band, as determined from artificial star experiments in the image of HD 172649. The solid and long-dashed curves delineate the achievable contrast for the AO coronagraphic observations of the Palomar (24 min) and Keck (6 min) components of the survey, respectively. The short-dashed line shows the detection limits for the non-coronagraphic component of the PALAO survey. The dotted lines represents the 4σ r.m.s. deviation of counts in the PSF halo as a function of separation, normalized to an aperture with radius 4 pix ($0.1''$)—equal to the FWHM of the K_S-band PALAO PSF. The vertical dash-dotted line shows the edge of the occulting spot at Palomar and Keck.

match the approximate spatial correlation scale in the image. This procedure imposes a more stringent requirement on the significance of the detection of a candidate point source by precluding single pixel peaks from dominating annulus statistics. We show the thus-obtained 4σ r.m.s. noise profile of the halo by the dotted line in Figure 5.2. The bumps and spikes in the dotted line correspond to bright features in the image of HD 172649, e.g., to the corners of the waffle pattern at $1.0''$ and to projected companions to the star at $2.1''$, $4.8''$, and $8.6''$. The 4σ line closely follows the visually determined detection limits, potentially indicating that the multitude of additive Gaussian and non-Gaussian sources of noise in the speckle-limited regime (Racine et al., 1999) may eventually behave in a nearly Gaussian manner because of the central limit theorem. The strongest systematic deviation of the 3σ r.m.s. profile from the visually-determined contrast limits is at angular separations $>7''$, in the region where the visual limits have been adjusted for CR angle image mis-registration.

The agreement between the detection limits from visual inspection and from r.m.s. statistics is dependent on a number of factors, such as the radius of the normalization aperture (here equal to 1 FWHM of the PSF), the treatment of point source photon statistics (ignored in this case), and the appropriate functional treatment of non-Gaussian sources of error (speckles, shape of the PSF core and halo; also ignored here). Therefore, the 4σ dotted line in Figure 5.2 does not carry the statistical significance of a confidence level at which 99.997% of random fluctuations are rejected. However, because of its close representation of the visually-determined detection limits, we will use it to build ensemble detection limits on a per-star basis, as in the discussion following section.

5.2.4 Ensemble Detection Limits for the Deep Sample

The empirical detection limits in Figure 5.2 were obtained for observations that benefited from good AO correction (Strehl ratio of $\approx$50%) on a bright star ($V = 7.5$) and median atmospheric conditions for the survey ($1.2''$ seeing, scattered cirrus). While high-quality AO performance on bright stars at Palomar and Keck is

now achieved consistently under average to good atmospheric conditions, fainter stars and worse weather incur a toll on the quality of the AO correction, expressed in poorer contrast and shallower imaging depth. Indeed, a comparison with the detection limits of the Carson et al. (2005, Fig. 4) PALAO companion survey shows that the by-eye contrast limits from Figure 5.2 are similar to their "best 10%" contrast limits (modulo the level of the sky background limit at large separations). The by-eye limits are ≈2.5 mag deeper than the median sensitivity reported in Carson et al. (2005), and are ≈4.5 mag deeper than the authors' "worst 10%" sensitivity limits. PALAO performance has undoubtedly improved as a result of several upgrades since 2000–2002, when the Carson et al. (2005) data were taken. In addition, the lowest quality data in our campaign were either re-taken or excluded from the survey. Hence, we do not expect such a dramatic range of sensitivity for the different images in our survey. Nevertheless, the Carson et al. (2005) result exemplifies the need to monitor the achieved contrast on a per-star basis. For the purpose of estimating the completeness of the survey in §6, we discuss the range of survey contrast and depth in the following.

To determine the detection limits for each star in the deep sample, instead of pursuing artificial point source experiments in each case, we use the r.m.s. PSF profile for the star, normalized to an aperture with radius equivalent to the FWHM of the PSF. As observed in §5.2.3, the 4σ r.m.s. noise level closely approximates the visual detection limits. In the cases where multiple coronagraphic images of the same star were taken at different epochs, we selected the deepest of the images (as marked in the last column of Table 5.3). This formed a set of 59 Palomar and 42 Keck images, which represented the deepest single-epoch observations of the 101 stars in the deep sample. For flux calibration and measurements of the PSF FWHM of the Palomar images, we relied on the short non-coronagraphic exposures taken of each star immediately before or after the coronagraphic observations. For the Keck images, we measured the FWHM of the PSF directly from the residual stellar profile seen through the coronagraph and relied on the earlier calibration of the coronagraph transmissivity (Table 5.5).

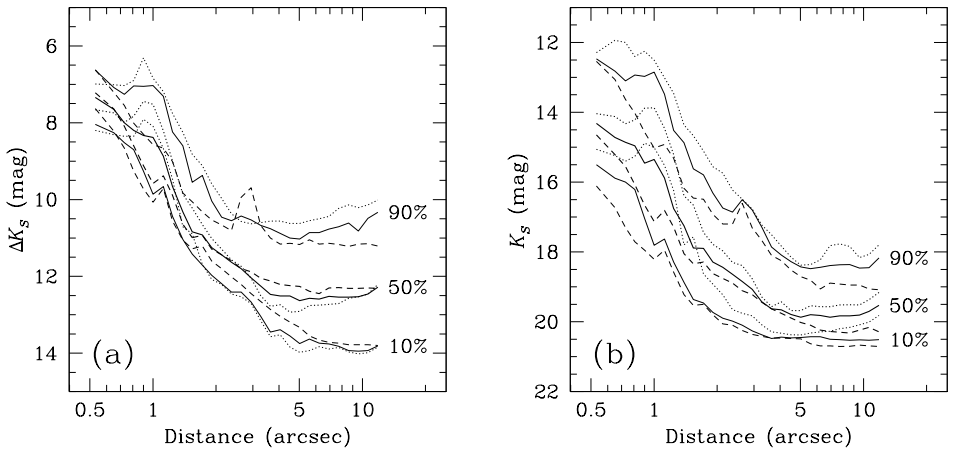

Figure 5.3: Contrast (a) and flux (b) completeness of the deep survey at K_S. The various sets of lines represent the 10%, 50% (bold set of lines), and 90% completeness of the Palomar (dotted line), Keck (dashed line), and combined (solid line) surveys. The percentile completeness labels are printed opposite the solid lines, though they also refer to the nearest dashed line underneath and the nearest dotted line above.

Figure 5.3a depicts the range of achieved K_S-band contrast for the coronagraphic observations from the entire survey (solid line), and from the Palomar (dotted line) and Keck (dashed line) portions of it. The bold set of curves delineates the median (50%) survey completeness, while the two sets of 3 lines above and below delineate the 90% and 10% completeness. Figure 5.3b uses the same notation scheme to depict the completeness of the survey in terms of apparent K_S magnitude (i.e., with the magnitude of the primary added). The peaks in the 90% completeness levels at $\approx 2.5''$ and $7''$–$9''$ in the two panels are not real, but are due to chance alignments of the radial separations of candidate companions to the 101 stars in the deep sample. The upward trend of the Palomar completeness limits between $4''$–$12.5''$ is partially due to the aforementioned mis-registration of images taken at different CR angles (§5.1.3), and partially to the sometimes smaller depth of observations at $11 - 12.5''$ separations because of a $0.5''$–$1.5''$ offset of the coronagraphic spot from the center of the PHARO array.

It is evident from Figures 5.3a,b that the Palomar and Keck components of the deep survey achieve comparable contrast and depth. We will therefore treat the two components together. The median sensitivities of the combined survey range from $\Delta K_S = 8.4$ mag at $1''$ to $\Delta K_S \approx 12.5$ mag over $4''$–$12.5''$ in contrast and from $K_S = 15.4$ mag at $1''$ to $K_S \approx 19.7$ mag in flux. The detection limits will be used in §6 to estimate the overall survey completeness to sub-stellar companions.

5.3 Detected Candidate Companions

In the course of the 3-year survey, we discovered 288 candidate companions brighter than $K_S = 20.6$ mag within $12.5''$ from 132 out of 266 sample stars. Of these candidate companions 199 were near 63 (out of 101) stars in the deep sample. The remaining 89 were in the vicinity of 69 (out of 165) shallow-sample targets. Candidate companions around stars in the deep and shallow samples are listed in Tables 5.6 and 5.7, respectively. The Tables list the sample star (col. 1), the candidate companion number N_C (col. 2), the angular separation ρ and position angle θ of the candidate companion from the primary (cols. 3 and 4), the K_S-band magnitude difference ΔK_S between the candidate companion and the primary (col. 5), the absolute magnitude M_{K_S} of companions if physically associated (col. 6), the measured $J - K_S$ color for objects with obtained J-band data (col. 7), the epoch t_0 of discovery of the candidate companion (col. 8), the telescope used at the discovery epoch for the candidate companion (col. 9: "P"–Palomar, "K"–Keck), the physical association of the candidate companion with the primary (col. 10), and a pointer to a literature reference (col. 11) if the companion was already known. The tabulated K_S-band magnitude differences are with respect to the 2MASS K_S magnitudes of the sample stars. Since the 2MASS observations are seeing-limited, binaries with separations smaller than $2''$ have had their component magnitudes re-calculated based on the measured magnitude difference and the total 2MASS magnitude. The various physical association codes are as described in §5.4: "yes(a)," "yes(c)," and "yes(p)"—bona fide companions confirmed, respectively, from the present as-

trometry, from their near-IR colors, and from prior astrometry from the literature; "no(a)," "no(c)," "no(e)"—non-physical companions as determined, respectively, from the present astrometry, from their near-IR colors, and from their extended PSFs; "?"—undecided candidate companions, for which none of the physical association criteria (§5.4) produced definitive results. Figure 5.4 shows all detected candidate companions as a function of ΔK_S and ρ.

Thirty-eight stars in the deep sample and 96 in the shallow sample showed no projected companions within $12.5''$. These stars are listed in Tables 5.8 and 5.9, respectively.

Table 5.6: Candidate Companions in the Deep Sample

Star	N_C	ρ (arcsec)	θ (deg)	ΔK_S (mag)	K_S (mag)	$J-K_S$ (mag)	t_0 (UT Date)	Tel.	Assoc.	Ref.
QT And	1	7.696 ± 0.019	239.56 ± 0.22	11.56 ± 0.22	18.91 ± 0.22	1.57 ± 0.31	2002-08-29	P	no(a)	
HD 15526	1	0.077 ± 0.004	177.96 ± 0.75	0.00 ± 0.05	8.76 ± 0.06	0.61 ± 0.08	2003-09-20	P	yes(c)	
1RXS J025216.9+361658	1	5.811 ± 0.020	10.63 ± 0.41	10.26 ± 0.09	17.86 ± 0.09	$\cdots$	2002-11-18	P	no(a)	
RX J0258.4+2947	1	0.086 ± 0.011	220.82 ± 4.14	0.60 ± 0.30	10.15 ± 0.30	0.58 ± 0.42	2002-02-28	P	yes(c)	
HD 19668	1	6.565 ± 0.020	148.98 ± 0.19	10.58 ± 0.03	17.28 ± 0.04	$\cdots$	2002-08-27	P	no(a)	
AP 93	1	4.135 ± 0.026	83.86 ± 0.23	7.57 ± 0.30	16.93 ± 0.30	$\cdots$	2003-09-20	P	no(a)	
	2	12.452 ± 0.021	64.09 ± 0.13	7.23 ± 0.32	16.59 ± 0.32	$\cdots$	2004-10-03	P	?	
	3	10.680 ± 0.043	126.00 ± 0.20	9.98 ± 0.20	19.34 ± 0.20	$\cdots$	2004-10-08	K	?	
1RXS J031907.4+393418	1	7.656 ± 0.030	286.56 ± 0.25	8.77 ± 0.09	18.26 ± 0.09	0.87 ± 0.24	2002-08-29	P	no(a)	
	2	10.157 ± 0.024	333.52 ± 0.18	9.69 ± 0.09	19.18 ± 0.09	1.14 ± 0.24	2002-08-29	P	no(a)	
HE 622	1	7.275 ± 0.017	48.24 ± 0.18	6.38 ± 0.22	15.97 ± 0.22	0.66 ± 0.31	2003-09-20	P	?	
	2	9.756 ± 0.024	311.79 ± 0.17	6.51 ± 0.22	16.10 ± 0.22	0.83 ± 0.31	2003-09-20	P	?	
	3	12.478 ± 0.021	107.92 ± 0.12	8.76 ± 0.22	18.35 ± 0.22	1.03 ± 0.31	2004-10-08	K	?	
	4	12.368 ± 0.023	109.57 ± 0.12	9.58 ± 0.22	19.17 ± 0.22	0.98 ± 0.31	2004-10-08	K	?	
	5	10.436 ± 0.017	224.37 ± 0.12	8.10 ± 0.22	17.69 ± 0.22	1.12 ± 0.31	2004-10-08	K	?	
RX J0329.1+0118	1	3.761 ± 0.004	303.35 ± 0.09	3.62 ± 0.08	12.82 ± 0.08	0.90 ± 0.14	2003-09-21	P	yes(c)	
HE 1101	1	5.828 ± 0.025	323.66 ± 0.25	6.58 ± 0.09	15.89 ± 0.09	0.34 ± 0.13	2003-09-20	P	no(a)	

continued on next page

Table 5.6–continued from previous page

Star	N_C	ρ (arcsec)	θ (deg)	ΔK_S (mag)	K_S (mag)	$J-K_S$ (mag)	t_0 (UT Date)	Tel.	Assoc.	Ref.
	2	5.911 ± 0.010	276.86 ± 0.12	8.25 ± 0.09	17.56 ± 0.09	0.14 ± 0.13	2004-10-07	K	no(c)	
	3	5.316 ± 0.009	247.23 ± 0.12	9.13 ± 0.09	18.44 ± 0.09	0.53 ± 0.13	2004-10-07	K	no(c)	
	4	10.100 ± 0.017	113.32 ± 0.12	9.63 ± 0.09	18.94 ± 0.09	0.61 ± 0.13	2004-10-07	K	?	
	5	2.173 ± 0.006	29.19 ± 0.14	10.11 ± 0.09	19.42 ± 0.09	1.15 ± 0.17	2004-10-07	K	?	
HD 22179	1	6.536 ± 0.029	236.26 ± 0.24	8.82 ± 0.10	16.24 ± 0.10	···	2002-11-09	P	no(a)	
	2	6.616 ± 0.029	235.44 ± 0.23	9.30 ± 0.11	16.73 ± 0.11	···	2002-11-16	P	no(a)	
	3	9.200 ± 0.027	179.64 ± 0.23	10.20 ± 0.12	17.62 ± 0.12	···	2002-11-09	P	no(a)	
HII 120	1	3.549 ± 0.008	119.15 ± 0.14	5.75 ± 0.21	14.85 ± 0.21	1.21 ± 0.25	2003-09-20	P	no(a)	
	2	10.633 ± 0.023	70.53 ± 0.13	5.43 ± 0.15	14.53 ± 0.15	1.22 ± 0.20	2003-09-20	P	yes(a)	
RX J0354.4+0535	1	11.128 ± 0.035	225.82 ± 0.18	7.27 ± 0.10	15.94 ± 0.10	0.62 ± 0.18	2003-01-13	P	no(c)	
	2	0.205 ± 0.004	357.44 ± 0.92	2.10 ± 0.20	10.92 ± 0.20	0.97 ± 0.28	2004-02-07	P	yes(c)	
RX J0357.3+1258	1	10.086 ± 0.025	115.72 ± 0.19	6.56 ± 0.08	15.54 ± 0.08	0.64 ± 0.22	2003-01-11	P	no(a)	
	2	3.831 ± 0.026	338.31 ± 0.26	10.50 ± 0.10	19.48 ± 0.10	···	2003-01-11	P	?	
HD 286179	1	10.124 ± 0.024	237.40 ± 0.19	7.20 ± 0.20	15.66 ± 0.20	···	2002-01-31	P	no(a)	
	2	3.406 ± 0.009	194.68 ± 0.22	10.72 ± 0.18	19.18 ± 0.18	···	2004-10-07	K	?	
HD 31950	1	2.596 ± 0.007	264.22 ± 0.18	4.13 ± 0.04	12.51 ± 0.05	0.67 ± 0.07	2002-11-16	P	yes(a)	
	2	3.106 ± 0.007	137.92 ± 0.18	3.70 ± 0.04	12.08 ± 0.05	0.49 ± 0.07	2002-11-16	P	no(c)	
	3	6.925 ± 0.016	146.81 ± 0.18	6.35 ± 0.04	14.73 ± 0.05	0.89 ± 0.07	2002-11-16	P	?	
	4	3.117 ± 0.015	327.86 ± 0.35	8.53 ± 0.05	16.91 ± 0.06	0.31 ± 0.08	2002-11-16	P	no(c)	
	5	10.013 ± 0.027	351.17 ± 0.16	9.91 ± 0.09	18.29 ± 0.09	···	2002-11-16	P	?	
	6	6.528 ± 0.020	28.55 ± 0.14	10.73 ± 0.11	19.11 ± 0.11	···	2002-11-16	P	?	
	7	6.313 ± 0.019	248.03 ± 0.20	10.36 ± 0.08	18.74 ± 0.08	···	2002-11-16	P	?	
HD 36869	1	8.230 ± 0.014	152.30 ± 0.12	3.10 ± 0.35	9.95 ± 0.35	0.93 ± 0.35	2003-01-14	P	yes(a)	
	2	8.043 ± 0.016	249.72 ± 0.20	7.59 ± 0.15	14.44 ± 0.15	···	2003-01-14	P	?	

continued on next page

Table 5.6–continued from previous page

Star	N_C	ρ (arcsec)	θ (deg)	ΔK_S (mag)	K_S (mag)	$J-K_S$ (mag)	t_0 (UT Date)	Tel.	Assoc.	Ref.
1RXS J053650.0+133756	1	1.839 ± 0.018	37.26 ± 0.54	8.88 ± 0.30	16.95 ± 0.30	···	2002-02-28	P	no(a)	
	2	12.096 ± 0.027	212.16 ± 0.17	8.10 ± 0.10	16.17 ± 0.10	···	2002-02-28	P	no(a)	
HD 245567	1	0.348 ± 0.002	330.66 ± 0.23	1.79 ± 0.04	9.57 ± 0.04	0.52 ± 0.08	2002-11-16	P	yes(c)	
	2	3.185 ± 0.007	198.88 ± 0.17	6.44 ± 0.24	14.03 ± 0.24	0.54 ± 0.34	2002-11-16	P	no(a)	
	3	6.748 ± 0.024	316.18 ± 0.22	8.28 ± 0.24	15.87 ± 0.24	0.97 ± 0.34	2002-11-16	P	no(a)	
	4	10.927 ± 0.024	315.63 ± 0.17	6.21 ± 0.24	13.80 ± 0.24	0.55 ± 0.34	2002-11-16	P	no(a)	
	5	2.724 ± 0.007	21.87 ± 0.13	11.55 ± 0.24	19.14 ± 0.24	···	2003-11-09	K	no(a)	
SAO 150676	1	8.375 ± 0.029	351.31 ± 0.14	9.30 ± 0.20	16.77 ± 0.20	···	2002-11-17	P	no(a)	
HD 49197	1	6.952 ± 0.016	345.82 ± 0.18	6.75 ± 0.06	12.82 ± 0.06	0.15 ± 0.12	2002-02-28	P	no(a)	
	2	0.948 ± 0.032	77.50 ± 1.03	8.22 ± 0.14	14.29 ± 0.14	1.63 ± 1.21	2002-02-28	P	yes(a)	
RE J0723+20	1	8.196 ± 0.013	80.86 ± 0.03	7.80 ± 0.20	14.68 ± 0.20	0.16 ± 0.22	2002-02-28	P	no(a)	
	2	5.532 ± 0.013	329.36 ± 0.09	8.40 ± 0.20	15.28 ± 0.20	1.06 ± 0.22	2002-02-28	P	no(a)	
HD 60737	1	7.657 ± 0.029	127.25 ± 0.18	9.40 ± 0.20	15.65 ± 0.20	···	2002-01-31	P	no(a)	
HD 70573	1	1.050 ± 0.066	294.24 ± 3.17	9.07 ± 0.15	16.26 ± 0.15	···	2002-02-01	P	?	
HD 82443	1	5.459 ± 0.010	190.30 ± 0.23	11.77 ± 0.14	16.89 ± 0.14	···	2004-02-07	P	?	
	2	8.154 ± 0.020	98.76 ± 0.15	12.59 ± 0.21	17.71 ± 0.21	···	2004-02-07	P	?	
	3	7.142 ± 0.027	253.71 ± 0.23	13.84 ± 0.30	18.96 ± 0.30	···	2004-02-07	P	?	
SAO 178272	1	10.082 ± 0.032	356.64 ± 0.18	9.67 ± 0.15	17.06 ± 0.15	···	2003-01-13	P	?	
	2	8.184 ± 0.046	274.53 ± 0.15	10.75 ± 0.22	18.14 ± 0.22	···	2003-01-13	P	?	
HD 90905	1	5.816 ± 0.027	191.77 ± 0.23	11.30 ± 0.10	16.82 ± 0.10	···	2002-02-01	P	no(a)	
	2	12.446 ± 0.031	176.73 ± 0.13	13.49 ± 0.19	19.01 ± 0.19	···	2004-06-05	K	no(e)	
HD 91782	1	1.002 ± 0.008	33.67 ± 0.46	4.30 ± 0.06	11.08 ± 0.06	0.90 ± 0.13	2002-03-02	P	yes(a)	
HD 92855	1	2.934 ± 0.005	291.33 ± 0.13	4.57 ± 0.09	10.46 ± 0.09	0.75 ± 0.15	2002-02-01	P	yes(a)	FM00
	2	12.216 ± 0.022	147.79 ± 0.25	8.90 ± 0.20	14.79 ± 0.20	···	2002-02-01	P	no(a)	

continued on next page

Table 5.6–continued from previous page

Star	N_C	ρ (arcsec)	θ (deg)	ΔK_S (mag)	K_S (mag)	$J-K_S$ (mag)	t_0 (UT Date)	Tel.	Assoc.	Ref.
BPM 87617	1	0.248 ± 0.002	273.22 ± 0.11	0.13 ± 0.06	8.58 ± 0.06	1.02 ± 0.08	2003-01-12	P	yes(a)	
	2	10.038 ± 0.009	325.65 ± 0.09	6.40 ± 0.06	14.16 ± 0.06	0.13 ± 0.09	2003-01-12	P	no(a)	
HD 104576	1	10.455 ± 0.028	19.66 ± 0.21	11.00 ± 0.50	17.68 ± 0.50	···	2002-06-22	P	no(e)	
HD 104860	1	3.803 ± 0.027	287.01 ± 0.28	10.92 ± 0.25	17.42 ± 0.25	0.00 ± 0.47	2002-06-23	P	no(a)	
	2	11.961 ± 0.033	260.09 ± 0.19	12.09 ± 0.18	18.59 ± 0.18	···	2004-06-05	K	no(e)	
SAO 15880	1	2.176 ± 0.018	293.93 ± 0.72	8.98 ± 0.17	16.27 ± 0.17	···	2004-02-06	P	no(a)	
HD 111456	1	3.783 ± 0.010	117.45 ± 0.30	12.72 ± 0.16	17.27 ± 0.16	···	2004-02-06	P	?	
HD 139498	1	0.311 ± 0.002	3.39 ± 0.21	0.00 ± 0.02	8.26 ± 0.03	0.50 ± 0.05	2003-07-15	P	yes(a)	
	2	11.246 ± 0.033	123.98 ± 0.19	8.48 ± 0.30	15.98 ± 0.30	···	2004-06-26	P	?	
	3	8.801 ± 0.026	61.50 ± 0.21	10.98 ± 0.30	18.49 ± 0.30	···	2004-06-26	P	?	
HD 142361	1	0.705 ± 0.001	236.41 ± 0.13	2.01 ± 0.10	9.19 ± 0.10	0.85 ± 0.14	2002-06-21	P	yes(a)	
	2	11.207 ± 0.046	164.99 ± 0.17	5.85 ± 0.17	12.88 ± 0.17	0.77 ± 0.28	2002-06-21	P	no(a)	
HD 143006	1	8.355 ± 0.026	130.27 ± 0.25	9.28 ± 0.16	16.33 ± 0.16	1.18 ± 0.23	2002-06-23	P	?	
	2	6.626 ± 0.028	0.32 ± 0.23	10.40 ± 0.16	17.45 ± 0.16	1.40 ± 0.23	2002-06-23	P	?	
	3	8.502 ± 0.029	268.41 ± 0.23	10.66 ± 0.16	17.71 ± 0.16	1.27 ± 0.23	2002-06-23	P	no(a)	
	4	7.698 ± 0.023	357.97 ± 0.12	12.11 ± 0.16	19.16 ± 0.16	1.30 ± 0.23	2003-05-18	K	?	
	5	12.279 ± 0.028	102.74 ± 0.12	11.29 ± 0.16	18.34 ± 0.16	0.88 ± 0.23	2003-05-18	K	?	
(PZ99) J155847.8–175800	1	9.118 ± 0.034	224.72 ± 0.35	11.25 ± 0.22	19.58 ± 0.22	···	2004-06-06	K	?	
ScoPMS 21	1	6.221 ± 0.014	36.94 ± 0.13	7.39 ± 0.02	15.91 ± 0.03	1.05 ± 0.05	2002-06-22	P	no(a)	
	2	9.888 ± 0.027	74.26 ± 0.18	8.06 ± 0.04	16.58 ± 0.05	0.67 ± 0.06	2002-06-22	P	no(c)	
	3	9.351 ± 0.020	308.13 ± 0.16	8.93 ± 0.02	17.45 ± 0.03	1.11 ± 0.08	2002-06-22	P	no(a)	
(PZ99) J160302.7–180605	1	1.572 ± 0.006	190.97 ± 0.19	9.59 ± 0.09	18.32 ± 0.09	2.42 ± 0.17	2003-05-18	K	no(a)	
	2	5.797 ± 0.013	272.51 ± 0.13	7.58 ± 0.62	16.31 ± 0.62	···	2003-05-18	K	no(a)	
	3	9.065 ± 0.020	73.35 ± 0.12	10.58 ± 0.49	19.31 ± 0.49	···	2003-05-18	K	?	

continued on next page

Table 5.6–continued from previous page

Star	N_C	ρ (arcsec)	θ (deg)	ΔK_S (mag)	K_S (mag)	$J-K_S$ (mag)	t_0 (UT Date)	Tel.	Assoc.	Ref.
	4	9.653 ± 0.023	107.18 ± 0.12	11.81 ± 0.53	20.54 ± 0.53	···	2003-05-18	K	?	
ScoPMS 27	1	0.079 ± 0.006	77.04 ± 0.77	0.60 ± 0.20	9.14 ± 0.20	0.83 ± 0.28	2004-06-28	P	yes(c)	
	2	11.113 ± 0.025	218.10 ± 0.22	10.33 ± 0.30	18.37 ± 0.30	···	2004-06-28	P	no(a)	
	3	5.807 ± 0.027	87.35 ± 0.20	10.59 ± 0.30	18.63 ± 0.30	···	2004-06-28	P	?	
	4	5.346 ± 0.026	336.58 ± 0.21	10.47 ± 0.30	18.51 ± 0.30	···	2004-06-28	P	?	
ScoPMS 52	1	0.144 ± 0.005	162.15 ± 1.76	1.10 ± 0.10	8.93 ± 0.10	···	2002-08-31	P	yes(a)	G93
(PZ99) J161318.6–221248	1	3.770 ± 0.012	313.46 ± 0.22	11.00 ± 0.10	18.43 ± 0.10	···	2002-06-21	P	no(a)	
	2	3.333 ± 0.021	81.19 ± 0.41	11.20 ± 0.10	18.63 ± 0.10	···	2002-06-21	P	no(a)	
	3	8.860 ± 0.034	77.36 ± 0.23	11.00 ± 0.20	18.43 ± 0.20	···	2002-06-21	P	no(a)	
	4	7.957 ± 0.018	152.07 ± 0.13	10.83 ± 0.22	18.26 ± 0.22	···	2003-05-18	K	?	
	5	12.182 ± 0.029	259.12 ± 0.17	10.72 ± 0.21	18.15 ± 0.21	···	2003-05-18	K	?	
(PZ99) J161402.1–230101	1	5.366 ± 0.030	356.14 ± 0.49	7.76 ± 0.12	16.37 ± 0.12	···	2003-07-15	P	?	
	2	9.633 ± 0.015	128.34 ± 0.15	9.16 ± 0.17	17.77 ± 0.17	···	2004-06-05	K	?	
	3	7.858 ± 0.017	281.13 ± 0.13	10.35 ± 0.17	18.96 ± 0.17	···	2004-06-05	K	?	
(PZ99) J161411.0–230536	1	0.222 ± 0.003	304.76 ± 0.41	0.21 ± 0.10	8.32 ± 0.10	0.84 ± 0.18	2002-06-21	P	yes(a)	
	2	2.659 ± 0.007	100.46 ± 0.21	6.26 ± 0.03	13.72 ± 0.04	0.82 ± 0.11	2002-06-21	P	no(a)	
	3	2.808 ± 0.010	98.36 ± 0.14	10.25 ± 0.50	18.73 ± 0.50	···	2004-06-05	K	?	
	4	7.709 ± 0.017	341.92 ± 0.12	8.16 ± 0.10	15.62 ± 0.10	0.33 ± 0.22	2004-06-05	K	no(c)	
	5	8.037 ± 0.018	145.10 ± 0.12	9.50 ± 0.06	16.96 ± 0.07	···	2004-06-05	K	?	
	6	8.926 ± 0.021	80.29 ± 0.12	11.72 ± 0.17	19.18 ± 0.17	···	2004-06-05	K	?	
	7	9.243 ± 0.021	69.00 ± 0.15	12.51 ± 0.20	19.97 ± 0.20	···	2004-06-05	K	?	
(PZ99) J161459.2–275023	1	4.787 ± 0.025	264.80 ± 0.20	7.07 ± 0.15	15.76 ± 0.15	···	2003-07-15	P	?	
	2	5.554 ± 0.072	187.48 ± 0.58	7.40 ± 0.15	16.09 ± 0.15	···	2003-07-15	P	?	
	3	3.919 ± 0.010	153.63 ± 0.13	9.65 ± 0.17	18.34 ± 0.17	···	2004-06-05	K	?	

continued on next page

Table 5.6–continued from previous page

Star	N_C	ρ (arcsec)	θ (deg)	ΔK_S (mag)	K_S (mag)	$J-K_S$ (mag)	t_0 (UT Date)	Tel.	Assoc.	Ref.
	4	12.299 ± 0.027	253.55 ± 0.12	8.89 ± 0.18	17.58 ± 0.18	···	2004-06-05	K	?	
	5	11.464 ± 0.026	72.94 ± 0.12	9.91 ± 0.17	18.60 ± 0.17	···	2004-06-05	K	?	
	6	6.241 ± 0.015	259.72 ± 0.17	10.65 ± 0.18	19.34 ± 0.18	···	2004-06-05	K	?	
	7	7.936 ± 0.018	55.55 ± 0.14	10.59 ± 0.19	19.28 ± 0.19	···	2004-06-05	K	?	
(PZ99) J161618.0–233947	1	9.119 ± 0.028	160.44 ± 0.06	7.26 ± 0.30	15.36 ± 0.30	···	2004-06-27	P	?	
	2	10.049 ± 0.026	195.43 ± 0.06	7.57 ± 0.13	15.67 ± 0.13	···	2004-06-27	P	?	
	3	3.190 ± 0.015	184.47 ± 0.64	10.44 ± 0.15	18.54 ± 0.15	···	2004-06-27	P	?	
	4	10.938 ± 0.021	165.25 ± 0.18	10.03 ± 0.11	18.13 ± 0.11	···	2004-06-27	P	?	
	5	12.451 ± 0.020	251.52 ± 0.20	9.31 ± 0.18	17.41 ± 0.18	···	2004-06-27	P	?	
	6	3.671 ± 0.025	140.63 ± 0.22	10.81 ± 0.30	18.91 ± 0.30	···	2004-06-27	P	?	
	7	6.845 ± 0.025	144.15 ± 0.22	10.70 ± 0.30	18.80 ± 0.30	···	2004-06-27	P	?	
	8	9.452 ± 0.028	108.96 ± 0.21	10.68 ± 0.30	18.78 ± 0.30	···	2004-06-27	P	?	
	9	12.309 ± 0.025	38.57 ± 0.22	10.51 ± 0.30	18.61 ± 0.30	···	2004-06-27	P	?	
	10	3.711 ± 0.026	184.89 ± 0.20	11.43 ± 0.30	19.53 ± 0.30	···	2004-06-27	P	?	
HD 146516	1	5.738 ± 0.012	222.79 ± 0.13	7.60 ± 0.09	15.57 ± 0.09	0.80 ± 0.15	2003-05-10	P	no(a)	
	2	9.218 ± 0.028	333.77 ± 0.14	7.50 ± 0.09	15.47 ± 0.09	0.74 ± 0.15	2003-05-10	P	?	
	3	9.493 ± 0.021	81.79 ± 0.12	10.40 ± 0.18	18.37 ± 0.18	···	2004-06-05	K	?	
	4	6.256 ± 0.020	350.00 ± 0.13	11.67 ± 0.23	19.64 ± 0.23	···	2004-06-05	K	?	
ScoPMS 214	1	3.070 ± 0.010	121.17 ± 0.23	5.96 ± 0.09	13.72 ± 0.09	1.06 ± 0.13	2002-08-30	P	yes(a)	
	2	3.598 ± 0.009	350.09 ± 0.24	8.95 ± 0.02	16.71 ± 0.03	1.18 ± 0.05	2002-08-30	P	no(a)	
	3	4.623 ± 0.013	349.37 ± 0.19	9.87 ± 0.04	17.63 ± 0.05	1.22 ± 0.09	2002-08-30	P	no(a)	
	4	10.371 ± 0.019	353.28 ± 0.14	8.64 ± 0.08	16.40 ± 0.08	0.70 ± 0.09	2002-08-30	P	no(a)	
	5	9.674 ± 0.030	180.59 ± 0.23	10.72 ± 0.30	18.48 ± 0.30	···	2002-08-30	P	?	
	6	10.229 ± 0.034	137.12 ± 0.26	11.70 ± 0.30	19.46 ± 0.30	···	2002-08-30	P	?	

continued on next page

Table 5.6–continued from previous page

Star	N_C	ρ (arcsec)	θ (deg)	ΔK_S (mag)	K_S (mag)	$J-K_S$ (mag)	t_0 (UT Date)	Tel.	Assoc.	Ref.
	7	10.202 ± 0.032	351.32 ± 0.13	11.14 ± 0.18	18.90 ± 0.18	···	2004-06-05	K	?	
HD 151798	1	10.330 ± 0.018	335.94 ± 0.17	7.76 ± 0.02	14.24 ± 0.02	0.90 ± 0.04	2002-06-21	P	no(a)	
	2	4.682 ± 0.013	15.84 ± 0.22	10.40 ± 0.30	16.88 ± 0.30	···	2002-06-21	P	no(a)	
	3	7.363 ± 0.014	11.87 ± 0.17	11.66 ± 0.10	18.14 ± 0.10	···	2002-06-21	P	no(a)	
	4	4.212 ± 0.042	222.87 ± 0.29	14.07 ± 0.17	20.55 ± 0.17	···	2003-05-16	K	?	
	5	7.393 ± 0.087	198.06 ± 0.27	13.87 ± 0.30	20.35 ± 0.30	···	2003-05-16	K	?	
	6	8.391 ± 0.062	132.59 ± 0.32	12.66 ± 0.38	19.14 ± 0.38	···	2003-05-16	K	?	
	7	6.737 ± 0.041	117.42 ± 0.50	12.92 ± 0.36	19.40 ± 0.36	···	2003-05-16	K	?	
	8	8.609 ± 0.077	188.86 ± 0.22	13.15 ± 0.54	19.63 ± 0.54	···	2003-05-16	K	?	
	9	6.635 ± 0.046	255.47 ± 0.29	13.17 ± 0.17	19.65 ± 0.17	···	2003-05-16	K	?	
HD 165590	1	0.446 ± 0.001	90.22 ± 0.17	0.68 ± 0.01	5.61 ± 0.02	···	2004-06-28	P	yes(p)	Hip
	2	2.599 ± 0.015	62.65 ± 1.16	8.52 ± 0.10	12.98 ± 0.10	···	2004-06-28	P	?	
	3	12.462 ± 0.033	33.35 ± 0.24	10.56 ± 0.10	15.02 ± 0.10	···	2004-06-28	P	?	
	4	6.548 ± 0.011	111.35 ± 0.26	12.97 ± 0.10	17.43 ± 0.10	···	2004-06-28	P	?	
HD 170778	1	10.103 ± 0.057	39.62 ± 0.39	12.09 ± 0.11	18.14 ± 0.11	···	2004-06-27	P	?	
HD 171488	1	2.620 ± 0.006	30.85 ± 0.12	6.72 ± 0.24	12.57 ± 0.24	0.59 ± 0.34	2004-06-06	K	no(a)	
	2	1.796 ± 0.008	86.65 ± 0.22	11.02 ± 0.24	16.87 ± 0.24	0.39 ± 0.34	2004-06-06	K	no(a)	
	3	6.178 ± 0.015	306.56 ± 0.13	12.04 ± 0.24	17.89 ± 0.24	1.15 ± 0.34	2004-06-06	K	no(c)	
	4	12.301 ± 0.026	181.69 ± 0.12	11.69 ± 0.10	17.54 ± 0.10	···	2004-06-06	K	?	
	5	6.870 ± 0.017	114.19 ± 0.14	12.30 ± 0.10	18.15 ± 0.10	···	2004-06-06	K	?	
HD 172649	1	4.829 ± 0.011	356.29 ± 0.25	6.62 ± 0.07	12.85 ± 0.07	0.47 ± 0.26	2002-06-21	P	no(a)	
	2	2.092 ± 0.005	344.27 ± 0.49	8.80 ± 0.07	15.03 ± 0.07	0.61 ± 0.08	2002-06-21	P	no(a)	
	3	8.570 ± 0.026	33.81 ± 0.12	9.85 ± 0.08	16.08 ± 0.08	0.80 ± 0.09	2002-08-31	P	no(a)	
	4	11.795 ± 0.025	110.75 ± 0.17	11.64 ± 0.11	17.87 ± 0.11	0.98 ± 0.13	2002-08-31	P	no(a)	

continued on next page

Table 5.6–continued from previous page

Star	N_C	ρ (arcsec)	θ (deg)	ΔK_S (mag)	K_S (mag)	$J-K_S$ (mag)	t_0 (UT Date)	Tel.	Assoc.	Ref.
	5	11.771 ± 0.021	109.54 ± 0.19	11.85 ± 0.21	18.08 ± 0.21	···	2002-08-31	P	no(a)	
	6	7.847 ± 0.030	354.63 ± 0.26	13.77 ± 0.30	20.00 ± 0.30	···	2002-08-31	P	?	
HD 187748	1	7.924 ± 0.053	276.61 ± 0.20	12.00 ± 0.04	17.26 ± 0.05	···	2004-06-27	P	?	
	2	7.848 ± 0.044	277.01 ± 0.25	12.30 ± 0.12	17.56 ± 0.12	···	2004-06-27	P	?	
	3	4.885 ± 0.026	179.80 ± 0.23	13.40 ± 0.20	18.66 ± 0.20	···	2004-06-27	P	?	
HD 191089	1	10.893 ± 0.022	219.80 ± 0.13	7.80 ± 0.20	13.88 ± 0.20	···	2003-09-20	P	?	
	2	10.727 ± 0.030	147.93 ± 0.23	7.80 ± 0.20	13.88 ± 0.20	···	2003-09-20	P	?	
HD 200746	1	0.227 ± 0.049	355.26 ± 1.12	1.70 ± 0.20	8.29 ± 0.20	0.75 ± 0.36	2003-09-21	P	yes(a)	Hip
	2	4.295 ± 0.026	353.99 ± 0.23	11.20 ± 0.15	17.59 ± 0.15	···	2003-09-21	P	?	
	3	9.806 ± 0.029	165.81 ± 0.23	11.70 ± 0.16	18.09 ± 0.16	···	2003-09-21	P	?	
	4	2.730 ± 0.006	176.93 ± 0.42	11.09 ± 0.11	17.48 ± 0.11	···	2004-06-26	P	?	
	5	4.750 ± 0.026	261.46 ± 0.23	12.43 ± 0.30	18.82 ± 0.30	···	2004-06-26	P	?	
HD 203030	1	8.579 ± 0.014	314.20 ± 0.12	6.21 ± 0.09	12.86 ± 0.09	0.62 ± 0.15	2002-08-28	P	no(a)	
	2	8.610 ± 0.015	318.36 ± 0.12	8.42 ± 0.09	15.07 ± 0.09	0.84 ± 0.17	2002-08-28	P	no(a)	
	3	11.923 ± 0.021	108.76 ± 0.12	9.58 ± 0.11	16.23 ± 0.11	1.92 ± 0.22	2002-08-28	P	yes(a)	
	4	12.137 ± 0.019	215.15 ± 0.12	8.69 ± 0.11	15.34 ± 0.11	0.53 ± 0.17	2002-08-28	P	no(a)	
	5	9.933 ± 0.027	218.43 ± 0.20	11.29 ± 0.08	17.94 ± 0.08	···	2002-08-28	P	no(a)	
	6	3.365 ± 0.025	343.13 ± 0.23	11.76 ± 0.30	18.41 ± 0.30	···	2002-08-28	P	no(a)	
HD 209393	1	9.187 ± 0.018	6.57 ± 0.13	10.81 ± 0.10	17.13 ± 0.10	···	2002-11-17	P	no(a)	
	2	8.188 ± 0.017	71.50 ± 0.14	12.80 ± 0.20	19.12 ± 0.20	···	2002-11-17	P	no(a)	
	3	6.237 ± 0.013	317.66 ± 0.18	13.11 ± 0.22	19.43 ± 0.22	···	2002-11-17	P	no(a)	
	4	10.344 ± 0.025	210.77 ± 0.15	12.83 ± 0.11	19.15 ± 0.11	···	2002-11-17	P	no(a)	
V383 Lac	1	10.736 ± 0.020	91.89 ± 0.16	8.74 ± 0.04	15.24 ± 0.05	···	2002-08-27	P	no(a)	
	2	11.744 ± 0.024	140.12 ± 0.14	11.12 ± 0.09	17.62 ± 0.09	···	2002-08-27	P	no(a)	

continued on next page

Table 5.6–continued from previous page

Star	N_C	ρ (arcsec)	θ (deg)	ΔK_S (mag)	K_S (mag)	$J-K_S$ (mag)	t_0 (UT Date)	Tel.	Assoc.	Ref.
	3	9.240 ± 0.017	108.35 ± 0.18	10.97 ± 0.08	17.47 ± 0.08	···	2002-08-27	P	no(a)	
	4	4.427 ± 0.018	200.35 ± 0.16	11.10 ± 0.12	17.61 ± 0.12	···	2002-08-27	P	no(a)	
	5	4.231 ± 0.010	98.09 ± 0.56	11.57 ± 0.11	18.08 ± 0.11	···	2002-08-27	P	no(a)	
	6	11.594 ± 0.025	270.42 ± 0.13	11.44 ± 0.10	17.94 ± 0.10	···	2002-08-27	P	no(a)	
HD 218738	1	10.619 ± 0.026	97.59 ± 0.17	8.10 ± 1.00	13.76 ± 1.00	···	2003-12-10	P	no(a)	
	2	10.616 ± 0.025	97.81 ± 0.18	8.07 ± 1.00	13.73 ± 1.00	···	2003-12-10	P	no(a)	
	3	4.144 ± 0.014	182.07 ± 0.23	10.09 ± 0.23	15.75 ± 0.23	···	2003-12-10	P	no(a)	
	4	5.339 ± 0.016	120.60 ± 0.17	11.83 ± 0.27	17.49 ± 0.27	···	2003-12-10	P	no(a)	
	5	6.022 ± 0.022	38.28 ± 0.25	12.68 ± 0.25	18.34 ± 0.25	···	2003-12-10	P	no(a)	
	6	5.508 ± 0.028	33.36 ± 0.26	13.70 ± 0.50	19.36 ± 0.50	···	2003-12-10	P	no(a)	
	7	9.186 ± 0.032	42.22 ± 0.26	13.58 ± 0.30	19.24 ± 0.30	···	2003-12-10	P	?	
	8	2.134 ± 0.018	224.02 ± 0.33	10.96 ± 0.50	16.62 ± 0.50	···	2004-10-04	P	no(a)	
HD 218739	1	7.050 ± 0.030	221.73 ± 0.34	7.45 ± 0.50	13.12 ± 0.50	···	2003-12-10	P	no(a)	
	2	12.055 ± 0.055	238.54 ± 0.34	12.78 ± 0.30	18.45 ± 0.30	···	2003-12-10	P	no(a)	
	3	9.526 ± 0.039	287.92 ± 0.34	13.16 ± 0.50	18.83 ± 0.50	···	2003-12-10	P	no(a)	
HD 219498	1	8.862 ± 0.022	129.85 ± 0.19	8.69 ± 0.14	16.07 ± 0.14	···	2002-08-30	P	no(a)	
	2	9.792 ± 0.032	305.61 ± 0.25	11.76 ± 0.07	19.14 ± 0.07	···	2002-08-30	P	no(a)	

References.— FM00: Fabricius & Makarov (2000); G93: Ghez et al. (1993); Hip: Perryman et al. (1997, *Hipparcos)*.

Table 5.7: Candidate Companions in the Shallow Sample

Star	N	ρ (arcsec)	θ (deg)	ΔK_S (mag)	K_S (mag)	$J - K_S$ (mag)	t_0 (UT Date)	Tel.	Assoc.	Ref.
HD 224873	1	1.268 ± 0.002	171.44 ± 0.12	0.25 ± 0.02	7.57 ± 0.03	0.50 ± 0.05	2002-08-31	P	yes(a)	
HD 9472	1	2.793 ± 0.025	343.69 ± 0.30	5.79 ± 0.09	11.83 ± 0.09	1.04 ± 0.14	2002-11-18	P	yes(a)	
RE J0137+18A	1	1.691 ± 0.006	24.60 ± 0.12	0.05 ± 0.01	7.49 ± 0.02	0.76 ± 0.03	2002-01-31	P	yes(a)	
HD 13531	1	0.717 ± 0.003	16.79 ± 0.43	4.20 ± 0.08	9.88 ± 0.08	1.04 ± 0.15	2002-08-28	P	yes(a)	
1RXS J025223.5+372914	1	0.637 ± 0.003	91.28 ± 0.28	1.43 ± 0.08	10.77 ± 0.08	0.67 ± 0.12	2003-09-21	P	yes(a)	
	2	5.255 ± 0.016	76.85 ± 0.18	4.37 ± 0.09	13.45 ± 0.09	0.50 ± 0.13	2003-09-21	P	no(a)	
2RE J0255+474	1	2.131 ± 0.004	272.63 ± 0.16	0.08 ± 0.05	7.29 ± 0.06	0.72 ± 0.08	2002-02-28	P	yes(a)	WDS
	2	11.469 ± 0.033	46.40 ± 0.11	7.00 ± 0.10	14.21 ± 0.10	0.57 ± 0.14	2002-02-28	P	no(a)	
HD 18940	1	0.167 ± 0.002	8.59 ± 1.18	0.78 ± 0.03	6.71 ± 0.04	0.51 ± 0.08	2002-08-29	P	yes(c)	
	2	4.321 ± 0.012	207.38 ± 0.12	4.58 ± 0.03	10.08 ± 0.04	0.92 ± 0.07	2002-08-29	P	?	
	3	4.120 ± 0.010	203.78 ± 0.13	5.21 ± 0.03	10.71 ± 0.04	0.81 ± 0.07	2002-08-29	P	?	
vB 1	1	2.470 ± 0.006	200.63 ± 0.14	2.63 ± 0.03	8.62 ± 0.04	0.91 ± 0.06	2002-08-29	P	yes(c)	
HE 350	1	8.464 ± 0.016	109.22 ± 0.14	5.85 ± 0.21	15.11 ± 0.21	1.50 ± 0.37	2003-09-20	P	no(a)	
	2	6.896 ± 0.011	38.37 ± 0.19	7.66 ± 0.30	16.92 ± 0.30	$\cdots$	2004-10-04	P	?	
HE 373	1	2.081 ± 0.005	193.77 ± 0.18	5.24 ± 0.10	14.59 ± 0.10	0.98 ± 0.14	2003-09-20	P	yes(a)	
	2	11.598 ± 0.031	265.81 ± 0.25	7.51 ± 0.30	16.86 ± 0.30	$\cdots$	2003-09-20	P	?	
	3	8.478 ± 0.034	55.82 ± 0.22	8.37 ± 0.30	17.72 ± 0.30	$\cdots$	2003-09-20	P	?	

continued on next page

Table 5.7–continued from previous page

Star	Comp.	ρ (arcsec)	θ (deg)	ΔK_S (mag)	K_S (mag)	$J-K_S$ (mag)	t_0 (UT Date)	Tel.	Assoc.	Ref.
HE 389	1	9.023 ± 0.016	133.30 ± 0.12	5.47 ± 0.13	14.96 ± 0.13	1.10 ± 0.18	2003-09-20	P	no(a)	
HE 696	1	0.448 ± 0.001	357.22 ± 0.18	2.72 ± 0.08	12.50 ± 0.08	0.70 ± 0.12	2003-09-20	P	yes(a)	P02
HE 935	1	0.026 ± 0.025	247.44 ± 0.21	0.00 ± 0.20	9.21 ± 0.20	0.40 ± 0.28	2003-09-20	P	yes(c)	P02
	2	3.116 ± 0.025	109.45 ± 0.21	8.70 ± 0.30	17.16 ± 0.30	···	2003-09-20	P	?	
HII 102	1	3.599 ± 0.009	213.29 ± 0.14	3.07 ± 0.10	11.72 ± 0.10	1.05 ± 0.14	2003-09-20	P	yes(a)	B97
	2	9.959 ± 0.027	240.21 ± 0.16	5.75 ± 0.10	14.40 ± 0.10	1.05 ± 0.14	2003-09-20	P	?	
1RXS J034423.3+281224	1	0.425 ± 0.002	202.20 ± 0.10	1.13 ± 0.10	8.62 ± 0.10	0.48 ± 0.22	2002-11-17	P	yes(a)	
	2	5.711 ± 0.006	313.30 ± 0.12	7.11 ± 0.11	14.27 ± 0.11	···	2004-10-05	P	?	
HII 571	1	3.903 ± 0.005	66.10 ± 0.08	3.84 ± 0.08	13.07 ± 0.08	0.95 ± 0.12	2003-12-10	P	yes(a)	B97,M92
HII 1101	1	9.167 ± 0.016	104.93 ± 0.12	5.70 ± 0.09	14.46 ± 0.09	0.40 ± 0.16	2003-12-10	P	no(a)	
HII 1182	1	1.113 ± 0.009	219.69 ± 0.26	4.54 ± 0.19	13.48 ± 0.19	···	2003-12-10	P	yes(a)	B97
HII 1348	1	1.097 ± 0.003	346.79 ± 0.18	5.15 ± 0.09	14.88 ± 0.09	1.16 ± 0.13	2004-10-03	P	yes(a)	
HII 2106	1	0.240 ± 0.010	31.09 ± 0.59	1.71 ± 0.12	11.29 ± 0.12	···	2003-12-10	P	yes(a)	B97
RX J0348.9+0110	1	0.047 ± 0.007	41.50 ± 3.64	0.00 ± 0.05	9.02 ± 0.06	···	2003-12-10	P	yes(a)	
HII 2278	1	0.331 ± 0.005	179.20 ± 0.32	0.03 ± 0.02	9.57 ± 0.03	···	2003-12-10	P	yes(a)	B97
HII 2881	1	0.099 ± 0.005	335.73 ± 1.20	0.26 ± 0.09	9.94 ± 0.09	···	2003-12-10	P	yes(a)	B97
HD 285281	1	0.770 ± 0.001	188.34 ± 0.05	1.20 ± 0.10	9.12 ± 0.10	0.66 ± 0.14	2002-02-01	P	yes(a)	KL98
HD 284135	1	0.367 ± 0.002	253.23 ± 0.21	0.12 ± 0.01	8.58 ± 0.02	···	2002-01-31	P	yes(a)	WDS
HD 281691	1	6.768 ± 0.014	138.91 ± 0.13	1.90 ± 0.05	10.30 ± 0.06	0.74 ± 0.08	2002-11-18	P	yes(a)	KL98
HD 26182	1	0.818 ± 0.002	175.11 ± 0.11	0.92 ± 0.08	9.09 ± 0.08	0.42 ± 0.11	2003-12-10	P	yes(c)	WDS
HD 284266	1	0.569 ± 0.006	356.92 ± 0.11	1.90 ± 0.10	10.66 ± 0.10	0.89 ± 0.41	2002-01-31	P	yes(a)	KL98
HD 26990	1	0.123 ± 0.004	163.56 ± 1.40	0.38 ± 0.20	6.81 ± 0.20	0.67 ± 0.36	2003-12-10	P	yes(a)	

continued on next page

Table 5.7–continued from previous page

Star	Comp.	ρ (arcsec)	θ (deg)	ΔK_S (mag)	K_S (mag)	$J-K_S$ (mag)	t_0 (UT Date)	Tel.	Assoc.	Ref.
vB 49	1	2.139 ± 0.017	256.86 ± 0.16	4.60 ± 0.14	11.40 ± 0.14	···	2003-01-12	P	yes(c)	
vB 52	1	1.115 ± 0.002	236.40 ± 0.18	2.73 ± 0.06	9.10 ± 0.06	0.85 ± 0.08	2003-01-12	P	yes(a)	P98
vB 176	1	0.227 ± 0.003	307.06 ± 0.38	0.28 ± 0.09	7.67 ± 0.09	···	2003-12-10	P	yes(a)	Hip
vB 66	1	9.781 ± 0.023	248.88 ± 0.11	10.75 ± 0.10	16.91 ± 0.10	···	2002-11-17	P	?	
vB 91	1	0.133 ± 0.002	172.98 ± 2.79	0.37 ± 0.14	7.72 ± 0.14	···	2003-12-10	P	yes(a)	
vB 96	1	0.171 ± 0.003	264.05 ± 0.78	0.36 ± 0.10	7.41 ± 0.10	···	2003-12-10	P	yes(p)	P98
RX J0434.3+0226	1	1.340 ± 0.022	271.76 ± 0.30	2.38 ± 0.05	11.99 ± 0.06	0.77 ± 0.11	2003-01-12	P	yes(c)	
vB 106	1	7.230 ± 0.012	76.50 ± 0.44	9.50 ± 0.30	15.94 ± 0.30	···	2003-12-10	P	no(a)	
HD 282346	1	0.461 ± 0.001	272.14 ± 0.18	1.13 ± 0.04	8.91 ± 0.04	0.61 ± 0.17	2002-11-18	P	yes(a)	Hip
vB 142	1	6.070 ± 0.013	123.82 ± 0.16	11.30 ± 0.20	18.04 ± 0.20	···	2002-11-17	P	no(a)	
1RXS J051111.1+281353	1	0.495 ± 0.001	211.51 ± 0.10	0.39 ± 0.04	8.77 ± 0.05	0.69 ± 0.07	2002-02-28	P	yes(a)	
HD 61994	1	5.210 ± 0.008	77.00 ± 0.08	7.32 ± 0.13	12.67 ± 0.13	0.28 ± 0.30	2002-11-18	P	no(c)	
HD 69076	1	1.232 ± 0.005	101.06 ± 0.11	3.91 ± 0.05	10.38 ± 0.05	1.04 ± 0.21	2002-11-18	P	yes(a)	
HD 71974	1	0.383 ± 0.014	87.34 ± 0.63	0.42 ± 0.05	6.45 ± 0.06	0.35 ± 0.21	2002-03-03	P	yes(c)	S99
HD 72760	1	0.964 ± 0.007	215.08 ± 0.38	4.84 ± 0.01	10.28 ± 0.02	1.01 ± 0.04	2002-11-16	P	yes(c)	
HD 77407	1	1.659 ± 0.004	353.36 ± 0.04	2.00 ± 0.10	7.60 ± 0.10	0.90 ± 0.14	2002-01-31	P	yes(a)	M04
HD 78899	1	8.174 ± 0.013	75.76 ± 0.12	3.36 ± 0.08	9.17 ± 0.08	0.79 ± 0.13	2003-12-09	P	?	
HD 91962	1	0.842 ± 0.003	176.00 ± 0.11	1.37 ± 0.06	7.03 ± 0.06	0.73 ± 0.13	2002-03-02	P	yes(a)	
	2	0.142 ± 0.004	56.17 ± 1.76	1.25 ± 0.11	6.94 ± 0.11	0.98 ± 0.19	2003-05-10	P	yes(c)	
HD 99565	1	0.408 ± 0.001	6.13 ± 0.18	0.09 ± 0.05	6.55 ± 0.05	0.48 ± 0.06	2003-01-11	P	yes(a)	WDS
HD 108799	1	2.070 ± 0.006	338.46 ± 0.09	1.47 ± 0.02	6.30 ± 0.03	0.80 ± 0.06	2003-05-10	P	yes(a)	
HD 108944	1	1.941 ± 0.006	345.48 ± 0.18	3.49 ± 0.02	9.56 ± 0.03	0.85 ± 0.09	2002-03-03	P	yes(a)	

continued on next page

Table 5.7–continued from previous page

Star	Comp.	ρ (arcsec)	θ (deg)	ΔK_S (mag)	K_S (mag)	$J-K_S$ (mag)	t_0 (UT Date)	Tel.	Assoc.	Ref.
HD 112196	1	1.501 ± 0.001	55.52 ± 0.09	2.07 ± 0.01	7.77 ± 0.02	0.73 ± 0.04	2002-02-01	P	yes(a)	
HD 115043	1	1.639 ± 0.003	358.61 ± 0.05	4.87 ± 0.08	10.22 ± 0.08	0.86 ± 0.12	2003-12-09	P	yes(a)	L05
HD 129333	1	0.717 ± 0.009	172.77 ± 0.11	2.83 ± 0.05	8.82 ± 0.05	0.81 ± 0.07	2003-01-11	P	yes(a)	DM91,MH04
HD 134319	1	5.356 ± 0.020	260.77 ± 0.10	4.00 ± 0.10	10.79 ± 0.10	0.85 ± 0.11	2002-03-02	P	yes(a)	L05
HD 135363	1	0.251 ± 0.003	121.35 ± 0.46	0.68 ± 0.10	7.34 ± 0.10	0.57 ± 0.14	2002-02-01	P	yes(a)	
RX J1541.1–2656	1	6.261 ± 0.018	82.05 ± 0.13	3.13 ± 0.02	12.05 ± 0.03	···	2003-07-15	P	?	
	2	6.250 ± 0.015	224.11 ± 0.15	7.19 ± 0.11	16.11 ± 0.11	···	2003-07-15	P	no(a)	
(PZ99) J161329.3–231106	1	1.430 ± 0.002	91.41 ± 0.05	2.70 ± 0.05	11.28 ± 0.05	0.87 ± 0.08	2003-05-10	P	yes(a)	
HD 150554	1	11.595 ± 0.023	183.44 ± 0.08	3.06 ± 0.10	9.37 ± 0.10	1.03 ± 0.14	2003-05-10	P	yes(p)	WDS,Mip
HD 152555	1	3.819 ± 0.008	56.86 ± 0.15	3.78 ± 0.02	10.14 ± 0.03	0.81 ± 0.05	2002-08-31	P	yes(a)	
HD 155902	1	0.062 ± 0.007	0.28 ± 6.05	0.50 ± 0.30	6.26 ± 0.30	0.39 ± 0.42	2003-09-21	P	yes(c)	Mip
HD 157664	1	0.036 ± 0.002	118.76 ± 3.21	0.00 ± 0.10	7.46 ± 0.10	0.31 ± 0.14	2003-05-10	P	yes(a)	
HD 166435	1	2.653 ± 0.022	273.69 ± 0.26	10.67 ± 0.20	15.99 ± 0.20	-0.15 ± 0.28	2002-06-23	P	no(a)	
	2	10.376 ± 0.030	281.28 ± 0.12	11.90 ± 0.20	17.22 ± 0.20	0.54 ± 0.22	2002-06-23	P	no(a)	
	3	9.496 ± 0.020	183.40 ± 0.19	11.48 ± 0.20	16.80 ± 0.20	0.18 ± 0.28	2002-06-23	P	no(a)	
	4	3.293 ± 0.009	239.04 ± 0.45	13.50 ± 0.30	18.82 ± 0.30	···	2002-08-30	P	no(a)	
HD 175742	1	2.637 ± 0.043	88.98 ± 0.83	10.75 ± 0.09	16.88 ± 0.09	···	2004-06-28	P	?	
	2	9.362 ± 0.044	198.76 ± 0.28	11.21 ± 0.09	17.34 ± 0.09	···	2004-06-28	P	?	
	3	9.454 ± 0.049	308.56 ± 0.28	10.86 ± 0.09	16.99 ± 0.09	···	2004-06-28	P	?	
	4	7.567 ± 0.020	335.36 ± 0.52	13.00 ± 0.23	19.13 ± 0.23	···	2004-06-28	P	?	
HD 193216	1	8.693 ± 0.016	44.48 ± 0.12	10.54 ± 0.15	16.94 ± 0.15	···	2003-07-16	P	no(a)	
	2	11.674 ± 0.023	231.85 ± 0.18	12.01 ± 0.24	18.41 ± 0.24	···	2003-07-16	P	no(a)	

continued on next page

Table 5.7–continued from previous page

Star	Comp.	ρ (arcsec)	θ (deg)	ΔK_S (mag)	K_S (mag)	$J-K_S$ (mag)	t_0 (UT Date)	Tel.	Assoc.	Ref.
	3	4.209 ± 0.026	66.51 ± 0.23	12.20 ± 0.24	18.60 ± 0.24	$\cdots$	2003-07-16	P	no(a)	
	4	11.330 ± 0.021	326.18 ± 0.12	12.08 ± 0.14	18.49 ± 0.14	$\cdots$	2004-06-27	P	?	
HD 199143	1	1.053 ± 0.002	324.20 ± 0.14	2.08 ± 0.08	8.04 ± 0.08	0.89 ± 0.12	2002-06-23	P	yes(a)	JB01
HD 201989	1	2.079 ± 0.013	159.56 ± 0.14	3.97 ± 0.08	9.70 ± 0.08	1.04 ± 0.14	2003-07-16	P	yes(c)	
RX J2312.0+2245	1	2.860 ± 0.005	27.94 ± 0.12	4.15 ± 0.10	12.40 ± 0.10	0.83 ± 0.14	2002-08-30	P	yes(a)	
RX J2313.0+2345	1	1.406 ± 0.003	54.60 ± 0.13	1.79 ± 0.01	10.60 ± 0.02	0.75 ± 0.04	2002-08-30	P	yes(c)	
HD 221613	1	0.173 ± 0.003	132.28 ± 1.33	1.22 ± 0.10	7.07 ± 0.10	0.58 ± 0.16	2002-11-18	P	yes(a)	WDS

REFERENCES.— WDS: Mason et al. (Washington Double Star Catalog: 2001); P02: Patience et al. (2002); B97: Bouvier et al. (1997); KL98: Kohler & Leinert (1998); P98: Patience et al. (1998); Hip: Perryman et al. (1997, *Hipparcos*); S99: Söderhjelm (1999); M04: Mugrauer et al. (2004); L05: Lowrance et al. (2005). DM91: Duquennoy & Mayor (1991); JB01: Jayawardhana & Brandeker (2001).

[†]HII 1348 is not a part of the unbiased survey for sub-stellar companions.

Table 5.8: Deep Sample Stars without Candidate Companions

HD 377	HD 691	HD 984
HD 1405	HD 7661	HIP 6276
HD 8907	HD 12039	HD 17925
1RXS J025751.8+115759	1RXS J030759.1+302032	1E 0307.4+1424
1E 0324.1-2012	HD 23208	HII 2147
1RXS J035028.0+163121	Pels 191	HD 285751
RX J0442.5+0906	HD 35850	HD 38949
HD 43989	HD 70516	HD 72905
HD 75393	HD 82558	HD 93528
HD 95188	HD 101472	HD 107146
SAO 2085	HD 132173	HD 139813
(PZ99) J160158.2-200811	HD 166181	HD 199019
HD 209779	HD 217343	

Table 5.9: Shallow Sample Stars without Candidate Companions

HD 6963	HD 8467	HD 8941	HD 11850
HD 13382	HD 13507	HD 13974	HD 19019
HD 19632	HE 699	HE 750	HE 767
HE 848	HE 1234	HD 22879	HII 152
HII 174	HII 173	HII 250	HII 314
HII 514	HII 1015	HII 1200	HII 1776
HII 2506	HII 2644	HII 2786	HII 3097

continued on next page

Table 5.9–continued from previous page

HII 3179	HD 27466	vB 39	vB 63
vB 64	vB 73	vB 79	vB 180
vB 88	1RXS J043243.2–152003	vB 92	vB 93
vB 183	vB 97	vB 99	vB 143
HD 286264	HD 32850	HD 37216	HD 37006
HD 38529	HD 64324	HD 66751	HD 72687
HD 73668	HIP 42491	HD 75302	HD 76218
HD 80606	HD 85301	HD 88638	HD 92788
HD 98553	HD 100167	HD 101959	HD 102071
HD 103432	HD 105631	HD 106156	HD 106252
HD 121320	HD 122652	HD 133295	HD 136923
HD 138004	HD 142229	RX J1600.6–2159	(PZ99) J160814.7–190833
HD 145229	HD 150706	HD 153458	HD 154417
HD 159222	HD 161897	HD 179949	HD 187897
HD 190228	HD 193017	HD 195034	HD 199598
HD 201219	HD 202108	HD 204277	HIP 106335
HD 205905	HD 206374	HD 212291	HD 216275

5.4 Deciding Physical Association

The physical association of all candidate companions was decided following on one of the following approaches: (1) common proper motion with the candidate primary, (2) a combination of expected absolute K_S magnitude (assuming equidistance with the primary), near-IR colors, and background star density arguments, (3) extent of the radial profile of the candidate companion beyond that of a point-source PSF, or (4) use of prior-epoch astrometry from the existing literature.

Criterion (1) is the argument of choice in companion studies, as it provides unambiguous evidence of association between two objects: whether as components of a gravitationally bound system or as members of a multi-star moving group

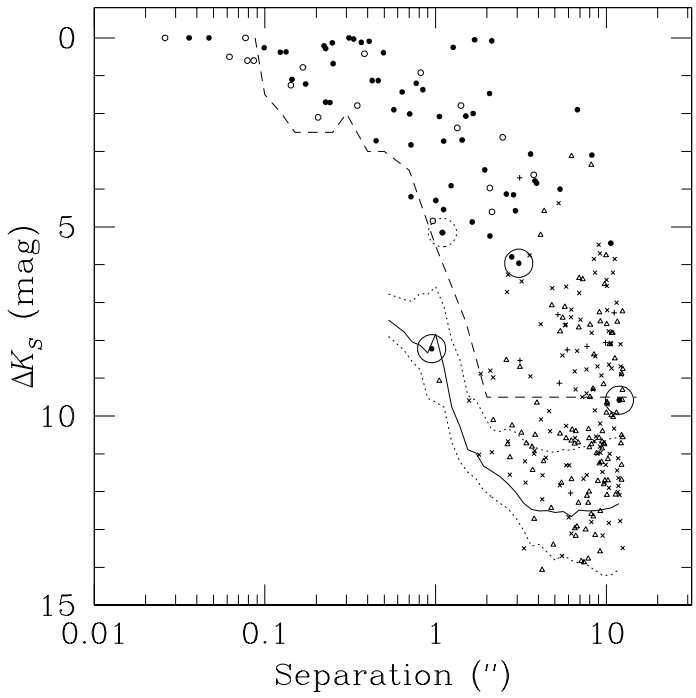

Figure 5.4: Magnitude difference ΔK_S vs. angular separation ρ for all candidate companions discovered during the deep and shallow surveys. The various symbols denote: "•"—astrometrically associated companions; "×"—astrometrically unassociated background stars; and for objects with insufficient astrometric data: "○"—companions associated based on their JK_S photometry; "+"—objects with JK_S photometry inconsistent with association; "△"—undecided objects. The encircled points show 3 brown-dwarf companions from the survey (encircled with solid lines) and 1 companion at the stellar/sub-stellar boundary (HII 1348B; encircled with a dotted line) that is not part of the unbiased survey for sub-stellar companions. Detection limits for the shallow (dashed line) and deep (solid and dotted lines) components of the survey are also shown. For the deep survey, the solid line shows the median contrast ΔK_S, while the dotted lines delimit the 10–90 percentile region (cf. Fig. 5.3a). Binaries with separations smaller than the PALAO K_S-band diffraction limit ($0.09''$) were resolved only at J-band. Correspondingly, the plotted magnitude difference for these companions is the one at J.

sharing a common origin. The majority (150 out of 183 or 82%) of associations and non-associations in this study are decided based on this approach (§5.4.1). Criterion (2) provides only a probabilistic estimate of physical association and was applied only when astrometric follow-up was not obtained or the proper motion data were inconclusive, and when additional J-band images were taken (§5.4.2). This criterion was applied in 9 cases to exclude background interlopers and in 18 cases to establish physical association of candidate *stellar* companions. Because of the larger scatter in near-IR colors for sub-stellar objects, this criterion was not useful for establishing physical association of candidate sub-stellar objects. Criterion (3) was used to weed out faint galaxies, which may otherwise have red near-IR colors, partially due to line-of-sight extinction in our own Galaxy, and thus pose as candidate sub-stellar objects for the preceding criterion. This criterion was applied in 3 cases (§5.4.3). We resorted to the last approach (4) only for 3 candidate companions, for which the previous criteria could not be applied and for which astrometry existed from the literature (§5.4.4).

None of the above criteria were applicable to 105 candidate companions (36% of the total) that remained "undecided." Most of these were faint and at large ($> 5''$) angular separations from their candidate host stars. Hence the vast majority are probably background stars (§5.4.5).

The association status of each candidate companion is indicated in the "Assoc." column of Tables 5.6 and 5.7. "Yes(a)" and "no(a)" entries indicate bona fide astrometric companions and dissociated background stars, respectively. "Yes(c)" entries indicate stellar companions with physical association constrained from their near-IR colors and projected absolute magnitude, while "no(c)" entries denote background objects identified through this criterion. "No(e)" entries denote extended sources, i.e., background galaxies. "Yes(p)" entries mark companions for which we have estimated association relying on prior-epoch astrometric measurements in the existing literature. Finally, a "?" indicates candidate companions with inconclusive or unavailable astrometry and near-IR colors.

5.4.1 Proper Motion

We measured the angular separations and position angles of all candidate companions with respect to their candidate primaries at all imaging epochs. The measurements were then used in conjunction with the expected proper motion of the primaries to determine whether any of the candidate companions share their motion. The application and examples of the technique, using the preliminary astrometric calibration, were described in §3.3.3.2. Here we apply the improved astrometric machinery of §4 to the entire sample.

Determining whether a field object shares the proper motion of the target star is based on the combined application of two requirements: (i) that the change in the position of the candidate companion relative to the primary is within 3σ of zero, and (ii) that the expected change in relative position of the candidate companion, had it been a stationary background object, is more than 3σ discrepant from the observed change. Often in cases of candidate close ($\lesssim$20 AU) binaries, criterion (i) was not satisfied, because of appreciable orbital motion in such binaries. In such situations we have made sure (iii) that the observed change in relative position is much smaller (and less significant) than the expected change if the components of the candidate binary were not gravitationally bound.

When a relatively bright field star ($4 < \Delta K_S \lesssim 8$ mag), also visible in the shallow exposures, was present in the Palomar coronagraphic exposures, it was used as an additional astrometric reference. In cases where the subsequent astrometric measurements (with respect to the primary and fainter field objects) showed such bright field stars to be approximately stationary, they could be used to bootstrap the association of other candidate companions with the primary, circumventing the higher positional uncertainty arising from locating the primary behind the PHARO coronagraph (§4.6). This technique was particularly important in determining the association of systems in the distant USco (145 pc) and α Per (190 pc) regions, where the primaries have small proper motions ($\lesssim$40mas yr^{-1}), but where because of the low galactic latitude ($5^\circ < |b| < 25^\circ$) the images contain multiple background stars.

We monitored the change in relative position in terms of 4 measured quantities: change in right ascension ($\Delta\alpha$), change in declination ($\Delta\delta$), change in angular offset ($\Delta\rho$), and change in position angle ($\Delta\theta$). The statistical averages from multiple measurements of these quantities were monitored independently of one another, to minimize the need for covariant coordinate transformations between $(\Delta\alpha, \Delta\delta)$ and $(\Delta\rho, \Delta\theta)$. A 3σ change in any of the 4 quantities was regarded as significant. For all but the faintest candidate companions, we obtained independent measurements for these quantities from the distortion-corrected detector pixel coordinates in median-combined sub-sets (typically 4 per star) of the total number of exposures. For the faintest objects visible only in the final median-combined image, we used the single measurement from that image and adopted errors corresponding to the empirical r.m.s. scatter of the astrometric calibration (§4.6), in addition to the object centering error.

In the following astrometric example we provide a step-by-step description of the application of criteria (i–iii) above, which was omitted in the published paper (§3.3.3.2). The example re-visits the two candidate companions to HD 49197, one of which was already identified as a sub-stellar companion to the star.

5.4.1.1 Astrometric Example: The Candidate Companions to HD 49197 Re-visited

The first two epochs of imaging observations of HD 49197 were presented in Table 3.2 and Figure 3.5. An additional set of coronagraphic imaging observations was obtained at Palomar on 7 Feb, 2004. The astrometry was re-done using the updated pixel scale for PHARO (§4). The more distant and brighter of the two candidate companions to HD 49197 (object 1 in Table 5.6) was seen both in the shallow non-coronagraphic and in the deep coronagraphic exposures of the star and could thus be used as an additional astrometric reference to bootstrap the position of the primary behind the coronagraph with greater astrometric precision. (§4.6).

Table 5.10 lists the measured change in position ($\Delta\alpha$, $\Delta\delta$, $\Delta\rho$, and $\Delta\theta$), and the statistical significance of the change ($\sigma(\Delta\alpha)$, $\sigma(\Delta\delta)$, etc.), for the candidate

companions with respect to the primary ($R = 0$) and object 1 ($R = 1$). Table 5.11 lists the expected changes in relative positions ($\Delta\alpha_e$, $\Delta\delta_e$, $\Delta\rho_e$, and $\Delta\theta_e$), and the significance of the difference between the observed and the expected change ($\sigma(\Delta\alpha - \Delta\alpha_e)$, $\sigma(\Delta\delta - \Delta\delta_e)$, etc.), given the *Hipparcos* proper motion of the primary (Table 2.2) and assuming that the candidate companions were stationary background stars.

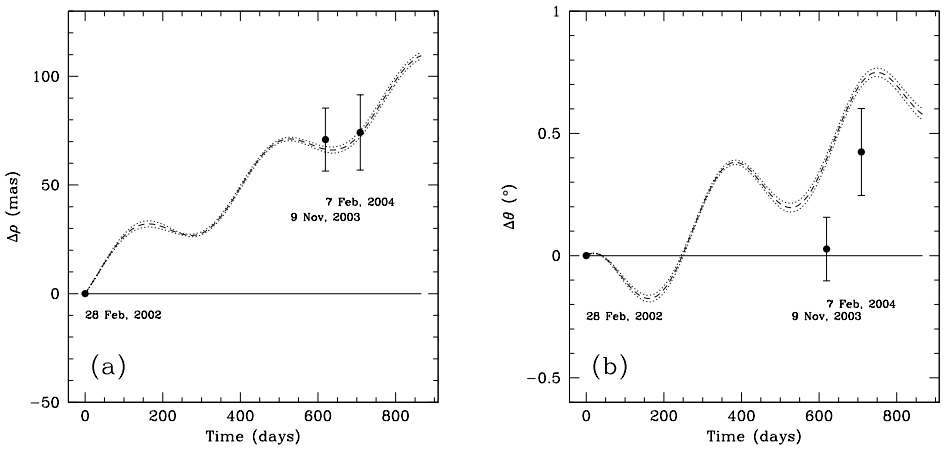

Figure 5.5: Proper motion diagrams of candidate companion 1 to HD 49197. The two panels depict the observed (data points) vs. expected (dashed lines) change in angular separation (panel a) and position angle (panel b) of object 1 with respect to HD 49197. The dotted lines encompass the 1σ error on the expected change in $\Delta\rho$ and $\Delta\theta$, assuming that the candidate companion is a stationary background object. The solid line shows the expected position of the companion, minus any possible orbital motion, had it been physically associated with the primary. Object 1 is thus not consistent with being a common proper motion companion to HD 49197 and is consistent with being a background field star. The cyclic appearance of the expected relative motion is due to the parallactic motion of the primary. The 1σ errorbars on the data points from the follow-up epochs include the 1σ uncertainty of the relative position of the object during the discovery epoch (data point without errorbar).

As seen from Table 5.10, the position of object 2 with respect to the primary

Table 5.10: Observed Change in Relative Position for Candidate Companions to HD 49197

N_C	R	$\Delta\alpha$ (arcsec)	$\Delta\delta$ (arcsec)	$\Delta\rho$ (arcsec)	$\Delta\theta$ (degrees)	$\sigma(\Delta\alpha)$	$\sigma(\Delta\delta)$	$\sigma(\Delta\rho)$	$\sigma(\Delta\theta)$
Follow-up epoch 1: 9 Nov, 2003, ΔJD = 619.24 days									
1	0	-0.0133 ± 0.0186	0.0697 ± 0.0175	0.0709 ± 0.0145	0.027 ± 0.130	0.7	4.0	4.9	0.2
2	0	-0.0043 ± 0.0344	0.0065 ± 0.0112	-0.0031 ± 0.0321	-0.414 ± 1.029	0.1	0.6	0.1	0.4
2	1	0.0176 ± 0.0150	-0.0643 ± 0.0114	0.0663 ± 0.0146	0.055 ± 0.096	1.2	5.6	4.5	0.6
Follow-up epoch 2: 7 Feb, 204, ΔJD = 708.88 days									
1	0	0.0333 ± 0.0191	0.0841 ± 0.0200	0.0742 ± 0.0173	0.424 ± 0.178	1.7	4.2	4.3	2.4
2	0	0.0056 ± 0.0347	0.0095 ± 0.0125	-0.0037 ± 0.0323	-0.606 ± 1.090	0.2	0.8	0.1	0.6
2	1	0.0303 ± 0.0163	-0.0757 ± 0.0150	0.0599 ± 0.0172	0.448 ± 0.154	1.9	5.0	3.5	2.9

Table 5.11: Expected Change in Relative Position for Candidate Companions to HD 49197

N_C	R	$\Delta\alpha_e$ (arcsec)	$\Delta\delta_e$ (arcsec)	$\Delta\rho_e$ (arcsec)	$\Delta\theta_e$ (degrees)	$\sigma(\Delta\alpha - \Delta\alpha_e)$	$\sigma(\Delta\delta - \Delta\delta_e)$	$\sigma(\Delta\rho - \Delta\rho_e)$	$\sigma(\Delta\theta - \delta\theta_e)$
Follow-up epoch 1: 9 Nov, 2003, ΔJD = 619.24 days									
1	0	0.0316 ± 0.0021	0.0757 ± 0.0009	0.0664 ± 0.0013	0.3950 ± 0.017	2.4	0.3	0.3	2.8
2	0	0.0316 ± 0.0021	0.0757 ± 0.0009	0.0487 ± 0.0013	-3.8915 ± 0.128	1.0	6.2	1.6	3.4
2	1	0.0316 ± 0.0021	0.0757 ± 0.0009	-0.0590 ± 0.0013	-0.4656 ± 0.017	0.9	12.2	8.5	5.3
Follow-up epoch 2: 7 Feb, 2004, ΔJD = 708.88 days									
1	0	0.0673 ± 0.0020	0.0913 ± 0.0010	0.0736 ± 0.0015	0.7070 ± 0.017	1.8	0.4	0.0	1.6
2	0	0.0673 ± 0.0020	0.0913 ± 0.0010	0.0873 ± 0.0015	-4.1847 ± 0.132	2.1	6.5	2.8	3.3
2	1	0.0673 ± 0.0020	0.0913 ± 0.0010	-0.0601 ± 0.0015	-0.7851 ± 0.016	5.9	11.1	7.0	8.0

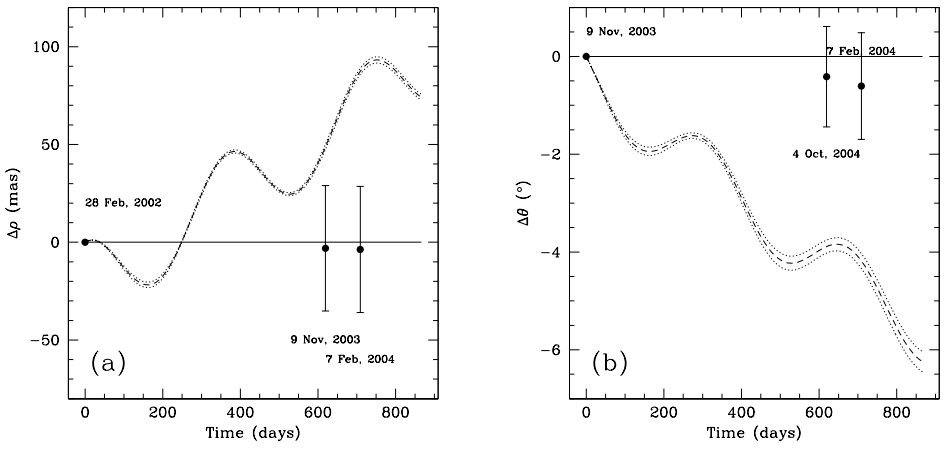

Figure 5.6: Proper motion diagrams of candidate companion 2 to HD 49197. The panels, symbols, and lines are the same as in Figure 5.5. The motion of object 2 relative to HD 49197 is consistent with being 0 and is inconsistent with that of a background star. Object 2 (HD 49197B) is therefore a common proper motion companion to HD 49197 and, hence, physically associated with the star.

($R = 0$) does not change significantly (at the $> 3\sigma$ level) in any of α, δ, ρ, or θ, over the course of almost 2 years. At the same time, an examination of the $R = 0$ lines for object 2 in Table 5.11 shows that the change in the relative position is significantly different from that expected of a stationary background star. Object 2, i.e., HD 49197B, is therefore a proper motion companion of HD 49197, as already established in §3.3.3.2. Object 1, on the other hand, shows significant changes in position relative to the primary (Table 5.10) and is indistinguishable from a background object at the 3σ level (Table 5.11). Therefore, it does not share the proper motion, and is not a physical companion, of HD 49197. Figures 5.5 and 5.6 depict this conclusion graphically for both objects, in terms of $\Delta\rho$ and $\Delta\theta$.

The analysis for object 2 can also be performed with respect to object 1 ($R = 1$ lines in Tables 5.10 and 5.11), realizing that, since the motion of object 1 with respect to the primary is consistent with that of a stationary background star, the conclusions change: small values for $\sigma(\Delta x)$ (where x is one of α, δ, ρ, or θ) and large values for $\sigma(\Delta x - \Delta x_e)$ indicate non-association with the primary,

whereas large values for $\sigma(\Delta x)$ and even larger values for $\sigma(\Delta x - \Delta x_e)$ potentially indicate common proper motion with the primary. The astrometric measurements for object 2 with respect to object 1 thus re-affirm the association of object 1 with HD 49197. However, because field stars may have non-negligible proper motion, especially at the high level of astrometric precision of this survey, the assumption that any field object is stationary needs to be considered with care. Therefore, astrometric measurements relative to field objects cannot be used to establish the physical association of another candidate companion with the primary, but need to be investigated in conjunction with the measurements with respect to the occulted star.

5.4.2 Absolute Magnitude, Near-IR Colors, and Background Object Density

Systems with bright close-in candidate secondaries sometimes lack dual-epoch astrometry in the survey. Such systems were given lower priority in follow-up observations, because they were almost certainly bound, with stellar-mass secondaries. The astrometric analysis of §5.4.1 is inapplicable in such cases. However, the candidate stellar secondaries in these systems are bright enough to be seen in the shallow non-coronagraphic exposures of each target, which in most cases were obtained also in the J and H, in addition to the K_S filter. Hence, for the majority of the candidate stellar systems lacking astrometric data, physical association can be estimated based on the near-IR colors and expected absolute magnitudes of the components. This approach can also be applied to fainter candidate companions, for which single-epoch J- and K_S-band coronagraphic data stars were taken at Keck.

In evaluating the association of a candidate companion based on its near-IR photometry, we looked for $J - K_S$ colors and apparent K_S magnitude consistent with those of an object on the same isochrone (usually, the main sequence) and at the same heliocentric distance as the primary. For the sub-stellar regime, where the isochrones are not well-constrained, especially near the L/T transition ($12 <$

$M_K < 14$), we have relied on the empirical main sequence as traced by nearby M–T dwarfs with known parallaxes (Dahn et al., 2002; Leggett et al., 2002; Reid et al., 2004). All candidate companions with available J-band photometry, for which the astrometry was inconclusive, have had their physical association with the candidate primary evaluated in this manner (Fig. 5.7). To limit the probability of misclassifying field stars as companions, positive associations have been adopted only for candidate companions within $5''$.

This approach was successful mostly for stellar-mass companions bluer than $J - K_S = 0.8$ (earlier than spectral type M0) because of the narrow width of their expected locus on the color-magnitude diagram. Therefore, projected companions in the background were apparent via their discrepant absolute magnitudes. For early M dwarfs (M0–M6), the main sequence is nearly degenerate in $J - K_S$ over $\sim$4 mag in M_{K_S} to within the errorbars and does not allow reliable association estimates. At even later spectral types, potentially representative of fainter brown-dwarf companions, the higher photometric uncertainties and the larger empirical color scatter at sub-stellar masses prevented the conclusive determination of physical association in all but a handful of faint projected companions. H-band photometry, where available, did not improve the analysis because of the smaller spread in $H - K_S$ with respect to $J - K_S$ colors.

In addition to using near-IR colors, it is also possible to obtain a probabilistic estimate of the physical association for a candidate companion to its corresponding primary by comparing the number of detected objects within the $12.5''$ survey radius to the surface density of stars at the relevant galactic coordinates down to the limiting magnitude of the survey. Because of the lack of large-area deep ($K_S \lesssim 20$) near-IR survey data, we have constrained this type of analysis to only candidate companions in the shallow survey. Although the depth of the shallow survey varies depending on the use of the ND filter at Palomar, it is roughly comparable to the completeness limit of the 2MASS survey: $K_S < 14.3$ in unconfused regions of the sky. Therefore, for all candidate companions brighter than $K_S = 14.3$, an empirical estimate of the association probability is possible

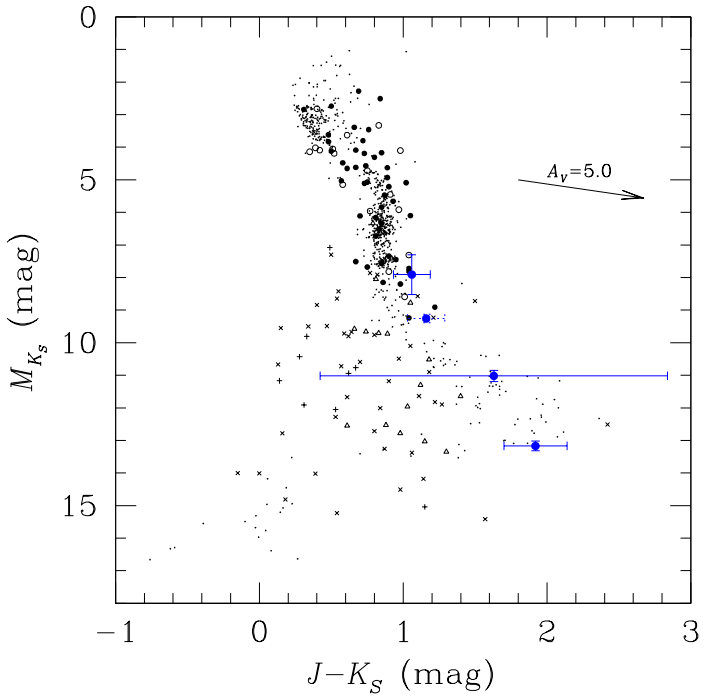

Figure 5.7: M_{K_S} vs. $J - K_S$ color-magnitude diagram for candidate companions in the sample with obtained J-band photometry. The symbols are the same as in Figure 5.4. The additional small dots denote M0–T8 dwarfs ($M_{K_S} \gtrsim 4.5$) with parallaxes from Leggett et al. (2002), Dahn et al. (2002), and Reid et al. (2004), and the F5–K5 sample stars ($M_{K_S} \lesssim 4.0$ mag). The points with errorbars represent 3 confirmed brown-dwarf companions from the survey (solid errorbars) and 1 companion at stellar/sub-stellar boundary (HII 1348B; dotted errorbars) that does not belong to the unbiased survey for sub-stellar companions (§6). The errorbars are representative of the photometric precision of the survey, except for the large $J - K_S$ uncertainty of HD 49197B, which is unique. The vector in the upper right corresponds to 5 mag of V-band extinction, equivalent to a distance of ∼3 kpc, or a distance modulus of 12 mag in the galactic plane.

from 2MASS. Given that the faintest primaries in the sample have K_S magnitudes of 9.6, such a probabilistic analysis can be performed on all candidate companions with $\Delta K_S \leq 4.7$ mag.

To estimate the contamination from $K_S \leq 14.3$ field stars, we counted the number of 2MASS objects within a 5′-radius circular area offset by 12′ (to avoid bright artifacts) from each sample star, and from that estimated the expected number of background objects in the 5″-radius field of interest. We use this estimate as an equivalent of the purely geometrical chance alignment probability:

$$\text{CAP} \;=\; (\text{number of 2MASS sources within } 5') \times \frac{\pi(5'')^2}{\pi(5 \times 60'')^2}. \qquad (5.1)$$

Table 5.12 lists the separations, ΔK_S and K_S magnitudes, and the CAPs for all sample stars with color companions (i.e., the ones with "yes(c)" entries in Tables 5.6 and 5.7). Most color companions have chance alignment probabilities $\lesssim$2%, with the exception of HD 155902B and HE 935B, both of which are in very tight ($< 0.1''$), and thus certainly physical, binaries. (These two systems are in fact below the resolution limits of the 95 mas PALAO K_S-band PSF. Their binarity was only appreciated from PALAO J-band images, where the PSF is 50 mas wide.) The ensemble probability of at least one of the 17 color companions being a false positive is 33%, or 16% after excluding HD 155902 and HE 935.

5.4.3 Source Extent

Only 3 of the detected sources have been flagged as extended, although a more careful object profile analysis will probably reveal a somewhat larger number, based on rough expectations of the surface density of background galaxies down to $K_S \approx 20$ mag. Determining source angular extent was not a primary objective of the survey, and source extent was judged only by eye. This is not a trivial task when the quality of the AO correction and, hence, the size of the PSF, change throughout the course of a single night, depending on guide star brightness and atmospheric stability. Furthermore, source elongation in AO imaging is a function of distance

Table 5.12: Color Companions and Their Chance Alignment Probabilities

Companion to	N_C	ρ (arcsec)	ΔK_S (mag)	K_S (mag)	CAP (%)
HD 15526	1	0.0770	0.00	8.01 ± 0.10	0.8
HD 155902	1	0.0620	0.50	5.73 ± 0.10	14.3
HD 18940	1	0.1670	0.78	6.28 ± 0.10	1.5
HD 201989	1	2.0790	3.97	9.70 ± 0.08	0.9
vB 1	1	2.4700	2.63	8.62 ± 0.10	0.9
HD 245567	1	0.3480	1.79	9.38 ± 0.10	0.8
HD 26182	1	0.8180	0.92	8.71 ± 0.10	2.3
vB 49	1	2.1390	4.56	11.36 ± 0.10	1.3
HD 71974	1	0.3830	0.42	5.89 ± 0.10	1.7
HD 72760	1	0.9640	4.84	10.26 ± 0.10	0.9
HD 91962	2	0.1420	1.25	6.64 ± 0.10	0.9
HE 935	1	0.0260	0.30	8.76 ± 0.10	6.7
RX J0329.1+0118	1	3.7610	3.62	12.82 ± 0.10	0.7
RX J0354.4+0535	2	0.2050	2.10	10.77 ± 0.10	1.4
RX J0434.3+0226	1	1.3400	2.38	11.88 ± 0.10	1.2
RX J2313.0+2345	1	1.4060	1.79	10.41 ± 0.10	1.4
ScoPMS 27	1	0.0790	0.60	8.64 ± 0.10	0.7

from the guide star. The effect is due to anisoplanatism and is characterized by the size of the isoplanatic angle θ_0 over which the atmospheric perturbations applied to a wavefront of a given wavelength λ are correlated. The value of θ_0 is proportional to the atmospheric Fried parameter r_0, is inversely proportional to the height h of the turbulent layer of the atmosphere, and scales as $\lambda^{6/5}$ (Roddier, 1999). Typical values for θ_0 at 2μm are 10″–20″, where a larger value of θ_0 translates into sharper, more uniform PSFs, out to a larger angular separation from the guide star. Beyond an angular separation of θ_0, the PSF becomes noticeably elongated in the radial direction from the guide star. The effect is especially noticeable in J-band Keck exposures with the 40 mas pix^{-1} camera, where the PSF near the field edges can be elongated in the radial direction by factors of 2–3.

Therefore, departures from the nominal, diffraction-limited PSF size and from a centrally symmetric PSF shape were regarded with caution. These were used to classify an object as an extended source only when they were in disagreement with the size and radial behavior of the profiles of other point source in the same image, if such were present.

5.4.4 Astrometry from the Literature

We have confirmed physical association for 3 sample stars using published astrometric measurements from prior epochs in the literature. These are vB 96 (Patience et al., 1998) and HD 150554 (Washington Double Star Catalog; Mason et al., 2001) in the shallow sample, and HD 165590 (*Hipparcos*; Perryman et al., 1997) in the deep sample.

5.4.5 Undecided Objects

A large fraction (36%) of the candidate companions remain astrometrically undecided at the end of the 3-year survey. The vast majority of these are faint objects in the fields of distant (>100 pc) stars with small apparent proper motions (<50 mas yr^{-1}), often at low galactic latitudes ($b < 15°$), such as targets in α Per or in USco. Indeed, nearly all deep-sample stars belonging to these two young as-

sociations have multiple companions at $\gtrsim 3''$ separations and with $\Delta K_S > 7$ mag with undecided association status. These were often discovered only in follow-up deeper imaging with Keck and thus also lack the full time-span of observations. Judging by the large number of such candidate companions per star, and based on expectations of the background star contamination rate at low galactic latitudes, likely all of these candidate companions are unassociated.

A smaller number of undecided companions reside around nearby (20–100 pc) stars at higher galactic latitudes, which were only added to the program in the last year of the survey: e.g., the 20 stars in the extension of the FEPS sample (§2.3.2). Although second-epoch astrometry is not available for all candidate companions around these stars, they have been included in the analysis because their higher proper motions ensured that quick (4–6 months) follow-up of any potential "interesting" companions would produce meaningful astrometric results. Such was indeed possible for candidate close-in faint companions to 4 of the newly-added stars (SAO 15880, HD 171488, HD 218738, and HD 218739).

Chapter 6

Survey Results and Analysis

Preliminary results from the survey for select stars were already presented in §3. These included the discovery of the first brown-dwarf companion from the survey, HD 49197B, and of three low-mass stellar companions to HD 129333, V522 Per, and RX J0329.1+0118. In this chapter we analyze the results from the complete survey, most notably the discovery of two additional bona fide brown-dwarf companions, HD 203030B and ScoPMS 214B. In addition, we present results on a companion to HII 1348 at the stellar/sub-stellar limit, previously discovered by Bouvier et al. (1997), but with unknown association status until now. Finally, 45 new stellar companions to stars in the sample are discussed.

6.1 Brown Dwarf Secondaries

All three of the bona fide sub-stellar companions were found in the deep survey. The remaining low-mass companion, HII 1348B, was observed only because the existence of a faint candidate companion to HII 1348 was a priori known. The HII 1348A/B system is thus not part of the unbiased survey for sub-stellar companions. Here we address each of the four companions individually. Near-IR JHK_S photometry for all is presented in Table 6.1. Their estimated physical properties are summarized in Table 6.2. Figure 6.1a compares the obtained M_{K_S} absolute magnitudes and $J-K_S$ colors of the brown-dwarf companions with those predicted by the DUSTY (Chabrier et al., 2000) and COND (Baraffe et al., 2003) sub-stellar

cooling models of the Lyon group. Figure 6.1b re-iterates the comparison in terms of the predicted luminosities and effective temperatures by the DUSTY models. (Burrows et al., 1997).

6.1.1 HD 49197B

The newly-discovered L-dwarf companion to HD 49197 was already discussed in §3.3. The updated astrometric analysis in §5.4.1.1 re-affirms the proper motion association of the sub-stellar companion with the primary. The adopted temperature and bolometric luminosity (Table 6.2) for the brown dwarf are based on the already determined spectral type (§3.3.3.3.1) and on spectral type vs. effective temperature and bolometric correction data for L and T dwarfs from Vrba et al. (2004).

At a an age of ∼500 Myr and a spectral type of L4±1, HD 49197B is one of very few known young ultra-cool (later than M7) brown dwarfs (§3.3.4.4). As such, it will be an important reference point in future studies of the evolution of young sub-stellar objects.

6.1.2 HD 203030B

6.1.2.1 Astrometric Confirmation

The star HD 203030 was observed coronagraphically during three epochs at Palomar: 28 Aug, 2002, 16 Jul, 2003, and 26 Jun, 2004. The time spans between the first and the subsequent epochs were ΔJD = 332.11 days and 668.17 days, respectively. The combined proper and parallactic motion of HD 203030 between the first and the final epoch amounted to 266 mas. A total of 8 candidate companions were identified in the deep image of the $25.6'' \times 25.6''$ PHARO field, 6 of which within the $12.5''$ survey radius (Fig. 6.2a). Such a high number of field objects was typical for the $b = -16^{\circ}$ galactic latitude of HD 203030. The brightest of the field objects (candidate companion 1 in Table 5.6) was also seen in the shallow exposures of HD 203030 (Fig. 6.2b). The relative motion of this candidate companion

Table 6.1: Near-IR Photometry of the Confirmed and Candidate Brown Dwarfs

Object	ΔK_S (mag)	$J-H$ (mag)	$H-K_S$ (mag)	$J-K_S$ (mag)	K_S (mag)	M_{K_S} (mag)	$M_{\rm bol}$ (mag)
HD 49197B	8.22 ± 0.11	1.2 ± 1.2	0.33 ± 0.20	1.6 ± 1.2	14.29 ± 0.14	11.04 ± 0.24	14.38 ± 0.24
HD 203030B	9.58 ± 0.11	1.45 ± 0.22	0.47 ± 0.16	1.92 ± 0.22	16.23 ± 0.11	13.17 ± 0.15	$16.1^{+0.3}_{-0.2}$
ScoPMS 214B	5.96 ± 0.09	0.67 ± 0.13	0.39 ± 0.13	1.06 ± 0.13	13.72 ± 0.09	7.91 ± 0.61	10.9 ± 0.6
HII 1348B[†]	5.15 ± 0.09	0.74 ± 0.13	0.42 ± 0.13	1.16 ± 0.13	14.87 ± 0.09	9.25 ± 0.13	12.20 ± 0.16

[†] Not a member of the unbiased survey.

Table 6.2: Estimated Physical Properties of the Sub-stellar Companions

Object	Spectral Type[†]	$T_{\rm eff}$ (K)	Luminosity $\log(L/L_\odot)$	Age (Myr)	Mass ($M_\odot$)	Mass ratio	Projected Separation (AU)
HD 49197B	L4±1	1800 ± 150	-3.86 ± 0.10	260–790	$0.060^{+0.012}_{-0.020}$	0.052	43
HD 203030B	T0.5±1	1400 ± 50	$-4.54^{+0.08}_{-0.12}$	400 ± 200	0.035 ± 0.005	0.031	490
ScoPMS 214B	M6±1	2700 ± 300	-2.46 ± 0.24	5 ± 1	0.025 ± 0.005	0.023	450
HII 1348B[‡]	M6.5±1	2600 ± 300	-2.98 ± 0.06	125 ± 8	0.070 ± 0.005	0.093	145

[†] Except for that of HD 49197B, all other spectral types are estimated from near-IR photometry.

[‡] Not a member of the unbiased survey.

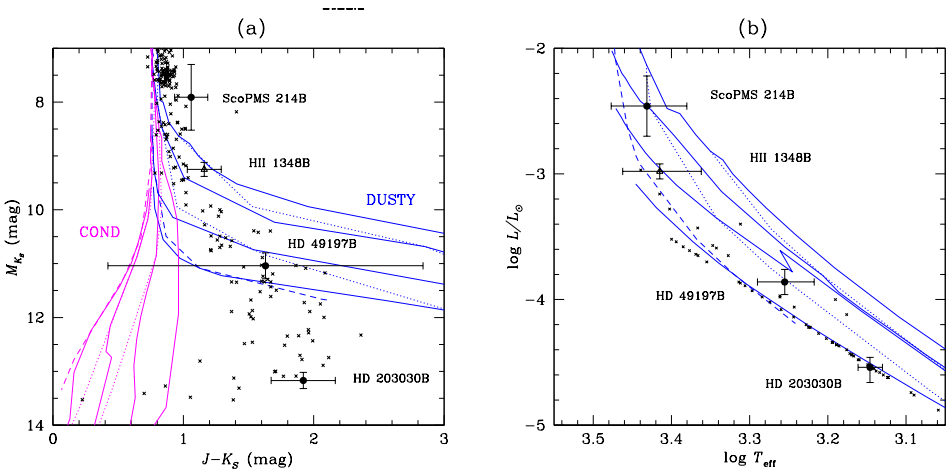

Figure 6.1: H–R diagrams of the new bona fide (circles) and candidate (triangle) brown dwarfs. (a) Near-IR color-magnitude diagram with the predictions of the Lyon group DUSTY and COND models overlaid. Solid lines delineate 1, 10, 100, and 1000 Myr isochrones: from top to bottom in the DUSTY models, and from right to left in the COND models. Dotted lines show tracks of constant mass for 0.010 $M_\odot$ and 0.030 $M_\odot$ objects, whereas the dashed lines show the hydrogen-burning limit (0.072 $M_\odot$) at solar metallicity. Mass also increases from top to bottom in the DUSTY models, and from right to left in the COND models. The small $\times$ points represent M–T dwarfs with known parallaxes Leggett et al. (2002); Reid et al. (2004); Gelino et al. (2004). (b) L vs. $T_{\rm eff}$ diagram, comparing the new brown dwarfs to predictions from the Lyon group DUSTY models. The COND models are nearly identical to DUSTY in $L - T_{\rm eff}$ space. Symbols and line designations are the same as in panel (a). The degeneracy between sub-stellar age and mass is clearly identifiable from the nearly parallel sets of evolutionary tracks for the two parameters. Note the much better agreement of the models with the estimated parameters of HD 203030B in L vs. $T_{\rm eff}$ space, compared to the inability of the models to predict the photometric properties (panel a) of this T0.5 dwarf.

with respect to the primary was consistent with that of a stationary background star, as established from the shallow images. Thus, we used object 1 as an additional astrometric reference for all other candidate companions to bootstrap the position of the primary behind the coronagraph with greater astrometric precision (§4.6).

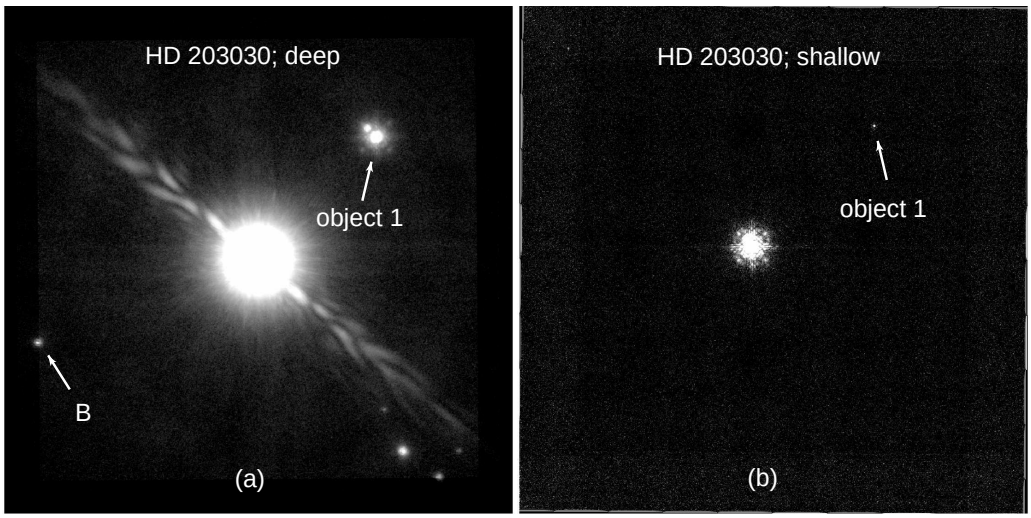

Figure 6.2: Deep coronagraphic (a) and shallow non-coronagraphic (b) K_S-band images of HD 203030 from 28 Aug, 2002. The proper motion brown-dwarf companion HD 203030B is indicated by an arrow in panel (a). The astrometry was done relative to the position of background object 1, seen in both images. The broad 45°-inclined jet-like feature in the deep image is due to an oil streak across the secondary mirror of the Palomar 5 m telescope. The secondary was periodically cleaned subsequent to our identification of this feature, and the 2003–2005 Palomar data lack this contamination. The images are 25.6″ on a side; north is up and east is to the left.

We found that the third candidate companion to HD 203030 (Table 5.6) shared the apparent motion of the primary, while its motion was discrepant from that of a stationary background star at the 7.1σ level in $\Delta\rho$ at the final imaging epoch. Therefore, object 3 is a proper motion companion to HD 203030, and henceforth we refer to it as HD 203030B. Figure 6.3 shows the $\Delta\rho$ and $\Delta\theta$ proper motion

diagrams for HD 203030B with respect to the primary. At an angular separation of 11.9″ from the primary, HD 203030B is near the outer edge of the 12.5″ survey radius and resides at a projected separation of 490 AU from the primary.

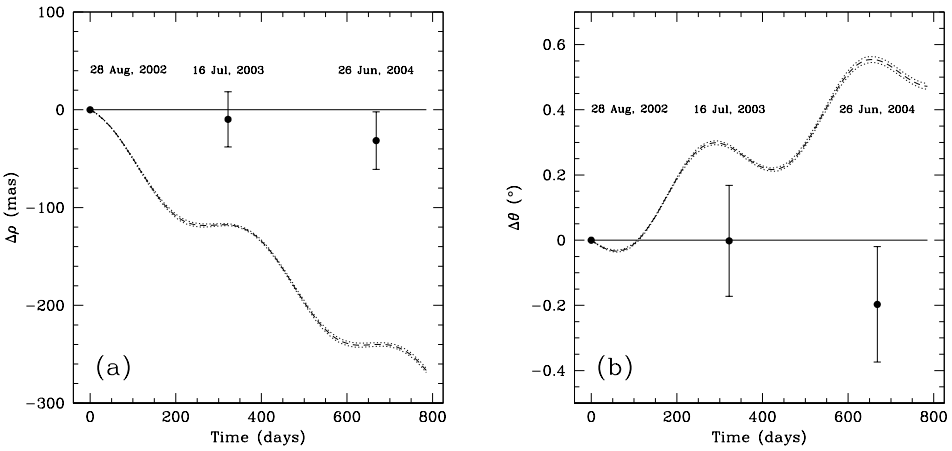

Figure 6.3: Proper motion diagrams of HD 203030B. Panel (a) depicts the apparent motion in $\Delta\rho$ and panel (b), in $\Delta\theta$. The lines and symbols are the same as in Figure 5.5.

6.1.2.2 Spectral Type and Mass of HD 203030B

We estimate the spectral type of HD 203030B from its near-IR colors and from its absolute K_S magnitude. In addition to the coronagraphic survey observations, non-coronagraphic saturated JHK_S images of HD 203030 were obtained with PALAO/PHARO on 28 Aug, 2002. HD 203030 B is visible in the H and K_S images, but drops out at J band. Deeper coronagraphic J-band exposures were subsequently obtained with Keck AO and NIRC2 on 14 Jul, 2005. The final near-IR photometry of HD 203030B is bootstrapped with respect to the brightest object in the field—object 1—and its magnitude difference from HD 203030.

The photometry of HD 203030B (Table 6.1) shows the characteristic red $J-K_S$ color of late L dwarfs—a fact confirmed by the object's faint absolute magnitude. Using the empirical J and K_S absolute magnitude—spectral-type relations from Kirkpatrick et al. (2000), calibrated for L dwarfs with known trigonometric paral-

laxes, we identically obtain a spectral type of L8.5±0.5 from both the J- and K_S-band photometry, where the uncertainty comes from the error on the photometry. The scatter in the Kirkpatrick et al. relations is approximately 1 spectral sub-type, which we adopt as the total error on the spectral type of HD 203030B (the formal error is ±1.1 sub-type). A spectral type of L8.5 translates to T0.5 on the near-IR spectroscopic sequence, which currently does not extend pas L8 in the L dwarfs. Although Kirkpatrick et al. do not present absolute magnitude—spectral-type relations for T dwarfs, and thus the extrapolated spectral type may be suspect, a comparison with the M_{K_S} magnitudes and $J-H$ colors of an expanded sample of L and T dwarfs with trigonometric parallaxes (Vrba et al., 2004) confirms that the near-IR flux and colors of HD 203030B are most consistent with those of a T0.5 dwarf. We therefore adopt that as the spectral type for HD 203030B, with the ±1 sub-type error range translating to L7.5–T1.5. The corresponding effective temperature, nearly constant across the L/T transition (e.g., Golimowski et al., 2004) is 1400 ± 50 K. Using a bolometric correction $BC_K = M_{\rm bol} - M_K = 2.9^{+0.3}_{-0.1}$ mag, where the $M_{\rm bol}$ and M_K magnitudes for L7.5–T1.5 dwarfs are taken from Table 9 of Vrba et al. (2004), we find a bolometric magnitude of $M_{\rm bol} = 16.1^{+0.3}_{-0.2}$ mag, i.e., a luminosity of $\log(L/L_\odot) = -4.54^{+0.08}_{-0.12}$ for HD 203030B, where we have assumed $M_{\rm bol} = 4.74$ mag for the Sun (Drilling & Landolt, 2000). HD 203030B is thus the coolest, least luminous companion found around a young (<1 Gyr) star. Recently obtained K-band spectroscopy of this object is expected to open new insights on the elusive L/T transition in ultra-cool dwarfs in evolutionary context.

We estimate the mass of HD 203030B using pre-main sequence tracks from the Lyon groups, assuming that the companion is co-eval with the primary. Given that the object is at the L/T transition, we obtain mass estimates by matching the near-IR flux of HD 203030B to predictions from both the DUSTY (Chabrier et al., 2000) and COND (Baraffe et al., 2003) models. We also compare the estimated effective temperature and bolometric luminosity to predictions from both the Lyon and the Arizona (Burrows et al., 1997) groups.

The adopted age for HD 203030, based on its R'_{HK} value, is 400 Myr (Ta-

ble 2.2). Since the R'_{HK} index is only a secondary age indicator (see discussion in §2.2.2), we compare this estimate to the ages inferred from other age indicators. Based on its galactic space motion, Montes et al. (2001b) list the star as a member of the IC 2391 supercluster, with an age of 35–55 Myr. However, the relatively small Li I equivalent width of $\approx 60 \pm 10$ Å seen in high-resolution optical spectra of HD 203030 (Strassmeier et al., 2000, White et al., in preparation) does not support such a young age at the late spectral type (G8) of the star. The observed Li I absorption is less than the amount seen in 125 Myr old G8 Pleiades members and is comparable to the one seen in members of the 500 ± 100 Myr old Ursa Major moving group (King et al., 2003). Combining the R'_{HK} and lithium age estimates, we adopt an age of 400±200 Myr for HD 203030. The corresponding mass range for the M_{K_S} magnitude of HD 203030B is ∼0.020–0.035 $M_\odot$ from both the DUSTY and the COND models (Fig. 6.1). However, neither of the models correctly predicts the $J - K_S$ color of HD 203030B. The DUSTY models over-predict it by ∼3 mag, while the COND models it by ∼1 mag (Fig. 6.1a). Therefore, we do not use this mass estimate. Instead, we adopt an estimate based on the inferred bolometric luminosity and effective temperature of HD 203030B. These two indicators provide a more accurate rendition of the true thermodynamic state in brown-dwarf photospheres near the L/T transition (Baraffe et al., 2003), as is evident from a comparison of panels (a) and (b) in Figure 6.1. The estimated mass is 0.030–0.040 $M_\odot$, identically confirmed from the models of Burrows et al. (1997). That is, HD 203030B is a brown dwarf.

The fact that HD 203030B is a brown dwarf could have been inferred, of course, without relying on theoretical models, but just based on the late spectral type the object. Its estimated effective temperature of ∼1400 K, is far cooler than the minimum effective temperature attained by main-sequence stars (∼2000 K, Fig. 1.2).

6.1.3 ScoPMS 214B

6.1.3.1 Astrometric Confirmation

ScoPMS 214 has a very small proper motion, only 22.8 mas yr^{-1} (bottom tenth percentile of the sample) and as a result required imaging at multiple epochs to discern whether any of the 7 candidate companions within 12.5″ shared the proper motion of the primary. The star was observed over 5 epochs between 2002 and 2005: on 30 Aug 2002 and 27 June 2004 at Palomar, and on 16 May 2003, 5 June 2004, and 13 Jul 2005 at Keck. The time spans between the first and the subsequent epochs were ΔJD=258.81, 645.37, 667.15, and 1048.19 days. The combined proper and parallactic motion of ScoPMS 214 between the first and the last epoch was 65.7 mas. This was sufficient to decide the physical association of the 3 closest and the brightest of the remaining 4 candidate companions, but remained inadequate for the 3 faint ($\Delta K_S = 10.7 - 11.1$) companions at angular separations $> 10''$.

Most astrometric measurements for the star were calibrated with respect to the binary WDS 18055+0230, except for the 16 May 2003 Keck data, which were calibrated from an observation of WDS 15360+3948 taken on the following night. WDS 15360+3948 was not one of the stars monitored at Palomar, and the astrometry calibrated with respect to it displays a significant offset from the remaining observations. We ignore this data point in the following discussion and consider only the remaining 4 epochs.

As in the cases of HD 49197 and HD 203030, one of the candidate companions in the field of ScoPMS 214, object 1 (later identified as ScoPMS 214B itself), was bright enough to be visible with sufficient signal-to-noise in the shallow non-coronagraphic Palomar images (Fig. 6.4). The changes in the relative positions of the remaining fainter candidate companions could thus be bootstrapped with respect to object 1. However, given that object 1 itself turned out to be the proper motion companion to the primary, the context of the relative motions of the other objects with respect to it had to be accordingly re-considered.

The astrometric motion of object 1 relative to ScoPMS 214A is shown in Fig-

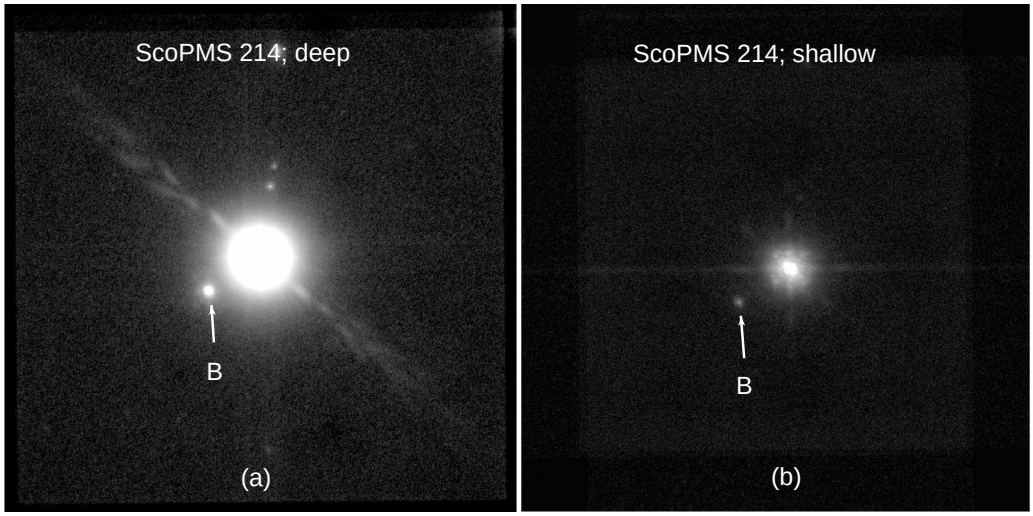

Figure 6.4: Deep coronagraphic (a) and shallow non-coronagraphic (b) K_S-band images of ScoPMS 214 from 30 Aug, 2002. The proper motion brown-dwarf companion ScoPMS 214B ($\equiv$ object 1) is visible in both panels and is indicated by an arrow. The images are $25.6''$ on a side; north is up, and east is to the left.

ure 6.5. Only at the final follow-up epoch is it possible to conclude that the apparent motion of object 1 is inconsistent with that of a background object. Even though the observed change $\delta\rho$ in angular separation from the star is not inconsistent with that of a stationary background object, the lack of significant change in the position angle disagrees with that expected of a background object at the 3.6σ level. On the other hand, the remaining 6 candidate companions all stay within 1σ of their expected positions. Therefore, object 1 is a common proper motion companion of ScoPMS 214, and we will henceforth refer to it as ScoPMS 214B. At an angular separation of $3.07''$ from the primary and a heliocentric distance of 145 pc, the projected separation between the pair is 450 AU.

6.1.3.2 Spectral Type and Mass of ScoPMS 214B

ScoPMS 214B is visible in all shallow JHK_S exposures of the primary. We therefore obtain the apparent magnitude of the companion by direct comparison with the 2MASS magnitudes of ScoPMS 214A. We find $J - H = 0.67 \pm 0.13$ mag,

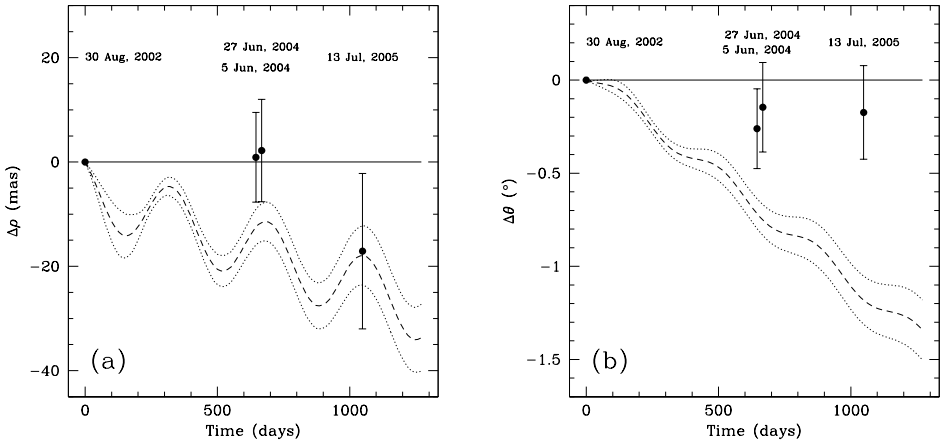

Figure 6.5: Proper motion diagrams of ScoPMS 214B. Panel (a) depicts the apparent motion in $\Delta\rho$ and panel (b), in $\Delta\theta$. The lines and symbols are the same as in Figure 5.5.

$J - K_S = 1.06 \pm 0.13$ mag and, assuming the same heliocentric distance as that of the primary, $M_{K_S} = 7.91 \pm 0.61$ mag. Using the "rough guide" to absolute near-IR magnitudes of K/M dwarfs (Reid et al., 2004), compiled from a 20 pc volume limited survey of cool dwarfs from the NLTT proper motion catalog (Luyten, 1980), we find that the spectral type of ScoPMS 214B is in the range M4–M6. The earlier spectral type is favored by the value of the K_S absolute magnitude, whereas the later spectral type corresponds to the observed $J - K_S$ color. Given the young age of ScoPMS 214 (member of the $\sim$5 Myr old USco association), and hence its expected lower-than-dwarf gravity, the higher K_S-band flux of ScoPMS 214B likely arises from a larger object radius, rather than from a higher effective temperature. ScoPMS 214A is itself a sub-giant and is over-luminous by $\sim$3 mag ($M_{K_S} = 2.0$ mag) with respect to main-sequence stars of similar color ($J - K_S = 0.9$ mag). Since at such young ages and at masses $\lesssim 0.6 M_\odot$ stellar and sub-stellar evolution proceeds nearly along a constant-temperature Hayashi track, we adopt the spectral type based on the $J - K_S$ color (M6) and a ± 1 spectral sub-type error for ScoPMS 214B. We then use calibrations of the bolometric corrections, luminosities, and effective temperatures for M dwarfs from

Leggett et al. (1999) and Leggett et al. (2002) to obtain $T_{\rm eff} = 2700 \pm 300$ K and $M_{\rm bol} = 10.9 \pm 0.6$ mag, i.e., $\log L/L_{\odot} = -2.46 \pm 0.24$. Based on the M_{K_S} magnitude, luminosity, and effective temperature of ScoPMS 214B, its mass from the Lyon DUSTY tracks is inferred to be 0.020–0.030 $M_{\odot}$, as is also confirmed from the Arizona tracks. Therefore ScoPMS 214B is a brown dwarf.

6.1.4 HII 1348B: A Secondary at the Stellar/Sub-stellar Boundary

6.1.4.1 Astrometric Confirmation

HII 1348 was not observed as part of the unbiased sub-stellar companion survey. It was targeted because a close-in ($1.09''$) faint ($\Delta K_S = 5.15$ mag) candidate companion was a priori known to exist around this star from the AO survey of the Pleiades by Bouvier et al. (1997). Without a second astrometric epoch or multi-band near-IR observations of this candidate, Bouvier et al. (1997) could not decide its association with HII 1348, and assumed that it was an unrelated background object. Here we present a single-epoch PHARO non-coronagraphic observation of the star on 3 October 2004 that, in conjunction with the Bouvier et al. data, confirms the proper motion association of the pair.

An image of HII 1348 and its candidate companion is shown in Figure 6.6. The proper motion diagrams for the 2927 ± 3 day (8.0 year) time-span between the Bouvier et al. observation (taken between 25 September and 1 October 1996) and the Palomar observation are presented in Figure 6.7. For the first-epoch astrometry of the system, we have adopted the nominal $0.005''$ and 0.15° errors in angular separation and position angle quoted by Bouvier et al. (1997).

The change in angular separation between the components of the candidate binary is fully consistent with zero and 12.4σ inconsistent with the candidate secondary being a stationary field object (Fig. 6.7a). Although the change in the position angle of the secondary is 4.7σ inconsistent with zero, it is entirely within the range of possible $\Delta\theta$ due to orbital motion for a face-on, circular orbit

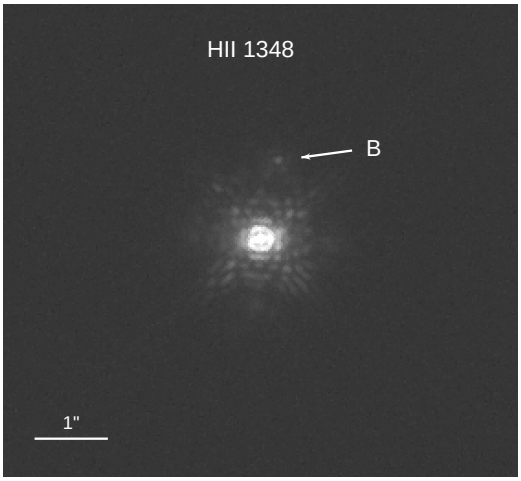

Figure 6.6: K_S-band images of HII 1348A/B. North is up, and east is to the left. Note the finer angular scale of this image ($7''$ on a side), compared to the ones in Figures 6.2 and 6.4.

(enclosed within the long-dashed lines in Fig. 6.7b). HII 1348B is therefore a bona fide proper motion companion to HII 1348, with the observed change in position angle indicating appreciable orbital motion between the two observational epochs.

6.1.4.2 Spectral Type and Mass of HII 1348B

From a comparison with the compilations of M-dwarf near-IR photometry of Leggett et al. (2002) and Reid et al. (2004), we find that the near-IR colors and K_S absolute magnitude of HII 1348B correspond to a spectral type of M6–M7. Without spectroscopic observations, we conservatively adopt a ± 1 sub-type error: M6.5$\pm$1. The corresponding effective temperature and bolometric correction are $T_{\rm eff} = 2600 \pm 300$ K and $BC_K = 2.95 \pm 0.10$ mag, where the errorbars correspond to the approximate range of $T_{\rm eff}$ and BC_K for M5.5–M7.5 in Leggett et al. (1999) and Leggett et al. (2002). The bolometric magnitude of HII 1348B is thus $M_{\rm bol} = 12.20 \pm 0.16$ mag, and its luminosity is $\log L/L_\odot = -2.98 \pm 0.06$.

HII 1348 is a Pleiades member (van Maanen, 1945; Johnson & Mitchell, 1958), hence it is 125$\pm$8 Myr old (Stauffer et al., 1998). For its absolute magnitude of $M_{K_S} = 9.25 \pm 0.13$ mag, the DUSTY models predict a mass of $0.070 \pm 0.005 M_\odot$.

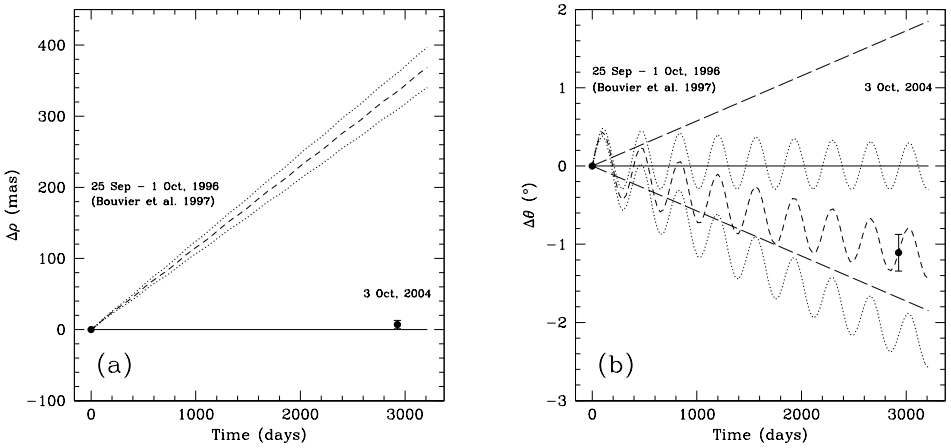

Figure 6.7: Proper motion diagrams of HII 1348B. Panel (a) depicts the apparent motion in $\Delta\rho$ and panel (b), in $\Delta\theta$. The long-dashed lines in panel (b) delimit the possible change in $\Delta\theta$, as estimated for a face-on circular orbit and a combined system mass of $0.82M_{\odot}$: a $0.75M_{\odot}$ primary (K5 V) and a $0.07M_{\odot}$ secondary. The remaining lines and symbols are the same as in Figure 5.5.

This mass range includes the hydrogen-burning mass limit, estimated at 0.072–0.075 $M_{\odot}$ for solar metallicity (Chabrier et al., 2000; Burrows et al., 1997). It is therefore possible that the mass of HII 1348B lies above the hydrogen-burning limit and the object is, hence, a stellar companion. Because of the proximity of the mass of HII 1348B to the hydrogen-burning limit and the relatively narrow mass error range, the issue of whether the object has sufficient mass to fuse hydrogen becomes of reduced importance, since present theory does not distinguish between the formation scenarios for low-mass stellar and brown-dwarf secondaries (Bate et al., 2003; Padoan & Nordlund, 2004).

6.1.5 A Critical Discussion of Sub-stellar Model Masses: Are the Detected Companions Truly Brown Dwarfs?

The mass estimates of brown dwarfs throughout this work are based on predictions by theoretical models of sub-stellar evolution. The particular sets of models used are the DUSTY and COND cooling tracks from the Lyon group (Chabrier et al.,

2000; Baraffe et al., 2003) and the cooling tracks from the Arizona group (Burrows et al., 1997). At <1 Gyr ages and fixed effective temperature and luminosity, the models from the two groups predict sub-stellar masses that are consistent to within 15–20% of each other. However, both sets of models are still very poorly constrained empirically, hence it is often unclear how well the predicted masses correspond to reality. To answer the question posed here, we consider the current literature on empirical measurements of sub-stellar masses in its brief entirety. At each step, we compare the empirical checks to the masses predicted for the most closely corresponding new companions.

Dynamical masses in the sub-stellar regime exist only for two close binary brown dwarfs: Gl 569 Bab (Lane et al., 2001) and 2MASSW J0746425+2000321A/B (Bouy et al., 2004). The components in both systems are near the stellar/sub-stellar boundary and are inferred to be ∼300 Myr old. These parameters are closest to the mass and age determined for HD 49197B ($0.060 M_{\odot}$; 500 Myr) and could thus be used to test the model predictions for this object. In the case of 2MASSW J0746425+2000321A/B, the young age quoted by Bouy et al. (2004) is dependent on a comparison of the dynamical mass of the pair to theoretical models, and therefore cannot be used as an independent test of the models. While this is also the case for the age estimate adopted by Lane et al. (2001) for Gl 569Bab, the authors quote, in addition, an independently-obtained age, as constrained from the observed rotation velocity, chromospheric and coronal activity, and space motion of the M2.5 primary Gl 569A. The agreement between the independently-estimated (0.2–1.0 Gyr) and model-dependent (0.25–0.5 Gyr) ages for Gl 569 Bab indicates that the theoretical models provide an adequate prediction of the physical parameters of the pair, and, by extrapolation, of HD 49197B. A further indication of the sub-stellar mass of HD 49197B is that, at an age similar to that of Gl 569, HD 49197B has a later spectral type (L4±1; §3.3.3.3.1) than the 0.048–0.070 $M_{\odot}$ M9 brown dwarf Gl 569Bb (Lane et al., 2001).

At masses just above the hydrogen-burning limit, the success of model predictions at young ages has recently been brought into question by Close et al. (2005),

who compare model masses to their measurement of the dynamical mass of the newly-discovered component C in the AB Dor quadruple system. Close et al. find that, for an age of 50^{+50}_{-20} Myr for the AB Dor system (Zuckerman et al., 2004), both the Lyon and the Arizona group models underestimate the $0.090 \pm 0.005 M_{\odot}$ dynamical mass of AB Dor C by a factor of 1.3–2. That is, while both suites of theoretical models predict sub-stellar masses for AB Dor C, the mass of the companion is decidedly stellar. However, this result has been more recently brought into question by Luhman et al. (2005). By considering the location of all 4 components of the AB Dor system on an H-R diagram with respect to the loci of young open clusters with well-known ages, Luhman et al. find that the Zuckerman et al. (2004) age estimate is a factor of $\sim$2 in error. Luhman et al. find that AB Dor is of Pleiades age (100–125 Myr), which re-aligns the model mass predictions for AB Dor C with its dynamical mass. Therefore the mass estimate for HII 1348B, a Pleiades member at the sub-stellar/stellar boundary, may also be presumed safe, though its sub-stellar nature remains uncertain.

No dynamical masses have been measured for lower-mass, $\lesssim 0.050 M_{\odot}$, brown dwarfs. Model predictions for low-mass sub-stellar objects remain less certain. Nevertheless, semi-empirical tests of theoretical models at such masses exist (Mohanty et al., 2004). Mohanty et al. compare high-resolution spectra of young brown dwarfs in Upper Scorpius and Taurus to synthetic spectral templates, and use surface gravity-sensitive features in the spectra to calculate sub-stellar masses. While this approach does not rely on dynamical masses and hinges on the accuracy of the model spectra, it is independent of the evolutionary aspect of the models. Given the known ages of objects in Upper Scorpius (5 ± 1 Myr; Preibisch et al., 2002) and Taurus (≈ 1 Myr; Myers et al., 1987), the Mohanty et al. analysis allows a test of the mass-age relation in evolutionary models of sub-stellar objects. The authors find that the Lyon group models provide a good approximation to $\geq 0.030 M_{\odot}$ masses derived from fits to theoretical spectral templates. This lower mass limit is similar to the masses of the remaining 2 brown dwarfs, ScoPMS 214B and HD 203030B, though only the age of ScoPMS 214B is in the

age range addressed by Mohanty et al. (2004). The accuracy of the sub-stellar mass for ScoPMS 214B is therefore confirmed. However, the mass of HD 203030B remains less well-constrained.

Indeed, no currently existing empirical body of evidence can provide an independent check on the mass estimate of HD 203030B. However, as already established in §6.1.2.2, the sub-stellar mass of the companion is beyond reasonable doubt.

6.2 Incompleteness Analysis of the Deep Survey

Having discovered three bona fide brown-dwarf companions among the 101 stars in the deep sample, we now estimate what fraction of the true sub-stellar companion population to Sun-like stars they represent. In this section, we address the factors affecting the survey completeness, state the analytical assumptions, and estimate a detection success rate of sub-stellar companions as a function of the mass. We combine this estimate with the observational results to obtain the underlying sub-stellar companion frequency.

6.2.1 Factors Affecting Incompleteness

Several factors need to be taken into account when estimating the detectability of sub-stellar companions around stars. These include: (i) possible sample bias against stars harboring sub-stellar secondaries, (ii) choice of sub-stellar cooling models, (iii) observational constraints (i.e., imaging contrast and depth), and (iv) physical parameters of the stellar/sub-stellar system (flux ratio, age, heliocentric distance, orbit).

As already discussed in §2.4.2, the deep sample is, to a large extent, unbiased toward the presence of sub-stellar companions, i.e., factor (i) can be ignored.

The choice of sub-stellar cooling tracks (ii) was already addressed in §1.1.4. We have adopted the combination of DUSTY and COND models for sub-stellar objects from the Lyon group. These have been used, either alone, or in parallel

with Burrows et al. (1997) models of the Arizona group, in all other studies of sub-stellar multiplicity. Our results will therefore be comparable with the existing work on the subject.

The remaining factors (iii and iv) need to be considered on a per-star basis to create a realistic picture of the overall survey incompleteness. Ideally, this kind of analysis is performed using Monte Carlo simulations (e.g., Fischer & Marcy, 1992). A Monte Carlo approach would allow not only a precise test of the frequency of brown-dwarf companions, but also estimates of their mass and orbital distributions, given the three that have been detected. Such a comprehensive analysis is planned for the near future (Metchev, Carson, & Hillenbrand, in preparation). In the following, we adopt a probabilistic approach instead, realizing that, by extrapolating from a small number of successful detections, we also inherit the large relative uncertainties.

6.2.2 Assumptions

We will base the incompleteness analysis on three assumptions: (1) that the distribution of semi-major axes a of sub-stellar companions to stars follows a flat logarithmic distribution, i.e., that $dN/d\log a = 0$, between 10 AU and 2500 AU, (2) that this implies a flat logarithmic distribution in *projected* separations ρ, i.e., $dN/d\log a = 0$, and (3) that the logarithmic mass distribution of sub-stellar companions is flat, i.e., $dN/d\log M = 0$, between $0.01M_{\odot}$and $0.072M_{\odot}$. These assumptions, albeit simplistic, have some physical basis into what is presently known about binary systems and brown dwarfs. We outline the justification for each of them in the following.

Assumption (1). Adopting a total stellar+sub-stellar system mass of $1M_{\odot}$, the 10–2500 AU range of projected separations corresponds approximately to orbital periods of $10^4 - 10^{7.5}$ days. This straddles the peak (at $P = 10^{4.8}$ days) and falls along the down-sloping part (toward longer orbital periods/larger semi-major axes) of the Duquennoy & Mayor (1991) Gaussian period distribution of G-dwarf binaries. Assuming a similar formation scenario for brown dwarfs and for stars,

brown-dwarf secondaries would be expected to become rarer at wider separations, as is true for stellar secondaries. However, our limited amount of knowledge on brown-dwarf companions suggests the opposite: brown-dwarf secondaries appear as common as stellar secondaries at >1000 AU separations (Gizis et al., 2001), whereas a brown-dwarf desert exists at <3–5 AU semi-major axes (Marcy & Butler, 2000; Mazeh et al., 2003). A smattering of brown dwarfs have been discovered in between. Therefore, a logarithmically flat distribution of semi-major axes for sub-stellar companions represents a middle ground between the known distribution of stellar orbits and the probably incomplete orbital distribution of known brown-dwarf companions. The assumption is also attractive because of its conceptual and computational simplicity.

Assumption (2). For a random distribution of orbital inclinations i on the sky, true and apparent physical separations are related by a constant multiplicative factor—the mean value of $\sin i$. However, a complication is introduced when relating the true *semi-major axis* to the projected separation because of the consideration of orbital eccentricity. Because an object spends more of its orbital period near the apocenter than near the pericenter of its orbit, the ratio of the semi-major axis to the apparent separation will be biased toward larger values. Analytical treatment of the problem (Couteau, 1960; van Albada, 1968) shows that this happens in an eccentricity-dependent manner. However, when considering the eccentricity distributions of observed binary populations (Kuiper, 1935a,b; Duquennoy & Mayor, 1991; Fischer & Marcy, 1992), both analytical (van Albada, 1968) and empirical Monte Carlo (Fischer & Marcy, 1992) approaches yield the identical result: $\langle \log a \rangle \approx \langle \log \rho \rangle + 0.1$. This indicates that the true semi-major axis and the measured projected separation are, on average, related by a multiplicative factor of 1.26: $\langle a \rangle = 1.26 \langle \rho \rangle$ and confirms the appropriateness of the current assumption.

Assumption (3). The evidence for a flat sub-stellar mass distribution comes from spectroscopically-determined estimates of the initial mass function (IMF) of isolated sub-stellar objects in star-forming regions (Briceño et al., 2002; Luhman

et al., 2003a,b; Slesnick et al., 2004), which show a roughly constant number of sub-stellar objects per unit $\log M$ between 20 and $80 M_{\rm Jup}$. While recent results suggest (Mazeh et al., 2003) that the mass function of close (<4–5 AU) spectroscopic binary stars differs from the IMF of isolated stars, there is as yet no such indication for wide binary star systems, the evolution of the individual components in which is likely to be influenced less by the presence of the other. Furthermore, because of the limited number of known brown-dwarf companions to stars, the mass function of *sub-stellar* companions remains unknown. Therefore, for lack of a better empirical alternative, we assume that the isolated sub-stellar IMF is representative of the sub-stellar companion mass function, i.e., that the companion mass distribution is approximately logarithmically flat. In §6.2.3 we will show that a flat linear companion mass function, as may be assumed by an extrapolation of the Mazeh et al. (2003) data into the sub-stellar regime, will change the overall result negligibly. A decreasing mass function toward lower sub-stellar masses is also possible, though no supporting evidence exists for that yet. Indeed, just based on the three 0.060 $M_{\odot}$, 0.035 $M_{\odot}$, and 0.025 $M_{\odot}$ brown-dwarf companions discovered in the survey, the sub-stellar mass function of wide companions seems to increase toward lower masses.

6.2.3 Incompleteness Analysis

Adopting the preceding assumptions, we now return to the discussion of the remaining factors affecting survey incompleteness: (iii) and (iv) from §6.2.1. We address the individual factors in three incremental steps, as pertinent to: geometrical incompleteness, defined solely by the inner and outer working angles of the survey; observational incompleteness, defined by the flux limits of the survey; and orbital incompleteness, defined by the fraction of orbital phase space observed. Throughout, we adopt the r.m.s. detection limits as determined for each star in §5.2 and assume that the primary ages and distances are fixed at their mean values listed in Table 2.2. The planned future Monte Carlo analysis will also address the uncertainties in the ages and distances of the sample stars.

6.2.3.1 Geometrical Incompleteness

In deciding the range of projected separations that the study is most sensitive to, we look at the full range of separations that have been explored between the inner and outer working angles in the deep survey (§5.1). Figure 6.8 shows the fraction of sample stars (solid line) probing projected separations between 3 AU and 3000 AU. It is immediately obvious, that only a very narrow range of orbital separations, between 105 AU and 125 AU, is probed around 100% of the stars. All other orbital separations carry with them some degree of incompleteness, which needs to be taken into account. From a purely geometrical standpoint, i.e., ignoring imaging sensitivity, the limitations imposed by the inner ($0.55''$) and outer ($12.5''$) working angles of the survey amount to a factor of 1.96 incompleteness in $\log a$ between 6 AU and 2375 AU (the projected separation range contained between the IWA for the nearest star and the OWA for the farthest star). That is, provided that sub-stellar companions are detectable regardless of their brightness anywhere between $0.55''$ and $12.5''$ from each star, and provided that their distribution of semi-major axes a is logarithmically flat, only half of the companions residing in the 6–2375 AU projected separation range would be detected.

As is evident from Figure 6.8, such a wide range of orbital separations includes regions probed around only a small fraction of the stars. Consideration of the full 6–2375 AU range will thus induce poorly substantiated extrapolations of the companion frequency. Instead, we choose to limit the analysis to projected separations explored around at least one-third (i.e., 34) of the stars in the deep sample. The corresponding narrower range, 22–1262 AU, is delimited by the dashed lines in Figure 6.8. The region has a geometrical incompleteness factor of 1.40 (cf. 1.96 for the full 6–2375 AU range above). That is, $1/1.40 = 71.4\%$ of all companions with projected separations between 22-1262 AU should be recovered by the survey, if they are sufficiently bright.

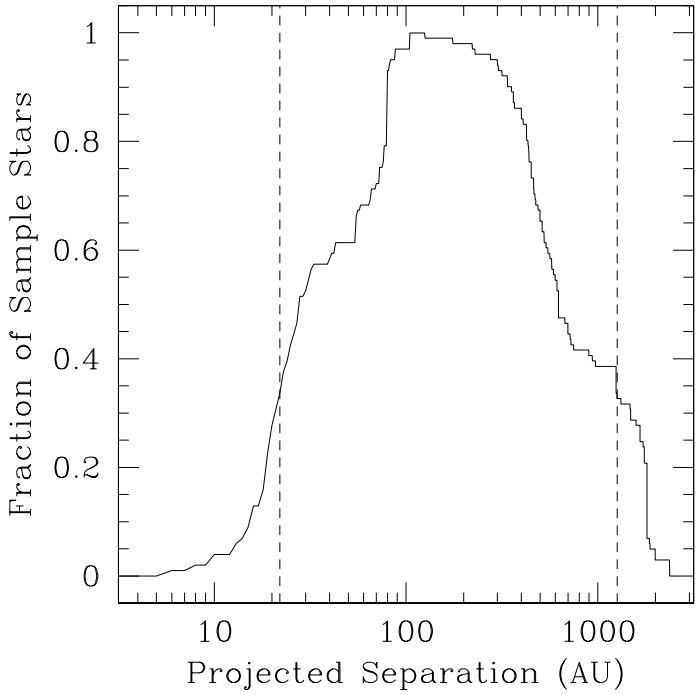

Figure 6.8: Projected physical separations probed in the deep sample survey. The vertical dashed lines delimit the region, 22–1262 AU, in which every apparent separation interval was probed around at least one third of the stars. The geometrical incompleteness factor is 1.40, i.e., $1/1.40 = 71.4\%$ of all companions in this separation range should have been detected.

6.2.3.2 Observational Incompleteness

Following an analogous approach to the one in the preceding discussion, we find the range of companion masses that have been effectively probed between the established physical separation limits of the deep survey. Because mass is not a direct observable, we use the absolute K-band magnitude of a sub-stellar object as a proxy for its mass, based on the Lyon suite of theoretical models. We do not apply a conversion between the observed K_S magnitudes and the CIT K-band magnitudes calculated by the Lyon group. The difference is < 0.1 mag throughout the L-dwarf regime and increases to only $K_{\rm CIT} - K_S \gtrsim 0.2$ mag for >T5 dwarfs (Stephens & Leggett, 2004). The discrepancy between the K and K_S magnitudes is thus likely to be smaller than the accuracy of the theoretical predictions.

We test for discrete values of the sub-stellar mass and age: 0.005, 0.010, 0.012, 0.015, 0.020, 0.030, 0.040, 0.050, 0.060, and 0.072 $M_{\odot}$, and 5, 10, 50, 100, and 500 Myr, respectively, as listed in the DUSTY model tables of Chabrier et al. (2000). These mass and age ranges reflect the range of possibly detectable sub-stellar masses and the age range of the stars in the deep sample. At the lowest sub-stellar masses, where at the older ages the models predict effective temperatures below 1400 K (the L/T dwarf transition temperature), we have used the COND models, which are better suited to model the cloudless photospheres of T dwarfs. We have rounded intermediate stellar ages to the nearest (in logarithmic space) of the discrete ages above. We then compare the companion fluxes for the range of sub-stellar masses to the flux limits for each star in the deep sample. In this manner, for each star in the sample, we obtain a range of projected separations over which a companion of a given mass would be visible. Summing over the stars in the entire sample, we estimate the observational incompleteness of the survey, i.e., with the actual flux limits taken into account.

The observational completeness at each discrete sub-stellar mass value is presented by the filled circles in Figure 6.9a. The geometrical (i.e., maximum possible) completeness limit, estimated above at 71.4% for the 22–1262 AU range, is shown by the horizontal continuous line. The vertical dotted lines mark the mass limits

of sustained deuterium (D) and hydrogen (H) burning ($0.012M_{\odot}$ and $0.072M_{\odot}$ respectively). Figure 6.9a demonstrates that the deep survey is not flux limited above the H-burning mass limit, where the observational completeness reaches the geometrical limit. The Figure also shows that the observational completeness is >50% for all sub-stellar objects above the D-burning limit, though it drops rapidly below that. We therefore define 0.012–$0.072M_{\odot}$ as the sub-stellar mass range, over which my survey achieves sufficient sensitivity. This comprises the entire brown-dwarf mass range, that is, if a "brown dwarf" is defined to be an object with mass lower than the H-burning limit and higher than the D-burning limit.

Adopting a uniform $dN/d\log M$ mass distribution for sub-stellar companions, we find that the survey is 65.3% complete to 0.012–$0.072M_{\odot}$ sub-stellar companions at apparent separations of 22–1252 AU from their host stars. The assumption of a uniform mass distribution per linear mass interval ($dN/dM = 0$) increases the observational completeness only slightly, to 68.4%.

What this means is that for every sub-stellar companion found at a projected separation between 22 AU and 1262 AU in the deep survey, another $\approx 1/3$ companions *within the same range of projected separations* were missed. Given that all 3 of the discovered sub-stellar secondaries in the survey reside within this range, we expect that one more companion has remained undiscovered. This companion could be a low-mass brown dwarf at a small angular separation from one of the distant stars in the sample, where it was either occulted by the coronagraph, or was lost in the glare of its host star. Alternatively, it could be a wide companion to one of the nearest stars, that was not considered or detected, because it fell outside the $12.5''$ OWA.

6.2.3.3 Orbital Incompleteness

The analysis so far has dealt only with the projected separation of sub-stellar companions. We now consider the full range of possible orbital inclinations and eccentricities, adopting the multiplicative factor of 1.26 in relating the projected separation ρ to the true semi-major axis a (§6.2.2). The range of orbital semi-

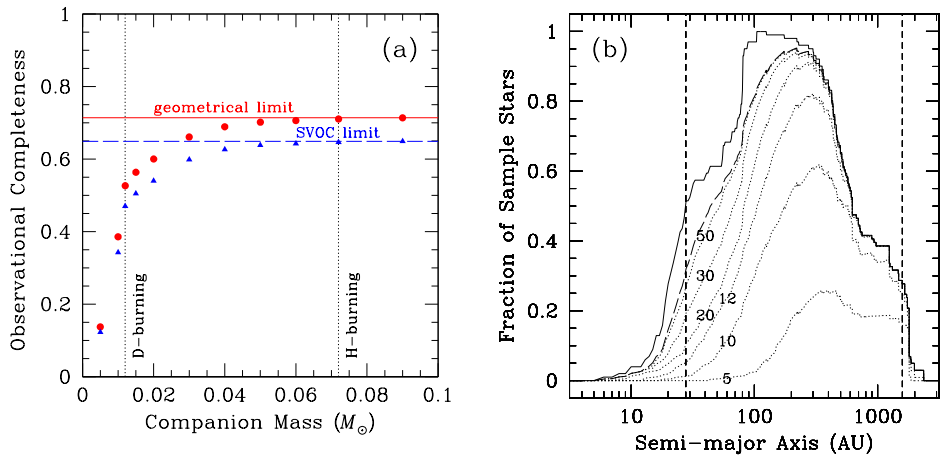

Figure 6.9: **(a)** Observational completeness without (circles) and with (triangles) the inclusion of single-visit obscurational completeness (SVOC; Brown, 2004) as a function of companion mass in the deep sample survey. The filled circles represent the fraction of companions of a given mass that would be detectable within a projected separation of 22–1262 AU from all sample stars (§6.2.3.2). The triangles represent a similarly defined fraction, but for a 28–1590 AU range of *semi-major axes* (i.e., projected separation × 1.26; §6.2.3.3). Both sets of fractions are calculated assuming a flat logarithmic distribution of orbital semi-major axes a. The horizontal lines delimit the maximum possible observational (continuous line) and orbital (long-dashed line) completeness at any given mass over these AU ranges. The vertical dotted lines mark the deuterium- (D) and hydrogen- (H) burning mass limits. **(b)** Same as Figure 6.8, but for the true semi-major axis and for a range of companion masses (dotted lines labeled with sub-stellar masses in $M_{\rm Jup}$). The solid curve delineates the geometrical completeness and the long-dashed curve, the SVOC (cf. panel a). The vertical short-dashed lines have been adjusted from their positions in Figure 6.8 to delimit the mean range of semi-major axes, 28–1590 AU, probed by the survey.

major axes probed by the survey is therefore on average a factor of 1.26 wider and further from the star: 28–1590 AU.

However, the adoption of the multiplicative correction does not exhaust the discussion of orbital incompleteness. Because companions on orbits with non-zero inclinations and eccentricities spend most of their time at projected separations $\rho \neq a/1.26$, they may still be missed in the survey. The most likely scenarios in which this can occur are for companions on highly inclined and/or eccentric orbits. A sub-stellar companion on an inclined orbit may by missed because its projected separation from the star was too small (<22 AU) and fell in a region where the imaging contrast was insufficient. Alternatively, an object on a highly eccentric orbit may be missed because it spends most of its time near apocenter and could conceivably fall outside the survey OWA.

With a small number of successful sub-stellar companion detections, orbital incompleteness issues are best addressed through Monte Carlo simulations. Such have been performed for a wide range of realistic orbital inclinations and eccentricities in a study by Brown (2004), the results of which we adopt here.

Brown's work investigates the detectability of populations of habitable extrasolar terrestrial planets with a range of orbital distributions by the *Terrestrial Planet Finder–Coronagraph (TPF–C)*. Although the angular scales and the levels of imaging contrast between the present coronagraphic survey and the design specifications for *TPF–C* are vastly different (*TPF–C* is expected to have a factor of ≈2.5 smaller IWA and attain $\sim 10^6$ higher contrast!), the problem is conceptually the same: determine the completeness to orbits with a certain semi-major axis, given a coronagraph of a fixed radius. Brown (2004) presents his results in terms of the ratio α of the semi-major axis to the obscuration radius, so they are universally scalable. His analysis does not include treatment of imaging contrast or limiting flux (these are addressed in a follow-up work: Brown, 2005), which makes it suitable to apply to results that have already been corrected for these effects: as already done in §6.2.3.2.

Brown (2004) finds that the detectability of orbiting companions in a single-

visit observation is a strong function of α between $\alpha = 1$ and 2. What he terms the "single visit obscurational completeness" (SVOC), varies between ≈30% at $\alpha = 1$ and ≈85% at $\alpha = 1.9$ (Fig. 6.10). Higher SVOC, at the 95% and 99% levels, is achieved only for $\alpha = 3.2$ and 7.1, respectively. The result is largely independent ($< 10\%$) of the assumed orbital eccentricity e for $0 \leq e \leq 0.35$.

We adopt the results of Brown's analysis and use the SVOC values for an eccentricity of 0.35 (Table 4 in Brown, 2004)—a value near the peak of the eccentricity distribution of G-dwarf binaries with $> 10^3$ day periods (Duquennoy & Mayor, 1991). We calculate the SVOC on the image of each star in the sample, for each of the discrete candidate companion masses in the 0.005–0.072 $M_\odot$ range (§6.2.3.2). We define the minimum projected separation at which a companion of a given mass is detectable as the effective obscuration radius for that mass. The results from the combined treatment of observational completeness (§6.2.3.2) and SVOC are shown in Figure 6.9a by filled triangles and in Figure 6.9b with the dotted lines. The long-dashed lines in Figures 6.9a,b delimit the maximum attainable SVOC, if companion brightness is not a limiting factor. In panel (b), the SVOC limit coincides with the $75M_{\rm Jup}$ ($0.072M_\odot$) line, indicating that the deep survey observations are maximally complete to objects at and above the H-burning limit, i.e., to stars.

The additional consideration of the SVOC does not affect significantly the overall incompleteness of the survey. With the assumed companion mass and orbital semi-major axis distribution, the overall completeness becomes 59.1%. This we adopt as the final estimate for the survey. That is, given 3 detected companions with semi-major axes estimated in the 28–1590 AU range, two more companions with semi-major axes in the same range probably have been missed. The assumption of a linearly uniform mass distribution changes the completeness estimate only slightly, to 62.1%, i.e., not significantly affecting the overall completeness.

Finally, the consideration of the SVOC, as defined by Brown (2004), does not address all possibilities for orbital incompleteness. As mentioned in the beginning of this discussion, a companion on a highly-eccentric orbit may fall outside the

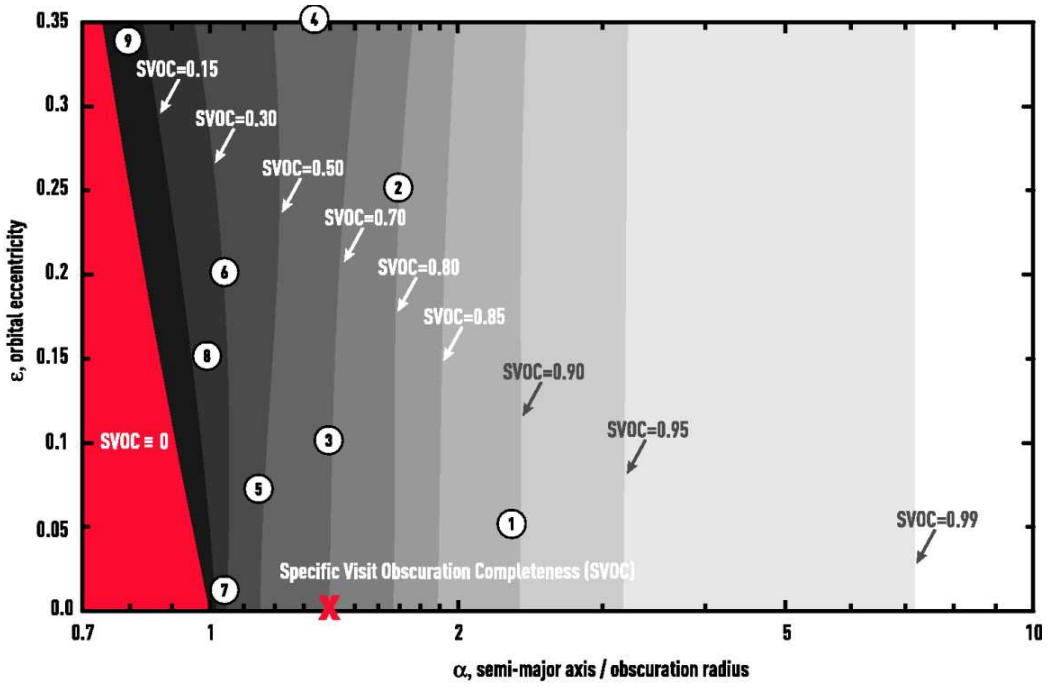

Figure 6.10: Orbital incompleteness (termed SVOC in Brown, 2004) of a single observation at a random epoch for companions having a particular size and shape of orbit. α is the ratio of the orbital semi-major axis of a hypothetical companion to the projected separation obscured by a coronagraph. In the red area (SVOC=0), the apastron distance is smaller than the obscuration radius, and no companions are ever found. Contours in the gray area show values $0 < \mathrm{SVOC} < 1$. The numbered points and the red X are irrelevant to the present discussion. (Brown, 2004)

OWA, even if its semi-major axis was in the explored range. This additional factor, among possible other sources of orbital incompleteness, will be addressed in the forthcoming Monte Carlo analysis of the present data (Metchev et al., in preparation). However, judging by the small change (-6.2%) in the incompleteness correction induced by the consideration of the SVOC, it is unlikely that inclusion of the remaining factors affecting orbital incompleteness will decrease the overall survey detection rate below 50%.

6.2.3.4 Further Incompleteness: Undecided Companion Candidates

Because the physical association status of a large fraction (37%) of candidate companions discovered in the survey remains undecided (§5.4), it is possible that more bona fide sub-stellar companions may be confirmed in this data set in the future. This is not very likely, given that the vast majority of the undecided candidates are faint, reside in relatively high-density fields, and are at wide angular separations from their candidate primaries (Fig. 5.4), i.e., they have very high probabilities of being background stars. Nevertheless, the example of HD 203030B—the faint, distant, sub-stellar companion to HD 203030, singled out from 5 other candidate companions within $12.5''$ in the same image (given an average of 2 per star in the sample)—presents a strong indication that all projected companions need to be followed up astrometrically. A final round of observations to do so is in progress.

The confirmation of an additional brown-dwarf companion would increase the total number to 4 and would imply that we have underestimated the success rate of the survey by a factor of 1.25. That is, the survey could conceivably be 45% complete, and hence, the 59% completeness estimate from §6.2.3.3 is an upper limit. Taking into account other possible sources of incompleteness that have been ignored, such as the small selection bias against massive sub-stellar companions to K0–K5 dwarfs (§2.4.2), and the partial consideration of orbital incompleteness (§6.2.3.3), the overall detection rate may be even lower. However, given the small anticipated magnitudes of each of these two remaining effects, we expect that the overall completeness is not less than 40%.

A lower estimate for the survey completeness will drive the expected rate of brown-dwarf companions higher. Because of the presently unquantified and likely unimportant nature of the additional sources of incompleteness, and for the sake of preserving statistical rigor, we will assume that the derived value of 59% provides an accurate estimate of the survey completeness.

6.3 Frequency of Wide Sub-stellar Companions to Young Solar Analogs

We have now described the survey sample, the successful brown-dwarf companion detections, and the incompleteness of the survey. Based on 3 detections around 101 stars, and an estimated ≈60% detection rate, we find that an ideal survey of the same size as ours will most likely detect 0.012–0.072 $M_{\odot}$ companions with 28–1590 AU (or, approximately, 30–1600 AU) semi-major axes around 5% of the stars in the sample. In order to determine the agreement of this estimate with previous ones reported in the literature, we need to determine confidence limits. In addition, as we shall demonstrate shortly, while 3% (or 5%, for an ideal survey) may be the most likely detection rate, it is not the expectation (mean) frequency of substellar companions.

Throughout the remainder of this work, we will use the terms "sub-stellar companion" and "brown dwarf companion" to refer to a brown-dwarf secondary to a young Sun-like star, with mass and orbital semi-major axis as defined in the preceding paragraph.

First, we address the statistical uncertainty arising from the small number of successful detections: only 3 in 101 trials. The large number of experiments and the small number of successful outcomes mean that the probability of detecting x brown dwarfs given an expected number μ is governed by a Poisson probability distribution:

$$P(x|\mu) = \frac{\mu^x \mathrm{e}^{-\mu}}{x!}. \tag{6.1}$$

We are interested in finding what is the probability distribution for μ given x detections, i.e., we need $P(\mu|x)$.

This is a standard problem in Bayesian statistical analysis (Bayes, 1763; Rainwater & Wu, 1947). The result follows from Bayes' Theorem (Rainwater & Wu, 1947; Papoulis, 1984):

$$P(\mu|x) = \frac{P(x|\mu)P(\mu)}{P(x)}, \tag{6.2}$$

where the P's denote "probability distribution" rather than identical functional forms. $P(\mu)$ is called the "prior" and summarizes our expectation of the state of nature prior to the observations. $P(x|\mu)$ is the "likelihood" that x outcomes are observed given a mean of μ, and $P(\mu|x)$ is the "posterior" probability that the state of nature is μ, given x positive outcomes. $P(x)$ is a normalization factor, which ensures that the sum of all probable outcomes $P(x|\mu')$, given some probability $P(\mu')$, is unity:

$$P(x) = \int_0^\infty P(x|\mu')P(\mu')d\mu'. \tag{6.3}$$

The physical (or philosophical, if you will) interpretation of Bayes' Theorem can be summarized in the following:

$$P(\text{state of nature} \mid \text{evidence}) = \frac{P(\text{evidence} \mid \text{state of nature})P(\text{state of nature})}{\text{normalizing factor}}. \tag{6.4}$$

Equation 6.3 is defined for the continuous, rather than discrete (in which the integral would be replaced by a sum), formulation of Bayes' Theorem. The P's are therefore, technically, not probabilities, but probability density functions (p.d.f.). Given that the formation of a brown-dwarf companion is a process that may occur around any Sun-like star, not just the 101 in the present sample, the use of the continuous limit is a valid approach because in principle the survey could be performed on an arbitrarily large sample.

As is standard practice in Bayesian analysis, we will assume that we have no a priori knowledge of the state of nature, i.e., we choose a uniform flat prior: $P(\mu) = 1$. In the context of the survey, this means that we have assumed that all

sub-stellar companion frequencies $0 \leq \mu \leq 1$ are equally probable. Indeed, this is not a completely inadequate representation of our current state of knowledge on the subject. We also performed tests with different uniform priors that place more weight on smaller expected companion frequencies: $P(\mu) = \log \mu$ and $P(\mu) = 1/\mu$ ($\mu > 0$ in both cases). It may be argued that such priors better approximate the expectation that the sub-stellar companion frequency is small. The effect of these was to increase, rather than decrease, the estimated mean brown-dwarf companion frequency.

Inserting Equation 6.1 into Equations 6.2 and 6.3, we obtain

$$P(\mu|x) = P(x|\mu) = \frac{\mu^x \mathrm{e}^{-\mu}}{x!}. \tag{6.5}$$

This result makes intuitive sense: the p.d.f. for μ is a distribution, that peaks at the observed success rate x. That is, by assumption, x is the most likely observational outcome. We now find that the mean number of sub-stellar companion detections per survey, if the survey were to be repeated multiple times on different samples of stars, is

$$\langle \mu \rangle = \frac{\int_0^\infty \mu \frac{\mu^x \mathrm{e}^{-\mu}}{x!} d\mu}{\int_0^\infty \frac{\mu^x \mathrm{e}^{-\mu}}{x!}} = 4. \tag{6.6}$$

This may at first seem surprising, given that the number of successful experiment outcomes was 3, rather than 4, out of a total of 101. The appearance of this "extra" sub-stellar companion is due neither to the incompleteness of the survey (§6.2.3.1–6.2.3.3) nor to the possible existence of more bona fide companions among the undecided ones (§6.2.3.4). Rather, the difference between the maximum-likelihood and the expectation (mean) value is a property of the continuous Poisson distribution (Fig. 6.11) due to its asymmetry around the mean.

To obtain the $n\sigma$ upper and lower ($\mu_{+n\sigma}$ and $\mu_{-n\sigma}$) confidence intervals for $\langle \mu \rangle$, we set the definite integral of $P(\mu|x)$ between $\mu_{+n\sigma}$ and $\mu_{-n\sigma}$ to the corresponding

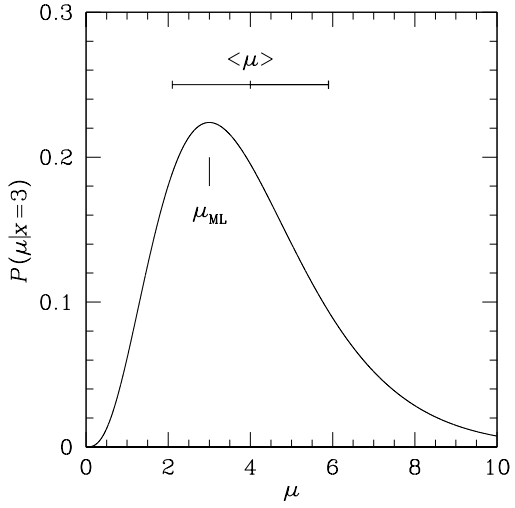

Figure 6.11: Probability density distribution $P(\mu|x = 3)$ for the sub-stellar companion frequency per 101 stars, given $x = 3$ detections. The curve is a continuous Poisson distribution (Eqn. 6.5), with a maximum likelihood value of $\mu_{\rm ML} = 3$ (equal to the number of detections x), but a mean value of $\langle\mu\rangle = x + 1 = 4$. The 68% ($1\sigma$) confidence interval on $\langle\mu\rangle$ is indicated by the horizontal errorbar above the curve.

$n\sigma$ significance level:

$$\int_0^{u_{n\sigma}} \frac{\mu^x \mathrm{e}^{-\mu}}{x!} = \begin{cases} 0.841 & n = 1 \\ 0.977 & n = 2 \\ 0.9987 & n = 3 \end{cases} \tag{6.7}$$

$$\int_0^{l_{n\sigma}} \frac{\mu^x \mathrm{e}^{-\mu}}{x!} = \begin{cases} 0.159 & n = 1 \\ 0.023 & n = 2. \\ 0.0013 & n = 3 \end{cases} \tag{6.8}$$

The resulting 1, 2, and 3σ (68.2%, 95.4%, and 99.7%) confidence limits are 2.1–5.9, 1.1–8.9, and 0.5–12.7 detectable companions on average for a survey of 101 stars.

Having addressed the statistical uncertainties associated with the small number of companion detections, we now apply the estimated survey completeness

correction (59%) to the mean value and to the confidence interval limits of μ. We thus find that $6.8^{+3.2}_{-3.2}$% (1σ limits; $^{+8.3}_{-4.9}$: 2σ limits; $^{+14.7}_{-5.9}$: 3σ limits) of F5–K5 stars in the 3–500 Myr age range have sub-stellar companions with semi-major axes between 30 AU and 1600 AU.

6.4 Stellar Secondaries

The entire survey produced 45 new stellar companions to 44 stars. Physical association of a further 31 known and suspected binary stars was confirmed (§6.4.3). One star, HD 91962, a priori considered single, was resolved into a triple system. No higher-order multiples were resolved. However, some of the newly-resolved binary systems are themselves known to be components of higher-order visual and/or spectroscopic binaries. The statistics and multiplicity of these systems will be the subject of a future study.

The majority (57 out of 75) of the binaries and the triple system were members of the shallow survey, as a result of the requirement that no $\Delta K_S < 4.0$ candidate companions were present around stars in the deep survey (§2.3.2). The binaries found in the deep survey either have low mass ratios, such that the secondary is more than 4 mag fainter than the primary at K_S, or have $< 0.8''$ angular separations, so that the PSFs of both components could be fit under the $1''$ coronagraph.

K_S-band magnitudes and $J - K_S$ colors of the stellar companions were already included in Tables 5.6 and 5.7. From these we infer K_S-band absolute magnitudes for the companions, using the known distance to the primary (Table 2.2), and masses, using the stellar evolutionary models of Baraffe et al. (1998). Table 6.3 lists these two quantities for each bona fide stellar companion, along with projected separations and system mass ratios.

Table 6.3: Properties of the Detected Stellar Companions

Companion	M_{K_S} (mag)	Projected Separation (AU)	M_2 ($M_\odot$)	q
HD 224873B	4.12 ± 0.24	62.1	0.99	0.98
HD 9472B	9.24 ± 0.11	92.2	0.10	0.10
RE J0137+18B	2.74 ± 0.29	108.2	1.06	1.00
HD 13531B	7.81 ± 0.12	18.6	0.19	0.20
HD 15526B	3.79 ± 0.54	8.2	0.90	0.79
1RXS J025223.5+372914B	4.62 ± 1.09	108.3	0.70	0.61
2RE J0255+474B	3.82 ± 1.09	106.5	0.91	1.00
RX J0258.4+2947B	5.15 ± 1.09	8.6	0.58	0.67
HD 18940B	3.28 ± 0.11	5.7	0.84	0.73
vB 1B	5.45 ± 0.10	106.5	0.56	0.47
HE 373B	8.20 ± 0.16	395.4	0.11	0.09
HE 696B	5.91 ± 0.16	85.1	0.44	0.43
RX J0329.1+0118B	7.82 ± 1.09	376.1	0.11	0.12
HE 935B	2.98 ± 0.16	4.9	1.15	0.86
HII 102B	6.10 ± 0.14	478.7	0.43	0.39
HII 120B	8.91 ± 0.18	1414.2	0.09	0.08
1RXS J034423.3+281224B	3.62 ± 1.09	42.5	0.96	0.74
HII 571B	7.70 ± 0.14	519.1	0.17	0.17
HII 1182B	7.85 ± 0.13	148.0	0.13	0.12

continued on next page

Table 6.3 – continued from previous page

Companion	M_{K_S} (mag)	Projected Separation (AU)	M_2 ($M_\odot$)	q
HII 2106B	5.95 ± 0.14	31.9	0.46	0.50
RX J0348.9+0110B	4.52 ± 1.09	4.7	0.85	0.81
HII 2278B	3.96 ± 0.14	44.0	0.87	0.79
HII 2881B	4.47 ± 0.13	13.2	0.81	0.87
RX J0354.4+0535B	5.92 ± 1.09	20.5	0.48	0.48
HD 285281B	3.41 ± 1.09	107.8	0.87	0.46
HD 284135B	2.90 ± 1.09	51.4	0.94	0.72
HD 281691B	4.20 ± 1.09	947.5	0.75	0.66
HD 26182B	4.09 ± 1.09	81.8	0.79	0.66
HD 284266B	6.16 ± 1.09	79.7	0.43	0.39
HD 26990B	4.09 ± 0.16	4.3	0.83	0.77
vB 49B	7.60 ± 0.15	123.0	0.22	0.19
vB 52B	5.84 ± 0.11	50.0	0.51	0.45
vB 176B	4.26 ± 0.11	10.9	0.79	0.83
vB 91B	4.84 ± 0.10	6.1	0.66	0.70
vB 96B	4.33 ± 0.11	7.8	0.77	0.76
RX J0434.3+0226B	5.78 ± 0.35	215.7	0.40	0.45
HD 282346B	4.45 ± 0.44	32.7	0.70	0.67
HD 31950B	7.51 ± 1.09	259.6	0.13	0.12
1RXS J051111.1+281353B	3.51 ± 0.33	98.5	1.39	0.62
HD 36869B	5.66 ± 0.64	592.6	0.36	0.30
HD 245567B	3.85 ± 0.40	41.4	0.30	0.24
HD 69076B	7.61 ± 0.26	41.9	0.24	0.26
HD 71974B	4.14 ± 0.12	11.1	0.81	0.78
HD 72760B	8.59 ± 0.11	21.0	0.13	0.15
HD 77407B	6.70 ± 0.12	49.8	0.54	0.49

continued on next page

Table 6.3 – continued from previous page

Companion	M_{K_S} (mag)	Projected Separation (AU)	M_2 ($M_\odot$)	q
HD 91782B	8.16 ± 0.15	56.1	0.23	0.20
HD 91962B	4.19 ± 0.15	31.2	0.81	0.67
HD 91962C	7.60 ± 0.16	5.2	0.83	0.69
HD 92855B	7.91 ± 0.12	105.6	0.16	0.14
HD 99565B	3.83 ± 0.21	14.3	0.88	0.82
BPM 87617B	5.09 ± 1.09	12.4	0.61	0.83
HD 108799B	4.31 ± 0.13	51.8	0.78	0.67
HD 108944B	8.62 ± 0.18	85.4	0.41	0.34
HD 112196B	9.13 ± 0.16	51.0	0.61	0.53
HD 115043B	8.13 ± 0.11	42.6	0.17	0.15
HD 129333B	5.93 ± 0.12	24.4	0.38	0.36
HD 134319B	6.77 ± 0.10	235.7	0.22	0.22
HD 135363B	5.04 ± 0.12	7.3	0.60	0.72
HD 139498B	2.74 ± 0.20	39.5	1.22	0.75
HD 142361B	4.14 ± 0.32	71.2	0.37	0.29
ScoPMS 27B	3.33 ± 0.61	11.5	0.64	0.61
ScoPMS 52B	2.34 ± 0.61	20.9	0.56	0.28
(PZ99) J161329.3–231106B	5.47 ± 0.61	207.3	0.15	0.12
(PZ99) J161411.0–230536B	2.56 ± 0.61	32.2	1.20	0.60
HD 150554B	6.10 ± 0.14	521.8	0.45	0.39
HD 152555B	6.73 ± 0.17	183.3	0.32	0.28
HD 155902B	4.02 ± 0.13	1.7	0.84	0.77
HD 157664B	2.89 ± 0.16	3.0	1.06	0.74
HD 165590B	2.73 ± 0.15	16.8	1.24	1.00
HD 199143B	4.75 ± 0.13	50.5	0.50	0.41
HD 200746B	8.82 ± 0.34	10.0	0.62	0.57

continued on next page

Table 6.3 – continued from previous page

Companion	M_{K_S} (mag)	Projected Separation (AU)	M_2 ($M_\odot$)	q
HD 201989B	7.31 ± 0.11	62.4	0.25	0.24
RX J2312.0+2245B	6.52 ± 1.09	429.0	0.38	0.31
RX J2313.0+2345B	4.72 ± 1.09	210.9	0.40	0.40
HD 221613B	4.32 ± 0.11	5.7	0.72	0.65

A comprehensive study of the incompleteness of the stellar component of the companion survey is deferred to a later time. The main goal of the present work was to determine the frequency of sub-stellar companions. Nevertheless, we briefly summarize the results on the observed frequency of stellar multiples and their distribution of mass ratios below. We also address the possibility for dynamical mass determination in the systems found from previous imaging campaigns, for about half of which the present data reveal significant orbital motion.

6.4.1 Frequency of Multiple Systems

It is perhaps surprising that such a large fraction of stellar multiples was discovered in the survey despite a series of requirements aimed at excluding known binary stars from the sample (§2.3). Seventy-two out of the 266 solar-type stars in the survey, or 27%, have $q > 0.1$ stellar companions in the probed angular separation range. We compare this to the most comprehensive study of multiplicity of solar analogs in the field to date: the combined study of spectroscopic and visual binaries by Duquennoy & Mayor (1991).

At first glance, the observed binarity frequency is a factor of $\approx$2 lower (though not inconsistent, given the bias against binaries) than the Duquennoy & Mayor (1991) estimate that 57% of G-dwarf primaries have $q > 0.1$ secondaries. However, the AO survey covers only a limited range of orbital separations, whereas the Duquennoy & Mayor study covers both spectroscopic and visual G-dwarf binaries, with orbital periods between < 1 and 10^{10} days. Given the range of stellar

heliocentric distances in the sample, 10–200 pc, and the angular limits of the survey, $0.1'' - 12.5''$, a least conservative estimate, without performing an analysis analogous to the one for sub-stellar masses (§6.2.3), puts the probed separation range at 1–2500 AU. For a binary system with a combined mass in the 1–2$M_{\odot}$ interval, the corresponding range of orbital periods is $10^{2.4}$–$10^{5.0}$ days. In reality, the survey may be up to 50% incomplete in this range of orbital periods or, equivalently, semi-major axes because of the inability to resolve close binaries at larger heliocentric distances and because of the omission of wide companions to nearby stars due to the limited detector field of view. Therefore, a completeness-corrected estimate of the binarity of the sample stars over $10^{2.4}$–$10^{5.0}$-day orbital periods will likely reside in the 40–50% range. Unfortunately, the complicated nature of the bias against binaries makes it difficult to obtain a more precise incompleteness correction.

Duquennoy & Mayor (1991) find that 22% of G dwarfs have $q > 0.1$ stellar companions with $10^{2.4}$–$10^{5.0}$-day periods, as estimated from their to the incompleteness-corrected period distribution. This is already lower than the observed fraction of 27% in the AO observations and likely significantly different from the probable 40–50% incompleteness-corrected estimate.

The most likely explanation for this discrepancy is evolution of the stellar multiplicity fraction—a phenomenon that has been inferred from multiplicity studies of young star-forming regions, intermediate-aged open clusters, and old field stars. It is well-established (Ghez et al., 1993; Leinert et al., 1993; Simon et al., 1995; Ghez et al., 1997; Kohler & Leinert, 1998) that the frequency of resolved 10–1000 AU solar-mass multiples in 0.1–10 Myr star-forming regions (e.g., Taurus, Ophiucus, Centaurus, Lupus) is a factor of $\sim$2 higher (40–50%) than that of 1–10 Gyr-aged solar neighborhood G dwarfs ($\sim$20%; Abt & Levy, 1976; Duquennoy & Mayor, 1991). Multiplicity studies of intermediate-aged (90–660 Myr) open clusters have produced stellar companion frequencies that are either in between these two limits (Patience et al., 1998) or are more consistent with the frequency of the field dwarfs (Bouvier et al., 1997; Patience et al., 2002). Given a median sample age of

200 Myr for the (complete) present survey, it is not unexpected that the obtained frequency of multiple stars is higher than that of older stars in the field. Indeed, while the observed binary frequency is only 12% (7 out of 58) among $\geq$1 Gyr old stars in the sample, 43% (12 out of 28) of the $\leq$10 Myr old stars, the majority of which are members of the Upper Scorpius OB association, are resolved as binaries. Although the youngest stars in the sample were allowed to violate one of the binary exclusion criteria (criterion 6; §2.3.1), following FEPS sample selection policy, and therefore are not as strongly biased against binarity, the large difference between the observed frequencies of PMS and main-sequence binaries is likely the result of a real evolutionary effect.

6.4.2 Distribution of Mass Ratios

The salient characteristic of the present survey is its high sensitivity to low-mass ($M_2 < 0.1 M_\odot$) companions to solar analogs, i.e., to systems with mass ratios $q < 0.1$. The distribution of mass ratios q among the sample systems is presented in Figure 6.12, where the lowest mass ratio bin also contains the 3 brown dwarfs discovered in the deep survey. The dotted line in the lowest mass ratio bin denotes the frequency of $q < 0.1$ systems, corrected for the incompleteness to sub-stellar companions of the deep survey. The shallow survey data have not been corrected for incompleteness and bias, though a combination of these probably exists at all mass ratios. In addition, the estimates for the primary masses in close ($<2''$) binaries are based on the total 2MASS near-IR flux for the system and have not been corrected for binarity. As a result, mass ratios near unity in close binary systems may have been understimated by a small ($\leq$20%) factor. A thourough considertation of these factors and a quantitative analysis of the binarity is deferred to a future study. Here we only point out that, due to the superior dynamic range attained with the use of the high-order AO at Palomar, the present survey is able to detect a statistically significant number of $q < 0.1$ systems, unlike previous high-angular resolution imaging studies of stellar multiplicity.

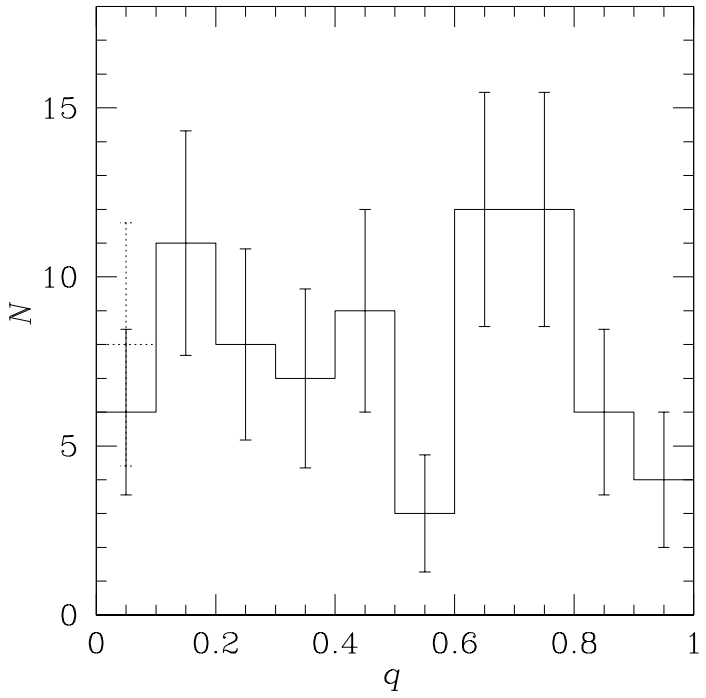

Figure 6.12: Observed distribution of companion mass ratios q (solid line) among the 76 binary and 1 triple system in the complete survey. A partial correction for incompleteness has been applied only to the lowest q bin. Numerous selection factors leading to bias against binary stars, especially at the high end of the 0.1–1.0 mass ratio range, prevent a quantitative assessment of the binary mass ratio distribution at present.

6.4.3 Orbital Motion in Previously Known Binary and Multiple Systems

The 31 physical companions that are known from previous resolved or radial-velocity observations have been marked in the last columns of Tables 5.6 and 5.7 with the appropriate reference. A large fraction of these (18 out of 31) were inferred in the high angular resolution AO and speckle work of Bouvier et al. (1997), Kohler & Leinert (1998), and Patience et al. (1998, 2002), who targeted stars in young open clusters. Although these studies do not include proper motion confirmation of the discovered companions, the authors infer physical association from the fact that the systems generally consist of very close ($<0.5''$), nearly equal-magnitude components. Our re-observation of these systems with AO confirms the common proper motion of the components and detects significant orbital motion in all of them. A campaign of sustained monitoring through direct imaging of these binaries will thus produce dynamical masses for a sizeable set of young solar analogs.

Chapter 7

Discussion and Summary

In this final Chapter, we discuss the answer to the main question raised at the onset of this work: what is the frequency of wide sub-stellar companions to solar analogs? Our robust statistical analysis of the results in §6 showed that, on average, 6.8% of 3–500 Myr-old Sun-like stars harbor 0.012–0.072 $M_{\odot}$ brown-dwarf companions in semi-major axes between 30 AU and 1600 AU. The 2σ ($\approx 95\%$) confidence interval on this estimate is 1.9%–15.1%. How does this compare to the frequencies of sub-stellar companions found in other surveys? Are brown-dwarf secondaries less common than extra-solar planets and stellar secondaries? Is the measured frequency consistent with a brown-dwarf desert at wide separations? The short answer to the last question is "No." For the reader seeking a more in-depth discussion, such is offered in §7.1 and §7.2. Emphasis is placed on a comparison with the results from the survey of McCarthy & Zuckerman (2004)–the most similar in scope to the present one. Section §7.3 offers various directions for future research, and the final Section (§7.4) summarizes the results from the entire study.

7.1 Comparison to the Results of McCarthy & Zuckerman (2004)

As already noted in §2.5.1, the only other direct imaging survey for sub-stellar companions that is similar in scope and sensitivity to the present work is the survey of McCarthy & Zuckerman (2004), performed for C. McCarthy's Ph.D. Thesis (McCarthy, 2001). The ensuing discussion compares the two surveys in parallel detail.

Both surveys focus on young stars visible from the northern hemisphere. The McCarthy & Zuckerman (2004) survey is done at J band, with follow-up at I. Similarly to the present work (done at K_S band), it consists of a deep (Keck) and a shallow (using 2.3–3 m Lick telescopes at Lick and Steward observatories) imaging component, with a nearly identical distribution of the targets between the two: 102 (deep) vs. 178 (shallow), compared to 101 (deep) vs. 165 (shallow) in this work. Unlike the present survey, the McCarthy & Zuckerman survey is seeing-limited, thus potentially of poorer contrast. In addition, McCarthy & Zuckerman use much wider (5–6″) occulting spots, compared to the 1″ coronagraph used here. Nevertheless, despite the differences in operating wavelength, contrast, and size of the occulting spot, the relative choices of sample age and heliocentric distance of the two surveys are such that the claimed sensitivities to companion masses and the probed orbital separation ranges are remarkably similar. Both surveys are expected to be sensitive to companions as small as $\sim 5 M_{\rm Jup}$ around the nearest and youngest sample stars, and cover projected separations in the approximate range ∼30–2000 AU. Yet, the results and conclusions are rather different. McCarthy & Zuckerman (2004) detect no brown-dwarf companions, from which they infer that the brown-dwarf desert extends out to at least 1200 AU from stars. We find a total of three sub-stellar companions and conclude the opposite (§7.2.2).

Taken at face value, without correcting for detection biases, a no-detection result in the present survey can be excluded at the $1 - {\rm e}^{-3} = 0.95$ confidence level, i.e., the two results are $\approx 2\sigma$ discrepant. It is therefore remotely possible, though

unlikely, that luck was unevenly distributed between the two studies. However, the increasing rate of success of recent, higher-contrast surveys (§2.5.4), suggests otherwise. There are thus reasons to believe that McCarthy & Zuckerman (2004) may have under-estimated the incompleteness and/or age of their survey sample. I address these two possibilities in the following, by considering only the results from McCarthy & Zuckerman (2004)'s deep sample.

7.1.1 Completeness Estimate of the McCarthy & Zuckerman (2004) Survey

McCarthy & Zuckerman (2004) quote typical detection limits for their imaging of $\Delta J = 12.5$ mag at $>5''$ from their primaries and a typical sample age of 300 Myr. They use these to infer that their survey is sensitive to sub-stellar companions down to the deuterium-burning limit (12 $M_{\rm Jup}$) around 97% of the stars, and down to 15 $M_{\rm Jup}$ around 100% of the stars observed at Keck. If "typical" in both cases is interpreted as "median," then, by definition, the adopted values for their sensitivity limits and stellar age over-estimate the sensitivity of the survey and under-estimate the age of the sample in exactly half of the cases for each of the two parameters. Therefore, the assumed incompleteness is correct only for $\sim$1/4 of their observations, while for the remaining 3/4, the sensitivity is over-estimated to varying degrees. This can indeed be gleaned from several discussions in the McCarthy & Zuckerman (2004) paper, such as the requirement that atmospheric transparency does not decrease the limiting magnitude below $J = 19$ mag (whereas a limiting magnitude of $J \geq 20$ mag is assumed throughout), and a cursory mentioning of the fact that sensitivities were computed for a 10–1000 Myr range of ages (though the 300 Myr typical age is assumed in estimating the brown-dwarf companion frequency). Because detections of sub-stellar companions made under the best contrast and at most favorable (i.e., youngest) stellar ages will generally be the ones governing the overall statistics, an over-estimate of the sensitivity of a survey in the above manner will lead to frequency estimates that are too conservative. In the case of the McCarthy & Zuckerman (2004) survey, this is

partially alleviated by the fact that they do not detect any sub-stellar companions, so there are no statistics to consider. However, the issues raised here will affect the minimum mass limits of the detectable sub-stellar companions. That is, the quoted minimum mass limits by McCarthy & Zuckerman (2004) are likely too optimistic for the majority of their observations. As a result, contrary to what is claimed, the authors have been unable to probe the entire brown-dwarf regime down to the deuterium-burning limit, and their upper limit on the frequency of brown-dwarf companions needs to be corrected for the fraction of the sub-stellar mass regime that is missed. For the present survey, this kind of incompleteness, termed "observational incompleteness," was addressed in §6.2.3.2 by assuming a mass distribution for sub-stellar companions (checked against the one observed in our survey).

The McCarthy & Zuckerman (2004) analysis also does not take into account either of the remaining two incompleteness terms discussed in §6.2.3: "geometrical," arising from the lack of full coverage of the entire orbital range of interest around all sample stars, and "orbital" (or "SVOC", following the terminology in Brown, 2004), resulting from the distribution of orbital parameters of the possible companions. Instead, the intrinsic assumption is of 100% completeness to all objects in the considered range of projected separations, and of face-on, circular orbits. As was found in §6.2.3 and as discussed in Brown (2004), the combined effect of these geometrical and the orbital incompleteness can be a factor of several for the lowest mass objects at the smallest separations from the effective obscuration.

Therefore, McCarthy & Zuckerman (2004) have probably over-stated the ensemble sensitivity of their survey by a factor of several, thus artificially lowering their estimate of the upper limit on the frequency of sub-stellar companions in wide orbits.

7.1.2 Age Estimate of the McCarthy & Zuckerman (2004) Sample

A likely reason for the lack of sub-stellar companion detections in McCarthy & Zuckerman (2004) altogether is that they may have over-estimated the youth of their sample. Around an older set of stars, any sub-stellar companions will be dimmer, hence more challenging to detect. Thus, assuming a sample age that is too young will lead to deriving a sub-stellar companion frequency that is too conservative. In the following discussion we address two reasons why the McCarthy & Zuckerman (2004) sample may be older than the ∼300 Myr median age assumed by the authors.

7.1.2.1 A Space-motion Selected Sample Needs Independent Age Verification

The primary selection criterion for the McCarthy & Zuckerman parent sample is stellar space motion, following the original idea of Eggen (1965) that young stellar populations inhabit a narrow region of (U, V, W) velocity phase space in the Galaxy. Discoveries of nearby co-moving groups of stars (e.g., Webb et al., 1999; Mamajek et al., 1999; Zuckerman et al., 2001a), confirmed to be young through a combination of age-dating criteria (§2.2.2), have shown that this approach is a viable tool for identifying young stars. The particular regions of phase space used by McCarthy & Zuckerman include the one presented in Eggen (1996, $-30 < V < 0, -25 < U < 50, -40 < W < 40$ km s^{-1}), which they apply to all single northern K and M dwarfs in the Third Catalog of Nearby Stars (Gliese & Jahreiß, 1991), and the UVW region identified by Jeffries (1995, $-30 < V < -20, -20 < U < 0, -20 < W < 20$ km s^{-1}), which they apply to all known single GKM stars within 25 pc. The latter, much narrower (4.4% of the UVW volume defined in Eggen, 1996) phase space includes a number of known young kinematic associations: the ∼100 Myr-old Pleiades moving group, the ∼10 Myr-old TW Hya association (Kastner et al., 1997), and the 8 Myr-old η Cha cluster (Mamajek et al., 1999). However, the

larger phase space includes dwarfs as old as 2 Gyr (Eggen, 1996). Therefore their parent sample may contain an appreciable fraction of Gyr-aged stars.

The authors do include a number of stars with youth established via other methods, including M dwarfs with strong Hα emission (Reid et al., 1995) and high x-ray luminosity (Fleming, 1998; Appenzeller et al., 1998), K dwarfs with high Li I equivalent width (Fischer, 1998), G and K dwarfs with Ca II H&K emission (Soderblom et al., 1993), as well as known members of the TW Hya association. However, these are apparently included in addition to the UVW-selected sample. That is, members of the latter have not undergone the same scrutiny for youth. Without consideration of additional age-dating criteria to confirm the youth of the kinematically selected stars, the true age distribution of the sample is unknown.

7.1.2.2 The McCarthy & Zuckerman (2004) Sample Is Statistically 1 Gyr Old

McCarthy & Zuckerman base their $\sim$300 Myr estimate for the median age of their sample on a combination of age-dating and statistical arguments. However, they do not list individual stellar ages. Instead, they provide an independent check on the overall age distribution by comparing the number of stars in their youth-selected sample that reside within 15 pc of the Sun to the number of $\leq$1 Gyr-old northern ($\delta > -30^{\circ}$) stars estimated to be present in the Gliese Catalog in the same volume of space. In particular, they cite Rocha-Pinto et al. (2000a) in adopting that 21% of surveyed stars in the solar neighborhood are younger than 1 Gyr. Hence, given their estimate of $\sim$400 single northern Gliese stars within 15 pc of the Sun, McCarthy & Zuckerman (2004) find that $\sim$80 of these should be younger than 1 Gyr. By comparing this number to the actual number of stars in their 15 pc sub-sample (102 for the Lick/Steward survey; 48 for the Keck survey), the authors argue that they have selected most of the known nearby stars younger than 1 Gyr.

However, the quoted fraction of 21% is an over-estimate of the fraction of $\leq$ 1 Gyr-old stars in the solar neighborhood. While indeed 21% of the G stars observed in the quoted survey by Rocha-Pinto et al. (2000a) are classified as younger

than 1 Gyr, that survey is not volume-complete. Rocha-Pinto et al.'s sample is flux-limited, extends out to 200 pc, and is therefore biased toward younger (brighter) stars, e.g., members of several known <1 Gyr-old associations at 40–200 pc from the Sun. Contrarily, very few members of such young associations are known within 15 pc of the Sun (e.g., Zuckerman & Song, 2004a). Therefore, the age distributions of Rocha-Pinto et al.'s sample and of Gliese stars within 15 pc are distinct. Indeed, in a separate study of the star-formation history in a volume-complete sample of nearby (5–22 pc) M dwarfs, Gizis et al. (2002) find that only ∼9% of M dwarfs are younger than 1 Gyr (Fig. 12 in Gizis et al., 2002). This result agrees with the completeness-corrected estimate of the local G-dwarf star-formation rate in Rocha-Pinto et al. (2000b), who find that only ∼10% of stars formed in the solar neighborhood are younger than 1 Gyr (Fig. 8 in Rocha-Pinto et al., 2000b). Both studies indicate a roughly uniform star-formation rate over the last 10 Gyr. Given that the Gliese Catalog is nearly volume-complete out to 15 pc for spectral types earlier than ∼M4 (Reid et al., 1995), the fraction of <1 Gyr-old Gliese stars within 15 pc is, accordingly, 9–10%.

Following McCarthy & Zuckerman's reasoning, we find that only 35–40 of the 102 stars in their Lick/Steward 15 pc sub-sample are younger than 1 Gyr, rather than ∼80. In fact, assuming that McCarthy & Zuckerman have managed to select the youngest quartile of the ∼400 suitable Gliese stars within 15 pc, the Rocha-Pinto et al. (2000b) and Gizis et al. (2002) results imply that the stellar ages in this sub-sample should be approximately uniformly distributed between 0 and 2.5 Gyr. Given that McCarthy & Zuckerman apply the same age-selection criteria to their Keck sample, its age distribution is likely to be the same. This argues for a median sample age of 1.25 Gyr for McCarthy & Zuckerman's combined sample, rather than 300 Myr, as the authors assume. In reality, after taking into account the UVW selection counter-argument described in §7.1.2.1, most of the UVW-selected members of the McCarthy & Zuckerman (2004) sample that do not belong to known kinematic groups of young stars are probably 1–10 Gyr old. While a number of bona fide young stars are included in their sample and they certainly

dilute the median age toward younger values, overall the median sample age is unlikely to be less than 1 Gyr.

7.1.3 Comparison of Sensitivities to Sub-stellar Companions

To compare the sensitivities of the two surveys, we use the median sample distances and ages to calculate the minimum sub-stellar mass detectable at the respective survey wavelengths (1.2μm and 2.15μm). Although, as argued in §7.1.1, the use of median sample statistics is incorrect in estimating ensemble sensitivities, it should provide at least a cursory idea of the relative survey sensitivities.

Judging from the fact that approximately equal numbers of stars are contained within and outside the 15 pc sub-sample of McCarthy & Zuckerman (2004), we adopt 15 pc as the median heliocentric distance of their deep sample. Building on the arguments presented in §7.1.2, we adopt a median sample age of 1 Gyr for the McCarthy & Zuckerman (2004) stars, recognizing however that their sample also contains ∼20 bona fide 10–100 Myr-old confirmed members of young kinematic groups. From the distribution of primary spectral types in their sample (Tab. 1 in McCarthy & Zuckerman, 2004), we estimate a median spectral type of M0, corresponding to a mass of $\approx 0.50 M_{\odot}$ (Cox, 2000, and references therein). Finally, we assume a typical limiting magnitude of $J = 20$ for their Keck NIRC data, as determined by the authors.

Taking the above values into account, the minimum detectable object mass in the McCarthy & Zuckerman (2004) survey is $\approx 40 M_{\rm Jup}$ at median sample statistics. At a typical limiting magnitude of $K_S = 19.5$ mag for the coronagraphic component of the present survey (Fig. 5.3b), and median deep sample age and distance of 80 Myr and 50 pc, respectively, the minimum detectable companion mass is 8–10 $M_{\rm Jup}$–a factor of 4 smaller. Therefore, the higher success rate of the present survey, in comparison with that of McCarthy & Zuckerman (2004), does not come as a surprise. Note, however, that using 8–10 $M_{\rm Jup}$ as a "typical" sensitivity limit of our survey leads to a gross overestimate the ensemble sensitivity, given that the completeness to such low masses is only 25–35% (Fig. 6.9a).

We therefore conclude that the $1 \pm 1\%$ upper limit on the sub-stellar companion frequency quoted by McCarthy & Zuckerman (2004) is too conservative, probably by a factor of several.

7.2 Comparison to Previous Multiplicity Results

7.2.1 Other Direct Imaging Surveys for Sub-stellar Companions

Does the estimate for the brown-dwarf companion frequency in this survey agree with those found in other surveys?

The three previous large surveys that report at least one detection (Oppenheimer et al., 2001; Lowrance et al., 2005; Chauvin et al., 2005b) produce results that are consistent with the present rate of success (3/101) at least at the 2σ. This comparison does not take into account the differences in the probed separation ranges and survey completeness. The detection rates for the surveys are 1/164, 2/45, and 1/50, respectively, with the Oppenheimer et al. (2001) survey (performed with only low-order tip-tilt AO at the Palomar 1.5 m telescope) being least sensitive, and covering the smallest orbital separation range (10–100 AU). A rough comparison of the various degrees of sensitivity and completeness indicates that the probable correction factors will make the incompleteness-corrected estimates in all cases fully consistent with the one presented here. Naturally, smaller surveys, reporting at least one detection (Potter et al., 2002; Neuhäuser & Guenther, 2004, success rates of 1/31 and 1/25, respectively), also produce results that are highly consistent with the present one.

High-contrast surveys that do not detect sub-stellar companions (other than that of McCarthy & Zuckerman (2004)) are published in Schroeder et al. (2000, 23 stars), Brandner et al. (2000, 24 stars), Masciadri et al. (2005, 28 stars), Carson et al. (2005, 80 stars), and Luhman et al. (2005, 150 stars). The samples of the first three surveys are far too small for meaningful comparison, given the expected low detection success rates. The Carson et al. (2005) survey has poorer sensitivity to sub-stellar masses than the present survey, because it targets 1–10 Gyr stars in

the solar neighborhood. A detailed Monte Carlo analysis by Carson et al. (2004) shows that, despite the null detection result, brown-dwarf companion frequencies as high as 9.7% cannot be excluded. Finally, the Luhman et al. (2005) survey is very sensitive to sub-stellar masses, as it is performed with *HST*/WFPC2 and targets the very young (2 Myr) star-forming region IC 348. It also probes a very similar range of projected separations (120–1600 AU), to the one probed here (22–1260 AU). The non-detection of sub-stellar companions by Luhman et al. may therefore appear puzzling. However, the Luhman et al. result needs to be considered in the context of the mass distribution of their sample stars.

The vast majority of the Luhman et al. targets are in the 0.08–0.5 $M_{\odot}$ mass range, with only 29 stars in the 0.5–1.5 $M_{\odot}$ range (i.e., similar to the mass range explored in the present survey). The non-detection of companions around the 29 higher-mass stars is not surprising, given the small size of the sub-sample. The lack of detections around the lower-mass stars, on the other hand, may be an indication that lower-mass primaries cannot retain wide companions. Such a mass-dependent effect has already been reported in the companion survey of $\approx$0.1 $M_{\odot}$ primaries by Close et al. (2003). Close et al. observe that the distribution of orbital separations in very low mass binaries (total mass $\leq 0.19 M_{\odot}$) peaks at 4 AU and cuts off after 16 AU. The authors reason that dynamical perturbations by passing stars disrupt the shallow potential wells of wide very low-mass binaries, leading to the preferential survival of the hardest systems. Because the majority of the primaries in the Luhman et al. (2005) sample are of similarly low mass, and because of the relatively large heliocentric distance of IC 348 (315 pc), the majority of the binary systems in the Luhman et al. sample would span $\leq 0.05''$ and would not have been resolved. The non-detection of sub-stellar companions by Luhman et al. (2005) is thus probably due to the low mean mass of their sample and to the dependence of the binary semi-major axis distribution on total mass.

The above interpretation is also in line with the decreasing incidence of $q \leq 0.2$ systems among resolved binaries from early-type (B–A) stars (35–40%; Tokovinin et al., 1999; Shatsky & Tokovinin, 2002; Kouwenhoven et al., 2005), to G–K dwarfs

(10–20%; Duquennoy & Mayor, 1991), and to M8–L0 dwarfs (0%; Close et al., 2003). Binary systems, consisting of a late-type (K–M) primary and a sub-stellar secondary have mass ratios $q \lesssim 0.2$. In the context of a decreasing frequency of such systems toward later spectral types, the absence of sub-stellar companions around late-type stars is not surprising. Volume-limited surveys (Oppenheimer et al., 2001), or other surveys dominated by K and M dwarf primaries (McCarthy & Zuckerman, 2004; Luhman et al., 2005), will be expected see a brown-dwarf desert at wide separations.

An alternative hypothesis, that could also explain the lower success rate of direct imaging surveys for sub-stellar companions targeting 1–10 Gyr-old stars, is evolution of the sub-stellar companion frequency. Evolution in the occurrence rate of stellar binaries between the ages of $\sim$1 Myr-old star-forming regions and of 1–10 Gyr-old solar neighborhood stars is a well-documented effect, with the binary frequency dropping by a factor of 2 between the ages of these two stellar populations (Duquennoy & Mayor, 1991; Ghez et al., 1993, 1997; Kohler & Leinert, 1998; Patience et al., 2002). If this process is due to the dynamical disruption of wider binaries by passing stars, it seems plausible that the same effect could be responsible for the "disappearance" of low-mass companions around older stars.

We therefore conclude, that while the present imaging survey has one of the highest published success rates of sub-stellar companion detection, the obtained results are not inconsistnent with those of other teams, given appropriate consideration of survey incompleteness in each case. Instead, the higher success rate is a direct result of an appropriately-selected sample of young stars, and ability to attain high imaging contrast. The McCarthy & Zuckerman (2004) claim that wide brown-dwarf companions to young stars occur in only $1 \pm 1\%$ of cases can be refuted at the $> 2\sigma$ level.

7.2.2 Comparison to Planetary and Stellar Multiplicity: No Brown Dwarf Desert at >30 AU from Solar Analogs

The brown-dwarf desert at 0–3 AU semi-major axes (the present completeness limit of RV surveys) is defined with respect to the observed frequencies of extra-solar planets (5–15%; Marcy & Butler, 2000; Fischer et al., 2002) and stellar companions (11%; Duquennoy & Mayor, 1991) around Sun-like stars in the same semi-major axis range. The frequency of brown dwarfs in such orbits is <0.5% (Marcy & Butler, 2000)–a factor of ∼20 lower than that of either planetary or stellar companions. This ratio we adopt as a quantitative definition for the term "brown-dwarf desert."

The wider, 30–1600 AU, semi-major axes probed around solar analogs in the present survey prevent a comparison with the RV planet regime. The frequency of stellar companions over this semi-major axis range is estimated to be ≈22%, based on the Duquennoy & Mayor (1991) period distribution. Our inferred frequency of brown dwarfs is 6.8%–a factor of 3 smaller. If we consider the inferred companion frequencies per logarithmic mass interval, recognizing the narrower mass range spanned by brown dwarfs in comparison to $\leq 1 M_{\odot}$ stars, the 0.012–0.072$M_{\odot}$ sub-stellar companion frequency becomes 8.7% per unit of $\log M$–a factor of 2.5 less than that for 0.1–1.0$M_{\odot}$ stellar companions. A difference in the sub-stellar and stellar companion frequencies by a factor of 20, as in the RV brown-dwarf desert, is excluded at the ≈99% confidence level. Given that the ratio between the frequencies of brown-dwarf and stellar companions has increased by nearly an order of magnitude between 0–3 AU and the wide orbital separations probed here, we consider "desert" to be an incorrect term. Nevertheless, a deficiency may exist.

7.3 Future Directions

This work has focused exclusively on young stars, because of the advantage that they offer in direct imaging searches for sub-stellar secondaries. However, this far from exhausts the scientific interest in studying sub-stellar companions to young stars. In addition to being suitable hosts for the imaging of brown-dwarf com-

panions, young stellar/sub-stellar systems are also good chronometers for tracing brown-dwarf evolution. While a number of age-dating techniques exist for hydrogen-burning stars (e.g, §2.2.2), brown-dwarf ages are much harder to constrain, because of the degeneracy between effective temperature and mass. Given an independent age estimate from a primary stellar companion, the interplay between these three quantities can be easily determined. Measurements of surface gravity and effective temperatures from low-resolution spectroscopy can then be accurately placed in evolutionary context. This provides both a test for brown-dwarf cooling models and a reference point for the empirical calibration of a much larger body of isolated sub-stellar objects.

This is of particular interest for the study of young and cool sub-stellar objects, none of which are known at a spectral type later than L7. On one hand, such brown dwarfs are interesting, because they may have masses similar to those of known extra-solar planets. Their characterization can thus offer much-needed insight into the mechanisms that govern planet and low-mass brown-dwarf formation. On the other hand, such brown dwarfs can be used to trace evolution in brown-dwarf photospheres. For example, brown dwarfs of known ages near the L/T spectral type transition can provide a direct estimate of the lifetime of dust grains in sub-stellar photospheres prior to grain condensation.

This latter issue will be addressed in the immediate future. The coolest of the three detected brown dwarfs, HD 203030B, at a photometrically-estimated spectral type of T0.5 and an age of $\sim$400 Myr, is likely to be the first young L/T transition object observed. Low-resolution near-IR spectra already at hand will be used to confirm this, as well as to obtain a measurement of the sub-stellar gravity. HD 203030B will thus offer the first empirical glimpse into the photospheres young T dwarfs.

Looking beyond companion statistics and photospheres of brown dwarfs, the stellar multiplicity and astrometric results from the present study will be combined with results from previous imaging campaigns and from on-going RV monitoring of a sub-sample of the stars to obtain accurate dynamical masses. This

will fill a presently sparsely-populated area in our knowledge of dynamical stellar masses at young ages. The superior power of combining astrometric and RV data in estimating dynamical masses was already employed in the orbital calculation for HD 129333A/B in §3.3.4.3. The idea is certainly extendable to sub-stellar masses through astrometric monitoring with the *Space Interferometry Mission (SIM)*, which will usher in a new era of precise knowledge of sub-stellar masses.

Finally, high-contrast imaging of young stars has only just taken off the ground as an effective technique to detect both candidate extra-solar planets and scattered light from the circum-stellar disks that they may be embedded in. Recent detections of planetary-mass companions with AO (Chauvin et al., 2004, 2005a; Neuhäuser et al., 2005), and high-contrast imaging studies of debris disks with AO (Liu et al., 2004, Metchev et al., 2005: Appendix A) and *HST* (Krist et al., 2005; Kalas et al., 2005), have pre-viewed the scientific gains to be expected in the fields of extra-solar planets and planet formation the next few years. Ground-based AO capabilities are fast improving with the increasing availability of laser guide stars (Lick, Palomar, Keck), near-IR wavefront sensors (VLT), sensitive high-order AO systems (AEOS, Palomar, Keck, VLT), and interferometric baselines (Keck, VLT). These are being followed closely by the implementation of novel contrast-enhancing detection techniques, based on optimized coronagraphy (e.g., Sivaramakrishnan et al., 2001; Kasdin et al., 2003), simultaneous differential imaging at multiple bandpasses (Close et al., 2005; Marois et al., 2005) and polarizations (Apai et al., 2004). In combination with the present-day sensitivity of *Spitzer* and of the *HST*, these technological advances are bound to push the envelope of our knowledge of extra-solar planetary systems in preparation for the detection and direct imaging of Earth-like planets, with *SIM* and the *Terrestrial Planet Finder*.

7.4 Summary

We have presented results from an adaptive optics survey conducted with the Palomar and Keck telescopes over 3 years, aimed at measuring the frequency of

stellar and sub-stellar companions to Sun-like stars. The survey sample contains 266 stars in the 3 Myr–10 Gyr age range at heliocentric distances between 8 and 200 parsecs and spectral types between F5–K5. A sub-sample of 101 stars, between 3 and 500 Myr old, was observed in deep exposures with a coronagraph to search for faint sub-stellar companions. A total of 288 candidate companions were discovered around the sample stars, which were re-imaged at subsequent epochs to determine physical association with the candidate host stars by checking for common proper motion. Benefiting from a highly-accurate astrometric calibration of the observations, we were able to successfully apply the common proper motion test in the majority of the cases, including stars with proper motions as small as 20 milli-arcseconds year^{-1}.

The results from the survey include the discovery of three new brown-dwarf companions, HD 49197B, HD 203030B, and ScoPMS 214B, 43 new stellar binaries, and a triple system. The physical association of an additional, a priori suspected, candidate sub-stellar companion to the star HII 1348 is astrometrically confirmed. The newly-discovered and confirmed young brown-dwarf companions span a range of spectral types between M5 and T0.5 and will be of prime significance for constraining evolutionary models of young brown dwarfs and extra-solar planets.

Based on the 3 new detections of sub-stellar companions in the 101 star sub-sample, and following a careful estimate of the survey incompleteness, a Bayesian statistical analysis shows that the frequency of 0.012–0.072 solar-mass brown dwarfs in 30–1600 AU orbits around young solar analogs is $6.8^{+8.3}_{-4.9}$% (2σ limits). While this is a factor of 3 lower than the frequency of stellar companions to G-dwarfs in the same orbital range, it is significantly higher than the frequency of brown dwarfs in 0–3 AU orbits, discovered through precision radial velocity surveys. It is also fully consistent with the observed frequency of 0–3 AU extra-solar planets. Thus, the result demonstrates that the radial-velocity "brown-dwarf desert" does not extend to wide separations, contrary to previous belief.

Appendix A

Adaptive Optics Imaging of the AU Microscopii Circumstellar Disk: Evidence for Dynamical Evolution

[†]Stanimir A. Metchev[a], Lynne A. Hillenbrand[a], Joshua A. Eisner[a], & Sebastian Wolf[b]

[a]California Institute of Technology, Division of Physics, Mathematics & Astronomy, MC 105–24, Pasadena, California 91125

[b]Max-Planck-Institut für Astronomie, Königstuhl 17, D–69117 Heidelberg, Germany

Abstract

We present an H-band image of the light scattered from circumstellar dust around the nearby (10 pc) young M star AU Microscopii (AU Mic, GJ 803, HD 197481), obtained with the Keck adaptive optics system. We resolve the disk both vertically and radially, tracing it over 17–60 AU from the star. Our AU Mic observations thus offer the possibility to probe at high spatial resolution ($0.04''$ or 0.4 AU per resolution element) for morphological signatures of the debris disk on Solar-System scales. Various sub-structures (dust clumps and gaps) in the AU Mic disk may point to the existence of orbiting planets. No planets are seen in our H-band

[†]A version of this appendix was published in *The Astrophysical Journal*, vol. 622, 451

image down to a limiting mass of 1 $M_{\rm Jup}$ at >20 AU, although the existence of smaller planets can not be excluded from the current data. Modeling of the disk surface brightness distribution at H-band and R-band, in conjunction with the optical to sub-millimeter spectral energy distribution, allows us to constrain the disk geometry and the dust grain properties. We confirm the nearly edge-on orientation of the disk inferred from previous observations and deduce an inner clearing radius ≤10 AU. We find evidence for a lack of small grains in the inner (<60 AU) disk, either as a result of primordial disk evolution or because of destruction by Poynting-Robertson and/or corpuscular drag. A change in the power-law index of the surface brightness profile is observed near 33 AU, similar to a feature known in the profile of the β Pic circumstellar debris disk. By comparing the time scales for inter-particle collisions and Poynting-Robertson drag between the two systems, we argue that the breaks are linked to one of these two processes.

A.1 Introduction

The existence of dust disks around main-sequence stars has been known since the first days of the *Infrared Astronomy Satellite (IRAS)* mission, when Aumann et al. (1984) reported the detection of strong far-infrared (far-IR) excess emission toward Vega (α Lyr). Over 200 other main-sequence stars have since been reported to possess such excesses, found almost exclusively with *IRAS* and the *Infrared Space Observatory* (e.g., Backman & Paresce, 1993; Mannings & Barlow, 1998; Silverstone, 2000; Habing et al., 2001; Spangler et al., 2001; Laureijs et al., 2002; Decin et al., 2003), though recently also with *Spitzer* (e.g., Meyer et al., 2004; Gorlova et al., 2004), and through ground-based sub-millimeter observations (Carpenter et al., 2004). Too old to possess remnant primordial dust, which would be cleared by radiation pressure and Poynting-Robertson (P-R) drag within several million years (Myr) in the absence of gas, these stars owe their far-IR excess to emission by "debris disks," formed by the collisional fragmentation of larger bodies (the so-called "Vega phenomenon"; Backman & Paresce, 1993, and references therein).

Subsequent imaging at optical to millimeter wavelengths of the nearest sub-sample of Vega-like stars has resolved intricate disk-like structures, with gaps and concentrations (Holland et al., 1998, 2003; Greaves et al., 1998; Schneider et al., 1999; Krist et al., 2000; Koerner et al., 2001; Wilner et al., 2002; Weinberger et al., 2002; Clampin et al., 2003).

The most favored explanation for such structures is the gravitational perturbation by embedded planets orbiting at semi-major axes comparable to the disk size (Moro-Martín & Malhotra, 2002; Kenyon & Bromley, 2004). The existence of perturbing planets may be revealed by clumps of dust trapped in mean motion resonances, as has been suggested for Vega (Wilner et al., 2002; Wyatt, 2003), ϵ Eri (Ozernoy et al., 2000; Quillen & Thorndike, 2002), and Fomalhaut (α PsA; Wyatt & Dent, 2002; Holland et al., 2003), and observed by the *Cosmic Background Explorer* satellite along the Earth's orbit (Reach et al., 1995). Stochastic collisions between large planetesimals that result in dust clumps lasting several hundreds of orbital periods are another means of producing disk asymmetries (Stern, 1996). Spiral density waves (as seen in the disk of HD 141569A, and inferred around β Pic; Clampin et al., 2003; Kalas et al., 2000) and warps in the disk inclination (as in the disk of β Pic; Heap et al., 2000; Wahhaj et al., 2003) may indicate perturbation by nearby stars (Kalas et al., 2000, 2001; Kenyon & Bromley, 2002; Augereau & Papaloizou, 2004). Finally, dust migration in a gas-rich disk can produce azimuthally symmetric structures, as observed in the HR 4796A circumstellar disk (Takeuchi & Artymowicz, 2001).

High-resolution imaging observations, such as those of HR 4796A (Schneider et al., 1999), β Pic (Heap et al., 2000), HD 141569A (Weinberger et al., 1999) and TW Hya (Krist et al., 2000; Weinberger et al., 2002) with the *Hubble Space Telescope (HST)* can help single out the most likely physical process behind the disk morphology. The resolution achievable with adaptive optics in the near-infrared on large ground-based telescopes rivals that of *HST* and is the method employed in this paper for investigating disk structure.

The young (8–20 Myr; Barrado y Navascués et al., 1999; Zuckerman et al.,

2001b) M1 V (Keenan, 1983) star AU Mic has a known 60μm excess from *IRAS*, likely due to orbiting dust (Song et al., 2002). Because of its relative proximity (*Hipparcos* distance of 9.94±0.13 pc; Perryman et al., 1997), AU Mic is a good target for high-resolution imaging of scattered light to characterize the circumstellar disk morphology. Recent 450μm and 850μm observations by Liu et al. (2004) confirmed the existence of dust, and follow-up R-band (0.65μm) coronagraphic imaging revealed a nearly edge-on disk extending 210 AU (Kalas et al., 2004) from the star. Because the age of AU Mic is larger than the collision timescale between particles in the disk (0.5–5 Myr at 200 AU), Kalas et al. (2004) infer that most of the dust particles have undergone at least one (destructive) collision, and hence the AU Mic disk is a debris disk. However, because the P-R time scale for 0.1–10μm particles at $\gtrsim$100 AU from the star is greater than the stellar age, Kalas et al. expect that most of the disk at large radii consists of primordial material. Liu et al. find a fractional infrared luminosity, $L_{IR}/L_* = 6 \times 10^{-4}$ and fit the far-IR to sub-millimeter excess by a 40 K modified blackbody with constant emissivity for $\lambda < 100\mu$m and following $\lambda^{-0.8}$ for longer wavelengths. From the lack of excess at 25μm, Liu et al. infer an inner disk edge at 17 AU from the star, or 1.7″ at the distance of AU Mic. They speculate that such a gap may have been opened by an orbiting planet, which, given the youth of the system, could be detectable in deep adaptive optics (AO) observations in the near IR. Such high contrast observations could also be used to search for signatures of planet/disk interaction.

The AU Mic circumstellar disk is not resolved with the 14″ beam of the JCMT/SCUBA observations of Liu et al., and the Kalas et al. optical coronagraphic observations are insensitive to the disk at separations <5″ because of the large sizes of their occulting spots (diameters of 6.5″ and 9.5″) and because of point-spread function (PSF) artifacts. Taking advantage of the higher angular resolution and dynamic range achievable with adaptive optics on large telescopes, Liu (2004) used the Keck AO system to investigate the disk morphology at separations as small as 15–20 AU from the star. We present our own set of Keck AO data that confirms Liu's observations and places upper limits on the presence of

potential planetary companions. In addition, we combine our spatially resolved H-band information with the R-band imaging data from Kalas et al. (2004) and with the optical to sub-millimeter spectral energy distribution (SED) of AU Mic from Liu et al. (2004), to put self-consistent constraints on the disk morphology and the dust properties, as done previously for β Pic (Artymowicz, Burrows, & Paresce, 1989). We use a full three-dimensional radiative transfer code to model simultaneously the SED and the H-band and R-band surface brightness profiles (SBPs). We find that our model consisting of a single dust population does not reproduce the observed break in the H-band SBP, whereas a two-component dust model, as proposed for β Pic, fits the data well. Drawing from a comparison with the β Pic system, we deduce that dynamical evolution of the disk provides the simplest explanation for the morphology of the SBPs of both disks.

A.2 Observations and Data Reduction

We observed AU Mic at H band (1.63μm) with the NIRC2 instrument (Matthews et al., in prep.) and the AO system (Wizinowich et al., 2000) on the Keck II telescope. The data were acquired on 5 June 2004 under photometric conditions. We employed coronagraphic spots of different sizes ($0.6''$–$2.0''$ diameter) to block out the light from the star. The observations were taken with the wide, $0.04''$ pix^{-1} camera in NIRC2, which delivers a $41'' \times 41''$ field of view (FOV) on the 1024×1024 InSb Alladin-3 array.

We obtained nine 54 sec exposures at H band, three with each of the $0.6''$, $1.0''$, and $2.0''$-diameter coronagraphic spots. We observed the nearby (2.4° separation) M2/3 III star HD 195720 as a PSF standard, with similar colors, but 0.9 mag brighter than AU Mic at H. We spent equal amounts of time on the target, on the PSF star, and on the blank sky. The observations were carried out according to the following sequence, repeated 3 times: 3 exposures of AU Mic, 3 exposures of HD 195720, and 3 exposures of the blank sky (taken at three dithered positions: $60''$, $50''$, and $40''$ away from the PSF star). The total on-source exposure time

was 8.1 min. Throughout the observations, the field rotator was set in "position angle mode," preserving the orientation of the sky on the detector. The image quality was estimated from the Strehl ratios of point sources observed at higher spatial resolution (with the narrow camera, $0.01''$/pix) at the beginning of each night. Our H band images had Strehls of 17–20%.

Data reduction followed the standard steps of sky-subtraction, flat-fielding, and bad-pixel correction. The images in the individual sets of 3 exposures were then median-combined to improve the sensitivity to faint objects. The AU Mic dust disk was barely discernible at this stage (Figure A.1a). To enhance the visibility of the dust disk, we subtracted the stellar PSF. The PSF was obtained by first rotating the image of HD 195720 to match the orientation of the diffraction pattern in the AU Mic image, and then scaling it by a centrally symmetric function $f(r)$ to match the radial dependence of the AU Mic profile. The objective of the scaling was to compensate for variations in the seeing halo between AU Mic and the control star caused by changing atmospheric conditions and fluctuating quality of the AO correction. The function $f(r)$ was obtained as the median radial profile of the ratio of the AU Mic to the HD 195720 images, with the telescope spikes and the edge-on disk masked. Figure A.2 shows $f(r)$ for the images with the three different coronagraphic spot sizes. Two remarks on this procedure should be made here. First, the function $f(r)$ does not vary by more than 15% for any given spot size and for large radii tends to 0.4—the H-band flux ratio between AU Mic and the PSF star. Second, because the AU Mic disk happens to be edge-on, the centrally symmetric scaling of the PSF does not introduce any spurious features in the result and so does not interfere with the morphology of the disk. The procedure would not be viable for disks that are far from edge-on.

The scaled version of HD 195720 for the image with the $0.6''$ coronagraph is presented in Figure A.1b. Panel (c) of Figure A.1 shows the final AU Mic image, obtained by median-combining all coronagraphic exposures. In panel (d) a digital mask has been employed to enhance the appearance of the circumstellar disk. The mask encompasses the innermost $1.7''$ from AU Mic, as well as the hexagonal

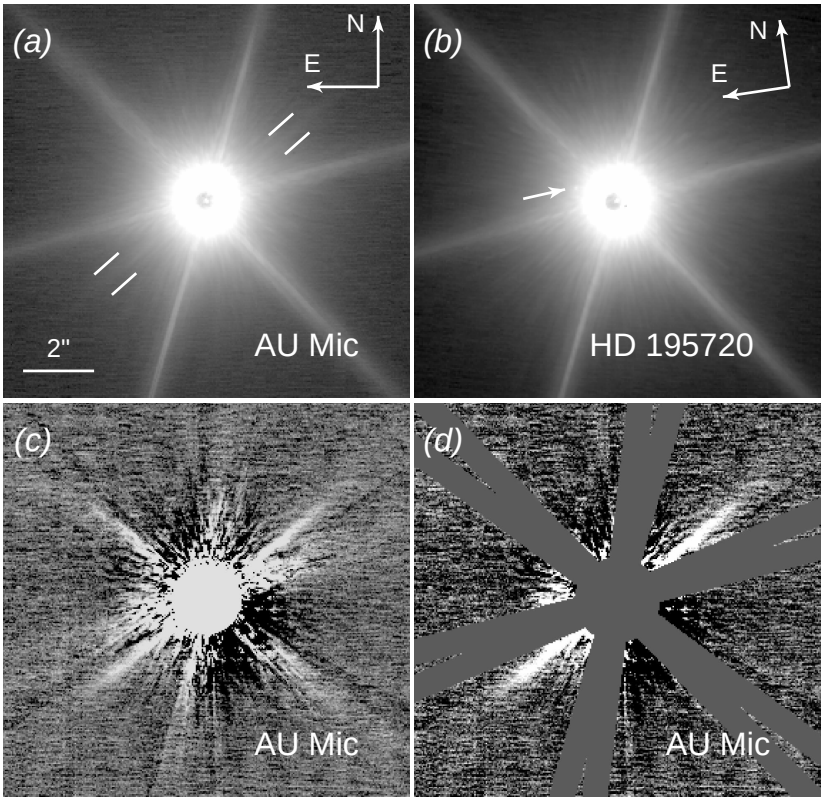

Figure A.1: H-band images of AU Mic. *(a)* A median-combined image of three sky-subtracted 54.3 sec exposures with the 0.6″ coronagraph. The star is visible through the semi-transparent coronagraph. The disk is discernible as a faint pair of diametrically opposite spikes along the SE–NW direction (traced by the two pairs of parallel lines). *(b)* An image of the PSF star, HD 195720, with the same coronagraph, scaled to the intensity of the AU Mic image in panel *(a)*. An arrow points to the location of a faint projected companion (§A.3.3). *(c)* The final median-combined image of AU Mic obtained from PSF-subtracted images with 0.6″, 1.0″, and 2.0″ spot diameters. All surface brightness photometry is performed on this image. *(d)*. Same as in *(c)*, but with an overlaid digital mask covering the star and the telescope diffraction pattern. The residual noise in the central region (3.4″-diameter circle) is greater than the surface brightness of the edge-on disk.

diffraction spikes from 2 of the 3 image sequences where they did not subtract well (as seen in panel (c) of the Figure).

For flux calibration we adopted the 2MASS magnitude for AU Mic ($H = 4.831 \pm 0.016$) and relied on the residual transmission of the NIRC2 coronagraphic spots. The PSF star, HD 195720, is saturated in 2MASS and is therefore unusable for flux calibration. We measured the flux from AU Mic through the $1.0''$ and $2.0''$ coronagraphs in a 6 pix ($0.24''$) diameter aperture. From non-coronagraphic images taken with the 10 mas/pix camera on NIRC2, we found that this aperture contained 68% of the total power in the PSF. The H-band transmissivity of the $2''$ NIRC2 coronagraph was measured at $(7.32 \pm 0.24) \times 10^{-4}$ (extinction of 7.84 ± 0.03 mag). AU Mic is known to exhibit a large V-band photometric amplitude (0.35 mag) due to star spots with a period of 4.9 days (Torres & Ferraz Mello, 1973). Although we do not expect measurable variability over the $\approx$1 hour time span of our observations, our absolute flux calibration is uncertain. Nevertheless, in the near IR the contrast between the spots and the stellar photosphere is less pronounced than in the optical, so the uncertainty is also smaller—likely of order $\lesssim$0.1 mag.

The absolute orientation of the dust disk arms was calibrated through observations of a binary star standard, WDS 18055+0230, with well-known orbital elements (grade 1; Hartkopf & Mason, 2003; Pourbaix, 2000). The y-axis of the NIRC2 detector was measured to be offset by $1.24^\circ \pm 0.10^\circ$ clockwise from north. All position angles quoted below have been corrected for this offset.

A.3 Results and Analysis

A.3.1 Circumstellar Dust Morphology

The disk is seen out to a distance of $\sim 6''$ (60 AU) from the star in our combined H-band image (Figure A.1c,d). Inwards it can be traced inwards to $\approx 1.7''$ (17 AU) from the star, at which point residual speckle noise from the PSF subtraction overwhelms the emission from the disk. Thus, our imaging data cannot directly

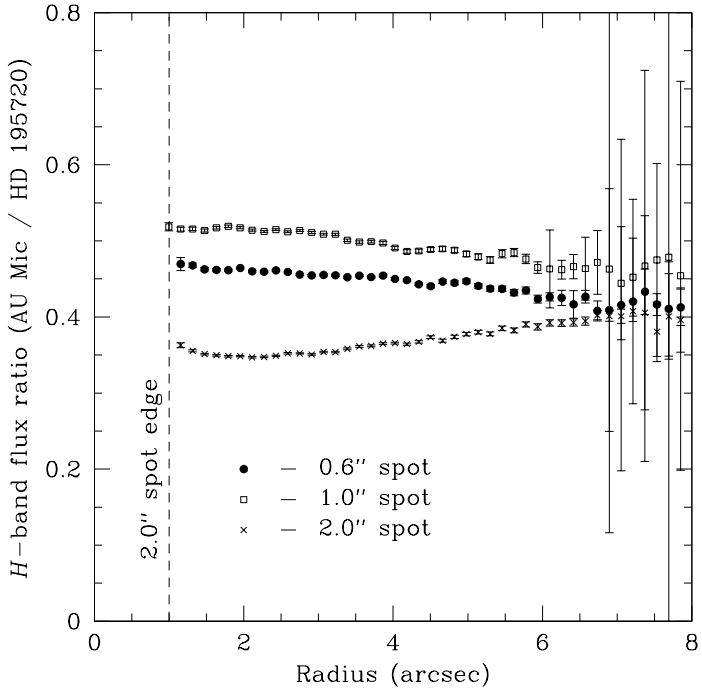

Figure A.2: Median ratios $f(r)$ of the radial profiles of AU Mic and HD 195720 (the PSF star) at H band for the images taken with the various coronagraphs. The vertical dashed line shows the edge of the largest coronagraph. Our PSF images were multiplied by $f(r)$ before subtracting them from the corresponding AU Mic images. For any given coronagraphic spot size, $f(r)$ varies by less than 15% in the range $r = 1 - 8''$.

test the existence of the proposed disk clearing interior to 17 AU from the star (Liu et al., 2004). We confirm the sharp mid-plane morphology of the disk (Kalas et al., 2004; Liu, 2004), indicating a nearly edge-on orientation, and resolve the disk thickness, with the SE arm appearing somewhat thicker (FWHM = 2.8–4.4 AU) than the NW arm (FWHM = 2.2–4.0 AU). There is also evidence of an increase in the FWHM of each of the arms with separation: from 2.2–2.8 AU at 20 AU to 4.0–4.4 AU at 40 AU from the star, indicating a potential non-zero opening angle of the disk. Within $5''$ of AU Mic, the position angles (PAs) of the two sides of the disk are nearly 180° away from each other: we measure PA = 310.1°±0.2° for

the NW arm, and PA =129.5°±0.4° for the SE arm. These PAs are in agreement with those reported in Liu (2004, 311.4°±1.0° and 129.3°±0.8°), though they are more accurate, likely as a result of our proper calibration of the orientation of the NIRC2 detector (§A.2).

The radial SBP of the disk was measured on the reduced image (Figure A.1c; before applying the digital mask) using the IRAF task POLYPHOT. The photometry regions are indicated by the rectangles overlapped onto a contour map of the image in Figure A.3a. We used 4 pix × 12 pix ($0.16'' \times 0.48''$) rectangular apertures, where the long side of the rectangular regions was chosen to span 1–2 FWHMs of the disk thickness and was aligned normally to the disk arm. The distance between the aperture centers was 4 pix ($0.16''$). Even though the image was PSF- and sky-subtracted, to offset for flux biases introduced by the centrally symmetric scaling of the PSF (§A.2), we employed additional background subtraction, with the background flux estimated as the median pixel value in $0.16''$-wide concentric annuli centered on the star. The photometric uncertainty was estimated as the quadrature sum of the standard deviation of the background and the photon noise from the disk. For the standard deviation of the background we adopted the root mean square (r.m.s.) of the pixel values in the annulus, multiplied by $\sqrt{\pi/2}$ (to properly account for the standard deviation of the median; Kendall & Stuart, 1977) and normalized by the size of the photometry aperture.

The radial SBPs of the NW (upward pointing triangles) and SE (downward pointing triangles) arms of the projected disk are shown in Figure A.4. The two SBPs agree well throughout the region over which we can trace the disk (17–60 AU). Unlike the observed shape of the R-band SBP at 50–210 AU, the H-band SBP at 17–60 AU from the star cannot be fit by a single power law. Instead, the SBPs of both the NW and the SE arms "kink" and flatten inwards of 30–40 AU, with the transition being more abrupt in the SE arm at ≈33 AU, and more gradual in the NW arm. While the power-law exponent of the mean SBP over the entire range (17–60 AU) is -2.3 ± 0.2, over 17–33 AU separations it flattens to -1.2 ± 0.3, while over 33–60 AU, it increases to -4.0 ± 0.6. These are consistent

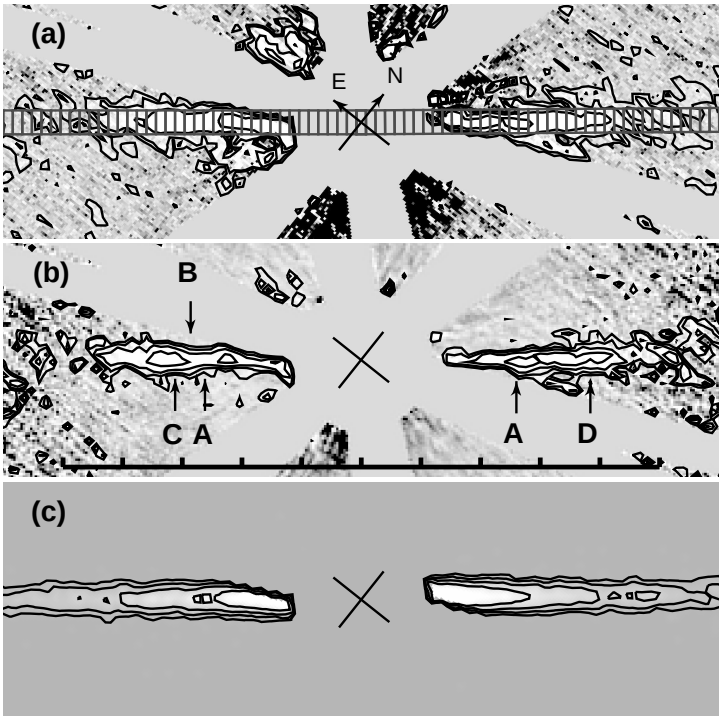

Figure A.3: $12.0'' \times 4.0''$ images of the AU Mic disk, with the SE arm oriented horizontally. (a) Locations of the photometry regions for measuring the disk surface brightness superimposed on the final, masked image of AU Mic. The regions are $0.16'' \times 0.48''$ and sample 1–2 FWHMs of the disk thickness. The circular mask is $2''$ in radius. The crossed arrows mark the location of AU Mic. The contour levels trace surface brightness from 17.5 mag arcsec^{-2} to 14.3 mag arcsec^{-2} in steps of 0.8 mag arcsec^{-2}. (b) Small-scale structure in the AU Mic disk. The capital letters correspond to sub-structures identified by Liu (2004). The bar at the bottom is $10''$ (100 AU) long, extending from -50 AU to $+50$ AU along the disk plane, with tick marks every 10 AU. To enhance the appearance of the clumps in the disk, we have multiplied the pixel values by the square of the distance from the star. The contour levels follow a squared intensity scale. (c) The preferred scattered light model of the AU Mic disk at H-band, created using the MC3D code (§A.4; Table A.1). The same software mask as in the other two panels has been applied. The contour levels follow the same spacing as in panel (a). No background noise is added, though Poisson-noise "clumps" due to low signal-to-noise of the model can be seen. These do not represent discrete physical structures.

with the measurements of Liu (2004) over the same separation range.

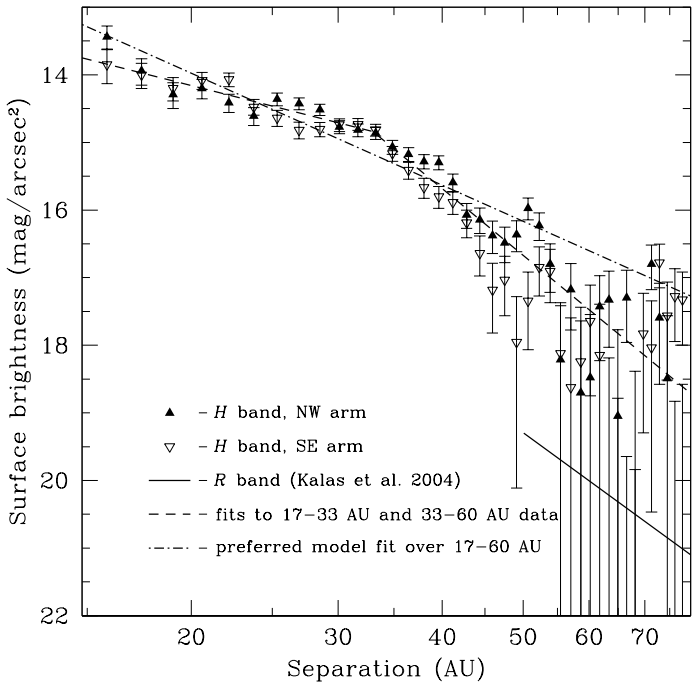

Figure A.4: H-band surface brightness profiles of the NW (upward pointing solid triangles) and the SE (downward pointing open triangles) arms of the AU Mic disk. A gradual flattening of the SBPs of both arms is observed inwards of 30–40 AU. The dashed lines represent the power-law fits to the mean SBP at 17–33 AU (index of -1.2 ± 0.2) and 33–60 AU (index of -4.0 ± 0.6). The solid line represents the mean R-band SBP from Kalas et al. (2004) with a power-law index of -3.75. The dot-dashed line shows the preferred model with a power-law index -2.2, matching that (-2.3 ± 0.2) of the mean SBP over 17–60 AU.

A closer look at the SBP of the NW and SE arms reveals several small-scale asymmetries, all of which can be linked to regions of non-uniform brightness in the AU Mic disk (Figure A.3a). The sub-structure is enhanced by scaling the reduced image by a radially symmetric function centered on the star, with magnitude proportional to the radius squared (Figure A.3b). The lettered structures denote features identified in the (deeper) image of Liu (2004): clumps of enhanced emission

(A, and C), a gap (B), and a region elevated with respect to the inner disk mid-plane (D). In general, we confirm the presence of these features in the AU Mic disk, although the gap (B) and the clump (A) appear misplaced by ∼5 AU toward the star in our image. The NW arm also looks more uniform in brightness between 17–40 AU in our image compared to that in Liu (2004, Figures 3 and 4), where clump A is very prominent. These discrepancies may be caused by residual speckle noise from the PSF subtraction in either data set. In addition to the features described by Liu, we see a faint clump in the NW arm at $\gtrsim$50 AU from the star, coincident with the location of the bump in the SBP of this arm (Figure A.4). The concentration is not reported by Liu and, being at a relatively low signal-to-noise (≈3), may be a noise spike.

A.3.2 Disk Luminosity, Optical Depth, and Geometry

The integrated disk brightness (over 17–60 AU from the star) is 2.7±0.8 mJy at H band; hence $L_{\rm scat}/L_* = 2.3 \times 10^{-4}$. This is comparable to the fractional dust luminosity in emitted mid-IR to sub-mm light, $f_d = L_{IR}/L_* = 6 \times 10^{-4}$ Liu et al. (2004), and hence suggests that the disk mid-plane may be optically thin to radiation at wavelengths as short as ∼1.5μm, at the peak of the AU Mic spectrum. Indeed, f_d is similar to that of other known debris disks ($10^{-5}-10^{-3}$; e.g., Sylvester & Mannings, 2000; Habing et al., 2001; Spangler et al., 2001), all of which are optically thin to ultra-violet and optical light in the direction perpendicular to the disk plane ($\tau_\perp \ll 1$). In the mid-plane, the optical depth of grains along a radial line from the star to infinity is $\tau_\parallel \sim f_d/\sin\delta$ if the grains are in a "wedge" or "flaring" disk with thickness proportional to radius and opening angle 2δ (Backman & Paresce, 1993). Because of the generally unknown viewing geometry of circumstellar disks, $\tau_\parallel$ tends to be poorly constrained. Assuming edge-on orientation ($i = 90°$), we can estimate the maximum allowed opening angle 2δ from the observed disk thickness. For smaller values of i, δ will be smaller because of projection effects. Assuming a perfectly flat, thin disk, we find a lower limit on the inclination $i > 87°$ over 20–50 AU. The projected appearance of an inclined disk of

zero thickness would however be inconsistent with the apparent thickening of the disk with increasing separation (§A.3.1). Therefore, the disk likely has non-zero scale height and/or opening angle and is viewed within only a degree of edge-on. To put a limit on δ, we observe that at a radius of 40 AU the disk FWHM is $\sim$4 AU. Thus we obtain that for $i \lesssim 90^\circ$, $\delta \lesssim 3^\circ$. Hence, $\tau_\parallel \geq 6 \times 10^{-3}$, and probably less than unity, i.e., the disk is optically thin in the radial direction.

A.3.3 Detection Limits on Sub-Stellar Companions

Dynamical influence by embedded planets is a frequently invoked explanation for substructure in dust disks. Because of its youth, proximity, and late spectral type, AU Mic is an ideal target for direct imaging of planets. However, no point sources are seen in our combined 8.1 min PSF-subtracted H band exposure. Figure A.5 delineates our 5σ sensitivity limits as a function of angular separation from the star in the PSF-subtracted image. The 1σ level at each distance is defined as the r.m.s. scatter of the pixel values in one-pixel wide annuli centered on the star. This was divided by $\sqrt{28.3 - 1}$ to adjust for the finite size of the aperture used for photometry (six-pixel diameter, or an area of 28.3 pix^2). The sensitivity to point sources within the disk is up to 1 mag poorer because of the higher photon noise. This is shown in Figure A.5 with the points, each of which has the photon noise from the disk signal added in quadrature. These detection limits, calculated in a statistical manner, were confirmed through limited experiments with artificially planted stars.

At the location of the inferred gap in the SE arm ($\sim$25–30 AU), we can detect planets down to 1 Jupiter mass ($M_{\rm Jup}$) for an assumed stellar age of 10 Myr and using brown-dwarf cooling models from Burrows et al. (1997). Dynamical models of planet-disk interactions in other systems exhibiting similar disk morphology (ϵ Eri, α Lyr) require planets 0.1–3 $M_{\rm Jup}$ (Quillen & Thorndike, 2002; Wilner et al., 2002). Provided that the clumps in the AU Mic disk are caused by such a planet, our point source detection limits constrain its mass to the lower part of this range.

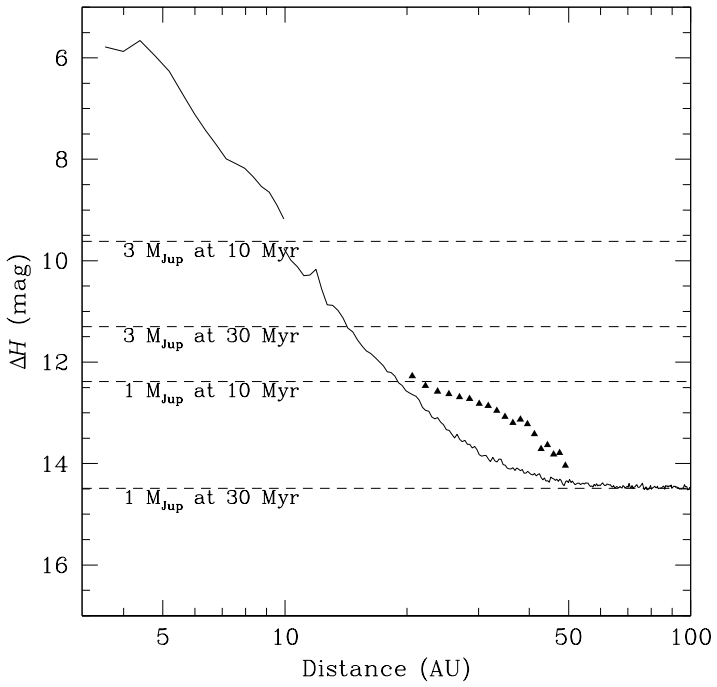

Figure A.5: H-band 5σ detection limits for companions to AU Mic. The solid line delineates the limits in regions away from the disk. The break at 10 AU ($1''$) corresponds to the edge of the largest ($2''$-diameter) coronagraphic spot. To determine the detection limits at separations $\leq 1''$, we used only the series of images taken with the $0.6''$ spot, constituting a third of the total exposure time. Thus, our sensitivity at small separations is somewhat worse than what the extrapolation from distances >10 AU would predict. The triangle symbols trace the poorer sensitivity to point sources in the plane of the disk. Limited experimentation with planting artificial sources in the image confirmed these detection limits. The dashed lines indicate the expected contrast for 1 and $3M_{\rm Jup}$ planets around AU Mic (Burrows et al., 1997) for system ages of 10 and 30 Myr.

A faint candidate companion is seen around our PSF star, HD 195720 ($H = 3.88 \pm 0.24$ from 2MASS). The object is 9.5±0.2 mag fainter at H, at a projected separation of 1.19″ and PA of 81° (Figure A.1b). Given that HD 195720 is a distant giant star (spectral type M2–3 III from SIMBAD), if associated, the companion would be a main-sequence K star. Because of the large magnitude difference, the presence of the projected companion does not affect our PSF subtraction or the analysis of the AU Mic circumstellar disk.

A.4 Dust Disk Modeling

It has already been suggested that the structures in the AU Mic disk (dust concentrations, gaps, vertically displaced clumps) are likely signposts of the existence of perturbing planetary-mass bodies in the AU Mic disk (Liu, 2004). The proposed clearing in the disk inwards of 17 AU (Liu et al., 2004) supports such a hypothesis. From our imaging data we cannot trace the disk to separations <17 AU to directly test the existence of a gap. However, by combining our knowledge of the optical to sub-mm data on the AU Mic debris disk with an appropriate model, we can still probe some of the physical properties of the disk, including the size of the inner gap. In this section we present results from a three-dimensional continuum radiative transfer code, MC3D (Wolf & Henning, 2000; Wolf, 2003), to simultaneously model the AU Mic SED and the scattered light from the disk, and to place constraints on the dust grain size distribution, the radial particle density distribution, and the inner disk radius.

A.4.1 Model and Method

The MC3D code is based on the Monte Carlo method and solves the radiative transfer problem self-consistently. It estimates the spatial temperature distribution of circumstellar dust and takes into account absorption and multiple scattering events. Given the non-vanishing mid-plane optical depth of the AU Mic disk (§A.3.2), we believe that the use of a multi-scattering approach is warranted. The

code employs the concept of enforced scattering (Cashwell & Everett, 1959), where in a medium of optical depth τ, a fraction $e^{-\tau}$ of each photon leaves the model space without interaction, while the remaining part $(1 - e^{-\tau})$ is scattered. The code is therefore applicable to the low-density environments of circumstellar debris disks. The dust grains are assumed to be spherical with a power-law size distribution, $n(a) \propto a^{-3.5}$ (Mathis, Rumpl, & Nordsieck, 1977). We used a standard interstellar medium (ISM) mixture of 62.5% astronomical silicate and 25% + 12.5% graphite (Draine & Malhotra, 1993; Weingartner & Draine, 2001), with optical properties from Draine & Lee (1984). The extinction and scattering cross sections and the scattering distribution function are modeled following the Mie scattering algorithm of Bohren & Huffman (1983).

We use the MC3D code to model the R and H band scattered light in the AU Mic disk and the IR to sub-mm excess in the SED. The AU Mic photosphere is best approximated by a 3600 K NextGen model (Hauschildt, Allard, & Baron, 1999), as expected from its spectral type (M1 V). The fit was performed over the 1–12μm wavelength range, where the emission is photospheric. Data from the literature at shorter wavelengths were ignored, as they are not taken simultaneously, and hence are strongly affected by the $V = 0.35$ mag variability of the star. By matching the model K_S-band flux density to that of a blackbody of the same temperature and by adopting the *Hipparcos* distance of 9.94 pc to the star, we find that its luminosity and radius are $0.13 L_\odot$ and $0.93 R_\odot$, respectively. For the debris disk we adopt a flat (unflared) geometry with a number density profile proportional to $r^{-\gamma}$, where r denotes radial distance from the star, and γ is a constant. We set the outer radius of the model to 1000 AU, so that it is larger than the size of the R-band scattered light emission (210 AU) and than the JCMT/SCUBA beam used for the sub-mm measurements (FWHM of $14'' = 140$ AU). The disk inclination and opening angle were already constrained in §A.3.2. For our modeling purposes we assume $i = 89°$, $\delta = 0°$, and a flat disk model with a constant scale height h=0.8 AU. We find that models based on these parameters approximate the mean observed disk thickness well.

The remaining free parameters in the disk model are the exponent of the volume density profile γ, the dust mass $M_{\rm dust}$, the minimum and maximum dust grain sizes $a_{\rm min}$ and $a_{\rm max}$, and the inner radius $r_{\rm in}$. A fit to the mean NW and SE SBP between 17–60 AU results in a best-fit power-law index of $-\nu = -2.3 \pm 0.2$, indicating that the number density profile varies as $r^{-1.3\pm0.2}$, i.e., $\gamma = \nu - 1 = 1.3 \pm 0.2$ (as is true for an edge-on disk of isotropically scattering grains; Nakano, 1990; Backman, Witteborn, & Gillett, 1992)[1]. This value is in agreement with the range inferred for P-R drag dominated disks (1.0–1.3; e.g., Briggs, 1962). Given the error on our fit, we decide to fix the value of the power-law index at the theoretically expected value of $\gamma = 1.0$ for a continuously replenished dust cloud in equilibrium under P-R drag (Leinert, Röser, & Buitrago, 1983; Backman & Gillett, 1987). The effects of varying γ are considered at the end of §A.4.2.

A.4.2 Breaking Degeneracies in the Model Parameters

We subsequently follow a trial-and-error by-eye optimization scheme to determine the values of $M_{\rm dust}$, $a_{\rm min}$, $a_{\rm max}$, and $r_{\rm in}$. With a sophisticated dust disk model containing many parameter choices, it is possible to find combinations of parameters that have degenerate effects on the SED and/or on the SBP. By fitting simultaneously the SED and the imaging data we can avoid some, but not all, of the complications. Here we discuss the specific degeneracies and how we can break them via the observational constraints in hand. We first consider the interaction between $M_{\rm dust}$, $a_{\rm min}$, and $a_{\rm max}$, which are strongly degenerate. We then consider the effect of changing $r_{\rm in}$, which is more weakly coupled with the rest of the parameters. Finally, we extend our discussion to consider variations in the power-law index γ, which is otherwise kept fixed during the modeling.

The dust mass, $M_{\rm dust}$, and the minimum and maximum grain sizes, $a_{\rm min}$ and

[1]Forward scattering, to the extent to which it is characteristic of the dust grains in the AU Mic disk, tends to increase γ. Even though forward scattering is ignored in the approximation $\gamma = \nu - 1$, it is modeled by the MC3D code, where its amount is determined by the input grain parameters and Mie theory.

$a_{\rm max}$, have degenerate effects on both the SBP and the SED. Decreasing $M_{\rm dust}$ or increasing $a_{\rm min}$ or $a_{\rm max}$ result in a decrease in the amount of mass residing in small grains (the bulk of the scatterers) and lower the flux of the SBP. Each of these changes similarly lowers the thermal SED flux. However, dust mass variations can be disentangled from grain size variations because of the different magnitudes of their effects on the SBP and on the SED. Optically thin thermal emission is a more accurate proxy of dust mass, whereas optical-IR scattering is more sensitive to small differences in the mean grain size. We therefore constrain $M_{\rm dust}$ from the sub-mm data, while we use the color and absolute flux of the scattered light to determine $a_{\rm min}$ and $a_{\rm max}$. Here we should note that $M_{\rm dust}$ represents only the dust mass contained in grains comparable in size or smaller than the maximum wavelength ($\lambda_{\rm max}$) at which thermal emission is observed. In the case of AU Mic, the currently existing longest-wavelength observations are at 850μm (Liu et al., 2004). Consequently, we are free to adjust $a_{\rm min}$ and $a_{\rm max}$, as long as $a_{\rm min} \leq a_{\rm max} \lesssim$ 1 mm. We will not consider cases for which $a_{\rm max} > 1$ mm.

As a first step in finding the optimum model parameters, we confirm the Liu et al. (2004) estimate of the dust mass, $M_{\rm dust} = 0.011 M_{\oplus}$, calculated from the 850μm flux. This value matches the sub-mm data points for a wide range (an order of magnitude) of minimum and maximum grain sizes, whereas changing $M_{\rm dust}$ by a factor of >1.5 introduces significant discrepancies from the observed 850μm emission. As a next step, we constrain $a_{\rm min}$ by modeling the optical-near-IR color of the scattered light in the overlap region (50–60 AU) between the Kalas et al. R-band and our H-band data. Because the size of the smallest grains is likely comparable to the central wavelengths of the R and H bands, $R - H$ is a sensitive diagnostic for $a_{\rm min}$. We smooth the R- and H-band model images to the respective image resolutions (1.1$''$ at R and 0.04$''$ at H) and use the appropriate aperture widths (1.2$''$ at R [Kalas et al., 2004] and 0.48$''$ [this work]). For the adopted grain size distribution we find that models with $a_{\rm min} \approx 0.5\mu$m, with a probable range of 0.3–1.0μm, best approximate the disk color. Having constrained $M_{\rm dust}$ and $a_{\rm min}$, we find that $a_{\rm max} = 300\mu$m matches best the R- and H-band flux

levels of the disk. The probable range for $a_{\rm max}$ is 100–1000μm. Since we have not considered models with $a_{\rm max} > 1$ mm, we cannot put an upper limit to the maximum grain size.

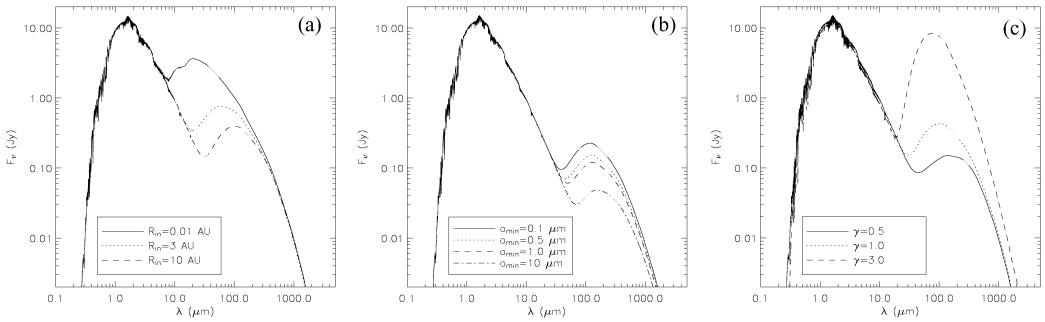

Figure A.6: Examples of degeneracies in the SED. Larger inner gap radii (a) are degenerate with larger minimum grain sizes (b) and with shallower number density distributions (c). Various combinations of these parameters can produce roughly the same SED. The normalizations of the emitted mid-IR flux from the disk are different among the three panels.

The inner radius $r_{\rm in}$ of the disk is degenerate with the mean dust grain size in the SED. Greater values of $r_{\rm in}$ decrease the mid-IR flux and shift the peak of the excess to longer wavelengths (Figure A.6a), as do greater values of $a_{\rm min}$ (Figure A.6b) and $a_{\rm max}$. Because the AU Mic disk is optically thin in the mid-plane (§A.3.2), the inner disk radius has no effect on the flux and color of the SBP, facilitating the isolation of the $r_{\rm in}$ parameter. Having already determined $a_{\rm min}$ and $a_{\rm max}$, we find $r_{\rm in} \approx 10$ AU, which is smaller than the 17 AU gap estimated from the single-temperature blackbody fit in Liu et al. (2004). A firm upper limit of $r_{\rm in} < 17$ AU can be set based on the fact that we do not observe a decrease in the intensity of the scattered light with decreasing separation down to 17 AU (Figure A.4; see also Figure 2 in Liu, 2004).

Finally, although we had fixed the value of the power-law index γ, a brief discussion of its variation is warranted given the change in the SBP with radius. The action of γ on the SED is degenerate with the dust size and with the radius of the inner gap. Larger values of γ are degenerate with smaller particles and

Table A.1: Preferred Model Parameters for the AU Mic System

Parameter	Value	Range
Stellar luminosity L_*	$0.13 L_\odot$	fixed
Stellar radius R_*	$0.93 R_\odot$	fixed
Stellar temperature $T_{\rm eff}$	3600 K	fixed
Dust mass $M_{\rm dust}$	$0.011 M_\oplus$	0.008–$0.016 M_\oplus$
Dust size distribution	$a^{-3.5}$	fixed
Number density profile	$r^{-1.0}$	-0.2 to -3.0, fixed†
Outer disk radius $r_{\rm out}$	1000 AU	fixed
Inner disk radius $r_{\rm in}$	10 AU	1–10 AU
Inclination angle i	89°	$\gtrsim 89^\circ$
Scale height H	0.8 AU at $r = 40$ AU	$\lesssim$1.0 AU at $r = 40$ AU
Opening angle 2δ	0°	$\lesssim 6^\circ$
Minimum grain size $a_{\rm min}$	0.5μm	0.3–1μm
Maximum grain size $a_{\rm max}$	300μm	100–1000μm‡

† Treated as a fixed parameter during the MC3D model fitting. The listed range corresponds to the range of fits to the SBP over 17–60 AU.

‡ The SED data are not sensitive to emission from grains $\gtrsim$1000μm in size, so we have not run models with $a_{\rm max} > 1000 \mu$m.

smaller inner gap radii (Figure A.6). Given that at $\leq$33 AU the power-law index of the SBP decreases to -1.2 (i.e., $\gamma \approx 0.2$), and that most of the mid-IR flux is produced close (10–20 AU) to AU Mic, the inner disk clearing may therefore be smaller than 10 AU in radius. Indeed, recent *HST* scattered light imaging (Krist et al., 2005) detects the disk in to 7.5 AU (although the authors invoke forward scattering to account for the apparent filling in of the inner gap). Compounding this with evidence for an increasing minimum grain size with decreasing radial separation (§A.5.1), we find that inner gap sizes as small as $r_{\rm in} \sim 1$ AU cannot be ruled out.

Table A.1 lists our preferred model parameters for the AU Mic star-disk system. The optical depth of the model along the disk mid-plane is $\tau_{\|} \approx 0.08$ at both R and H bands, in agreement with the estimates in §A.3.2. The model SBP and SED are over-plotted on the data in Figures A.4 and A.7, respectively. Figure A.3c shows the noiseless scattered light model of the AU Mic disk with the same greyscale and contour spacing as the image in Figure A.3a. The model disk extends to larger radial separations than the AU Mic disk, an effect of the steeper power law of the AU Mic SBP at >33 AU.

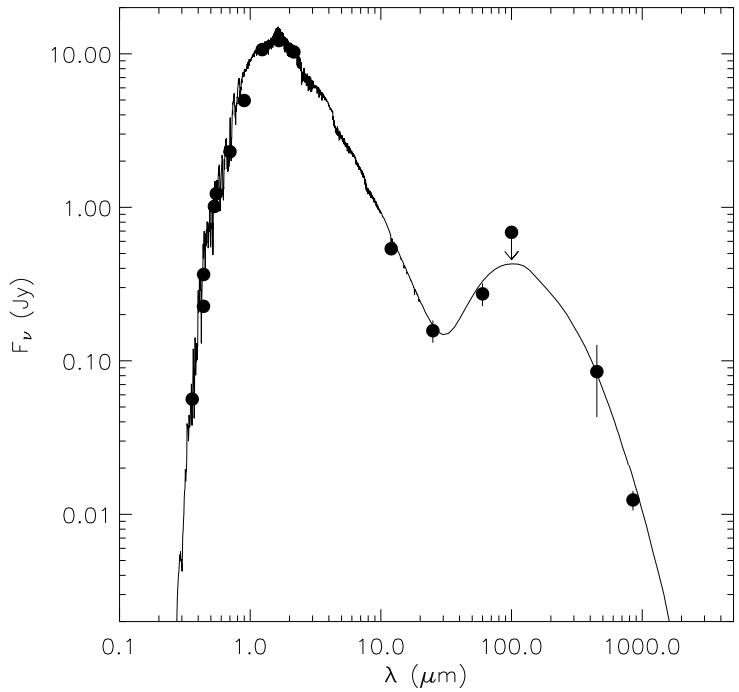

Figure A.7: SED of AU Mic (data points from Liu et al., 2004, and references therein). The photophere is fit by a 3600 K NextGen model (Hauschildt et al., 1999), and the circumstellar excess emission is fit using the MC3D code (§A.4) with model parameters listed in Table A.1.

A.5 Discussion

Two important new results are evident from our simultaneous modeling of the SBP and SED of the AU Mic debris disk: (1) there is a pronounced lack of small ($<0.3\mu$m) grains in the inner disk, and (2) the radius of the inner clearing may be smaller (1–10 AU) than estimated (17 AU) from a simple black-body fit to the IR excess (Liu et al., 2004). The latter point was already discussed in §A.4.2, and, given the shortcomings of our model in reproducing the changing slope of the SBP, will not be belabored further. Here we discuss the derived minimum grain size along with recent evidence for its dependence on disk radius. We then focus on the change in slope of the SBP of the AU Mic debris disk and draw a parallel with the β Pic system. We propose that identical dynamical processes in the two debris disks can explain the observed homology.

A.5.1 Minimum Grain Size as a Function of Disk Radius

From the model fits to the color and absolute flux of the scattered light from the AU Mic debris disk, we find that the dust grains are between $a_{\rm min} = 0.5^{+0.5}_{-0.2}\mu$m and $a_{\rm max} = 300^{+700}_{-200}\mu$m in size (although the 1 mm upper limit on the maximum grain size is not robust). In reality, our constraints on the grain parameters are valid only over the 50–60 AU region, where we have information from both the $R-H$ color of the scattered light and the SED. We have very few constraints for the outer disk (>60 AU), which is seen only in R-band scattered light and is too cold to be detected in emission at wavelengths <1 mm.

Shortly before receiving the referee report for this paper, sensitive high-resolution 0.4–0.8μm images of AU Mic became available from *HST* (Krist et al., 2005). These show the debris disk over 7.5–150 AU separations from the star and thus provide complete overlap with our AO data. A brief discussion of the two data sets in the context of the minimum grain size is therefore warranted. For consistency with Krist et al., we re-did our surface photometry with the $0.25'' \times 0.25''$ apertures used by these authors. Because the two data sets have similar angular resolution

($0.04''$ vs. $0.07''$) and because the aperture size is much larger than the FWHM of the PSFs, the systematics of the photometry should be negligible. The Krist et al. *HST* $F606W$ (0.59μm) data are consistent with the Kalas et al. ground-based R-band (0.65μm) observations over 50–60 AU from the star, and thus our conclusions about the grain sizes in this region remain unchanged. However, a comparison of the H-band and the $F606W$-band SBP over the region of overlap shows that the $F606W - H$ color changes from 2.9±0.2 mag (i.e., approximately neutral, since $R - H = 2.9$ for AU Mic) at 17–20 AU to 2.0±0.3 mag at 50–60 AU. That is, the debris disk becomes increasingly bluer at larger radii. The effect is gradual and is also reported in Krist et al., where it is observed over a narrower wavelength range (0.4–0.8μm) at 30–60 AU from the star.

The neutral color of the dust at 20 AU indicates that the majority of scatterers there are larger than 1.6μm. Compared with the minimum grain size ($0.5^{+0.5}_{-0.2}\mu$m) that we derived at 50–60 AU, this indicates that at smaller separations grains are bigger. Such a dependence of grain size on radius would further imply that the radius at which the SBP changes power-law index should be wavelength-dependent, occurring farther away from the star at shorter wavelengths. Evidence for this may indeed be inferred from a comparison between the *HST* and Keck AO data: in the $F606W$ ACS filter the break in the SBP is seen at ≈43 AU (Krist et al., 2005), whereas at H-band it occurs near 33–35 AU (§A.3.1; Liu, 2004). The indication that the minimum grain size decreases with disk radius is thus confirmed from two independent observations.

Particles smaller than $a_{\rm min}$ may be removed as a result of either coagulation into larger particles (grain growth), destruction by P-R and/or corpuscular drag, or radiation pressure blow-out. Given that $a_{\rm min}$ is larger than the radiation pressure blow-out size (0.14μm, for a radiation pressure to gravity ratio β=0.5 and a grain density of 2.5 g cm^{-3}), grain collisions and drag forces dominate the dynamics of >0.14μm grains around AU Mic. Therefore, the origin of the sub-micron grains scattering visible light at wide separations (where the collision and P-R time scales are longer than the age of the star) may also be primordial: rather than being blown

out from the inner disk, these grains may be remnant from the proto-stellar cloud that never coagulated beyond an ISM grain size distribution.

A.5.2 The Change in the SBP Power-law Index: A Comparison with β Pic

It is not surprising that our preferred model cannot reproduce the detailed structure of our high angular resolution IR image. The model parameters were found only after a coarse sampling of the parameter space and through a number of simplistic assumptions that merely approximate the physical conditions in the AU Mic debris disk. In particular, under the assumption of a uniform grain size and density distribution over 10–1000 AU, the MC3D model cannot mimic the SBP slope change at $\sim$33 AU and the clumpy substructure over 17–60 AU described in Liu (2004) and confirmed in §A.3.1. While the dust clumps are high-order perturbations that may require dynamical considerations for proper modeling, the change in the SBP potentially could be explained in the framework of existing dust disk scenarios.

The occurrence of the power-law break at similar radii in the SBPs of both arms of the projected disk suggests that this is a ring-like structure surrounding the star, rather than a discrete feature at one location in the disk. Models involving dynamical interaction with planets have been proposed to explain ring-like structures in circumstellar disks (e.g., Roques et al., 1994; Liou & Zook, 1999; Kenyon et al., 1999; Kenyon & Bromley, 2004), and the clumpy structure of the AU Mic disk does suggest the presence of unseen planets (Liu, 2004). However, such models tend to produce discrete rings, as around HR 4796A and HD 141569A, rather than the radially dimming SBP of the AU Mic disk. Similar changes in the power-law index have also been seen in the SBPs of other resolved circumstellar disks: β Pic (Artymowicz, Paresce, & Burrows, 1990, Heap et al., 2000), TW Hya (Krist et al., 2000; Weinberger et al., 2002), and HD 100546 (Pantin, Waelkens, & Lagage, 2000; Augereau et al., 2001). A different mechanism, not necessarily involving planets, may be at play in these systems.

The TW Hya and HD 100546 circumstellar disks are gas-rich and have large mid-plane optical depths, and hence are very much unlike the gas-poor (Roberge et al., 2004), optically thin AU Mic debris disk. However, a comparison with β Pic is particularly illuminating because of the similar viewing geometry of the two systems and their identical ages. In the remainder of this section we seek a common disk architecture that can self-consistently account for the broken power-law morphology of the SBPs of these two debris disks.

The SBP of β Pic exhibits a break at 5–6″ (100–120 AU) from the star (e.g., Golimowski, Durrance, & Clampin, 1993, Heap et al., 2000), with similar values (from –1 to –4) of the power-law index on either side of the break as in the SBP of AU Mic. From K'-band (0.21μm) AO observations resolving the β Pic disk over 1.5″–6″, Mouillet et al. (1997) observe the break at a somewhat smaller radius, 4–4.5″ (75–85 AU), with a smaller change in the SBP power-law index (from –1 to –3). This may be the inner edge of the SBP break observed in the visible or may indicate a wavelength-dependence of the β Pic break radius similar to the one potentially seen in the AU Mic disk (§A.5.1). However, because the Mouillet et al. $K\prime$-band data do not extend beyond the optical break radius (6″) and because the change in the power-law index observed at $K\prime$ does not span the full range of power-law indices inferred from optical imaging, this data set will not be considered further.

Artymowicz et al. (1989) model the break in optical SBP of the β Pic disk using two different power laws for the number density of dust particles in the disk for radii less than or greater than 100 AU, respectively. Backman et al. (1992) consider the possibility of differing grain sizes, in addition. While either model may correctly describe the architecture of the β Pic disk, both are purely phenomenological, as they do not model the physics behind the discontinuity in the disk. Based on the apparent homology between these two debris disks, we believe that a plausible two-component model should be able to explain both systems self-consistently. In light of this, several physical scenarios from the subsequent literature are considered below. We find that none of them offer a unique explanation and propose separate

hypotheses in §A.5.2.3 and A.5.2.4.

A.5.2.1 Ice or Comet Evaporation

Backman et al. (1992) and Pantin, Lagage, & Artymowicz (1997) suggest that the discontinuity in the SBP of β Pic may correspond to the location of the "ice boundary" in the disk: all dust particles at separations >100 AU are covered with ice, while at shorter separations some may not be. This results in a deficiency of highly reflective particles in the inner regions, creating a shallower power-law index for the scattered light profile. In an optically thin disk the radius of the ice boundary should scale as the square root of the stellar luminosity. Adopting $L_{\rm AUMic} = 0.13 L_{\odot}$ (Table A.1) and $L_{\beta{\rm Pic}} = 8.7 L_{\odot}$, and assuming identical grain chemistry in the two systems, we find that the corresponding boundary around AU Mic should scale down to a radius of 13–15 AU, too close to account for the break at 33 AU.

An alternative hypothesis, involving dust extraction through evaporation of gas from a reservoir of cometary bodies around β Pic, is proposed by Lecavelier des Etangs, Vidal-Madjar, & Ferlet (1996). However, the radial distance of this evaporating reservoir should scale in the same manner as that of the ice boundary. Hence, neither of these two hypotheses can be applied simultaneously to AU Mic and β Pic.

A.5.2.2 A Belt of Parent Bodies

A reservoir of parent bodies at a discrete range of separations from AU Mic could explain the kink in the SBP. Gorkavyi et al. (1997) calculate that the Main asteroid belt in the Solar System should produce a break in the power-law index of the number density distribution of interplanetary grains from -1.3 to -6.4 at 0.5–3.0 AU from the Sun. These predictions are consistent with empirical data from radar meteors and from impact detectors on spacecraft (Divine, 1993). The inner edge of this belt of asteroids in the AU Mic and β Pic systems would be at the location of the kinks, at $\sim$33 AU and $\sim$110 AU from the stars, respectively. By

continuing the analogy with the Solar System, such belts of parent bodies would likely need to be maintained in a discrete range of orbits through mean motion resonances with planets (e.g., Liou & Zook, 1997, and references therein). That is, this particular scenario may provide further indication for the existence of planets in the two disks, in addition to the evidence arising from the their clumpy structure. However, this model is poorly constrained, as we are free to invoke a belt of parent bodies at any distance from either star.

A.5.2.3 Collisional Evolution

For two stars of the same age, the disk around the more massive star is expected to be collisionally evolved out to a greater radius because of the inverse scaling of the orbital period (and hence, collision frequency) with orbital radius and stellar mass. The collisional time scale for particles of mean size a on a circular orbit of radius r from a star of mass M_* is

$$t_{\rm coll} \sim \frac{P}{4\pi^2 a^2 r n(r)} \propto \frac{r^{1/2}}{M_*^{1/2} n_0 r^{-\gamma}} = \frac{r^{\gamma+1/2}}{M_*^{1/2} n_0}, \tag{A.1}$$

where P is the orbital period, and n_0 is the normalization constant for the number density distribution, which we presume scales as $M_{\rm dust}$. Given the approximate ratios of the stellar masses of AU Mic and β Pic (0.28, assuming $M_{\beta\ \rm Pic} = 1.8 M_\odot$), and of their circumstellar dust masses, (0.2 ± 0.1, where the mass of the β Pic disk was taken as the average of the estimates from Sheret, Dent, & Wyatt (2004) and Dent et al. (2000)) and assuming 33 AU and 110 AU as the radii of the kinks in the corresponding SBPs, we find that for $\gamma = 1.5^{+0.3}_{-0.4}$ the collisional time scales at the respective separations around the two stars are equal. This would imply SBPs decreasing approximately as $r^{-\gamma-1} = r^{-2.5}$, which is within the ranges found in §A.3.1 for AU Mic and in Heap et al. (2000) for β Pic, and agrees with the fit to the mean AU Mic H-band SBP (power-law index of -2.3 ± 0.2; Figure A.4). Therefore, in this scenario the two disk systems scale correctly within the errors, indicating that whatever process we are observing may scale with the mean time

between inter-particle collisions. Although the collisional time-scale at the location of the break in the AU Mic SBP is considerably shorter (1–3 Myr) than the age of the star (8–20 Myr), other, slower processes in the disk, e.g., grain growth, may scale linearly with the time between particle collisions. As noted in §A.5.1, grain growth could also explain the observed dependence of grain size with orbital radius.

A.5.2.4 Poynting-Robertson Drag

The observed change in the power-law index of the SBP may be a reflection of the finite lifetimes of sub-micron grains in the inner disk. Having ruled out radiation pressure as a dominant force on grains larger than 0.14μm (§A.5.1), we propose a hypothesis based on drag forces for grain removal, in particular P-R drag. Although corpuscular drag may dominate the dynamics of dust around M stars (e.g., Fleming, Schmitt, & Giampapa, 1995), the strength of stellar winds from M dwarfs remains largely unknown. We therefore ignore corpuscular drag in the following analysis (see Plavchan, Jura, & Lipscy, 2005, for a discussion of the role of corpuscular drag in the AU Mic disk) and consider only P-R drag. As long as the magnitude of the corpuscular drag force around AU Mic is not much greater than the magnitude of the P-R drag force, the conclusions remain unchanged.

If P-R drag was responsible for the depletion of micron-sized grains in the inner disks of AU Mic and β Pic, then the P-R lifetime ($t_{\rm PR}$) of the smallest grains $a_{\rm min}$ should be constant as a function of disk radius r and should equal the age of the stars ($t_{\rm age}$). This can be inferred from the expression for the P-R lifetime of a particle of size a (see, e.g., Burns, Lamy, & Soter, 1979):

$$t_{\rm PR}(a,r) = \left(\frac{4\pi a\rho}{3}\right)\left(\frac{c^2 r^2}{L_*}\right), \tag{A.2}$$

where ρ is the mean grain density (2.5 g cm^{-3} for silicates), and c is the speed of light. Based on the assumption that P-R drag is the dominant removal mechanism for grains larger than the blow-out size (0.14μm), the P-R lifetime of the smallest

grains is $t_{\rm PR}(a_{\rm min}, r) = t_{\rm age} = {\rm const}$. Note, however, that the size of the smallest grains, $a_{\rm min}$, is not a constant, but varies as $a_{\rm min} \propto r^{-2}$.

For AU Mic we found $a_{\rm min} \geq 0.3\mu$m at 50–60 AU and $a_{\rm min} \geq 1.6\mu$m at 17–20 AU (§A.5.1). We obtain $t_{\rm PR}(0.3\mu{\rm m}, 50{\rm AU}) = 9.9$ Myr and $t_{\rm PR}(1.6\mu{\rm m}, 20{\rm AU}) = 8.4$ Myr. We do not have information about the change in $a_{\rm min}$ as a function of radius in β Pic. We only note that from mid-IR and visual images, Artymowicz et al. (1989) find that they require "few-micron-sized" silicate grains[2] to model the scattered light at $>6.0''$ (>115 AU) from the star. Assuming a minimum grain size of 3μm, we find $t_{\rm PR}(3\mu{\rm m}, 115{\rm AU}) = 7.8$ Myr around β Pic. Given the uncertainty in $a_{\rm min}$, the obtained P-R time-scales are not constrained to better than a factor of 1.5–2. Nevertheless, they are remarkably similar and agree well with the ages of AU Mic and β Pic.

A.5.2.5 Summary of Proposed Scenarios

We find that dynamical scenarios based on collisional evolution or P-R drag in debris disks offer simpler and more self-consistent accounts of the homology between the SBPs of the AU Mic and β Pic debris disks, compared to scenarios relying on ice/grain evaporation or belts of orbiting parent bodies. Moreover, both our hypotheses can account for the inferred decrease in the minimum grain size with increasing separation from AU Mic. We therefore conclude that both are plausible. Given the similarities in their predictions, we do not single out which one of them is more likely, but defer that analysis to a more detailed theoretical work. Regardless of which of the two processes is found to be dominant, we can confidently claim that optically thin circumstellar disks exhibiting breaks in their SBPs are observed in transition between a primordial and a debris state.

[2] A second solution involving 1–15μm ice grains is found to be equally plausible. However, its grain properties differ widely from the ones adopted for the AU Mic circumstellar dust in this paper.

A.6 Conclusion

We have used AO H-band observations of scattered light to probe the morphology of the debris disk at 17–60 AU from the young nearby M dwarf AU Mic. We find that the disk is within $\sim$1° of edge-on and that it exhibits a number of morphological peculiarities: radial asymmetry, spatially resolved clumps, and a change in the power-law index of the surface brightness profile near 33 AU. The observed morphology agrees with that reported in Liu (2004) and is suggestive of the existence of planetary perturbers in the disk. No planets are detected down to $1M_{\rm Jup}$ at >20 AU.

We use a Monte Carlo three-dimensional dust disk model to constrain the overall disk parameters by optimizing them against the AU Mic SED and near-IR and optical scattered light images of the disk (this paper; Kalas et al., 2004). The combined use of SED data tracing the thermal emission from large grains and of imaging data tracing grain properties allows us to break several important degeneracies in models of circumstellar disks that cannot be resolved using only one of the two data sets. From the SED we confirm the previously inferred (Liu et al., 2004) circumstellar dust mass of $0.011M_{\oplus}$, and from the properties of the scattered light we infer that the debris particles are $\geq 0.5^{+0.5}_{-0.2}\mu$m in size at 50–60 AU from AU Mic. We find tentative evidence for a maximum grain size of $300^{+500}_{-200}\mu$m. However, since the data are not sensitive to particles $\gg$1 mm, the result is consistent with no upper limit on the grain size. Assuming a single dust size and density distribution, we estimate that the radius of the inner disk clearing is 10 AU. However, smaller ($\sim$1 AU) gap sizes cannot be ruled out if a shallower density profile (as observed inwards of 33 AU) and/or larger grains in the inner disk (as evidenced from the optical-near-IR color of the disk) are adopted. We attribute the lack of sub-micron particles in the inner disk to grain growth, destruction by P-R and/or corpuscular drag (for grains >0.14μm), or to blow-out by radiation pressure (for grains <0.14μm). All of these mechanisms can explain the increase in relative density of small grains with increasing radius in the disk.

The MC3D model can account for the overall disk profile and colors to first order, although our one-component model fails to reproduce higher-order effects, such as the change in power-law index of the SBP. We have discussed a number of scenarios that may be capable of reproducing such a change in the joint context of the AU Mic and β Pic debris disks. We find that models dividing the disk into two separate components, with different grain distribution and/or composition, represent the combined SED and imaging data best. In particular, classes of models that scale with the collision or the P-R time-scale are most likely to explain both debris disks self-consistently.

Future high-dynamic range imaging observations probing closer to AU Mic (e.g., with nulling interferometry in the mid-IR) will further narrow down the architecture of its debris disk. Photometric and spectroscopic observations with *Spitzer* could better constrain the SED of AU Mic and could be used to look for spectroscopic features. These could trace small amounts of dust and gas in the inner disk, even if no continuum excess is seen at $< 25\mu$m.

Bibliography

Abt, H. A., & Levy, S. G. 1976, ApJS, 30, 273

Ackerman, A. S., & Marley, M. S. 2001, ApJ, 556, 872

Adams, J. D., Stauffer, J. R., Monet, D. G., Skrutskie, M. F., & Beichman, C. A. 2001, AJ, 121, 2053

Ali, B., Carr, J. S., Depoy, D. L., Frogel, J. A., & Sellgren, K. 1995, AJ, 110, 2415

Allende Prieto, C., & Lambert, D. L. 1999, A&A, 352, 555

Andersen, J. 1991, A&A Rev., 3, 91

Apai, D., Pascucci, I., Brandner, W., Henning, T., Lenzen, R., Potter, D. E., Lagrange, A.-M., & Rousset, G. 2004, A&A, 415, 671

Appenzeller, I., Thiering, I., Zickgraf, F.-J., Krautter, J., Voges, W., Chavarria, C., Kneer, R., Mujica, R., Pakull, M., Rosso, C., Ruzicka, F., Serrano, A., & Ziegler, B. 1998, ApJS, 117, 319

Artymowicz, P., Burrows, C., & Paresce, F. 1989, ApJ, 337, 494

Artymowicz, P., Paresce, F., & Burrows, C. 1990, Advances in Space Research, 10, 81

Augereau, J. C., Lagrange, A. M., Mouillet, D., & Ménard, F. 2001, A&A, 365, 78

Augereau, J. C., & Papaloizou, J. C. B. 2004, A&A, 414, 1153

Aumann, H. H., Beichman, C. A., Gillett, F. C., de Jong, T., Houck, J. R., Low, F. J., Neugebauer, G., Walker, R. G., & Wesselius, P. R. 1984, ApJ, 278, L23

Backman, D., & Gillett, F. C. 1987, Lecture Notes in Physics, Berlin Springer Verlag, 291, 340

Backman, D. E., & Paresce, F. 1993, in Protostars and Planets III, 1253–1304

Backman, D. E., Witteborn, F. C., & Gillett, F. C. 1992, ApJ, 385, 670

Bahcall, J. N., & Soneira, R. M. 1980, ApJS, 44, 73

Baraffe, I., Chabrier, G., Allard, F., & Hauschildt, P. H. 1995, ApJ, 446, L35+

—. 1998, A&A, 337, 403

Baraffe, I., Chabrier, G., Barman, T. S., Allard, F., & Hauschildt, P. H. 2003, A&A, 402, 701

Barrado y Navascués, D. 1998, A&A, 339, 831

Barrado y Navascués, D., Stauffer, J. R., Song, I., & Caillault, J.-P. 1999, ApJ, 520, L123

Basri, G., Marcy, G. W., & Graham, J. R. 1996, ApJ, 458, 600

Bate, M. R., Bonnell, I. A., & Bromm, V. 2002, MNRAS, 332, L65

—. 2003, MNRAS, 339, 577

Bayes, T. 1763, Philosophical Transactions of the Royal Society of London, 53, 370, can also be found at: http://www.stat.ucla.edu/history/essay.pdf

Bertin, E., & Arnouts, S. 1996, A&AS, 117, 393

Bessell, M. S. 1991, AJ, 101, 662

Bessell, M. S., & Brett, J. M. 1988, PASP, 100, 1134

Beust, H., Lagrange-Henri, A. M., Vidal-Madjar, A., & Ferlet, R. 1989, A&A, 223, 304

Beust, H., Vidal-Madjar, A., Ferlet, R., & Lagrange-Henri, A. M. 1990, A&A, 236, 202

Beuzit, J.-L., Ségransan, D., Forveille, T., Udry, S., Delfosse, X., Mayor, M., Perrier, C., Hainaut, M.-C., Roddier, C., Roddier, F., & Martín, E. L. 2004, A&A, 425, 997

Bloemhof, E. E. 2003, ApJ, 582, L59

Bloemhof, E. E., Marsh, K. A., Dekany, R. G., Troy, M., Marshall, J., Oppenheimer, B. R., Hayward, T. L., & Brandl, B. 2000, in Proc. SPIE Vol. 4007, Adaptive Optical Systems Technology, Peter L. Wizinowich; Ed., 889–898

Boccaletti, A., Riaud, P., & Rouan, D. 2002, PASP, 114, 132

Bodenheimer, P. 1965, ApJ, 142, 451

Bodenheimer, P., Tohline, J. E., & Black, D. C. 1980, ApJ, 242, 209

Bohren, C. F., & Huffman, D. R. 1983, Absorption and scattering of light by small particles (New York: Wiley, 1983)

Boss, A. P. 2002, ApJ, 576, 462

Bouvier, J., Rigaut, F., & Nadeau, D. 1997, A&A, 323, 139

Bouy, H., Brandner, W., Martín, E. L., Delfosse, X., Allard, F., & Basri, G. 2003, AJ, 126, 1526

Bouy, H., Duchêne, G., Köhler, R., Brandner, W., Bouvier, J., Martín, E. L., Ghez, A., Delfosse, X., Forveille, T., Allard, F., Baraffe, I., Basri, G., Close, L., & McCabe, C. E. 2004, A&A, 423, 341

Brandner, W., Zinnecker, H., Alcalá, J. M., Allard, F., Covino, E., Frink, S., Köhler, R., Kunkel, M., Moneti, A., & Schweitzer, A. 2000, AJ, 120, 950

Breger, M. 1986, ApJ, 309, 311

Briceño, C., Luhman, K. L., Hartmann, L., Stauffer, J. R., & Kirkpatrick, J. D. 2002, ApJ, 580, 317

Briggs, R. E. 1962, AJ, 67, 710

Brown, R. A. 2004, ApJ, 607, 1003

—. 2005, ApJ, 624, 1010

Burgasser, A. J., Kirkpatrick, J. D., Brown, M. E., Reid, I. N., Burrows, A., Liebert, J., Matthews, K., Gizis, J. E., Dahn, C. C., Monet, D. G., Cutri, R. M., & Skrutskie, M. F. 2002, ApJ, 564, 421

Burgasser, A. J., Kirkpatrick, J. D., Reid, I. N., Brown, M. E., Miskey, C. L., & Gizis, J. E. 2003, ApJ, 586, 512

Burns, J. A., Lamy, P. L., & Soter, S. 1979, Icarus, 40, 1

Burrows, A., Hubbard, W. B., Lunine, J. I., & Liebert, J. 2001, Reviews of Modern Physics, 73, 719

Burrows, A., & Liebert, J. 1993, Reviews of Modern Physics, 65, 301

Burrows, A., Marley, M., Hubbard, W. B., Lunine, J. I., Guillot, T., Saumon, D., Freedman, R., Sudarsky, D., & Sharp, C. 1997, ApJ, 491, 856

Buscombe, W. 1998, VizieR Online Data Catalog, 3206, 0

Buscombe, W., & Foster, B. E. 1997, VizieR Online Data Catalog, 3189, 0

Campbell, B., Walker, G. A. H., & Yang, S. 1988, ApJ, 331, 902

Cannon, A. J., & Pickering, E. C. 1901, Ann. Astron. Obs. Harvard Coll., 131, 28(II)

Cardelli, J. A., Clayton, G. C., & Mathis, J. S. 1989, ApJ, 345, 245

Carpenter, J. M. 2001, AJ, 121, 2851

Carpenter, J. M., & Stauffer, J. 2003, fEPS internal report

Carpenter, J. M., Wolf, S., Schreyer, K., Launhardt, R., & Henning, T. 2004, ArXiv Astrophysics e-prints

Carson, J., Eikenberry, S., Brandl, B., Wilson, J. C., & Hayward, T. L. 2003, in IAU Symposium, 271

Carson, J. C., Eikenberry, S. S., Brandl, B. R., Wilson, J. C., & Hayward, T. L. 2004, American Astronomical Society Meeting Abstracts, 205, 0

—. 2005, ArXiv Astrophysics e-prints:astro-ph/0506287

Carter, B. D., Butler, R. P., Tinney, C. G., Jones, H. R. A., Marcy, G. W., McCarthy, C., Fischer, D. A., & Penny, A. J. 2003, ApJ, 593, L43

Cashwell, E. D., & Everett, C. J. 1959, A Practical Manual on the Monte Carlo Method for Random Walk Problems (New York: Pergamon Press, 1959)

Chabrier, G., & Baraffe, I. 1997, A&A, 327, 1039

—. 2000, ARA&A, 38, 337

Chabrier, G., Baraffe, I., Allard, F., & Hauschildt, P. 2000, ApJ, 542, 464

Chauvin, G., Lagrange, A.-M., Dumas, C., Zuckerman, B., Mouillet, D., Song, I., Beuzit, J.-L., & Lowrance, P. 2004, A&A, 425, L29

—. 2005a, A&A, 438, L25

Chauvin, G., Lagrange, A.-M., Zuckerman, B., Dumas, C., Mouillet, D., Song, I., Beuzit, J.-L., Lowrance, P., & Bessell, M. S. 2005b, A&A, 438, L29

Chauvin, G., Thomson, M., Dumas, C., Beuzit, J.-L., Lowrance, P., Fusco, T., Lagrange, A.-M., Zuckerman, B., & Mouillet, D. 2003, A&A, 404, 157

Ciardi, D. R., van Belle, G. T., Akeson, R. L., Thompson, R. R., Lada, E. A., & Howell, S. B. 2001, ApJ, 559, 1147

Clampin, M., Krist, J. E., Ardila, D. R., Golimowski, D. A., Hartig, G. F., Ford, H. C., Illingworth, G. D., Bartko, F., Benítez, N., Blakeslee, J. P., Bouwens, R. J., Broadhurst, T. J., Brown, R. A., Burrows, C. J., Cheng, E. S., Cross, N. J. G., Feldman, P. D., Franx, M., Gronwall, C., Infante, L., Kimble, R. A., Lesser, M. P., Martel, A. R., Menanteau, F., Meurer, G. R., Miley, G. K., Postman, M., Rosati, P., Sirianni, M., Sparks, W. B., Tran, H. D., Tsvetanov, Z. I., White, R. L., & Zheng, W. 2003, AJ, 126, 385

Close, L. M., Lenzen, R., Guirado, J. C., Nielsen, E. L., Mamajek, E. E., Brandner, W., Hartung, M., Lidman, C., & Biller, B. 2005, Nature, 433, 286

Close, L. M., Siegler, N., Freed, M., & Biller, B. 2003, ApJ, 587, 407

Close, L. M. e. a. 2004, in ESO Workshop on Adaptive Optics, ASP, in press, http://exoplanet.as.arizona.edu/ lclose/talks/ins/close1.ps

Cooper, C. S., Sudarsky, D., Milsom, J. A., Lunine, J. I., & Burrows, A. 2003, ApJ, 586, 1320

Couteau, P. 1960, Journal des Observateurs, 43, 41

Cox, A. N. 2000, Allen's astrophysical quantities (4th ed. Publisher: New York: AIP Press; Springer, 2000. Edited by Arthur N. Cox. ISBN: 0387987460)

Crawford, D. L., & Perry, C. L. 1976, AJ, 81, 419

Cutri, R. M., Skrutskie, M. F., van Dyk, S., Beichman, C. A., Carpenter, J. M., Chester, T., Cambresy, L., Evans, T., Fowler, J., Gizis, J., Howard, E., Huchra, J., Jarrett, T., Kopan, E. L., Kirkpatrick, J. D., Light, R. M., Marsh, K. A., McCallon, H., Schneider, S., Stiening, R., Sykes, M., Weinberg, M., Wheaton, W. A., Wheelock, S., & Zacarias, N. 2003, VizieR Online Data Catalog, 2246, 0

Dahn, C. C., Harris, H. C., Vrba, F. J., Guetter, H. H., Canzian, B., Henden, A. A., Levine, S. E., Luginbuhl, C. B., Monet, A. K. B., Monet, D. G., Pier, J. R., Stone, R. C., Walker, R. L., Burgasser, A. J., Gizis, J. E., Kirkpatrick, J. D., Liebert, J., & Reid, I. N. 2002, AJ, 124, 1170

Dannerbauer, H., Lehnert, M. D., Lutz, D., Tacconi, L., Bertoldi, F., Carilli, C., Genzel, R., & Menten, K. 2002, ApJ, 573, 473

D'Antona, F., & Mazzitelli, I. 1997, Memorie della Societa Astronomica Italiana, 68, 807

de La Reza, R., Torres, C. A. O., Quast, G., Castilho, B. V., & Vieira, G. L. 1989, ApJ, 343, L61+

de Zeeuw, P. T., Hoogerwerf, R., de Bruijne, J. H. J., Brown, A. G. A., & Blaauw, A. 1999, AJ, 117, 354

Decin, G., Dominik, C., Waters, L. B. F. M., & Waelkens, C. 2003, ApJ, 598, 636

Delfosse, X., Forveille, T., Ségransan, D., Beuzit, J.-L., Udry, S., Perrier, C., & Mayor, M. 2000, A&A, 364, 217

Dent, W. R. F., Walker, H. J., Holland, W. S., & Greaves, J. S. 2000, MNRAS, 314, 702

Devillard, N. 2001, in ASP Conf. Ser. 238: Astronomical Data Analysis Software and Systems X, 525–+

Diolaiti, E., Bendinelli, O., Bonaccini, D., Close, L., Currie, D., & Parmeggiani, G. 2000, A&AS, 147, 335

Divine, N. 1993, J. Geophys. Res., 98, 17029

Donahue, R. A. 1993, Ph.D. Thesis, New Mexico State University, University Park, New Mexico

Donahue, R. A. 1998, in ASP Conf. Ser. 154: Cool Stars, Stellar Systems, and the Sun, 1235–+

Donnison, J. R., & Mikulskis, D. F. 1995, MNRAS, 272, 1

Dorren, J. D., & Guinan, E. F. 1994, ApJ, 428, 805

Draine, B. T., & Lee, H. M. 1984, ApJ, 285, 89

Draine, B. T., & Malhotra, S. 1993, ApJ, 414, 632

Drilling, J. S., & Landolt, A. U. 2000, in Allen's Astrophysical Quantities, ed. A. Cox, 4th edn. (New York: Springer), 382

Duncan, D. K. 1981, ApJ, 248, 651

Duncan, D. K., & Jones, B. F. 1983, ApJ, 271, 663

Duquennoy, A., & Mayor, M. 1991, A&A, 248, 485

Eggen, O. J. 1965, ARA&A, 3, 235

—. 1996, AJ, 111, 466

Els, S. G., Sterzik, M. F., Marchis, F., Pantin, E., Endl, M., & Kürster, M. 2001, A&A, 370, L1

Endl, M., Hatzes, A. P., Cochran, W. D., McArthur, B., Allende Prieto, C., Paulson, D. B., Guenther, E., & Bedalov, A. 2004, ApJ, 611, 1121

EROS Collaboration, Goldman, B., Delfosse, X., Forveille, T., Afonso, C., Alard, C., Albert, J. N., Andersen, J., Ansari, R., Aubourg, É., Bareyre, P., Bauer, F., Beaulieu, J. P., Borsenberger, J., Bouquet, A., Char, S., Charlot, X., Couchot, F., Coutures, C., Derue, F., Ferlet, R., Fouqué, P., Glicenstein, J. F., Gould, A., Graff, D., Gros, M., Haissinski, J., Hamilton, J. C., Hardin, D., de Kat, J., Kim, A., Lasserre, T., Lesquoy, É., Loup, C., Magneville, C., Mansoux, B., Marquette, J. B., Martín, E. L., Maurice, É., Milsztajn, A., Moniez, M.,

Palanque-Delabrouille, N., Perdereau, O., Prévot, L., Regnault, N., Rich, J., Spiro, M., Vidal-Madjar, A., Vigroux, L., & Zylberajch, S. 1999, A&A, 351, L5

Fabricius, C., & Makarov, V. V. 2000, A&A, 356, 141

Farihi, J., Becklin, E. E., & Zuckerman, B. 2005, ArXiv Astrophysics e-prints:astro-ph/0506017

Fischer, D. A. 1998, Ph.D. Thesis, University of California, Santa Cruz, California

Fischer, D. A., & Marcy, G. W. 1992, ApJ, 396, 178

Fischer, D. A., Marcy, G. W., Butler, R. P., Vogt, S. S., Walp, B., & Apps, K. 2002, PASP, 114, 529

Fleming, T. A. 1998, ApJ, 504, 461

Fleming, T. A., Schmitt, J. H. M. M., & Giampapa, M. S. 1995, ApJ, 450, 401

Freeman, P. E., Kashyap, V., Rosner, R., & Lamb, D. Q. 2002, ApJS, 138, 185

Frink, S., Röser, S., Neuhäuser, R., & Sterzik, M. F. 1997, A&A, 325, 613

Gaidos, E. J. 1998, PASP, 110, 1259

Gatewood, G., & de Jonge, J. K. 1995, ApJ, 450, 364

Geballe, T. R., Knapp, G. R., Leggett, S. K., Fan, X., Golimowski, D. A., Anderson, S., Brinkmann, J., Csabai, I., Gunn, J. E., Hawley, S. L., Hennessy, G., Henry, T. J., Hill, G. J., Hindsley, R. B., Ivezić, Ž., Lupton, R. H., McDaniel, A., Munn, J. A., Narayanan, V. K., Peng, E., Pier, J. R., Rockosi, C. M., Schneider, D. P., Smith, J. A., Strauss, M. A., Tsvetanov, Z. I., Uomoto, A., York, D. G., & Zheng, W. 2002, ApJ, 564, 466

Gelino, C. R., Kirkpatrick, J. D., & Burgasser, A. J. 2004, American Astronomical Society Meeting Abstracts, 205, 0

Ghez, A. M., McCarthy, D. W., Patience, J. L., & Beck, T. L. 1997, ApJ, 481, 378

Ghez, A. M., Neugebauer, G., & Matthews, K. 1993, AJ, 106, 2005

Gizis, J. E., Kirkpatrick, J. D., Burgasser, A., Reid, I. N., Monet, D. G., Liebert, J., & Wilson, J. C. 2001, ApJ, 551, L163

Gizis, J. E., Reid, I. N., & Hawley, S. L. 2002, AJ, 123, 3356

Gliese, W., & Jahreiß, H. 1991, Preliminary Version of the Third Catalogue of Nearby Stars, Tech. rep., Astronomisches Rechen-Institut, Heidelberg, Germany

Goldader, J. D., Meurer, G., Heckman, T. M., Seibert, M., Sanders, D. B., Calzetti, D., & Steidel, C. C. 2002, ApJ, 568, 651

Golimowski, D. A., Durrance, S. T., & Clampin, M. 1993, ApJ, 411, L41

Golimowski, D. A., Leggett, S. K., Marley, M. S., Fan, X., Geballe, T. R., Knapp, G. R., Vrba, F. J., Henden, A. A., Luginbuhl, C. B., Guetter, H. H., Munn, J. A., Canzian, B., Zheng, W., Tsvetanov, Z. I., Chiu, K., Glazebrook, K., Hoversten, E. A., Schneider, D. P., & Brinkmann, J. 2004, AJ, 127, 3516

Gorkavyi, N. N., Ozernoy, L. M., Mather, J. C., & Taidakova, T. 1997, ApJ, 488, 268

Gorkavyi, N. N., & Taidakova, T. A. 2001, Bulletin of the American Astronomical Society, 33, 1431

Gorlova, N., Padgett, D. L., Rieke, G. H., Muzerolle, J., Morrison, J. E., Gordon, K. D., Engelbracht, C. W., Hines, D. C., Hinz, J. C., Noriega-Crespo, A., Rebull, L., Stansberry, J. A., Stapelfeldt, K. R., Su, K. Y. L., & Young, E. T. 2004, ApJS, 154, 448

Gorlova, N. I., Meyer, M. R., Rieke, G. H., & Liebert, J. 2003, ApJ, 593, 1074

Gray, R. O. 1992, A&A, 265, 704

Greaves, J. S., Holland, W. S., Moriarty-Schieven, G., Jenness, T., Dent, W. R. F., Zuckerman, B., McCarthy, C., Webb, R. A., Butner, H. M., Gear, W. K., & Walker, H. J. 1998, ApJ, 506, L133

Green, P. J., Ali, B., & Napiwotzki, R. 2000, ApJ, 540, 992

Gulliver, A. F., Hill, G., & Adelman, S. J. 1994, ApJ, 429, L81

Habing, H. J., Dominik, C., Jourdain de Muizon, M., Laureijs, R. J., Kessler, M. F., Leech, K., Metcalfe, L., Salama, A., Siebenmorgen, R., Trams, N., & Bouchet, P. 2001, A&A, 365, 545

Hale, A. 1994, AJ, 107, 306

Harper, D. A., Loewenstein, R. F., & Davidson, J. A. 1984, ApJ, 285, 808

Hartkopf, W. I., & Mason, B. D. 2000, in IAU Commission on Double Stars, 1–2

Hartkopf, W. I., & Mason, B. D. 2003, http://ad.usno.navy.mil/wds/orb6/orb6c.html

—. 2005, http://ad.usno.navy.mil/wds/orb6.html

Hartkopf, W. I., Mason, B. D., & McAlister, H. A. 1996, AJ, 111, 370

Hartkopf, W. I., Mason, B. D., & Worley, C. E. 2001, AJ, 122, 3472

Harvey, P. M., Wilking, B. A., & Joy, M. 1984, Nature, 307, 441

Hauschildt, P. H., Allard, F., & Baron, E. 1999, ApJ, 512, 377

Hayashi, C., & Nakano, T. 1963, Prog. Theo. Physics, 30, 4

Hayward, T. L., Brandl, B., Pirger, B., Blacken, C., Gull, G. E., Schoenwald, J., & Houck, J. R. 2001, PASP, 113, 105

Heap, S. R., Lindler, D. J., Lanz, T. M., Cornett, R. H., Hubeny, I., Maran, S. P., & Woodgate, B. 2000, ApJ, 539, 435

Heckmann, O., Dieckvoss, W., & Kox, H. 1956, Astronomische Nachrichten, 283, 109

Heinrichsen, I., Walker, H. J., & Klaas, U. 1998, MNRAS, 293, L78

Heintz, W. D. 1978, Geophysics and Astrophysics Monographs, 15

Henry, T. J., Soderblom, D. R., Donahue, R. A., & Baliunas, S. L. 1996, AJ, 111, 439

Herbig, G. H. 1965, ApJ, 141, 588

Hertzspring, E. 1947, Annalen van de Sterrewacht te Leiden, 19, 1

Hillenbrand, L. A., Mamajek, E. E., Stauffer, J. R., Soderblom, D. R., & Meyer, M. R. 2005, ApJ, submitted

Hillenbrand, L. A., & White, R. J. 2004, ApJ, 604, 741

Hines, D., Carpenter, J. M., Bouwman, J., Kim, J. S., Silverstone, M. D., Pascucci, I., Meyer, M. R., Cohen, M., Stauffer, J. R., Stobie, B., & Watson, D. M. 2005, FEPS Data Explanatory Supplement, v. 2.0, Tech. rep., *Spitzer* Science Center, California Institute of Technology, http://data.spitzer.caltech.edu/popular/feps/20050608_enhanced_v1/Documents/FEPS_Data_Explan_S

Høg, E., Fabricius, C., Makarov, V. V., Urban, S., Corbin, T., Wycoff, G., Bastian, U., Schwekendiek, P., & Wicenec, A. 2000, A&A, 355, L27

Holland, W. S., Greaves, J. S., Dent, W. R. F., Wyatt, M. C., Zuckerman, B., Webb, R. A., McCarthy, C., Coulson, I. M., Robson, E. I., & Gear, W. K. 2003, ApJ, 582, 1141

Holland, W. S., Greaves, J. S., Zuckerman, B., Webb, R. A., McCarthy, C., Coulson, I. M., Walther, D. M., Dent, W. R. F., Gear, W. K., & Robson, I. 1998, Nature, 392, 788

Hollenbach, D., Gorti, U., Meyer, M., Kim, J. S., Morris, P., Najita, J., Pascucci, I., Carpenter, J., Rodmann, J., Brooke, T., Hillenbrand, L., Mamajek, E., Padgett, D., Soderblom, D., Wolf, S., & Lunine, J. 2005, ArXiv Astrophysics e-prints:astro-ph/0506252

Houdashelt, M. L., Bell, R. A., & Sweigart, A. V. 2000, AJ, 119, 1448

Jayawardhana, R., & Brandeker, A. 2001, ApJ, 561, L111

Jefferies, S. M., & Christou, J. C. 1993, ApJ, 415, 862

Jeffries, R. D. 1995, MNRAS, 273, 559

Johnson, D. R. H., & Soderblom, D. R. 1987, AJ, 93, 864

Johnson, H. L., & Mitchell, R. I. 1958, ApJ, 128, 31

Jones, H. R. A., Paul Butler, R., Tinney, C. G., Marcy, G. W., Penny, A. J., McCarthy, C., Carter, B. D., & Pourbaix, D. 2002, MNRAS, 333, 871

König, B., Guenther, E. W., Woitas, J., & Hatzes, A. P. 2005, A&A, 435, 215

Kalas, P., Deltorn, J., & Larwood, J. 2001, ApJ, 553, 410

Kalas, P., Graham, J. R., & Clampin, M. 2005, Nature, 435, 1067

Kalas, P., & Jewitt, D. 1996, AJ, 111, 1347

Kalas, P., Larwood, J., Smith, B. A., & Schultz, A. 2000, ApJ, 530, L133

Kalas, P., Liu, M. C., & Matthews, B. C. 2004, Science, 303, 1990

Kasdin, N. J., Vanderbei, R. J., Spergel, D. N., & Littman, M. G. 2003, ApJ, 582, 1147

Kastner, J. H., Zuckerman, B., Weintraub, D. A., & Forveille, T. 1997, Science, 277, 67

Keenan, P. C. 1983, Bulletin d'Information du Centre de Donnees Stellaires, 24, 19

Kendall, M., & Stuart, A. 1977, The advanced theory of statistics. Vol.1: Distribution theory (London: Griffin, 1977, 4th ed.)

Kenyon, S. J., & Bromley, B. C. 2002, AJ, 123, 1757

—. 2004, AJ, 127, 513

Kenyon, S. J., Dobrzycka, D., & Hartmann, L. 1994, AJ, 108, 1872

Kenyon, S. J., Wood, K., Whitney, B. A., & Wolff, M. J. 1999, ApJ, 524, L119

King, J. R., Villarreal, A. R., Soderblom, D. R., Gulliver, A. F., & Adelman, S. J. 2003, AJ, 125, 1980

Kirkpatrick, J. D., Dahn, C. C., Monet, D. G., Reid, I. N., Gizis, J. E., Liebert, J., & Burgasser, A. J. 2001, AJ, 121, 3235

Kirkpatrick, J. D., Reid, I. N., Liebert, J., Cutri, R. M., Nelson, B., Beichman, C. A., Dahn, C. C., Monet, D. G., Gizis, J. E., & Skrutskie, M. F. 1999, ApJ, 519, 802

Kirkpatrick, J. D., Reid, I. N., Liebert, J., Gizis, J. E., Burgasser, A. J., Monet, D. G., Dahn, C. C., Nelson, B., & Williams, R. J. 2000, AJ, 120, 447

Klaas, U., Haas, M., Müller, S. A. H., Chini, R., Schulz, B., Coulson, I., Hippelein, H., Wilke, K., Albrecht, M., & Lemke, D. 2001, A&A, 379, 823

Kleinmann, S. G., & Hall, D. N. B. 1986, ApJS, 62, 501

Koerner, D. W., Sargent, A. I., & Ostroff, N. A. 2001, ApJ, 560, L181

Kohler, R., & Leinert, C. 1998, A&A, 331, 977

Kouwenhoven, M. B. N., Brown, A. G. A., Zinnecker, H., Kaper, L., & Portegies Zwart, S. F. 2005, A&A, 430, 137

Krist, J. E., Ardila, D. R., Golimowski, D. A., Clampin, M., Ford, H. C., Illingworth, G. D., Hartig, G. F., Bartko, F., Benítez, N., Blakeslee, J. P., Bouwens, R. J., Bradley, L. D., Broadhurst, T. J., Brown, R. A., Burrows, C. J., Cheng, E. S., Cross, N. J. G., Demarco, R., Feldman, P. D., Franx, M., Goto, T., Gronwall, C., Holden, B., Homeier, N., Infante, L., Kimble, R. A., Lesser, M. P., Martel, A. R., Mei, S., Menanteau, F., Meurer, G. R., Miley, G. K., Motta, V., Postman, M., Rosati, P., Sirianni, M., Sparks, W. B., Tran, H. D., Tsvetanov, Z. I., White, R. L., & Zheng, W. 2005, AJ, 129, 1008

Krist, J. E., Stapelfeldt, K. R., Ménard, F., Padgett, D. L., & Burrows, C. J. 2000, ApJ, 538, 793

Kuchner, M. J., Brown, M. E., & Koresko, C. D. 1998, PASP, 110, 1336

Kuhn, J. R., Potter, D., & Parise, B. 2001, ApJ, 553, L189

Kuiper, G. P. 1935a, PASP, 47, 15

—. 1935b, PASP, 47, 121

Kumar, S. S. 1963, ApJ, 137, 1121

Lachaume, R., Dominik, C., Lanz, T., & Habing, H. J. 1999, A&A, 348, 897

Lane, B. F., Zapatero Osorio, M. R., Britton, M. C., Martín, E. L., & Kulkarni, S. R. 2001, ApJ, 560, 390

Laureijs, R. J., Jourdain de Muizon, M., Leech, K., Siebenmorgen, R., Dominik, C., Habing, H. J., Trams, N., & Kessler, M. F. 2002, A&A, 387, 285

Lecavelier des Etangs, A., Vidal-Madjar, A., & Ferlet, R. 1996, A&A, 307, 542

Leggett, S. K. 1992, ApJS, 82, 351

Leggett, S. K., Allard, F., Geballe, T. R., Hauschildt, P. H., & Schweitzer, A. 2001, ApJ, 548, 908

Leggett, S. K., Golimowski, D. A., Fan, X., Geballe, T. R., Knapp, G. R., Brinkmann, J., Csabai, I., Gunn, J. E., Hawley, S. L., Henry, T. J., Hindsley, R., Ivezić, Ž., Lupton, R. H., Pier, J. R., Schneider, D. P., Smith, J. A., Strauss, M. A., Uomoto, A., & York, D. G. 2002, ApJ, 564, 452

Leggett, S. K., Toomey, D. W., Geballe, T. R., & Brown, R. H. 1999, ApJ, 517, L139

Leinert, C., Röser, S., & Buitrago, J. 1983, A&A, 118, 345

Leinert, C., Zinnecker, H., Weitzel, N., Christou, J., Ridgway, S. T., Jameson, R., Haas, M., & Lenzen, R. 1993, A&A, 278, 129

Lindegren, L. 1997, The Hipparcos and Tycho Catalogues, Vol. 1 (ESA. Edited by M. A. C. Perryman. ESA SP–1200), 87–102

Liou, J., & Zook, H. A. 1997, Icarus, 128, 354

—. 1999, AJ, 118, 580

Lissauer, J. J. 1993, ARA&A, 31, 129

Liu, M. C. 2004, Science, 305, 1442

Liu, M. C., Fischer, D. A., Graham, J. R., Lloyd, J. P., Marcy, G. W., & Butler, R. P. 2002, ApJ, 571, 519

Liu, M. C., Matthews, B. C., Williams, J. P., & Kalas, P. G. 2004, ApJ, 608, 526

López Martí, B., Eislöffel, J., Scholz, A., & Mundt, R. 2004, A&A, 416, 555

Lowrance, P. J. Becklin, E. E., Schneider, G., Kirkpatrick, J. D., Weinberger, A. J., Zuckerman, B., Dumas, C., Beuzit, J. L., Plait, P., Malmuth, E. M., Heap, S. R., Terrile, R. J., & Hines, D. C. 2005, ArXiv Astrophysics e-prints:astro-ph/0506358

Lowrance, P. J. 2001, Ph.D. Thesis, University of California, Los Angeles, California

Lowrance, P. J., McCarthy, C., Becklin, E. E., Zuckerman, B., Schneider, G., Webb, R. A., Hines, D. C., Kirkpatrick, J. D., Koerner, D. W., Low, F., Meier, R., Rieke, M., Smith, B. A., Terrile, R. J., & Thompson, R. I. 1999, ApJ, 512, L69

Lowrance, P. J., Schneider, G., Kirkpatrick, J. D., Becklin, E. E., Weinberger, A. J., Zuckerman, B., Plait, P., Malmuth, E. M., Heap, S. R., Schultz, A., Smith, B. A., Terrile, R. J., & Hines, D. C. 2000, ApJ, 541, 390

Lowrance, P. J., The Nicmos Environments Of Nearby Stars Team, & STIS 8176 Team. 2003, in IAU Symposium, 295

Lucas, P. W., Roche, P. F., Allard, F., & Hauschildt, P. H. 2001, MNRAS, 326, 695

Luhman, K. L. 2004, ApJ, 614, 398

Luhman, K. L., Briceño, C., Stauffer, J. R., Hartmann, L., Barrado y Navascués, D., & Caldwell, N. 2003a, ApJ, 590, 348

Luhman, K. L., & Jayawardhana, R. 2002, ApJ, 566, 1132

Luhman, K. L., Stauffer, J. R., & Mamajek, E. E. 2005, ApJ, 628, L69

Luhman, K. L., Stauffer, J. R., Muench, A. A., Rieke, G. H., Lada, E. A., Bouvier, J., & Lada, C. J. 2003b, ApJ, 593, 1093

Luyten, W. 1980, NLTT catalogue. Vol.3: 0 deg. to -10 deg. (Minneapolis: University of Minnesota, 1980)

Luyten, W. J. 1963, in Bruce proper motion survey. The general catalogue (vol 1,2). (1963), 0–+

Lyra, W., & Porto de Mello, G. F. 2005, A&A, 431, 329

Mamajek, E. E. 2004, Ph.D. Thesis, University of Arizona, Tucson, Arizona

Mamajek, E. E., Lawson, W. A., & Feigelson, E. D. 1999, ApJ, 516, L77

Mamajek, E. E., Meyer, M. R., & Liebert, J. 2002, AJ, 124, 1670

Mannings, V., & Barlow, M. J. 1998, ApJ, 497, 330

Marcy, G. W., & Benitz, K. J. 1989, ApJ, 344, 441

Marcy, G. W., & Butler, R. P. 1998, ARA&A, 36, 57

—. 2000, PASP, 112, 137

Marcy, G. W., Butler, R. P., Fischer, D. A., & Vogt, S. S. 2003, in ASP Conf. Ser. 294: Scientific Frontiers in Research on Extrasolar Planets, 1–58381

Marois, C., Doyon, R., Nadeau, D., Racine, R., Riopel, M., Vallée, P., & Lafrenière, D. 2005, PASP, 117, 745

Martin, E. L., Brandner, W., & Basri, G. 1999, Science, 283, 1718

Masciadri, E., Mundt, R., Henning, T., Alvarez, C., & Barrado y Navascués, D. 2005, ApJ, 625, 1004

Mason, B. D., Douglass, G. G., & Hartkopf, W. I. 1999, AJ, 117, 1023

Mason, B. D., Hartkopf, W. I., Wycoff, G. L., Pascu, D., Urban, S. E., Hall, D. M., Hennessy, G. S., Rafferty, T. J., Flagg, L., Kang, D., Ries, P., & Holdenried, E. 2004a, AJ, 127, 539

Mason, B. D., Hartkopf, W. I., Wycoff, G. L., Rafferty, T. J., Urban, S. E., & Flagg, L. 2004b, AJ, 128, 3012

Mason, B. D., Wycoff, G. L., Hartkopf, W. I., Douglass, G. G., & Worley, C. E. 2001, AJ, 122, 3466

Mathis, J. S. 1990, ARA&A, 28, 37

Mathis, J. S., Rumpl, W., & Nordsieck, K. H. 1977, ApJ, 217, 425

Mayor, M., & Queloz, D. 1995, Nature, 378, 355

Mazeh, T., Simon, M., Prato, L., Markus, B., & Zucker, S. 2003, ApJ, 599, 1344

McCarthy, C. 2001, Ph.D. Thesis, University of California, Los Angeles, California

McCarthy, C., & Zuckerman, B. 2004, AJ, 127, 2871

McCaughrean, M., Read, I. N., Tinney, C., Kirkpatrick, J. D., Hillenbrand, L. A., Burgasser, A. J., Gizis, J. E., & Hawley, S. L. 2001, Science, 291, 1487

McGovern, M. R., Kirkpatrick, J. D., McLean, I. S., Burgasser, A. J., Prato, L., & Lowrance, P. J. 2004, ApJ, 600, 1020

McLean, I. S., McGovern, M. R., Burgasser, A. J., Kirkpatrick, J. D., Prato, L., & Kim, S. S. 2003, ApJ, 596, 561

Mermilliod, J. C. 1981, A&A, 97, 235

Metchev, S. A. 2003, Pixel Scale and Orientation of PHARO. II., Tech. rep., California Institute of Technology, http://www.astro.caltech.edu/~metchev/AO/pharo_plate_scale_memo2.pdf

Metchev, S. A., Eisner, J. A., Hillenbrand, L. A., & Wolf, S. 2005, ApJ, 622, 451

Metchev, S. A., & Hillenbrand, L. A. 2004, ApJ, 617, 1330

Metchev, S. A., Hillenbrand, L. A., & Meyer, M. 2002, American Astronomical Society Meeting, 200, 0

Metchev, S. A., Hillenbrand, L. A., & White, R. J. 2003, ApJ, 582, 1102

Meyer, M. R., Hillenbrand, L. A., Backman, D. E., Beckwith, S. V. W., Bouwman, J., Brooke, T. Y., Carpenter, J. M., Cohen, M., Gorti, U., Henning, T., Hines, D. C., Hollenbach, D., Kim, J. S., Lunine, J., Malhotra, R., Mamajek, E. E., Metchev, S., Moro-Martin, A., Morris, P., Najita, J., Padgett, D. L., Rodmann, J., Silverstone, M. D., Soderblom, D. R., Stauffer, J. R., Stobie, E. B., Strom, S. E., Watson, D. M., Weidenschilling, S. J., Wolf, S., & Young, E. 2005, PASP, submitted

Meyer, M. R., Hillenbrand, L. A., Backman, D. E., Beckwith, S. V. W., Bouwman, J., Brooke, T. Y., Carpenter, J. M., Cohen, M., Gorti, U., Henning, T., Hines, D. C., Hollenbach, D., Kim, J. S., Lunine, J., Malhotra, R., Mamajek, E. E., Metchev, S., Moro-Martin, A., Morris, P., Najita, J., Padgett, D. L., Rodmann, J., Silverstone, M. D., Soderblom, D. R., Stauffer, J. R., Stobie, E. B., Strom, S. E., Watson, D. M., Weidenschilling, S. J., Wolf, S., Young, E., Engelbracht,

C. W., Gordon, K. D., Misselt, K., Morrison, J., Muzerolle, J., & Su, K. 2004, ApJS, 154, 422

Mohanty, S., Jayawardhana, R., & Basri, G. 2004, ApJ, 609, 885

Mohler, O. 1955, A Table of Solar Spectrum Wave Lengths, 11984A to 25578A (Ann Arbor, University of Michigan Press, 1955)

Montes, D., López-Santiago, J., Fernández-Figueroa, M. J., & Gálvez, M. C. 2001a, A&A, 379, 976

Montes, D., López-Santiago, J., Gálvez, M. C., Fernández-Figueroa, M. J., De Castro, E., & Cornide, M. 2001b, MNRAS, 328, 45

Morbey, C. L. 1975, PASP, 87, 689

Morgan, W. W., Keenan, P. C., & Kellman, E. 1943, An atlas of stellar spectra, with an outline of spectral classification (Chicago, Ill., The University of Chicago press)

Moro-Martín, A., & Malhotra, R. 2002, AJ, 124, 2305

Mouillet, D., Lagrange, A.-M., Beuzit, J.-L., & Renaud, N. 1997, A&A, 324, 1083

Mugrauer, M., & Neuhäuser, R. 2005, MNRAS, 361, L15

Mugrauer, M., Neuhäuser, R., Guenther, E. W., Hatzes, A. P., Huélamo, N., Fernández, M., Ammler, M., Retzlaff, J., König, B., Charbonneau, D., Jayawardhana, R., & Brandner, W. 2004, A&A, 417, 1031

Munari, U., Dallaporta, S., Siviero, A., Soubiran, C., Fiorucci, M., & Girard, P. 2004, A&A, 418, L31

Myers, P. C., Fuller, G. A., Mathieu, R. D., Beichman, C. A., Benson, P. J., Schild, R. E., & Emerson, J. P. 1987, ApJ, 319, 340

Naef, D., Mayor, M., Beuzit, J. L., Perrier, C., Queloz, D., Sivan, J. P., & Udry, S. 2004, A&A, 414, 351

Nakajima, T., Oppenheimer, B. R., Kulkarni, S. R., Golimowski, D. A., Matthews, K., & Durrance, S. T. 1995, Nature, 378, 463

Nakano, T. 1990, ApJ, 355, L43

Neuhäuser, R., & Guenther, E. W. 2004, A&A, 420, 647

Neuhäuser, R., Guenther, E. W., Alves, J., Huélamo, N., Ott, T., & Eckart, A. 2003, Astronomische Nachrichten, 324, 535

Neuhäuser, R., Guenther, E. W., Wuchterl, G., Mugrauer, M., Bedalov, A., & Hauschildt, P. H. 2005, A&A, 435, L13

Neuhäuser, R., Sterzik, M. F., Torres, G., & Martin, E. L. 1995, A&A, 299, L13+

Noyes, R. W., Hartmann, L. W., Baliunas, S. L., Duncan, D. K., & Vaughan, A. H. 1984, ApJ, 279, 763

Oppenheimer, B. R. 1999, Ph.D. Thesis, California Institute of Technology, Pasadena, California

Oppenheimer, B. R., Dekany, R. G., Hayward, T. L., Brandl, B., Troy, M., & Bloemhof, E. E. 2000a, in Proc. SPIE Vol. 4007, p. 899-905, Adaptive Optical Systems Technology, Peter L. Wizinowich; Ed., 899–905

Oppenheimer, B. R., Golimowski, D. A., Kulkarni, S. R., Matthews, K., Nakajima, T., Creech-Eakman, M., & Durrance, S. T. 2001, AJ, 121, 2189

Oppenheimer, B. R., Kulkarni, S. R., Matthews, K., & Nakajima, T. 1995, Science, 270, 1478

Oppenheimer, B. R., Kulkarni, S. R., & Stauffer, J. R. 2000b, Protostars and Planets IV, 1313

Ozernoy, L. M., Gorkavyi, N. N., Mather, J. C., & Taidakova, T. A. 2000, ApJ, 537, L147

Padoan, P., & Nordlund, Å. 2004, ApJ, 617, 559

Pan, X., Shao, M., & Kulkarni, S. R. 2004, Nature, 427, 326

Pantin, E., Lagage, P. O., & Artymowicz, P. 1997, A&A, 327, 1123

Pantin, E., Waelkens, C., & Lagage, P. O. 2000, A&A, 361, L9

Papoulis, A. 1984, Probability, Random Variables, and Stochastic Processes (New York: McGraw–Hill, 1984)

Patience, J., Ghez, A. M., Reid, I. N., & Matthews, K. 2002, AJ, 123, 1570

Patience, J., Ghez, A. M., Reid, I. N., Weinberger, A. J., & Matthews, K. 1998, AJ, 115, 1972

Perryman, M. A. C., Brown, A. G. A., Lebreton, Y., Gomez, A., Turon, C., de Strobel, G. C., Mermilliod, J. C., Robichon, N., Kovalevsky, J., & Crifo, F. 1998, A&A, 331, 81

Perryman, M. A. C., Lindegren, L., Kovalevsky, J., Hoeg, E., Bastian, U., Bernacca, P. L., Crézé, M., Donati, F., Grenon, M., van Leeuwen, F., van der Marel, H., Mignard, F., Murray, C. A., Le Poole, R. S., Schrijver, H., Turon, C., Arenou, F., Froeschlé, M., & Petersen, C. S. 1997, A&A, 323, L49

Pinsonneault, M. H., Stauffer, J., Soderblom, D. R., King, J. R., & Hanson, R. B. 1998, ApJ, 504, 170

Plavchan, P., Jura, M., & Lipscy, S. J. 2005, submitted

Potter, D., Martín, E. L., Cushing, M. C., Baudoz, P., Brandner, W., Guyon, O., & Neuhäuser, R. 2002, ApJ, 567, L133

Pounds, K. A., Allan, D. J., Barber, C., Barstow, M. A., Bertram, D., Branduardi-Raymont, G., Brebner, G. E. C., Buckley, D., Bromage, G. E., Cole, R. E., Courtier, M., Cruise, A. M., Culhane, J. L., Denby, M., Donoghue, D. O., Dunford, E., Georgantopoulos, I., Goodall, C. V., Gondhalekar, P. M., Gourlay, J. A., Harris, A. W., Hassall, B. J. M., Hellier, C., Hodgkin, S., Jeffries, R. D.,

Kellett, B. J., Kent, B. J., Lieu, R., Lloyd, C., McGale, P., Mason, K. O., Matthews, L., Mittaz, J. P. D., Page, C. G., Pankiewicz, G. S., Pike, C. D., Ponman, T. J., Puchnarewicz, E. M., Pye, J. P., Quenby, J. J., Ricketts, M. J., Rosen, S. R., Sansom, A. E., Sembay, S., Sidher, S., Sims, M. R., Stewart, B. C., Sumner, T. J., Vallance, R. J., Watson, M. G., Warwick, R. S., Wells, A. A., Willingale, R., Willmore, A. P., Willoughby, G. A., & Wonnacott, D. 1993, MNRAS, 260, 77

Pourbaix, D. 2000, A&AS, 145, 215

Prato, L., Simon, M., Mazeh, T., McLean, I. S., Norman, D., & Zucker, S. 2002, ApJ, 569, 863

Pravdo, S. H., Shaklan, S. B., & Lloyd, J. 2005, ArXiv Astrophysics e-prints:astro-ph/0505205

Preibisch, T., Brown, A. G. A., Bridges, T., Guenther, E., & Zinnecker, H. 2002, AJ, 124, 404

Preibisch, T., & Zinnecker, H. 1999, AJ, 117, 2381

Press, W. H., Teukolsky, S. A., Vetterling, W. T., & Flannery, B. P. 1992, Numerical recipes in C. The art of scientific computing (Cambridge: University Press, —c1992, 2nd ed.)

Prosser, C. F. 1992, AJ, 103, 488

Pye, J. P., McGale, P. A., Allan, D. J., Barber, C. R., Bertram, D., Denby, M., Page, C. G., Ricketts, M. J., Stewart, B. C., & West, R. G. 1995, MNRAS, 274, 1165

Quillen, A. C., & Thorndike, S. 2002, ApJ, 578, L149

Racine, R., Walker, G. A. H., Nadeau, D., Doyon, R., & Marois, C. 1999, PASP, 111, 587

Rainwater, L. J., & Wu, C. S. 1947, Nucleonics, 1, 60

Randich, S. 2000, in ASP Conf. Ser. 198: Stellar Clusters and Associations: Convection, Rotation, and Dynamos, 401

Reach, W. T., Franz, B. A., Weiland, J. L., Hauser, M. G., Kelsall, T. N., Wright, E. L., Rawley, G., Stemwedel, S. W., & Spiesman, W. J. 1995, Nature, 374, 521

Rebolo, R., Zapatero Osorio, M. R., Madruga, S., Bejar, V. J. S., Arribas, S., & Licandro, J. 1998, Science, 282, 1309

Reid, I. N., Cruz, K. L., Allen, P., Mungall, F., Kilkenny, D., Liebert, J., Hawley, S. L., Fraser, O. J., Covey, K. R., Lowrance, P., Kirkpatrick, J. D., & Burgasser, A. J. 2004, AJ, 128, 463

Reid, I. N., Cruz, K. L., Laurie, S. P., Liebert, J., Dahn, C. C., Harris, H. C., Guetter, H. H., Stone, R. C., Canzian, B., Luginbuhl, C. B., Levine, S. E., Monet, A. K. B., & Monet, D. G. 2003, AJ, 125, 354

Reid, I. N., Gizis, J. E., Kirkpatrick, J. D., & Koerner, D. W. 2001, AJ, 121, 489

Reid, I. N., Hawley, S. L., & Gizis, J. E. 1995, AJ, 110, 1838

Roberge, A., Weinberger, A. J., & Feldman, P. D. 2004, in Dust Disks and the Formation, Evolution and Detection of Habitable Planets. The Second TPF/Darwin International Conference, http://planetquest1.jpl.nasa.gov/TPFDarwinConf/index.cfm

Robichon, N., Arenou, F., Mermilliod, J.-C., & Turon, C. 1999, A&A, 345, 471

Rocha-Pinto, H. J., Maciel, W. J., Scalo, J., & Flynn, C. 2000a, A&A, 358, 850

Rocha-Pinto, H. J., Scalo, J., Maciel, W. J., & Flynn, C. 2000b, A&A, 358, 869

Roddier, F. 1999, Adaptive optics in astronomy (Adaptive Optics in Astronomy)

Roques, F., Scholl, H., Sicardy, B., & Smith, B. A. 1994, Icarus, 108, 37

Rousset, G., Lacombe, F., Puget, P., Gendron, E., Arsenault, R., Kern, P. Y., Rabaud, D., Madec, P., Hubin, N. N., Zins, G., Stadler, E., Charton, J., Gigan,

P., & Feautrier, P. 2000, in Proc. SPIE Vol. 4007, p. 72-81, Adaptive Optical Systems Technology, Peter L. Wizinowich; Ed., 72–81

Rucinski, S. M., & Krautter, J. 1983, A&A, 121, 217

Scardia, M. 1979, Astronomische Nachrichten, 300, 307

Schneider, G., Smith, B. A., Becklin, E. E., Koerner, D. W., Meier, R., Hines, D. C., Lowrance, P. J., Terrile, R. J., Thompson, R. I., & Rieke, M. 1999, ApJ, 513, L127

Schroeder, D. J., Golimowski, D. A., Brukardt, R. A., Burrows, C. J., Caldwell, J. J., Fastie, W. G., Ford, H. C., Hesman, B., Kletskin, I., Krist, J. E., Royle, P., & Zubrowski, R. A. 2000, AJ, 119, 906

Seifahrt, A., Neuhäuser, R., & Mugrauer, M. 2004, A&A, 421, 255

Shatsky, N., & Tokovinin, A. 2002, A&A, 382, 92

Sheret, I., Dent, W. R. F., & Wyatt, M. C. 2004, MNRAS, 348, 1282

Siegler, N., Close, L. M., & Freed, M. E. 2003, in Adaptive Optical System Technologies II. Edited by Wizinowich, Peter L.; Bonaccini, Domenico. Proceedings of the SPIE, Volume 4839, 114–120

Silverstone, M. D. 2000, Ph.D. Thesis, University of California, Los Angeles, California

Silverstone, M. D., Schneider, G., & Smith, B. A. 2002, Bulletin of the American Astronomical Society, 34, 770

Simon, M., Ghez, A. M., Leinert, C., Cassar, L., Chen, W. P., Howell, R. R., Jameson, R. F., Matthews, K., Neugebauer, G., & Richichi, A. 1995, ApJ, 443, 625

Simon, T., Herbig, G., & Boesgaard, A. M. 1985, ApJ, 293, 551

Sivaramakrishnan, A., Koresko, C. D., Makidon, R. B., Berkefeld, T., & Kuchner, M. J. 2001, ApJ, 552, 397

Skumanich, A. 1972, ApJ, 171, 565

Slesnick, C. L., Hillenbrand, L. A., & Carpenter, J. M. 2004, ApJ, 610, 1045

Smith, B. A., Fountain, J. W., & Terrile, R. J. 1992, A&A, 261, 499

Soderblom, D. R. 1983, ApJS, 53, 1

—. 1985, AJ, 90, 2103

Soderblom, D. R., & Clements, S. D. 1987, AJ, 93, 920

Soderblom, D. R., Stauffer, J. R., MacGregor, K. B., & Jones, B. F. 1993, ApJ, 409, 624

Söderhjelm, S. 1999, A&A, 341, 121

Song, I., Caillault, J.-P., Barrado y Navascués, D., & Stauffer, J. R. 2001, ApJ, 546, 352

Song, I., Weinberger, A. J., Becklin, E. E., Zuckerman, B., & Chen, C. 2002, AJ, 124, 514

Southworth, J., Maxted, P. F. L., & Smalley, B. 2005, A&A, 429, 645

Spangler, C., Sargent, A. I., Silverstone, M. D., Becklin, E. E., & Zuckerman, B. 2001, ApJ, 555, 932

Stauffer, J. 2000, in ASP Conf. Ser. 198: Stellar Clusters and Associations: Convection, Rotation, and Dynamos, 255–+

Stauffer, J. R., Barrado y Navascués, D., Bouvier, J., Morrison, H. L., Harding, P., Luhman, K. L., Stanke, T., McCaughrean, M., Terndrup, D. M., Allen, L., & Assouad, P. 1999, ApJ, 527, 219

Stauffer, J. R., Schultz, G., & Kirkpatrick, J. D. 1998, ApJ, 499, L199+

Stephens, D. C., & Leggett, S. K. 2004, PASP, 116, 9

Stern, S. A. 1996, A&A, 310, 999

Sterzik, M. F., Durisen, R. H., Brandner, W., Jurcevic, J., & Honeycutt, R. K. 1997, AJ, 114, 1555

Stetson, P. B. 1987, PASP, 99, 191

Stetson, P. B. 1992, in ASP Conf. Ser. 25: Astronomical Data Analysis Software and Systems I, 297–+

Stevenson, D. J. 1991, ARA&A, 29, 163

Strassmeier, K., Washuettl, A., Granzer, T., Scheck, M., & Weber, M. 2000, A&AS, 142, 275

Strassmeier, K. G., & Rice, J. B. 1998, A&A, 330, 685

Swenson, F. J., Faulkner, J., Rogers, F. J., & Iglesias, C. A. 1994, ApJ, 425, 286

Sylvester, R. J., & Mannings, V. 2000, MNRAS, 313, 73

Takeuchi, T., & Artymowicz, P. 2001, ApJ, 557, 990

Thompson, D., Egami, E., & Sawicki, M. 2001, The Keck Near-Infrared AO Camera. Pre-ship testing., California Institute of Technology, http://www2.keck.hawaii.edu/inst/nirc2/preship_testing.pdf

Tokovinin, A. A., Chalabaev, A., Shatsky, N. I., & Beuzit, J. L. 1999, A&A, 346, 481

Torres, C. A. O., da Silva, L., Quast, G. R., de la Reza, R., & Jilinski, E. 2000, AJ, 120, 1410

Torres, C. A. O., & Ferraz Mello, S. 1973, A&A, 27, 231

Troy, M., Dekany, R. G., Brack, G., Oppenheimer, B. R., Bloemhof, E. E., Trinh, T., Dekens, F. G., Shi, F., Hayward, T. L., & Brandl, B. 2000, in Proc. SPIE Vol. 4007, Adaptive Optical Systems Technology, Peter L. Wizinowich; Ed., 31–40

Tsuji, T. 2002, ApJ, 575, 264

Udry, S., Mayor, M., Naef, D., Pepe, F., Queloz, D., Santos, N. C., & Burnet, M. 2002, A&A, 390, 267

Udry, S., Mayor, M., & Santos, N. C. 2003, A&A, 407, 369

van Albada, T. S. 1968, Bull. Astron. Inst. Netherlands, 20, 47

van Bueren, H. G. 1952, Bull. Astron. Inst. Netherlands, 11, 385

van Dokkum, P. G. 2001, PASP, 113, 1420

van Leeuwen, F. 1999, A&A, 341, L71

van Leeuwen, F., Alphenaar, P., & Brand, J. 1986, A&AS, 65, 309

van Maanen, A. 1945, ApJ, 102, 26

Ventura, P., Zeppieri, A., Mazzitelli, I., & D'Antona, F. 1998, A&A, 334, 953

Vergely, J.-L., Egret, D., Freire Ferrero, R., Valette, B., & Koeppen, J. 1997, in ESA SP-402: Hipparcos—Venice '97, 603–606

Vilhu, O. 1984, A&A, 133, 117

Voges, W., Aschenbach, B., Boller, T., Bräuninger, H., Briel, U., Burkert, W., Dennerl, K., Englhauser, J., Gruber, R., Haberl, F., Hartner, G., Hasinger, G., Kürster, M., Pfeffermann, E., Pietsch, W., Predehl, P., Rosso, C., Schmitt, J. H. M. M., Trümper, J., & Zimmermann, H. U. 1999, A&A, 349, 389

Voges, W., Aschenbach, B., Boller, T., Brauninger, H., Briel, U., Burkert, W., Dennerl, K., Englhauser, J., Gruber, R., Haberl, F., Hartner, G., Hasinger, G., Pfeffermann, E., Pietsch, W., Predehl, P., Schmitt, J., Trumper, J., & Zimmermann, U. 2000, IAU Circ., 7432, 1

Vrba, F. J., Henden, A. A., Luginbuhl, C. B., Guetter, H. H., Munn, J. A., Canzian, B., Burgasser, A. J., Kirkpatrick, J. D., Fan, X., Geballe, T. R., Golimowski, D. A., Knapp, G. R., Leggett, S. K., Schneider, D. P., & Brinkmann, J. 2004, AJ, 127, 2948

Wahhaj, Z., Koerner, D. W., Ressler, M. E., Werner, M. W., Backman, D. E., & Sargent, A. I. 2003, ApJ, 584, L27

Wainscoat, R. J., Cohen, M., Volk, K., Walker, H. J., & Schwartz, D. E. 1992, ApJS, 83, 111

Wallace, L., & Hinkle, K. 1997, ApJS, 111, 445

Wallace, L., Meyer, M. R., Hinkle, K., & Edwards, S. 2000, ApJ, 535, 325

Walter, F. M., Vrba, F. J., Mathieu, R. D., Brown, A., & Myers, P. C. 1994, AJ, 107, 692

Webb, R. A., Zuckerman, B., Platais, I., Patience, J., White, R. J., Schwartz, M. J., & McCarthy, C. 1999, ApJ, 512, L63

Weinberger, A. J., Becklin, E. E., Schneider, G., Chiang, E. I., Lowrance, P. J., Silverstone, M., Zuckerman, B., Hines, D. C., & Smith, B. A. 2002, ApJ, 566, 409

Weinberger, A. J., Becklin, E. E., Schneider, G., Smith, B. A., Lowrance, P. J., Silverstone, M. D., Zuckerman, B., & Terrile, R. J. 1999, ApJ, 525, L53

Weingartner, J. C., & Draine, B. T. 2001, ApJ, 548, 296

Weissman, P. R. 1984, Science, 224, 987

Welsh, B. Y., Crifo, F., & Lallement, R. 1998, A&A, 333, 101

White, R. J. 2002, Pixel Scale and Orientation of PHARO Determined from the Binary Star HD 165341, Tech. rep., California Institute of Technology, http://www.astro.caltech.edu/~metchev/AO/pharo_plate_scale_memo1.pdf

Wichmann, R., Schmitt, J. H. M. M., & Hubrig, S. 2003, A&A, 399, 983

Wilner, D. J., Holman, M. J., Kuchner, M. J., & Ho, P. T. P. 2002, ApJ, 569, L115

Wilson, R. E., & Joy, A. H. 1950, ApJ, 111, 221

Wizinowich, P., Acton, D. S., Shelton, C., Stomski, P., Gathright, J., Ho, K., Lupton, W., Tsubota, K., Lai, O., Max, C., Brase, J., An, J., Avicola, K., Olivier, S., Gavel, D., Macintosh, B., Ghez, A., & Larkin, J. 2000, PASP, 112, 315

Wolf, S. 2003, Computer Physics Communications, 150, 99

Wolf, S., & Henning, T. 2000, Computer Physics Communications, 132, 166

Wright, C. O., Egan, M. P., Kraemer, K. E., & Price, S. D. 2003, AJ, 125, 359

Wright, J. T., Marcy, G. W., Butler, R. P., & Vogt, S. S. 2004, ApJS, 152, 261

Wyatt, M. C. 2003, ApJ, 598, 1321

Wyatt, M. C., & Dent, W. R. F. 2002, MNRAS, 334, 589

Zacharias, N., Urban, S. E., Zacharias, M. I., Wycoff, G. L., Hall, D. M., Monet, D. G., & Rafferty, T. J. 2004, AJ, 127, 3043

Zapatero Osorio, M. R., Béjar, V. J. S., Rebolo, R., Martín, E. L., & Basri, G. 1999, ApJ, 524, L115

Zucker, S., & Mazeh, T. 2002, ApJ, 568, L113

Zuckerman, B., & Becklin, E. E. 1992, ApJ, 386, 260

—. 1993, ApJ, 414, 793

Zuckerman, B., & Song, I. 2004a, ApJ, 603, 738

—. 2004b, ARA&A, 42, 685

Zuckerman, B., Song, I., & Bessell, M. S. 2004, ApJ, 613, L65

Zuckerman, B., Song, I., Bessell, M. S., & Webb, R. A. 2001a, ApJ, 562, L87

Zuckerman, B., Song, I., & Webb, R. A. 2001b, ApJ, 559, 388

Zuckerman, B., & Webb, R. A. 2000, ApJ, 535, 959

Zwahlen, N., North, P., Debernardi, Y., Eyer, L., Galland, F., Groenewegen, M. A. T., & Hummel, C. A. 2004, A&A, 425, L45